



UNIVERSITÀ DEGLI STUDI DI MILANO

Scuola di Dottorato in Fisica, Astrofisica e Fisica Applicata

Dipartimento di Fisica

Corso di Dottorato in Fisica, Astrofisica e Fisica Applicata

Ciclo XXV

Single and Dual-Domain Models to Assess the Effects of Heterogeneity on the Solute Transport in Alluvial Aquifers

Settore Scientifico Disciplinare FIS/06

Supervisori: Professor Guido PARRAVICINI
Professor Mauro GIUDICI

Coordinatore: Professor Marco BERSANELLI

Tesi di Dottorato di:
Fulvia BARATELLI

Anno Accademico 2012-2013

Commission of the final examination:

Membro docente (Presidente):

Prof. Timothy R. Ginn, Department of Civil Environment Engineering - University of California

Membro docente:

Prof. Ezio G. Bolzacchini, Università degli Studi di Milano-Bicocca - Dipartimento di Scienze dell'Ambiente e del Territorio e di Scienze della Terra

Membro docente:

Dr. Edie Miglio, Politecnico di Milano - Dipartimento di Matematica "F. Brioschi"

Membro esperto:

Prof. Ghislain de Marsily, Université Pierre et Marie Curie Paris VI, UMR 7619 SISYPHE

Final examination:

Wednesday, February 13, 2013

Università degli Studi di Milano, Dipartimento di Fisica, Milano, Italy

Cover illustration:

Lac Gelé - Valmasque (picture by Fulvia Baratelli)

MIUR subjects:

FIS/06 - Fisica per il sistema terra e il mezzo circumterrestre

PACS:

92.40.-t Hydrology and glaciology
92.40.Cy Modeling; general theory
92.40.Kf Groundwater

Contents

List of Symbols	viii
List of Figures	xii
List of Tables	xiv
1 Introduction	1
1.1 Motivation	1
1.2 Modeling solute transport in heterogeneous aquifers	4
1.2.1 Deterministic approaches	4
1.2.2 A short review of multi-domain models and their applications	5
1.2.3 Stochastic approaches	7
1.3 Objectives and outline of the study	9
2 Basic equations of the SDM and DDMs	12
2.1 Transport processes	12
2.2 The advective-dispersive equation	14
2.3 The single-domain model (SDM)	15
2.4 The dual-domain models (DDMs)	15
2.4.1 The dual-porosity model (DPorM)	16
2.4.2 The dual-permeability models (DPerMs)	18
2.5 Resident concentration, flux concentration, breakthrough curve and its temporal moments	22
2.6 Boundary conditions for the transport models	24
3 Analytical solutions for the SDM and the UDPerM for a pulse injection	27
3.1 Analytical solution for the SDM	27
3.2 Analytical solution for the UDPerM	29
3.3 Temporal moments of the BTC	30
4 Numerical implementation of the SDM and DDMs	32
4.1 Numerical scheme for the SDM	33
4.1.1 Discretization of the spatial domain	33
4.1.2 Discretization of the temporal domain	34
4.1.3 Discretization of the equation	34
4.1.4 Solution of the discrete equation	35

4.1.5	Correction of truncation errors	37
4.2	Numerical scheme for the DDMs	40
4.3	Validation of the codes by comparison with the results of the analytical models and of HYDRUS-1D	41
4.3.1	HYDRUS-1D	42
4.3.2	Results	43
5	Calibration of the transport models	46
5.1	The Levenberg-Marquardt method	46
5.1.1	The stopping criterium of the iterative LM process	48
5.1.2	Covariance, correlation and conditioning of the problem	49
5.2	Specific aspects of the calibration of the SDM and DDMs	50
5.2.1	Parameters to be estimated	50
5.2.2	Computational issues	50
6	Application of the transport models: interpretation of numerical tracer tests	54
6.1	Case study A. Numerical tracer tests on meter scale blocks of sediments from an alluvial aquifer in the Ticino basin (Northern Italy)	54
6.1.1	Geological and hydrostratigraphic features and geostatistical simulations of the blocks of sediments	55
6.1.2	Numerical experiments of non-reactive solute transport	57
6.1.3	Experimental data	58
6.1.4	Objective functions	61
6.1.5	Overview of the analysis	61
6.1.6	Calibration of the analytical models	62
6.1.7	Calibration of the numerical models	67
6.1.8	Characteristic transport times	71
6.1.9	Results on the conditioning of the Hessian matrix of the objective function and on the correlation matrix	75
6.1.10	Single and dual domain media in a multi-objective framework	75
6.1.11	Concluding remarks on case study A	77
6.2	Case study B. Numerical tracer tests on a decameter scale block from a point bar channel aquifer analogue in the Lambro basin (Northern Italy)	79
6.2.1	Geological and hydrostratigraphic features and ensembles of geostatistical simulations of the block of sediments	79
6.2.2	Numerical experiments of non-reactive solute transport on the ensembles of equiprobable realizations of the block	82
6.2.3	Connectivity analysis: flow and transport indicators, hydrofacies connectivity indicators, percolating clusters	84
6.2.4	Experimental data	85
6.2.5	Calibration of the analytical models	86
6.2.6	Principal component analysis of the equivalent flow and transport parameters and of the connectivity indicators	88
6.2.7	Concluding remarks on case study B	92
7	Application of the transport models: interpretation of laboratory and field tracer tests	94
7.1	Case study C. Real tracer test on a decimeter scale sand column	94
7.1.1	Experimental set up and data	94
7.1.2	Results of the calibration of the SDM and DDMs	95

7.1.3	Concluding remarks on case study C	96
7.2	Case study D. Large-scale natural gradient tracer test at hectometer scale performed in a sand and gravel aquifer at the Cape Cod site	100
7.2.1	Hydrologic characteristics of the site	101
7.2.2	The tracer test	101
7.2.3	Main features of the tracer cloud	101
7.2.4	Experimental data	102
7.2.5	Objective functions	105
7.2.6	Results of the calibration	105
7.2.7	Concluding remarks on case study D	106
7.3	Comments on the advantages of using either the solute concentration or the temporal moments of the BTC for the inversion of the transport models	112
8	Conclusions	115
	Appendices	121
A	Considerations on the analytical solution of the CDPeM	121
B	On the determination of the truncation errors for a Crank-Nicholson upwind approximation of the CDPeM	124
	References	127
	List of Publications	138
	Acknowledgments	139

List of Symbols

The main symbols and acronyms used in this thesis are reported in the following tables. Symbols that appear only in specific parts of the thesis and symbols related to the numerical scheme are omitted.

Symbol	Unit	Description
\mathcal{A}	-	Dimensionless number: advection over exchange (DPorM)
$\mathcal{A}^{(H)}$	-	Dimensionless number of the fast domain: advection over exchange (CDPerM)
$\mathcal{A}^{(L)}$	-	Dimensionless number of the slow domain: advection over exchange (CDPerM)
A	m^2	Area of the cross section of the porous medium
$A^{(H)}$	m^2	Area of the cross section occupied by the fast domain (DPerMs)
$A^{(L)}$	m^2	Area of the cross section occupied by the slow domain (DPerMs)
C	kg m^{-3}	Resident concentration
\tilde{C}	kg s m^{-3}	Laplace transform of the flux concentration
C_n^ℓ	kg m^{-3}	Equivalent 1D concentration (case study D)
C_0	kg m^{-3}	Concentration of the injected solution
C_F	kg m^{-3}	Flux concentration
$C_F^{(H)}$	kg m^{-3}	Flux concentration in the fast domain (DPerMs)
$C_F^{(L)}$	kg m^{-3}	Flux concentration in the slow domain (DPerMs)
$C^{(H)}$	kg m^{-3}	Resident concentration in the fast domain (DPerMs)
C^{im}	kg m^{-3}	Resident concentration in the immobile domain (DPorM)
$C^{(L)}$	kg m^{-3}	Resident concentration in the slow domain (DPerMs)
C^{mob}	kg m^{-3}	Resident concentration in the mobile domain (DPorM)
C_p^*	-	Intrinsic connectivity of the hydrofacies p
C_r	-	Courant number
d	$\text{m}^2 \text{s}^{-1}$	Molecular diffusion coefficient
\mathbf{D}	$\text{m}^2 \text{s}^{-1}$	Dispersion tensor (including molecular diffusion)
$\mathbf{D}^{(H)}$	$\text{m}^2 \text{s}^{-1}$	Dispersion tensor (including molecular diffusion) in the fast domain (DPerMs)
$\mathbf{D}^{(L)}$	$\text{m}^2 \text{s}^{-1}$	Dispersion tensor (including molecular diffusion) in the slow domain (DPerMs)

\mathbf{D}^*	$\text{m}^2 \text{s}^{-1}$	Hydrodynamic dispersion tensor
D	$\text{m}^2 \text{s}^{-1}$	Longitudinal component of \mathbf{D}
D_e	$\text{m}^2 \text{s}^{-1}$	Effective dispersion coefficient
D_L	$\text{m}^2 \text{s}^{-1}$	Longitudinal dispersion coefficient
D_{num}	$\text{m}^2 \text{s}^{-1}$	Numerical dispersion coefficient
D_T	$\text{m}^2 \text{s}^{-1}$	Transverse dispersion coefficient
$D^{(H)}$	$\text{m}^2 \text{s}^{-1}$	Longitudinal component of $\mathbf{D}^{(H)}$
$D^{(L)}$	$\text{m}^2 \text{s}^{-1}$	Longitudinal component of $\mathbf{D}^{(L)}$
h	m	Hydraulic head
\mathbf{H}		Hessian matrix of the objective function ¹
K	m s^{-1}	Hydraulic conductivity
K_{eq}	m s^{-1}	Equivalent hydraulic conductivity
$K^{(H)}$	m s^{-1}	Hydraulic conductivity of the fast domain (DPerMs)
$K^{(L)}$	m s^{-1}	Hydraulic conductivity of the slow domain (DPerMs)
L	m	Length
m_r	s^r	normalized r -th order temporal moment of the breakthrough curve
$m_s^{(H)}$	kg	Mass of solute in the fast domain (DPerMs)
m_s^{mob}	kg	Mass of solute in the mobile domain (DPorM)
M	kg m^{-2}	Mass of solute per unit surface injected in the porous medium
\mathcal{M}	kg m^{-3}	Cumulative breakthrough curve
M_r	$\text{kg m}^{-2} \text{s}^r$	r -th order temporal moment of the breakthrough curve
$M^{(H)}$	kg m^{-2}	Mass of solute per unit surface injected in the fast domain (DPerMs)
$M^{(L)}$	kg m^{-2}	Mass of solute per unit surface injected in the slow domain (DPerMs)
n	-	Porosity
n_e	-	Effective porosity
n_t	-	Total porosity
$n^{(H)}$	-	Porosity of the fast domain (DPerMs)
n^{im}	-	Porosity of the immobile domain (DPorM)
$n^{(L)}$	-	Porosity of the slow domain (DPerMs)
n^{mob}	-	Porosity of the mobile domain (DPorM)
Pe	-	Péclet number
Pe_{num}	-	Numerical Péclet number
$Pe^{(H)}$	-	Péclet number of the fast domain (DPerMs)
$Pe^{(L)}$	-	Péclet number of the slow domain (DPerMs)
\mathbf{q}, q	m s^{-1}	Darcy velocity
\mathbf{q}_{adv}	$\text{kg m}^{-2} \text{s}^{-1}$	Advective solute flux
\mathbf{q}_c, q_c	$\text{kg m}^{-2} \text{s}^{-1}$	Total solute flux
\mathbf{q}_{dif}	$\text{kg m}^{-2} \text{s}^{-1}$	Diffusive solute flux
\mathbf{q}_{disp}	$\text{kg m}^{-2} \text{s}^{-1}$	Solute flux by hydrodynamic dispersion
$\mathbf{q}^{(H)}, q^{(H)}$	m s^{-1}	Darcy velocity of the fast domain (DPerMs)
$\mathbf{q}^{(L)}, q^{(L)}$	m s^{-1}	Darcy velocity of the slow domain (DPerMs)
$\mathbf{q}_c^{\text{mob}}$	$\text{kg m}^{-2} \text{s}^{-1}$	Total solute flux in the mobile domain (DPorM)
$\mathbf{q}_c^{(H)}$	$\text{kg m}^{-2} \text{s}^{-1}$	Total solute flux in the fast domain (DPerMs)

¹The unit is different for each component of the matrix.

$\mathbf{q}_c^{(L)}$	$\text{kg m}^{-2} \text{s}^{-1}$	Total solute flux in the slow domain (DPerMs)
Q	$\text{m}^3 \text{s}^{-1}$	Volumetric flow rate
s	s^{-1}	Laplace coordinate
S	-	Skewness of the breakthrough curve
t	s	Time
t_T	s	Typical time of advective transport
T	s	Duration of the solute injection
\mathbf{v}, v	m s^{-1}	Average pore water velocity
$\mathbf{v}^{(H)}, v^{(H)}$	m s^{-1}	Average pore water velocity of the fast domain (DPerMs)
$\mathbf{v}^{(L)}, v^{(L)}$	m s^{-1}	Average pore water velocity of the slow domain (DPerMs)
V	m^3	Volume of porous medium
V_p	m^3	Volume of pores
V_p^e	m^3	Volume of pores effectively participating in the flow
$V^{(H)}$	m^3	Volume occupied by the fast domain (DPerMs)
$V^{(L)}$	m^3	Volume occupied by the slow domain (DPerMs)
$V_p^{(H)}$	m^3	Volume of pores in the fast domain (DPerMs)
$V_p^{(L)}$	m^3	Volume of pores in the slow domain (DPerMs)
V_p^{mob}	m^3	Volume of pores in the mobile domain (DPorM)
$\mathbf{x} = (x, y, z)$	m	Cartesian coordinates
α	s^{-1}	Solute exchange coefficient
α_L	m	Longitudinal dispersivity
α_T	m	Transverse dispersivity
χ_{m_1}	-	Relative error in the determination of m_1
χ_{μ_2}	-	Relative error in the determination of μ_2
χ^2	-	General objective function
χ_C^2	kg m^{-3}	Objective function (misfit between resident concentrations, case study D)
χ_{CF}^2	-	Objective function (misfit between flux concentrations)
$\chi_{\mathcal{M}}^2$	-	Objective function (misfit between cumulative breakthrough curves)
χ_n^2	kg m^{-3}	Objective function (misfit between concentrations of section n , case study D)
χ_μ^2	-	Objective function (misfit between temporal moments of the breakthrough curves)
Δ	-	Relative difference of the objective function of a DDM with respect to that of the SDM
$\varepsilon^{(H)}$	-	Fraction of the porous medium volume occupied by the fast domain (DPerMs)
$\varepsilon^{(L)}$	-	Fraction of the porous medium volume occupied by the slow domain (DPerMs)
$\mathbf{\Gamma}$		Covariance matrix of the model parameters ²
Γ_s	$\text{kg m}^{-3} \text{s}^{-1}$	Solute exchange term
κ_2	-	Condition number of the Hessian matrix
λ	-	Levenberg-Marquardt coefficient
μ_r	s^r	r -th order central temporal moment of the breakthrough curve

²The unit is different for each component of the matrix.

ρ	-	Correlation matrix between the model parameters
τ	-	Dimensionless time coordinate
τ_e	s	Typical time of solute exchange
ξ	-	Dimensionless space coordinate

Acronyms:

ADE	Advective-Dispersive Equation
BTC	Breakthrough Curve
CBTC	Cumulative Breakthrough Curve
CDPerM	Coupled Dual-Permeability Model
DDM	Dual-Domain Model
DPerM	Dual-Permeability Model
DPorM	Dual-Porosity Model
LM	Levenberg-Marquardt
MLS	Multilevel sampler
MPS	Multiple Point Simulation
PFP	Preferential Flow Path
SDM	Single-Domain Model
SISIM	Sequential Indicator Simulation
UDPerM	Uncoupled Dual-Permeability Model

List of Figures

1.1	BTCs for media with different degrees of heterogeneity	3
2.1	Schematic representation of the equivalent description of a real heterogeneous block according to the different transport models	16
2.2	Comparison of BTCs and CBTCs for a pulse injection and different magnitudes of the solute exchange coefficient	21
4.1	Schematic representation of the grid discretizing the domain	33
4.2	Comparison of the simulations of a pulse injection obtained with: analytical SDM, HYDRUS-1D, numerical SDM uncorrected and corrected for truncation errors	40
4.3	Comparison of the solute concentrations computed by our numerical model with those of HYDRUS-1D and with the analytical solution	45
5.1	Graph of the objective function, for the SDM, in the parameter space (with and without adaptive integration)	53
6.1	Case study A: results of the 3D geostatistical simulation of the three MBs	57
6.2	Case study A: evolution of the solute plumes for different flow orientations and for the different MBs	59
6.3	Optimal values of the objective function $\chi_{\mathcal{M}}$ for the different tests of case study A and for the different transport models	67
6.4	Case study A: experimental and model (SDM and UDPerM) CBTCs for MB1 EW and MB2 WE	68
6.5	Case study A: experimental and best-fit BTCs for MB1 EW, MB2 WE and MB3 WE	69
6.6	Case study A: components relative to the two domains of the BTC of the UDPerM and of the CDPPerM for MB1 EW, MB2 WE and MB3 WE	70
6.7	Qualitative estimate of the Pareto set for MB1 NS and MB2 WE	77
6.8	Case study B: results of one of the 50 equiprobable geostatistical simulations obtained with MPS and SISIM	80
6.9	Case study B: experimental and model variograms	81
6.10	Case study B: plots of the trajectories of the solute particles for six realizations obtained with SISIM and with MPS	83

6.11	Case study B: distribution of the values of D and v obtained with the optimization for the SDM of the realizations of ensembles \mathcal{A} and \mathcal{B}	86
6.12	Case study B: distribution of K_{xx} for the simulations of ensembles \mathcal{A} and \mathcal{B}	87
6.13	Case study B: experimental and model BTCs for a typical realization of ensemble \mathcal{A}	88
6.14	Case study B: experimental and model BTCs for three realizations of ensemble \mathcal{B}	89
6.15	Case study B: distribution of the values of $D^{(H)}$ and $D^{(L)}$ obtained with the optimization for the UDPerM of the realizations of ensembles \mathcal{A} and \mathcal{B}	90
6.16	Case study B: distribution of the values of $v^{(H)}$ and $v^{(L)}$ obtained with the optimization for the UDPerM of the realizations of ensembles \mathcal{A} and \mathcal{B}	91
6.17	Case study B: frequency distribution of the relative variation between SDM and UDPerM merit functions of the realizations of ensembles \mathcal{A} and \mathcal{B}	92
7.1	Experimental set up for case study C	95
7.2	Case study C: experimental and model flux-averaged concentrations at the bottom of the column	97
7.3	Tracer test at Cape Cod (LeBlanc et al., 1991)	100
7.4	Case study D: location of injection wells and MLSs, indication of the five sections for which the average concentrations have been computed, contours of the maximum bromide concentration	103
7.5	Case study D: representation of the sampled surface and of the surface over which the equivalent 1D concentration is computed	104
7.6	Case study D: experimental and model concentrations given by the calibration of the SDM with χ_C and χ_n	108
7.7	Case study D: experimental and model concentrations given by the calibration of the DPorM with χ_C and χ_n	109
7.8	Case study D: experimental and model concentrations given by the calibration of the UDPerM with χ_C and χ_n	110
7.9	Case study D: comparison of the best-fit obtained with SDM, DPorM and UDPerM (calibration with respect to χ_C)	111
7.10	Case study D: comparison of the best-fit obtained with UDPerM and CD-PerM (calibration with respect to χ_C)	111
7.11	Case study D: objective functions χ_C and χ_n , $n = 1, \dots, 5$, obtained with the minimization of χ_C^2 for each model	112
7.12	Comparison of the concentration curves and of their temporal moments for section $n=4$ of case study D	114

List of Tables

2.1	Correspondence between the main physical quantities defined by our CD-PerM and by the models developed by Skopp et al. (1981) and Gerke and van Genuchten (1993)	22
4.1	Ratio of numerical to real dispersion coefficients for different finite difference approximations of the ADE and a uniform grid	37
4.2	Parameters used for the simulation of the pulse injection shown in Figure 4.2	40
4.3	Input parameters of the transport models used for the code validation	42
4.4	Correspondence between the parameters of HYDRUS-1D and the parameters of the SDM and DDMs	44
5.1	Parameters to be estimated for the calibration of the transport models	51
6.1	Case study A: variance of the logarithm of the hydraulic conductivity, fraction of the total volume occupied by the hydrofacies G (open framework gravel) and intrinsic connectivity of G	57
6.2	Number of injected particles and experimental moments for the numerical tests of case study A	60
6.3	Case study A: results of the optimization of $\chi_{\mathcal{M}}^2$ for the analytical SDM	63
6.4	Case study A: results of the optimization of $\chi_{\mathcal{M}}^2$ for the analytical UDPerM	64
6.5	Case study A: values of Δ for the different tests and DDMs	66
6.6	Case study A: results of the optimization of χ_{μ}^2 for the analytical SDM	67
6.7	Case study A: results of the calibration of the numerical SDM	72
6.8	Case study A: results of the calibration of the DPorM	72
6.9	Case study A: results of the calibration of the numerical UDPerM	73
6.10	Case study A: results of the calibration of the CDPerM	73
6.11	Case study A: ratio of the characteristic exchange time to the characteristic time of advective transport and dimensionless numbers Pe and $\mathcal{A}E$ for the DPorM and the CDPerM	75
6.12	Case study A: condition numbers of the Hessian matrix of the objective function $\chi_{\mathcal{M}}$	75
6.13	Case study B: ensemble expected values of the spatial average and variance of hydraulic conductivity for ensembles \mathcal{A} and \mathcal{B}	82
7.1	Case study C: results of the calibration of the SDM	98

7.2	Case study C: results of the calibration of the DPorM	98
7.3	Case study C: results of the calibration of the UDPerM	98
7.4	Case study C: results of the calibration of the CDPerM	98
7.5	Case study C: values of Δ for the different DDMs	99
7.6	Case study C: ratio of the characteristic exchange time to the characteristic time of advective transport and dimensionless numbers Pe and $\mathcal{A}E$ for the DPorM and the CDPerM	99
7.7	Case study C: condition numbers of the Hessian matrix of the objective function χ_{CF}	99

1.1 Motivation

Groundwater slowly flows through the soil or is stored in subsurface natural reservoirs, so that the ions contained in the rocks and in the grains of soil can be released to the water with which they come into contact. In addition to these natural substances, other contaminants harmful to health may be present. Groundwater contamination by pollutants is an issue of fundamental importance, since aquifers are a major source of drinking water in many regions of the world (Fetter, 1999; Rausch et al., 2005; Charbenau, 2006), and is also used to irrigate crops. The contaminants can be introduced directly in groundwater, e.g., through abandoned wells used as illegal dumping; more frequently, the contaminants are released on the soil surface or in the shallow layers of ground, from where they can reach groundwater by infiltration through the unsaturated zone; moreover, the pollutants released in the atmosphere can be carried by precipitation to the soil surface, and then infiltrate in groundwater. Most of the contaminants have an anthropogenic source: for example, the industrial dumpings, the spreading of pesticides, fertilizers and slurry in agriculture, the urban drainage systems, possible accidents in the transport or use of harmful substances and the gaseous emissions of factories and traffic in the atmosphere. The contaminants in groundwater can come from natural sources as well: for example, the emissions of volcanoes in atmosphere, followed by precipitation and infiltration in the ground, or the change in the flow regime of a groundwater system, which can lead to changes in the composition of the groundwater because it reacts differently with the solids forming the aquifer material (Rausch et al., 2005); the different flow regimes may cause harmful substances to dissolve in groundwater, with a consequent deterioration of its quality.

The different kinds of solutes in groundwater can be grouped in reactive solutes and non-reactive (also called conservative) solutes. The former are substances that can take part in physical reactions (for example: radioactive decay, filtration), chemical reactions (for example: adsorption/desorption, ionic exchange, acid/base reactions, oxidation-reduction reactions, precipitation, dissolution) or biological reactions (for example, some bacteria can transform harmful organic compounds in other non-harmful substances). On the other hand, the conservative substances do not take part in any reaction and, in particular, do not interact with the porous medium.

The groundwater for drinking, civil use and irrigation is extracted, through pumping wells, from the aquifers, namely from the pores of unconsolidated materials, e.g., gravel, sand and silt, or from the fractures of rock formations. Therefore, the modeling of water flow and solute transport in the aquifers is a primary task to control the possible effects that the above mentioned sources of contaminants have on water quality, to understand the spatial and temporal scales at which the contaminants spread from the injection area

and reach a water well and finally to assist policymakers in planning possible interventions to prevent contamination of drinking water or to remediate a contaminated region.

A thorough description of the different sources of groundwater contamination, of the issues related to water quality, of the methods of remediation of a contaminated site and of the transport modeling approaches, with the presentation of several case studies, can be found, e.g., in the following textbooks: Bear (1979), Domenico and Schwartz (1998), Fetter (1999), Fetter (2001), Fitts (2002), Charbenau (2006) and Bear and Cheng (2010).

An important issue to be addressed in the modeling of groundwater flow and transport is the heterogeneity of the aquifers, which can occur at different spatial scales. In particular, the alluvial aquifers might be very heterogeneous as a result both of a possibly complex succession of sedimentation, erosion and diagenesis, controlled by climatic cycles, and of the tectonic evolution. The fine scale heterogeneity of the aquifers significantly affects groundwater flow and the transport of contaminants in groundwater at the scales of interest for practical applications. More specifically, the internal architecture of the alluvial sediments may be characterized by the presence of preferential flow paths (PFPs), that are connected bands of high-permeability sediments, e.g., gravel or sandy gravel, where water and solute can move faster than in the fine-grained sediments; on the other hand, there may be hydraulic barriers, that are impermeable components within the sediments, e.g., pebbles and cobbles, or low-permeability regions, e.g., fine sand or clay lenses. PFPs characterize also the fissured aquifers and the macroporous soils, i.e., those soils characterized by the presence of cavities formed by plant roots, earthworm and soil fauna or of drying cracks in case of swelling clay soils (Gerke, 2006). The fractures and the macropores clearly represent PFPs, where water flow and solute transport are much faster than in the matrix blocks. PFPs and hydraulic barriers control the travel times of the particles of solute and the pathways that they follow from the injection area: in particular, PFPs control the early travel times, whereas low-permeability materials control the late travel times.

An efficient transport modeling of such heterogeneous environments is essential in order to avoid the underestimation of the travel times of the solute and to correctly predict the spatial and temporal evolution of a solute plume released in an aquifer. For example, a transport model that does not take into account the PFPs might predict that the solute arrives to a certain area (e.g., to a water well) later than actually happens; moreover, the low-permeability material can slowly release the solute after having stored it for some time, so that the region of interest might still be contaminated at later times than predicted by a model that does not take into account this low-permeability material.

The effects of heterogeneity can be seen, for example, in the spatial distribution of the solute and in the shape of the solute breakthrough curve (BTC), which represents the temporal evolution of the mass of solute that crosses the unit surface of the porous medium per unit time. In particular, for a point injection in an infinite domain, the solute distribution is symmetrical in an homogeneous domain, whereas it is asymmetrical in an heterogeneous domain.

Moreover, for an instantaneous pulse injection of solute in a semi-infinite domain, the classical advective-dispersive equation (ADE) predicts that the BTC is an inverse Gaussian distribution, which is then the typical BTC obtained for a homogeneous domain. This situation is also called Fickian transport, since it results from the assumption that the dispersion of the solute is described by Fick's law.

On the other hand, for heterogeneous domains characterized by PFPs, the BTC resulting from a pulse injection in a semi-infinite domain is characterized by an early peak, which corresponds to the particles of solute that travel fast in the PFPs, and by a long tail, which corresponds to the particles of solute that travel in the low-permeability sed-

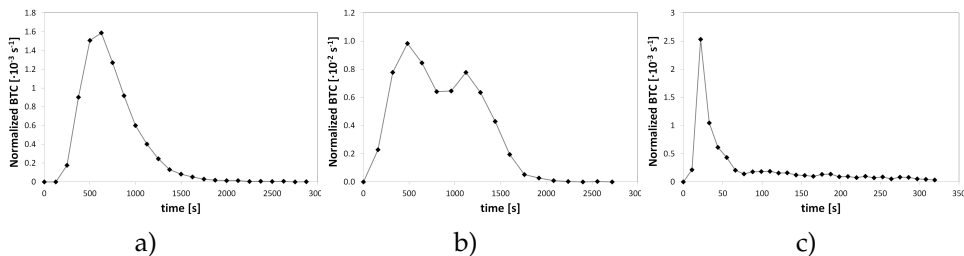


Figure 1.1: BTC resulting from numerical simulations of an instantaneous injection of solute in a semi-infinite medium characterized by homogeneity or random heterogeneity (a), structured heterogeneity with moderate (b) and large (c) permeability contrast between the PFPs and the soil matrix.

iments. The BTC can also show a double peak, in case of a moderate contrast between the velocity of the fast and slow particles. These situations, which cannot be described by the ADE, are also called anomalous or non-Fickian transport, since Fick's law is not a good description for the solute dispersion in these kinds of heterogeneous media.

As an example, Figure 1.1 shows three examples of BTCs obtained from numerical 3D transport experiments simulating an instantaneous injection of solute mass through the border of a semi-infinite domain along the average flow direction; the three BTCs correspond to porous domains characterized by different degrees of heterogeneity. Figure 1.1a) refers to a homogeneous domain (or to a domain with randomly distributed heterogeneity), for which the BTC follows an inverse Gaussian distribution. Figures 1.1b) and c), instead, refer to structured heterogeneous porous media characterized, respectively, by a moderate and large contrast between the permeability of the PFPs and that of the soil matrix.

As pointed out by Feyen et al. (1998), water flow and solute transport in natural soils are significantly influenced by the occurrence of macropores and structured elements, which they refer to as 'micro-heterogeneity', and by the spatial variability of soil properties ('macro-heterogeneity'), or by a combination of micro- and macro-heterogeneity.

As will be explained in section 1.3, the primary objective of this work is to implement and compare different models to effectively describe non-reactive solute transport in heterogeneous aquifers and to apply such models for the interpretation of numerical, laboratory and field tracer tests in different heterogeneous environments. In particular, the effects of heterogeneity at a fine scale will be examined by means of equivalent media, for which the classical ADE or simple modifications, involving few upscaled hydrodispersive parameters, can be applied.

Reactions might affect solute transport in groundwater, but the investigation of their influence on solute transport is outside the scope of this work, which focuses on the effects of the heterogeneity of the conductivity field only.

In order to introduce the precise statement of the objectives of this work, in the following section 1.2 the main approaches to the modeling of solute transport in heterogeneous aquifers are briefly recalled.

1.2 Modeling solute transport in heterogeneous aquifers

Experimental reasons prevent the complete characterization of the fine scale heterogeneity, especially for a large field site; moreover, taking into account the fine scale heterogeneity in a transport model would be computationally very expensive. In order to overcome this issue, several approaches to the modeling of preferential flow and solute transport in heterogeneous soils have been developed; a thorough review and a good list of related references, where those approaches are developed and applied, can be found, e.g., in Jarvis et al. (1991), Dagan and Neuman (1997), Feyen et al. (1998), Rausch et al. (2005), Gerke (2006), Köhne et al. (2009) and Neuman and Tartakovsky (2009).

The different approaches can be grouped into two classes: deterministic and stochastic approaches. According to the former, the model parameters are represented by single values, so that the outcomes of the model are uniquely determined as solution to boundary and initial value problems. The stochastic approaches, instead, assume that the model parameters, and therefore also the model outcomes, are random variables defined by probability distributions.

1.2.1 Deterministic approaches

The most common deterministic approaches to the modeling of preferential flow and solute transport in heterogeneous aquifers are represented by the single-domain model (SDM) and the multi-domain models. These models describe the heterogeneous domain at a fine scale as a simpler domain at a large scale: specifically, a homogeneous domain in the case of the SDM, or a superposition of two or more homogeneous domains characterized by different hydrodispersive parameters in the case of the multi-domain models. The simpler domain should be equivalent to the true heterogeneous domain in the sense that, under the same initial and boundary conditions, they share the same transport properties.

The classical approach to the modeling of solute transport in groundwater is represented by SDMs (see section 2.3), which consider the heterogeneous porous medium as an equivalent homogeneous volume and are based on the ADE. Such models have a straightforward application, but they have the drawback of being inadequate in the case of structured heterogeneous soils, since they cannot describe the effects of heterogeneity on solute transport; for example, the SDMs are not able to take into account the highest velocities of the particles of solute that travel in the PFPs.

The dual-domain models (DDMs, see section 2.4) are the most commonly used multi-domain models and consider the heterogeneous porous medium as a superposition of two domains. In particular, the dual-porosity model (DPorM) assumes that water can flow in one of the two domains (mobile domain) but not in the other (immobile domain), so that transport is dominated by advection in the mobile domain, while it mainly occurs by molecular diffusion in the immobile domain; moreover, the two domains can exchange water and solute and, consequently, the equations for the two domains are coupled. The dual-permeability models (DPerMs), instead, assume that both domains are mobile and that, in general, they have different hydrodispersive parameters (Darcy's velocities and dispersion coefficients); two formulations of such models can be defined depending on whether the two domains are considered either as coupled (CDPerM), i.e., they can exchange water and solute, or uncoupled (UDPerM).

An extension of the DPorM is represented by the multi-rate mass transfer (MRMT) model developed by Haggerty and Gorelick (1995), as briefly described in the following section 1.2.2. According to the MRMT model, the heterogeneous porous medium is

modeled as a superposition of a mobile domain and of a finite set of immobile domains that exchange solute with the mobile domain at different rates.

1.2.2 A short review of multi-domain models and their applications

The DDMs have been introduced in the context of the petroleum industry research, in order to study the possible exploitation of fissured groundwater and petroleum reservoirs, and to simulate observed pressure at wells that could not be reproduced by the standard SDM (Rausch et al., 2005); among these pioneering studies, it is worth mentioning Barenblatt et al. (1960), Warren and Root (1963), Coats and Smith (1964) and Bibby (1981).

In particular, the first applications of the DDMs aimed at the description of flow in fractured rocks or in partially saturated macroporous soils. Such porous media are characterised by large variations in pore water velocity between two sub-domains that correspond to the fractures or macropores (fast or mobile domains) and to the rock or soil matrix (slow or immobile domains).

For example, Warren and Root (1963) proposed a DPorM to simulate water flow in naturally fractured reservoirs, which were considered as superpositions of the matrix blocks (immobile domain, primary porosity) and the fracture network (mobile domain, secondary porosity), that exchanges water with the matrix. Zimmerman et al. (1993) and Lim and Aziz (1995) derived more accurate expressions for the fracture/matrix interaction than that assumed by Warren and Root (1963), which is linear and proportional to the difference of water pressure between fractures and matrix. Coats and Smith (1964) and Bibby (1981) developed DPorMs to describe not only the water flow but also the transport of solutes in fissured aquifers.

Later, the DDMs were also applied to model the transport of solutes in partially saturated media and structured soils. For example, van Genuchten and Wierenga (1976) extended the dual-porosity approach, initially developed for fractured reservoirs, to structured soils. Two dual-porosity approaches were also employed by Rao et al. (1980a,b) to describe different tracer tests in water saturated columns of aggregated and non-aggregated porous media consisting of porous ceramic spheres randomly distributed through packings of glass microbeads or fine sand; these tests were characterized either by a nearly symmetrical BTC or by a significant tailing of the BTC. The major relevance of the research conducted by Rao et al. (1980a,b) is in the fact that, analyzing the problem of radial diffusion from spherical porous spheres, they provide an expression for computing the mass transfer rate coefficient from the system parameters instead of estimating it by curve-fitting.

An important generalization of the DPorMs is represented by the MRMT model developed by Haggerty and Gorelick (1995). The MRMT model originates from the observation that real aquifers are characterized by a complex heterogeneity, with an extremely wide range of particle sizes, aggregates of particles and lenses of low-permeability material; therefore, different mass transfer processes occur at different scales and with different rates: for example, the pore-scale intra-particle diffusion, or the mass transfer between low-permeability lenses and the surrounding higher permeability regions, at centimeter to meter scale, or the mass transfer between fractures and rock matrix, at millimeter to kilometer scale. The MRMT model of Haggerty and Gorelick (1995) takes into account all these different mass transfer processes by modeling the heterogeneous domain as a superposition of one mobile domain and a finite set of immobile domains; each immobile domain is characterized by a different mass transfer coefficient to represent the different mass transfer processes that occur at different rates. These mass transfer pro-

cesses are modeled as linear (first-order). The concentration in the immobile domains is given by a time convolution of the mobile concentration and a memory function. The MRMT model developed by Haggerty and Gorelick (1995) is a deterministic approach, as the discrete distribution of domains is associated with the physical geometry at fine scale.

The DPorM represents a particular case of the more general MRMT model: it corresponds to the one-rate linear MRMT model, which is obtained by assuming that all mass transfers occur with the same rate, i.e., only one mobile domain and one immobile domain are considered to form the equivalent domain.

Skopp et al. (1981) introduced a DPerM, i.e., a DDM for which both regions are mobile and exchange solute through a linear interaction term, in the case of a steady state water flow. Ma and Selim (1995) showed that the DPerM developed by Skopp et al. (1981) permits describing the bimodal peaks of the BTCs. A similar approach was applied by Schwartz et al. (2000) to describe the reactive-transport of a solute in a fine-textured soil. Gerke and van Genuchten (1993, 1996) developed a DPerM for simulating variably saturated transient water flow and solute transport in structured porous media or fractured rocks; in particular, they introduced an interaction term between the two mobile regions which accounts for both advective and diffusive exchanges of solute.

More recently, the multi-domain models have also been applied to other kinds of heterogeneous geological formations: unconsolidated sediments, alluvial aquifers or structured soils. Such porous media are characterized by a less strong contrast of hydraulic conductivity than the fractured rocks or the macroporous soils; nevertheless, they can have connected bands of permeable material, e.g., gravel, that constitute channels for preferential flow and transport. For example, Flach et al. (2004) showed that the DPorM was able to simulate the tritium migration through the unconsolidated sediments at the Savannah River Site (South Carolina) with much more accuracy than the SDM. Among the examples of applications of DPorMs to alluvial aquifers, one of the most thorough is probably the interpretation of the tracer tests performed at the research site located in the Columbus Air Force Base in Mississippi, also called Macrodispersion Experiment (MADE) site, as reviewed by Zheng et al. (2011). The MADE site is highly heterogeneous and characterized by the presence of PFPs, at the centimeter to decimeter scale, which is smaller than the typical grid scale of a transport model, so that they cannot be taken into account in the heterogeneous field used in numerical models; nevertheless, these small scale PFPs strongly influence the transport of solutes, as shown, e.g., by Harvey and Gorelick (2000), Feehley and Zheng (2000), Julian et al. (2001) and Liu et al. (2010). In these papers, it was shown that the classical modeling approach, based on the ADE, is not suitable to describe the solute transport at the MADE site, while a dual-domain mass transfer model (DDMT), which is equivalent to the DPorM, is able to correctly reproduce the spatio-temporal evolution of the solute plume and to describe the effects of the small scale PFPs. In particular, Zheng and Gorelick (2003), Liu et al. (2004), Liu et al. (2007) and Ronayne et al. (2010) stress that the solute transport in a heterogeneous environment with small scale PFPs can be adequately described both by a transport model including only advection and molecular diffusion, i.e., by the standard ADE, in which the decimeter scale PFPs are explicitly taken into account in the heterogeneous field, and by a DDMT in which the small scale PFPs are not explicitly taken into account; the latter approach is clearly more practical for large scale field sites, for which it is not possible to map all the small scale PFPs.

1.2.3 Stochastic approaches

As already mentioned, aquifer heterogeneity occurs at different scales and, in practice, measurements of hydraulic conductivity, and other aquifer properties, can be performed only at a limited set of points of the domain under study, so that the real heterogeneity field is never known with certainty and the values of the hydraulic conductivity in the rest of the domain are subject to uncertainty. This observation has led to the development of stochastic approaches to the modeling of groundwater flow and solute transport. In other words, the uncertainty of the hydraulic conductivity suggests to consider this quantity as a random function of space and time, that may be conditioned on the measured data. As a consequence, whereas in the traditional deterministic approaches the model outcomes (water head, velocity, concentration) are represented by unique values, in the stochastic approach the model outcomes are random functions defined by the corresponding probability density functions (Dagan, 1983; Dagan and Neuman, 1997). An important merit of the stochastic approaches is that they provide not only predictions of solute concentrations and mass fluxes, but also measures of the associated prediction errors (Neuman, 2004; Neuman and Tartakovsky, 2009).

Different classes of stochastic approaches can be found in the literature.

A first class is represented by the Lagrangian approach developed by Dagan (1982, 1988, 1989, 1990), according to which the solute plume is considered as composed of several particles containing a certain mass of solute. The path and the velocity of each particle is considered as a stochastic process, for which the statistical moments can be approximated with the spatial moments, through the hypothesis of ergodicity. In particular, the dispersion tensor can be computed from the covariance of the components of the particle path. This theory predicts that, under proper hypotheses, the dispersion tensor increases linearly for small times and approaches a constant value for large times. This approach can be applied to describe transport in weakly heterogeneous aquifers as, for example, in Bellin et al. (1992).

Another approach is the generalized form of the MRMT model, which was extended by Haggerty and Gorelick (1998) by assuming an infinite set of immobile domains; in this case, a probability density function of the mass transfer rates must be defined to compute the memory function. Several forms of this probability density function can be assumed to properly describe the late time behaviour of the BTCs, as shown by Haggerty et al. (2000).

Another class of stochastic approaches is represented by the stream-tube models (see, e.g., Feyen et al. (1998)), according to which the heterogeneous soil is modeled as an ensemble of stream tubes that are independent, i.e., they do not exchange water and solute. Water flow and solute transport are described within each stream tube with a certain transport model, which may be a simple advective transport model for conservative solutes (Dagan and Bresler, 1979) or a more complex convective-dispersive-reactive transport model to describe systems with multicomponent nonlinear reactions (Ginn, 2001; Seeboonruang and Ginn, 2006).

Neuman and Tartakovsky (2009) reviewed four stochastic approaches for the description of non-Fickian transport in heterogeneous porous media. One of these approaches is represented by the stochastic ADE (or space time nonlocal ADE, stnADE). This approach assumes that, at a local scale, the groundwater flow is Darcian and solute transport is Fickian, i.e., well described by the ADE. Since the hydraulic parameters and the forcing terms entering in the local flow and transport equations are random variables, such equations become stochastic. The aim is that of computing the first two conditional moments of the concentration and of the mass flux. One way to solve the stochastic

flow and transport equations is that of the conditional Monte Carlo simulations: several realizations of the velocity are generated and the ADE is solved for each field, then the results obtained from the different realizations are averaged to obtain the sample moments. This approach is computationally very demanding. An alternative and computationally faster method of solution of the stochastic flow and transport equations can be found, e.g., in Guadagnini and Neuman (1999); Ye et al. (2004); Morales-Casique et al. (2006). This method consists in solving a system of statistical moments equations, which are integro-differential equations and include non-local parameters depending on more than one point in space-time. The major drawback of this method is that the integro-differential equations are not closed and the most common method to solve them is valid for mildly heterogeneous media or well-conditioned strongly heterogeneous media.

The continuous-time random walk (CTRW) represents another common stochastic approach (see, e.g., Berkowitz et al. (2006) for a review of this method). The CTRW model describes the transport of the solute particles in a heterogeneous medium as a random walk in space and time, so that both transition lengths and transition times are random variables (Dentz and Berkowitz, 2003). As highlighted by Dentz and Berkowitz (2003), CTRW methods are developed to describe BTCs in strongly heterogeneous porous media and, from this point of view, they are preferable to the stnADE approach.

Another class of stochastic approaches is based on the fractional advective-dispersive equation (f-ADE); an example of development and application of this approach can be found, e.g., in San Jose Martinez et al. (2007). While the ADE assumes that the solute dispersion results from the Brownian motion of the solute particles, the f-ADE assumes that the random movement of the solute particles is rather the Lévy motion, which, respect to the Brownian motion, allows more frequent large jumps of the particles from one point of the space to another. This assumption permits to describe the heavy-tailed distributions typical of non-Fickian transport. A drawback of this method is the lack of a link between the model parameters and the measurable medium properties (Neuman and Tartakovsky, 2009).

Under proper hypotheses, some equivalences between the different stochastic approaches can be established, as discussed, e.g., by Neuman and Tartakovsky (2009). It was shown by Dentz and Berkowitz (2003) that the CTRW is formally equivalent to the generalized form of the MRMT model, under the hypothesis that the joint transition time and length distribution decouples into spatially-dependent transition length and time-dependent transition times distributions. Moreover, as discussed by San Jose Martinez et al. (2007), both the ADE and the f-ADE are special cases of the CTRW formulation.

Some field tracer tests have been performed to develop and test different transport models in heterogeneous formations. The MRMT model (Zhang et al., 2007a), the f-ADE model (Zhang et al., 2007b; Zhang and Benson, 2008), and the CTRW method (Berkowitz and Scher, 1998) have been applied to interpret the tracer tests performed at the MADE site. Furthermore, natural gradient tracer tests have been conducted at the Borden site, Ontario, (Mackay et al., 1986), in a sand aquifer (well sorted, fine to medium sand) and at Cape Cod, Massachusetts, (LeBlanc et al., 1991), in a medium to coarse sand and gravel aquifer. For these two tests, the tracer clouds showed similar features: the spreading occurs mainly in the longitudinal direction, with a small spreading in the transverse and vertical directions. For the Borden test, a stochastic approach has been applied, e.g., by Sudicky (1986) and a deterministic fractal-multifractal approach by Puente et al. (2001).

A forced gradient tracer test in a stratified aquifer at the Rocky Mountain Arsenal, Colorado (Thorbjarnarson and Mackay, 1997), characterized by a range of three orders of magnitude in hydraulic conductivity, showed that the interpretation of the data with a model assuming homogeneity, as the SDM, results in erroneous estimates of transport

parameters. A dual-porosity approach was used to interpret the tracer tests at the Waste Isolation Pilot Plant (WIPP, Ostensen (1998)) in New Mexico, a nuclear waste repository located in an area characterized by the presence of fractured rocks formations; nevertheless, this study showed that the effects of the dual porosity formations on the contaminant transport was negligible, so that the formation can be adequately modeled as a single domain medium.

1.3 Objectives and outline of the study

Within the framework outlined in the previous sections, this work aims to contribute to:

1. the search of effective transport models, applicable to alluvial aquifers at the field scale, to correctly predict the transport of contaminants in heterogeneous aquifers;
2. the understanding of the link between the soil structure (sediments connectivity, presence of PFPs and hydraulic barriers) and the effective transport parameters of such models.

In order to reach these general goals, the specific objectives of this work can be summarized as follows:

- implement 1D single and dual-domain transport models (SDM, DPorM, UDPerM and CDPerM);
- calibrate the different models with the results of some numerical, laboratory or field experiments of conservative solute transport performed in portions of aquifers with different degrees of heterogeneity and at different scales;
- analyze the relation between the effective parameters of the models and the heterogeneity pattern of the particular case studies;
- compare the effectiveness of the different models in describing the effects of PFPs on the solute transport and, specifically, on the BTC.

Notice that, as mentioned in section 1.2.2, the development and most applications of DDMs refer to transport processes in unsaturated soils or fractured rocks, i.e., for media with a dramatic difference among the transport physical properties of two subdomains. Roughly speaking, differences of several orders of magnitude between the hydraulic conductivities of matrix and fractures, or of pores and macropores, makes it obvious the need for the DDM approach. This work aims to assess the relevance of DDMs even for alluvial sediments which could be characterised by a relatively narrow range of hydraulic conductivity, i.e., covering “few” orders of magnitude. Moreover, it is important to observe that, as briefly reviewed in section 1.2.2, most of the applications of DDMs to heterogeneous structured soils and fractured or alluvial aquifers that can be found in the literature refer to the DPorM, whereas very few applications of the CDPerM have been published so far, as this model requires the estimate of a larger set of parameters.

As emphasized by textbooks on flow and transport in porous media, solute transport simulation requires the knowledge of the groundwater velocity field, i.e., it requires to solve first a flow model. In this work, only the transport modeling is treated, and it is assumed that the flow field is either known (by estimation from direct measurements or by solution of a flow model) or calibrated from the concentration measurements. The latter approach can be useful in situations where concentration data are available, but

the groundwater flow is unknown and can be estimated through the calibration of the transport model against concentration data.

Feyen et al. (1998) and Gerke (2006) highlighted the importance of the solute transport modeling in the unsaturated zone of the ground, as this is the region through which chemicals must pass to reach the groundwater. In this work, in order to simplify the analysis and to focus on the most fundamental aspects of the solute transport in heterogeneous aquifers, only the solute transport through the saturated zone is considered and it is always assumed, even if not specified, that the solute is conservative and that it does not modify the physical properties of water (density and viscosity).

Four case studies are analyzed in this work, as described in chapters 6 and 7.

The first two examples (case studies A and B, chapter 6) refer to numerical experiments of non-reactive transport performed with a particle tracking technique in some prismatic blocks of sediments which were dug into two real aquifer analogues of Northern Italy and whose facies distribution was reconstructed by means of 3D geostatistical simulations in previous work (Zappa et al., 2006; dell’Arciprete et al., 2012a). In both cases, the numerical transport experiments simulate the instantaneous injection of solute through the upstream face of the blocks.

In particular, case study A consists of three meter-scale blocks coming from the same aquifer analogue but belonging to three different sedimentological facies; therefore, this case study permits to compare the effects of different sedimentary structures on the solute transport and to compare the performance of different transport models in describing such effects.

Case study B consists of a ten-meter-scale block belonging to a different aquifer analogue, so that it represents a further example of heterogeneous environment to test the transport models. Nevertheless, the major novelty with respect to the previous case study is that 50 equiprobable realizations were obtained for this block of sediments with two methods of geostatistical simulation (dell’Arciprete, 2010; dell’Arciprete et al., 2012a). The two ensembles of realizations show different features, e.g., they have different connectivity patterns, even if they refer to the same block of sediments and they are equiprobable; in addition, different structures are found also among the realizations of a single ensemble. A real aquifer can be considered as a single realization of a stochastic process; in other words, the ensembles of realizations of this case study represent equally likely situations that could be found in the field. Therefore, this case study allows to analyze the effects of different structures on the solute transport by means of a statistical analysis of the results: the assessment of the ensemble uncertainties on the effective parameters of the models gives an estimate of the uncertainty of the results drawn from a single realization. Finally, the correlation between the connectivity indicators and the flow and transport effective parameters can be studied within a stochastic framework in order to assess the relevance of this relation.

The two other case studies, which are described in chapter 7, refer to real tracer tests. Case study C consists of a laboratory tracer test performed on a 20 cm homogeneous sand column by Ivan Toloni (Toloni, 2011) at LHyGeS (Laboratoire d’Hydrologie et de Géochimie de Strasbourg, Université de Strasbourg). In this experiment, a dye was injected through the top surface of the column at a constant rate for a certain time interval; the results showed a significant tail in the BTC measured at the bottom of the column, which is unexpected for a homogeneous sand column. Case study D is represented by the field tracer test performed in a 200 m long region in a sand and gravel aquifer at the Cape Cod site (LeBlanc et al., 1991), that was already mentioned in section 1.2.3. Case studies C and D allow to improve the assessment of the relevance of the different transport models for different heterogeneous environments and for different scales;

moreover, since they are based on hard data from laboratory or from the field, they represent an important step towards the development of a transport modeling approach that is effectively applicable to real problems.

Summing up, these four case studies differ both for the degree of heterogeneity and for the spatial scales involved.

After the present introductory chapter, the main quantities and the basic equations of the SDM, DPorM and DPerM are recalled in chapter 2; moreover, the initial and boundary conditions describing the four case studies, that can be grouped in pulse and step injection, are specified.

Chapters 3 and 4 are devoted to the development of the forward transport models. In particular, chapter 3 presents the analytical solutions of the SDM and UDPerM for an instantaneous injection of solute in a semi-infinite domain; to the author's knowledge, the technique employed to derive such solutions, which is based on the Laplace transform, cannot be generalized for the solution of the CDPerM, as discussed in appendix A.

Therefore, as described in chapter 4, a numerical scheme has been developed to solve all the transport models for the initial and boundary conditions relevant to the case studies. The models have been implemented with a Crank-Nicholson finite difference scheme, an upwind technique for the convective term and a second-order correction to reduce numerical dispersion due to truncation errors. The codes are then validated by comparing their outcomes with results obtained with the analytical models and with the software HYDRUS-1D for the simulation of a pulse injection in a semi-infinite domain.

Chapter 5 describes the method used to calibrate the transport models, which is based on the Levenberg-Marquardt algorithm to minimize the misfit between the experimental data and the models outcomes.

In chapters 6 and 7 the results of the application of the transport models to the four case studies is presented and discussed.

Most of the results of this work have been published in the international scientific literature (Baratelli et al., 2011; Giudici et al., 2011) or are the subject of papers under revision or submitted for the publication (dell'Arciprete et al., 2012b; Baratelli et al., 2012). Here the results are shown with further details, so that a thorough and structured overview can be given. In particular some remarks about the relevance of the results obtained with this work are discussed in chapter 8.

Basic equations of the SDM and DDMs

In this chapter, the basic equations of the SDM and DDMs are presented. First of all, the transport processes of a conservative solute in groundwater and the advective-dispersive equation, with the corresponding single-domain model, are recalled, based on the textbooks by de Marsily (1986) and Rausch et al. (2005). The dual-porosity model is described following Rausch et al. (2005); the dual-permeability models are based on the papers by Skopp et al. (1981) and Gerke and van Genuchten (1993).

Then, some quantities are defined for later use in the model calibration: the resident and flux concentrations, the breakthrough curve, with the corresponding temporal moments, and the cumulative breakthrough curve.

Finally, the initial and boundary conditions, which are applied to the different transport models to describe the case studies analysed in this work, are presented.

2.1 Transport processes

The transport processes of a conservative solute in groundwater are represented by advection, molecular diffusion and hydrodynamic dispersion.

The displacement of water in the porous medium implies the displacement of the particles of solute, a process that is called advective (or convective) transport. The advective solute flux \mathbf{q}_{adv} represents the mass of solute that crosses by advection a unit surface of the porous medium perpendicular to the groundwater flow direction per unit time. It is given by:

$$\mathbf{q}_{\text{adv}} = C\mathbf{q}, \quad (2.1)$$

where C is the volumetric solute concentration, which from now on will be simply called concentration and represents the mass of solute per unit volume of solution, and \mathbf{q} is Darcy's velocity (or specific discharge), i.e., the volume of solution that crosses the unit surface of the porous medium per unit time. Notice that in the following we will deal only with saturated porous media, so that the volume of solution coincides with the volume of pores. The groundwater velocity (or average pore water velocity, \mathbf{v}) is linked to Darcy's velocity by $\mathbf{q} = n_e\mathbf{v}$, where $n_e = V_p^e/V$ is the effective porosity, i.e., the ratio of the volume of pores that effectively participate in the flow, V_p^e , to the volume of the porous medium, V .

Molecular diffusion is the displacement of solute determined by the possible gradient of concentration in the porous medium: the solute moves from high concentration regions to low concentration regions. The solute flux by molecular diffusion is given by Fick's law:

$$\mathbf{q}_{\text{dif}} = -n_t d \nabla C, \quad (2.2)$$

where $n_t = V_p/V$ is the total porosity, i.e., the ratio of the volume of all the pores, V_p , to the volume of the porous medium, and d is the molecular diffusion coefficient in the porous medium. Unlike advection, molecular diffusion occurs also in a stagnant fluid; this is the reason why the total porosity appears in equation (2.2) instead of the effective porosity. In particular, as discussed, e.g., by de Marsily (1986), the concentration C in the mobile fraction of water may be different from the concentration C' in the immobile fraction of water, i.e., in the water present in the dead-end pores or in the water adhering to the grain surfaces of the porous medium. Moreover, also the diffusion coefficient may change between the mobile (d) and the immobile (d') fraction of water, so that equation (2.2) should be written rigorously as:

$$\mathbf{q}_{\text{dif}} = -n_e d \nabla C - (n_t - n_e) d' \nabla C'. \quad (2.3)$$

The hydrodynamic dispersion of a solute is determined by variations of groundwater velocity which occur at different scales: at the scale of a single pore (zero velocity at the border of the grain, maximum velocity in the center of the pore), at the scale of two or more pores (for a given flow rate, the velocity is smaller in larger pores, but, for a Poiseuille flow, the flow rate increases with the fourth power of the pore radius, so that the velocity increases with the squared pore radius and is larger in larger pores¹; moreover, there are variations of the direction of velocity due to the spatial arrangement of the pores) and at scales larger than the pore scale (heterogeneous domains are characterized by spatially varying hydraulic conductivity and, therefore, by spatially varying flow velocity). The advective term takes into account, via Darcy's velocity, the mean flow field, while the dispersive term includes the effects of the heterogeneity, which determines the real flow field, whose details at fine scale are generally unknown. It is usually assumed that the solute flux by hydrodynamic dispersion has an expression analogous to Fick's law, i.e.:

$$\mathbf{q}_{\text{disp}} = -\mathbf{D}^* \nabla C, \quad (2.4)$$

where \mathbf{D}^* is the hydrodynamic dispersion tensor, which is a symmetrical second-order tensor whose principal directions are the direction of the groundwater velocity \mathbf{v} , and two orthogonal directions perpendicular to \mathbf{v} . In the reference system of its principal directions, \mathbf{D}^* has the following components:

$$\begin{bmatrix} D_L & 0 & 0 \\ 0 & D_T & 0 \\ 0 & 0 & D_T \end{bmatrix},$$

where D_L and D_T are called longitudinal and transverse dispersion coefficients respectively and depend on the module of Darcy's velocity, q , and on the longitudinal and transverse dispersivities, α_L and α_T , through the following relations: $D_L = \alpha_L q$, $D_T = \alpha_T q$. The longitudinal dispersivity is from five to hundred times larger than the transverse dispersivity (de Marsily, 1986), so that \mathbf{D}^* is anisotropic, and the solute plume spreads more along the direction of groundwater flow than along the perpendicular directions.

¹ For a given pressure gradient $\Delta p/L$, the flow rate for a Poiseuille flow across a circular pore of radius r varies according to

$$Q = \frac{\rho \pi}{8\eta} \frac{\Delta p}{L} r^4,$$

where ρ is density and η is viscosity. Therefore, the average velocity in a pore is given by:

$$v = \frac{Q}{\pi r^2} = \frac{\rho}{8\eta} \frac{\Delta p}{L} r^2.$$

2.2 The advective-dispersive equation

In a Cartesian coordinate system (x, y, z) , the transport equation for a conservative solute is obtained by applying the principle of mass conservation to a control volume, denoted with Ω , which is centered at a certain position \mathbf{x} in the porous medium and bounded by a surface $\partial\Omega$. Assuming that there are no sources or sinks of solute in Ω , the solute mass conservation in Ω is given by the following expression:

$$\frac{d}{dt} \int_{\Omega} [n_e C + (n_t - n_e) C'] d^3 \mathbf{x} = \int_{\partial\Omega} \mathbf{q}_c \cdot \mathbf{n}^{\text{in}} d^2 \mathbf{x}, \quad (2.5)$$

where $d^3 \mathbf{x}$ is the element of volume of Ω , $d^2 \mathbf{x}$ is the element of surface of $\partial\Omega$, \mathbf{n}^{in} is the unit vector normal to $\partial\Omega$ directed towards the inside of Ω and \mathbf{q}_c is the total solute flux, that is the sum of the advective, diffusive and dispersive solute fluxes defined in section 2.1: $\mathbf{q}_c = \mathbf{q}_{\text{adv}} + \mathbf{q}_{\text{dif}} + \mathbf{q}_{\text{disp}}$. Equation (2.5) states that the time derivative of the solute mass contained in Ω (left-hand side) equals the total solute flux entering the domain through its border $\partial\Omega$ (right-hand side). Considering the expressions of the solute fluxes (2.1), (2.3) and (2.4), \mathbf{q}_c is given by:

$$\mathbf{q}_c = \mathbf{q}C - n_e d \nabla C - (n_t - n_e) d' \nabla C' - \mathbf{D}^* \nabla C. \quad (2.6)$$

Applying the divergence theorem and considering the arbitrariness of the volume Ω , equation (2.5) becomes:

$$n_e \frac{\partial C}{\partial t} + (n_t - n_e) \frac{\partial C'}{\partial t} = -\nabla \cdot \mathbf{q}_c. \quad (2.7)$$

In the hypothesis that the concentrations in the mobile and immobile fraction are the same, i.e., C and C' instantaneously reach an equilibrium, $C \approx C'$ and $d \approx d'$. Moreover, assuming that $n_t \approx n_e$, equations (2.6) and (2.7) reduce respectively to:

$$\mathbf{q}_c = n(\mathbf{v}C - \mathbf{D} \nabla C), \quad (2.8)$$

$$n \frac{\partial C}{\partial t} = -\nabla \cdot \mathbf{q}_c, \quad (2.9)$$

where, denoting with \mathbf{I} the identity matrix, the tensor $\mathbf{D} = \mathbf{D}^*/n + d\mathbf{I}$ has been introduced. Notice that, from now on, we will refer to \mathbf{D} as dispersion tensor, without specifying that it includes the effects of both molecular diffusion and hydrodynamic dispersion; also, we will no more distinguish between the total and the effective porosity, and we will refer to the porosity n as approximating both n_t and n_e .

Combining equations (2.8) and (2.9), the classical form of the advective-dispersive equation describing the transport of a conservative solute in groundwater is obtained:

$$\frac{\partial C}{\partial t} = -\nabla \cdot (\mathbf{v}C - \mathbf{D} \nabla C). \quad (2.10)$$

Notice that the same equation is deduced by assuming that $C' \approx 0$ in equations (2.6) and (2.7), i.e., if there is no solute in the immobile fraction of water.

2.3 The single-domain model (SDM)

The single-domain model (SDM) is the classical approach to the modeling of solute transport in a porous medium. It considers the heterogeneous domain as an equivalent homogeneous domain, as represented in Figure 2.1. In this case, the average pore water velocity v and the elements of the dispersion tensor \mathbf{D} are constant effective parameters that characterize the equivalent homogeneous domain and they can be taken out from the divergence operator at the right-hand side of equation (2.10).

Therefore, for a one-dimensional flow and transport along the x direction (to which we restrict from now on), equations (2.8) and (2.10) respectively reduce to:

$$q_c(x, t) = n \left[vC(x, t) - D \frac{\partial C}{\partial x}(x, t) \right], \quad (2.11)$$

$$\frac{\partial C}{\partial t} = -v \frac{\partial C}{\partial x} + D \frac{\partial^2 C}{\partial x^2}, \quad (2.12)$$

where $D = D_L/n + d$ is the longitudinal component of the dispersion tensor \mathbf{D} . Notice that the dependence on x and t in equation (2.11) has been specified to highlight that the solute flux varies with space and time because the concentration varies in space and time, while the parameters n , v and D are constant. In equation (2.12), and elsewhere, the dependence of C on x and t is implied.

In the following, we will refer to the transport equation of the SDM (2.12) as advective-dispersive equation (ADE), even if it is a simplified form of the more general advective-dispersive equation (2.10).

2.4 The dual-domain models (DDMs)

The DDMs represent the heterogeneous domain as an equivalent superposition of two homogeneous domains, which are characterized by different hydrodispersive parameters. Different formulations of the DDMs have been defined in the literature depending on the following model assumptions:

- either both domains can be considered as mobile, i.e., water can flow in both domains, or water is mobile in one domain and immobile in the other domain;
- the two domains can be considered as either coupled, i.e., they can exchange water and solute, or uncoupled.

According to the first alternative, two classes of DDMs can be defined:

- dual-porosity model (DPorM, section 2.4.1), which assumes that water can flow in one of the two domains (mobile domain) but not in the other (immobile domain) and that the two domains can exchange water and solute (see Coats and Smith (1964) and other references in section 1.2.2); the DPorM is also called stagnant region model (Skopp et al., 1981), compartment model (Gerke, 2006) or mobile-immobile model;
- dual-permeability models (DPerMs, section 2.4.2), which assume that both domains are mobile. In this case, according to the second alternative, two subclasses of models can be defined: uncoupled (UDPerM) or coupled (CDPerM). The UDPerM is also called capillary bundle model (Skopp et al., 1981), while the CDPerM

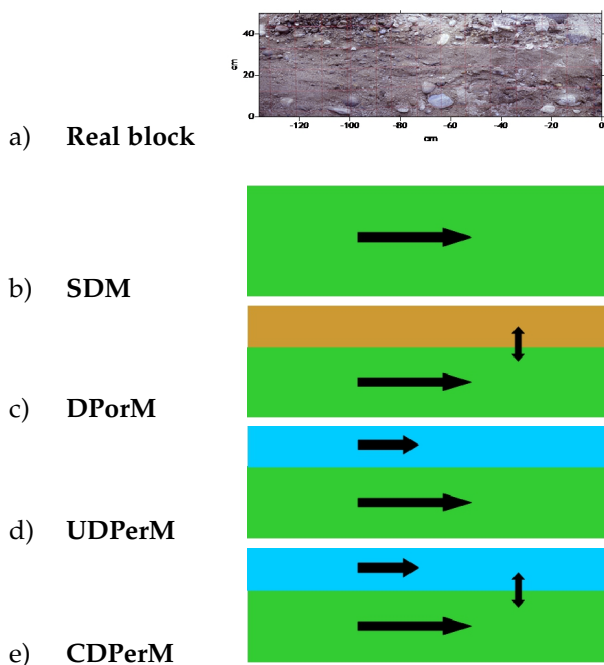


Figure 2.1: Schematic representation of the equivalent description of a real heterogeneous block, a), according to the different transport models: b) SDM, c) DPorM, d) UPerM and e) CDPorM. The arrows indicate the possible movement or transfer of water and solute.

is also referred to as two-region model (Skopp et al., 1981), dual-porosity model (Gerke and van Genuchten, 1993), dual-continuum or dual-domain model (Rausch et al., 2005).

2.4.1 The dual-porosity model (DPorM)

The DPorM (see Figure 2.1) describes the heterogeneous domain as an equivalent superposition of one mobile domain, in which water flows and the solute is transported both by advection and dispersion, and one immobile domain, in which water cannot flow and the solute is transported only by molecular diffusion. The mobile and immobile domains exchange solute if they have a different solute concentration; therefore, the solute can diffuse from the mobile to the immobile domain, which can store the solute for some time before diffusing it again in the mobile domain.

In order to obtain the transport equations of the DPorM, the principle of mass conservation is applied to each of the two domains with a method similar to that applied in section 2.2. In particular, the time variation of the solute mass contained in the mobile domain is balanced both by the solute flux crossing its border and by the solute mass exchanged with the immobile domain. On the other hand, the time variation of the solute mass contained in the immobile domain is assumed to be balanced only by the mass exchanged with the mobile domain; in fact, the only non-zero component of the solute flux in the immobile domain is q_{dif} , which can be considered negligible with respect to the solute exchange term. Therefore, the mass conservation equations for the mobile and

immobile domains are given respectively by:

$$\frac{d}{dt} \int_{\Omega} n^{\text{mob}} C^{\text{mob}} d^3 \mathbf{x} = \int_{\partial \Omega} \mathbf{q}_c^{\text{mob}} \cdot \mathbf{n}^{\text{in}} d^2 \mathbf{x} - \int_{\Omega} \Gamma_s d^3 \mathbf{x}, \quad (2.13)$$

$$\frac{d}{dt} \int_{\Omega} n^{\text{im}} C^{\text{im}} d^3 \mathbf{x} = \int_{\Omega} \Gamma_s d^3 \mathbf{x}, \quad (2.14)$$

where $C^{\text{mob}} = m_s^{\text{mob}}/V_p^{\text{mob}}$ is the local concentration in the mobile domain (mass of solute in the mobile domain, m_s^{mob} , per unit volume of solution in the mobile domain, V_p^{mob}), $n^{\text{mob}} = V_p^{\text{mob}}/V$ is the porosity of the mobile domain; C^{im} and n^{im} are the corresponding quantities for the immobile domain, with $n = n^{\text{mob}} + n^{\text{im}}$. Finally, Γ_s is the exchange term, that represents the mass of solute that is exchanged per unit volume of porous medium and unit time. A linear exchange term is commonly adopted for Γ_s (Coats and Smith, 1964; van Genuchten and Wierenga, 1976; Skopp et al., 1981):

$$\Gamma_s = \alpha (C^{\text{mob}} - C^{\text{im}}), \quad (2.15)$$

where α is the solute exchange coefficient, which has the dimensions of an inverse time, so that the solute is exchanged more rapidly for large values of α .

From equation (2.8), the expression of the solute flux in the mobile domain is given by:

$$\mathbf{q}_c^{\text{mob}} = n^{\text{mob}} (\mathbf{v} C^{\text{mob}} - \mathbf{D} \nabla C^{\text{mob}}), \quad (2.16)$$

which coincides with the solute flux in the total domain, \mathbf{q}_c , as the solute flux in the immobile domain is negligible. Therefore, from equations (2.13), (2.14) and (2.15), applying the divergence theorem and reducing to the one-dimensional case, the transport equations of the DPorM are obtained:

$$\frac{\partial C^{\text{mob}}}{\partial t} = -v \frac{\partial C^{\text{mob}}}{\partial x} + D \frac{\partial^2 C^{\text{mob}}}{\partial x^2} - \frac{\alpha}{n^{\text{mob}}} (C^{\text{mob}} - C^{\text{im}}), \quad (2.17)$$

$$\frac{\partial C^{\text{im}}}{\partial t} = \frac{\alpha}{n^{\text{im}}} (C^{\text{mob}} - C^{\text{im}}). \quad (2.18)$$

If L is the spatial length of the domain, equations (2.17) and (2.18) can be rewritten in terms of the dimensionless space and time coordinates $\xi = x/L$ and $\tau = vt/L$ as:

$$\frac{\partial C^{\text{mob}}}{\partial \tau} = -\frac{\partial C^{\text{mob}}}{\partial \xi} + \frac{1}{Pe} \frac{\partial^2 C^{\text{mob}}}{\partial \xi^2} - \frac{1}{\mathcal{A}E} (C^{\text{mob}} - C^{\text{im}}), \quad (2.19)$$

$$\frac{\partial C^{\text{im}}}{\partial \tau} = \frac{1}{\mathcal{A}E} (C^{\text{mob}} - C^{\text{im}}), \quad (2.20)$$

where the two following dimensionless numbers have been introduced:

- the Péclet number:

$$Pe = \frac{Lv}{D}, \quad (2.21)$$

which is given by the ratio of the coefficients of the convective and dispersive terms and represents the relative importance of the convective and dispersive transport processes; in particular, high Péclet numbers correspond to situations in which the solute transport is dominated by advection, while the dispersive transport is less important;

- the dimensionless number $\mathcal{A}E$:

$$\mathcal{A}E = \frac{n^{\text{mob}}v}{\alpha L}. \quad (2.22)$$

This number is given by the ratio of the coefficients of the advective and exchange terms and quantifies the relative importance of the solute exchange with respect to the advective solute transport; in particular, if $\mathcal{A}E \ll 1$, the solute exchange is more important, i.e., it is faster, than the convective solute transport. Notice that the inverse of this dimensionless number is equivalent to the first Damköhler number, which is defined as the ratio of the reaction rate to the advective transport rate (Cho et al., 2011; Kuntz and Grathwohl, 2009); in the case of the MRMT model, Haggerty and Gorelick (1995) associate a first Damköhler number DaI_j to each j -th mass transfer process. Reducing this definition to the one-rate mass transfer model, the relation $\mathcal{A}E^{-1} = DaI/n$ holds.

The effects of the dual-porosity, that is the effects of the presence of an immobile domain exchanging solute with the mobile domain, can be quantified also by comparing the typical time of advective transport, t_T with the typical time of solute exchange, τ_e , which are defined by Rausch et al. (2005) as:

$$t_T = \frac{L}{v}, \quad (2.23)$$

$$\tau_e = \frac{\ln 2}{\alpha}. \quad (2.24)$$

As discussed by Rausch et al. (2005), three different situations can be distinguished depending on the relative values of t_T and τ_e :

- $\tau_e/t_T \gg 1$: the mass exchange is so slow that it does not influence the solute concentrations for the transport times of interest; in this case, the solute transport can be described well also by the standard ADE (2.12) for a medium with the same porosity of the mobile domain n^{mob} , as the immobile domain does not contribute to the solute transport.
- $\tau_e/t_T \ll 1$: the mass exchange is so rapid that there is an instantaneous equilibrium between the mobile and immobile domains, which have the same solute concentration; in this case, the solute transport can be described well also by the standard ADE (2.12) for a medium with porosity n .
- $\tau_e/t_T \approx 1$: the typical times of mass exchange and advective transport share the same order of magnitude; in this case the effect of dual-porosity is strongest. In particular, for a pulse injection of solute, the BTC is asymmetric and characterized by tailing, so that it cannot be described by the ADE.

2.4.2 The dual-permeability models (DPerMs)

The DPerMs (see Figure 2.1) describe the heterogenous domain as an equivalent superposition of two domains: one fast domain (H) and one slow domain (L) characterized, respectively, by high and low values of hydraulic conductivity, $K^{(H)}$ and $K^{(L)}$. In the following, the superscripts (H) and (L) will be employed to refer the different physical

quantities to the corresponding domain. In particular, let $\varepsilon^{(H)}$ and $\varepsilon^{(L)}$ denote the fractions of the porous medium volume occupied by the (H) and (L) domains, respectively: $\varepsilon^{(H)} = V^{(H)}/V$, $\varepsilon^{(L)} = V^{(L)}/V$. The following trivial relation holds:

$$\varepsilon^{(H)} + \varepsilon^{(L)} = 1. \quad (2.25)$$

It is assumed that $\varepsilon^{(H)}$ and $\varepsilon^{(L)}$ characterise also the areal fractions of the fast and slow domains: $\varepsilon^{(H)} \simeq A^{(H)}/A$, $\varepsilon^{(L)} \simeq A^{(L)}/A$. The local porosity in the fast domain is denoted as $n^{(H)} = V_p^{(H)}/V^{(H)}$, where $V_p^{(H)}$ is the volume of pores in (H) ; the local porosity in the slow domain $n^{(L)}$ is defined in a similar way. Therefore, the porosity of the medium is given by $n = \varepsilon^{(H)}n^{(H)} + \varepsilon^{(L)}n^{(L)}$.

If a hydraulic gradient ∇h is applied to the porous medium, the fast and the slow domains will be subjected to the same hydraulic gradient, since the two domains are overlapped at every point. Therefore, if K_{eq} is the equivalent hydraulic conductivity, the Darcy velocities $\mathbf{q} = -K_{\text{eq}}\nabla h$, $\mathbf{q}^{(H)} = -K^{(H)}\nabla h$ and $\mathbf{q}^{(L)} = -K^{(L)}\nabla h$ can be defined as the flow rate across a unit surface of the respective domains and are related to the average pore water velocities by $\mathbf{q} = n\mathbf{v}$, $\mathbf{q}^{(H)} = n^{(H)}\mathbf{v}^{(H)}$ and $\mathbf{q}^{(L)} = n^{(L)}\mathbf{v}^{(L)}$. The link among the Darcy velocities is then given by:

$$\mathbf{q} = \varepsilon^{(H)}\mathbf{q}^{(H)} + \varepsilon^{(L)}\mathbf{q}^{(L)}, \quad (2.26)$$

which can be rewritten in terms of the average pore water velocities as:

$$\mathbf{v} = n^{-1} \left[\varepsilon^{(H)}n^{(H)}\mathbf{v}^{(H)} + \varepsilon^{(L)}n^{(L)}\mathbf{v}^{(L)} \right]. \quad (2.27)$$

The solute flux in each of the two domains is given by expressions analogous to (2.8):

$$\mathbf{q}_c^{(H)} = n^{(H)} \left[\mathbf{v}^{(H)}C^{(H)} - \mathbf{D}^{(H)}\nabla C^{(H)} \right], \quad (2.28)$$

$$\mathbf{q}_c^{(L)} = n^{(L)} \left[\mathbf{v}^{(L)}C^{(L)} - \mathbf{D}^{(L)}\nabla C^{(L)} \right], \quad (2.29)$$

where $\mathbf{q}_c^{(H)}$ represents the mass of solute contained in (H) that crosses the unit surface of (H) per unit time, $C^{(H)} = m_s^{(H)}/V_p^{(H)}$ is the concentration in (H) , given by the ratio of the solute mass contained in (H) to the volume of pores in (H) and $\mathbf{D}^{(H)}$ is the dispersion tensor in (H) ; $\mathbf{q}_c^{(L)}$, $C^{(L)}$ and $\mathbf{D}^{(L)}$ are the corresponding quantities for (L) .

The solute flux in the porous medium can then be obtained from the solute fluxes in the two domains according to the following relation:

$$\mathbf{q}_C = \varepsilon^{(H)}\mathbf{q}_C^{(H)} + \varepsilon^{(L)}\mathbf{q}_C^{(L)}. \quad (2.30)$$

For a 1D flow and transport along x , equation (2.30) can also be used to define the relation between the flux concentrations, which are defined for each of the two domains as in section 2.5:

$$C_F = q^{-1} \left[\varepsilon^{(H)}q^{(H)}C_F^{(H)} + \varepsilon^{(L)}q^{(L)}C_F^{(L)} \right]. \quad (2.31)$$

As already done in sections 2.2 and 2.4.1, the solute mass conservation can now be applied to each of the two domains:

$$\frac{d}{dt} \int_{\Omega} n^{(H)}C^{(H)}d^3\mathbf{x} = \int_{\partial\Omega} \mathbf{q}_c^{(H)} \cdot \mathbf{n}^{\text{in}}d^2\mathbf{x} - \int_{\Omega} \Gamma_s d^3\mathbf{x}, \quad (2.32)$$

$$\frac{d}{dt} \int_{\Omega} n^{(L)}C^{(L)}d^3\mathbf{x} = \int_{\partial\Omega} \mathbf{q}_c^{(L)} \cdot \mathbf{n}^{\text{in}}d^2\mathbf{x} + \int_{\Omega} \Gamma_s d^3\mathbf{x}, \quad (2.33)$$

where, as in Skopp et al. (1981), for Γ_s it is commonly assumed a linear expression analogous to (2.15):

$$\Gamma_s = \alpha \left(C^{(H)} - C^{(L)} \right). \quad (2.34)$$

Reducing to the one-dimensional case, equations (2.32), (2.33) and (2.34) give the equations governing the solute transport in the two domains:

$$\frac{\partial C^{(H)}}{\partial t} = -v^{(H)} \frac{\partial C^{(H)}}{\partial x} + D^{(H)} \frac{\partial^2 C^{(H)}}{\partial x^2} - \frac{\alpha}{\varepsilon^{(H)} n^{(H)}} \left[C^{(H)} - C^{(L)} \right], \quad (2.35)$$

$$\frac{\partial C^{(L)}}{\partial t} = -v^{(L)} \frac{\partial C^{(L)}}{\partial x} + D^{(L)} \frac{\partial^2 C^{(L)}}{\partial x^2} + \frac{\alpha}{\varepsilon^{(L)} n^{(L)}} \left[C^{(H)} - C^{(L)} \right]. \quad (2.36)$$

Two formulations of the DPerM can be defined according to the value of the solute exchange coefficient α . In particular, for the uncoupled dual-permeability model (UDPerM) $\alpha = 0$, which means that there is no exchange of solute between the two domains and that the solute is transported in each of the two domains independently of the other. In this case, equation (2.35) is uncoupled from (2.36), so that the transport equations of the UDPerM are given by a set of two uncoupled ADEs, one for each of the two domains. According to the coupled dual-permeability model (CDPerM), instead, α is, in general, different from zero, so that the two domains can exchange solute if they have a different solute concentration, and the transport equations (2.35) and (2.36) are coupled.

Notice that the UDPerM is, clearly, the limiting case of the CDPerM for vanishing α . Nevertheless, in this work the two models are considered as distinct models. This is explained by the fact that, as will be shown in chapter 5, the calibration of the two models requires the estimation of different sets of parameters; moreover, as will be shown in chapter 3 and appendix A, the UDPerM can be solved analytically, which is not the case for the CDPerM. Therefore, the implementation and inversion of the UDPerM requires less computational effort than the CDPerM.

The equations of the DPerMs can be rewritten in terms of the dimensionless coordinates ξ and τ , as already shown for the DPorM in section 2.4.1; in this case the dimensionless numbers Pe and $\mathcal{A}E$ can be defined separately for each of the two domains as in (2.21) and (2.22):

$$Pe^{(H)} = \frac{Lv^{(H)}}{D^{(H)}}, \quad Pe^{(L)} = \frac{Lv^{(L)}}{D^{(L)}}; \quad (2.37)$$

$$\mathcal{A}E^{(H)} = \frac{\varepsilon^{(H)} n^{(H)} v^{(H)}}{\alpha L}, \quad \mathcal{A}E^{(L)} = \frac{\varepsilon^{(L)} n^{(L)} v^{(L)}}{\alpha L}. \quad (2.38)$$

Moreover, the typical advective transport time t_T and the typical exchange time τ_e can be defined as in the DPorM by relations (2.23) and (2.24), where the characteristic transport velocity v is given by the 1D counterpart of equation (2.27).

As observed by Skopp et al. (1981), if the interaction is large, i.e., if $\tau_e \ll t_T$, then the CDPerM reduces to the SDM; the same holds for the DPorM. In other words, a large interaction is typical of homogeneous soils, whereas a small interaction is typical of structured soils and can explain early peaks or double peaks in the BTCs of conservative solutes. This is confirmed by Ma and Selim (1995), who showed that the bimodal shape of the BTC gradually changes into an unimodal shape as the interaction increases.

On the contrary, if the interaction is small, i.e., if $\tau_e \gg t_T$, the CDPerM does not necessarily reduce to the SDM, differently from the behaviour of the DPorM. In particular, if the parameters D and v of the two domains are similar, then the CDPerM is indeed

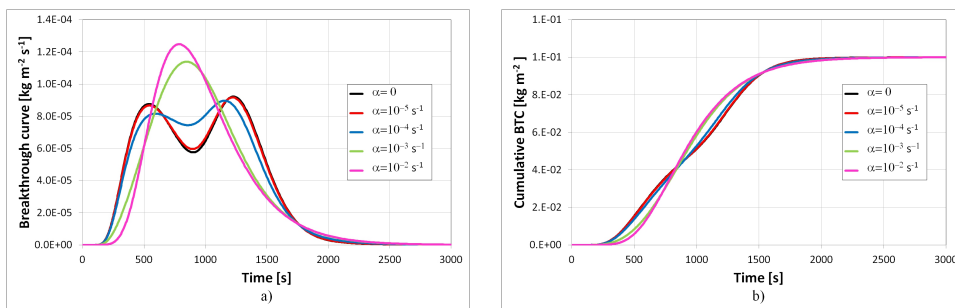


Figure 2.2: Comparison of the BTC (a) and CBTC (b) for a pulse injection and different magnitudes of the solute exchange coefficient α .

equivalent to the SDM; instead, if the parameters are different, then the CDPeM reduces to the UDPeM.

Finally, it should be considered that several expressions have been proposed for computing the exchange coefficient α : for example, Skopp et al. (1981) and Gerke and van Genuchten (1993) report some expressions that depend on parameters like the size and shape of the aggregates and of the interaggregate pores, or on the geometric properties of the fracture system. Gerke (2006) refers to the particular cases of uniformly sized spherical aggregates, solid cylindrical aggregates and parallel rectangular fracture systems. Nevertheless, such information about the geometry of the soil are usually difficult to obtain, and the method of calibrating α seems more easily applicable to practical situations.

Figure 2.2 compares the BTC and the cumulative breakthrough curve (CBTC, see section 2.5) obtained in the case of a pulse injection for different magnitudes of the solute exchange term. It can be seen that, for low values of the exchange term, the BTC is characterized by a bimodal shape, with two peaks corresponding to the fast and the slow domains. As the exchange term increases, the two peaks become less evident and the shape of the BTC is similar to that obtained with a SDM.

Comparison between the CDPeM and the models developed by Skopp et al. (1981) and Gerke and van Genuchten (1993)

The CDPeM is similar to the models developed by Skopp et al. (1981), where a steady state flow is assumed as in our CDPeM, and by Gerke and van Genuchten (1993), where, instead, a variably saturated flow is considered. In particular, the fast and slow domains correspond, respectively, to the fractures or macropores and to the soil or rock matrix, and the indices (H) and (L) in our CDPeM correspond, respectively, to A and B in Skopp et al. (1981) and to f and m in Gerke and van Genuchten (1993). For convenience, in Table 2.1 the correspondence between the main physical quantities defined by the different transport models is listed.

With the correspondences of Table 2.1, equations [3] and [4] in Skopp et al. (1981) coincide with the transport equations of the CDPeM (2.35) and (2.36). Moreover, notice that Skopp et al. (1981) define a dimensionless interaction coefficient which is equivalent to the inverse of \mathcal{A} , $\mathcal{A}^{(H)}$ or $\mathcal{A}^{(L)}$, where the porosity n and velocity v of the porous medium are used instead of the porosities and velocities of the mobile, fast or slow

CDPerM	Skopp et al. (1981)	Gerke and van Genuchten (1993)
$C^{(H)}, C^{(L)}$	A, B	c_f, c_m
$n, n^{(H)}, n^{(L)}$		$\varepsilon, \varepsilon_f, \varepsilon_m$
$\varepsilon^{(H)}, \varepsilon^{(L)}$		$w_f, 1 - w_f$
$\varepsilon^{(H)}n^{(H)}, \varepsilon^{(L)}n^{(L)}$	θ_A, θ_B	
α	L	$\alpha_s(1 - w_f)\theta_m$

Table 2.1: Correspondence between the main physical quantities defined by our CDPerM and by the models developed by Skopp et al. (1981) and Gerke and van Genuchten (1993).

domains. The dimensionless coefficient introduced by Skopp et al. (1981) is therefore representative of the whole porous medium.

Concerning the model of Gerke and van Genuchten (1993), the water flow is described by a coupled pair of Richards equations, while the solute transport is described by a coupled pair of ADEs; the latter are represented by Equations (17a) and (17b) of Gerke and van Genuchten (1993), which reduce to equations (2.35) and (2.36) in the case of a saturated flow and a conservative solute, which means that the water contents θ_f and θ_m coincide with the porosities ε_f and ε_m , the retardation coefficients R_f and R_m are equal to 1 and the first-order decay coefficients μ_f and μ_m vanish. Moreover, the solute mass transfer term Γ_s is given by Equation (19) of Gerke and van Genuchten (1993):

$$\Gamma_s = (1 - d)\Gamma_w\phi_f c_f + d\Gamma_w\phi_m c_m + \alpha_s(1 - w_f)\theta_m(c_f - c_m), \quad (2.39)$$

which includes both a convective and a diffusive component; the first two terms of equation (2.39) represent the convective component and depend on Γ_w , which is proportional to the difference in pressure heads between the fracture and the matrix pore systems; the coefficient d is 1 if the matrix pressure head is greater than the fracture pressure head, i.e., the water exchange is from the matrix to the fracture, whereas d is 0 if the exchange is from the fracture to the matrix; ϕ_f and ϕ_m are the volume of water in the fracture and, respectively, in the matrix per unit volume of water in the medium. The third term in equation (2.39) is the diffusive component of the mass transfer term and is proportional to the difference in concentrations between the two domains.

In our CDPerM it is assumed that the pressure height is the same in the two domains, so that the mass transfer term for solute transport includes only the dispersive/diffusive term, while the convective term vanishes; therefore, in equation (2.39), Γ_w is set to zero, while $\alpha_s(1 - w_f)\theta_m$ corresponds to α in equations (2.35) and (2.36).

2.5 Resident concentration, flux concentration, breakthrough curve and its temporal moments

Depending on the injection technique, the boundary conditions of the transport equations can be expressed in terms of two different kinds of concentrations defined by Kreft and Zuber (1978): the concentration in resident fluid, or resident concentration (C), and the concentration in fluid flux, or flux concentration (C_F). In the same way, the measurement technique determines if the experimental data refer to C or C_F . The resident concentration C represents the mass of solute per unit volume of fluid contained in an elementary volume of the system at a given instant, while the flux concentration C_F represents the mass of solute per unit volume of fluid passing through a given cross section

at an elementary time interval. In other words, C_F is the ratio of the solute flux to the Darcy's velocity: $C_F = q_c/q$.

The use of the appropriate definition depends on the problem under study and on the type of measurement. For instance, the injection of solute can be uniform in the inflow cross-section or proportional to the velocity at every point of the cross section; as a consequence, the boundary condition will be expressed in terms of C or C_F , respectively. Concerning the measurement technique, the concentrations measured in samples of fluid collected by samplers installed in the porous domain correspond to C , while the concentrations measured in the fluid crossing a given cross-section correspond to C_F .

In the case of the SDM, considering the expression of the solute flux (2.11), C_F is given by:

$$C_F(x, t) = \frac{q_c(x, t)}{q} = C(x, t) - \frac{D}{v} \frac{\partial C}{\partial x}(x, t). \quad (2.40)$$

In the case of the DDMs, C_F is obtained by substituting in definition (2.40) the corresponding expressions of the solute flux, which are given by the 1D counterpart of (2.16) for the DPorM and of (2.30) for the DPerMs.

The solute breakthrough curve (BTC) is defined as the mass of solute, that crosses a unit surface of the porous medium per unit time, as a function of time. The BTC at a certain position $x = L$ is then given by $q_c(L; t)$.

In the following, it will be useful also to consider the cumulative breakthrough curve (CBTC), which represents the total mass of solute that has crossed a unit surface of the porous medium until time t from the solute injection, as a function of t . The CBTC at a certain position $x = L$ is then given by:

$$\mathcal{M}(L; t) = \int_0^t q_c(L; t') dt'. \quad (2.41)$$

The temporal moments of the BTC can be as well useful quantities to characterize solute transport. Temporal moments have often been used (Naff, 1992; Cirpka and Kitadinis, 2000; Bardsley, 2003; Luo et al., 2006, 2008) to study solute transport and by Varni and Carrera (1998) and Ginn et al. (2009) to analyse groundwater ageing, even if these quantities could be affected by outliers especially in the tail of the BTC (Jacobsen et al., 1992). In the present work, the identification of the models parameters will be based also on the temporal moments of the BTCs for few tests.

The r -th order temporal moment $M_r(L)$ of the BTC in $x = L$ is defined as:

$$M_r(L) = \int_0^{+\infty} t^r q_c(L; t) dt, \quad (2.42)$$

where q_c is given by (2.11) for the SDM, and by the 1D counterpart of (2.16) and (2.30) for the DPorM and the DPerMs respectively. Recalling the physical meaning of q_c , $M_0(L)$ represents the total mass of the solute that crosses the unit surface of the porous medium at a distance L from the inflow boundary.

The r -th order moment normalized with respect to the zero-th order moment is denoted by $m_r(L) = M_r(L)/M_0(L)$ and the r -th order central moment μ_r is defined as:

$$\mu_r(L) = \frac{1}{M_0} \int_0^{+\infty} [t - m_1(L)]^r q_c(L; t) dt, \quad (2.43)$$

where $m_1(L)$ represents the average arrival time of the particles of solute at the distance L . The second-order central moment μ_2 is the variance of the distribution of the arrival

times of the particles of solute. Finally, we consider the skewness parameter, defined as $S = \mu_3/\mu_2^{3/2}$, which gives information about the asymmetry of the BTC. In particular, Stagnitti et al. (2000) highlight that the skewness can indicate the existence of preferential flow, observing that asymmetric BTCs with early peak and increased tailing to the right of the peak are characterized by $S > 0$.

Notice that μ_2 and μ_3 can also be computed from the normalised moments m_r , $r = 1, 2, 3$, according to the following relations:

$$\mu_2 = m_2 - m_1^2, \quad (2.44)$$

$$\mu_3 = m_3 + 2m_1^3 - 2m_1m_2. \quad (2.45)$$

In section 3.3 the analytical expressions of M_r , m_r and μ_r will be derived for the BTCs of the SDM and UDPerM in the case of a pulse injection of solute and for $r \leq 3$.

2.6 Boundary conditions for the transport models

Different initial and boundary conditions can be applied to the transport equations depending on the particular situation that is simulated.

The case studies analysed in this work (see chapters 6 and 7) can all be described as semi-infinite 1D domains, initially free of solute, in which a certain mass of solute is injected at an initial time either instantaneously (pulse injection) or continuously for a certain time interval (step injection). It is then useful to report here the general form of the boundary conditions describing these examples. In particular, a Dirichlet (or first-type) boundary condition is imposed at an infinite distance from the injection point, whereas a Cauchy (third-type) boundary condition is imposed at the inflow boundary, where the solute flux is assigned. Such conditions are first written for the SDM, and then they are easily generalized to the DDMs.

Boundary conditions for the SDM

Let $x = 0$ and $t = 0$ define the injection point and the injection time, respectively. Given the semi-infinite spatio-temporal domain $x \in [0, +\infty)$ and $t \in [0, +\infty)$, it is assumed that initially there is no solute in the domain, so that the initial condition is simply given by:

$$C(x, 0) = 0, \quad x > 0. \quad (2.46)$$

Boundary conditions commonly adopted in literature for $x \rightarrow +\infty$ assume either a zero concentration (Ogata and Banks, 1961; Lassey, 1988) or a vanishing concentration gradient (Parker and van Genuchten, 1984; van Genuchten and Parker, 1984; Toride et al., 1993; Vanderborght et al., 2005). The latter type of boundary condition implies that at an infinite distance from the injection point the solute flux is given by the advective flux only, which, given the zero concentration initial condition and considering that the solute propagation velocity is finite, must also vanish, and the zero-concentration boundary condition is obtained. Therefore, the boundary condition for $x \rightarrow +\infty$ used in this work is given by:

$$\lim_{x \rightarrow +\infty} C(x, t) = 0, \quad t \geq 0. \quad (2.47)$$

In the case of a pulse injection, let M be the mass of solute per unit surface which is injected instantaneously at $t = 0$ through the border of the domain at $x = 0$; the boundary

condition at $x = 0$ is then given by:

$$q_c(0, t) = M\delta(t), \quad t \geq 0, \quad (2.48)$$

where $\delta(t)$ is the Dirac delta.

In the case of a step injection, the solute is injected continuously with a constant rate for a certain duration T , so that the boundary condition at $x = 0$ becomes:

$$q_c(0, t) = \frac{M}{T} I_{[0, T]}(t), \quad t \geq 0, \quad (2.49)$$

where $I_{[0, T]}(t)$ is the characteristic function of the interval $[0, T]$.

Boundary conditions for the DPorM

The initial and boundary conditions for the DPorM are obtained from conditions (2.46) to (2.49), assuming that all the solute initially enters the mobile domain:

$$C^{\text{mob}}(x, 0) = 0, \quad C^{\text{im}}(x, 0) = 0, \quad x > 0, \quad (2.50)$$

$$\lim_{x \rightarrow +\infty} C^{\text{mob}}(x, t) = 0, \quad \lim_{x \rightarrow +\infty} C^{\text{im}}(x, t) = 0, \quad t \geq 0, \quad (2.51)$$

Pulse injection:

$$q_c^{\text{mob}}(0, t) = M\delta(t), \quad q_c^{\text{im}}(0, t) = 0, \quad t \geq 0, \quad (2.52)$$

Step injection:

$$q_c^{\text{mob}}(0, t) = \frac{M}{T} I_{[0, T]}(t), \quad q_c^{\text{im}}(0, t) = 0, \quad t \geq 0. \quad (2.53)$$

Boundary conditions for the DPerMs

The initial and boundary conditions for the DPerMs are obtained from conditions (2.46) to (2.49), assuming that the mass of solute injected in $x = 0$ splits between the two domains:

$$C^{(H)}(x, 0) = 0, \quad C^{(L)}(x, 0), \quad x > 0, \quad (2.54)$$

$$\lim_{x \rightarrow +\infty} C^{(H)}(x, t) = 0, \quad \lim_{x \rightarrow +\infty} C^{(L)}(x, t) = 0, \quad t \geq 0, \quad (2.55)$$

Pulse injection:

$$q_c^{(H)}(0, t) = M^{(H)}\delta(t), \quad q_c^{(L)}(0, t) = M^{(L)}\delta(t), \quad t \geq 0, \quad (2.56)$$

Step injection:

$$q_c^{(H)}(0, t) = \frac{M^{(H)}}{T} I_{[0, T]}, \quad q_c^{(L)}(0, t) = \frac{M^{(L)}}{T} I_{[0, T]}, \quad t \geq 0, \quad (2.57)$$

where $M^{(H)}$ denotes the mass of solute that initially enters the (H) domain per unit surface of the (H) domain and $M^{(L)}$ is defined similarly for the (L) domain, so that the following relation holds:

$$M = \varepsilon^{(H)} M^{(H)} + \varepsilon^{(L)} M^{(L)}. \quad (2.58)$$

Analytical solutions for the SDM and the UDPerM for a pulse injection

The SDM, UDPerM and DPorM can be solved analytically for general initial and boundary conditions in semi-infinite domains, as reported, e.g., by Vanderborght et al. (2005). Analytical solutions of the SDM can be found, e.g., in Lapidus and Amundson (1952); Ogata and Banks (1961); Parker and van Genuchten (1984); van Genuchten and Parker (1984). In particular, Lassey (1988) derived analytical solutions, in terms of both resident and flux concentration, for DPorMs generalized to include first-order solute decay processes, in a semi-infinite domain, with zero initial distribution concentration and general linear boundary condition. Toride et al. (1993) extended these solutions by including a zero-order production term in the DPorM.

To the author's knowledge, the equations of the CDPerM, instead, do not admit an analytical solution for general initial and boundary conditions. Appendix A presents some considerations on the analytical solution of problems similar to the CDPerM, showing that the analytical solution of the CDPerM could be obtained only under very restrictive hypotheses.

In this chapter, the analytical solutions of the equations of the SDM and of the UDPerM will be derived in a semi-infinite domain for an instantaneous injection of a solute mass through the border of the domain, which initially does not contain any solute.

3.1 Analytical solution for the SDM

We want to solve equation (2.12) in a semi-infinite spatio-temporal domain, $x \in [0, +\infty)$ and $t \in [0, +\infty)$, with boundary conditions simulating an instantaneous injection, i.e., conditions (2.46) to (2.48).

It is easy to check that the flux concentration C_F defined by (2.40) satisfies the ADE (2.12) as well. Moreover, also the initial condition (2.46) and the boundary condition (2.47) hold with C_F in place of C ; in fact, if the concentration C vanishes, then the gradient of the concentration $\partial C/\partial x$ also vanishes, so that C_F itself vanishes. Therefore, equation (2.12) and the conditions (2.46) to (2.48) can be respectively rewritten in terms of C_F as:

$$\frac{\partial C_F}{\partial t} = -v \frac{\partial C_F}{\partial x} + D \frac{\partial^2 C_F}{\partial x^2}, \quad (3.1)$$

$$C_F(x, 0) = 0, \quad x > 0, \quad (3.2)$$

$$\lim_{x \rightarrow +\infty} C_F(x, t) = 0, \quad t \geq 0, \quad (3.3)$$

$$C_F(0, t) = \frac{M}{q} \delta(t), \quad t \geq 0. \quad (3.4)$$

The solution of this problem can be obtained applying the Laplace transform with respect to the variable t . In particular, the Laplace transform \tilde{C} of the flux concentration C_F is defined as:

$$\tilde{C}(x, s) = \int_0^{+\infty} e^{-st} C_F(x, t) dt, \quad (3.5)$$

where s is the coordinate in the Laplace space. Notice that, taking conditions (3.2) and (3.3) into account, the Laplace transform of the left-hand side term of equation (3.1) is given by:

$$\frac{\partial \tilde{C}}{\partial t} = s\tilde{C}.$$

Therefore, applying the Laplace transform to equation (3.1) and condition (3.4) and recalling that the Laplace transform of the Dirac delta is $\tilde{\delta} = 1$, it is obtained:

$$s\tilde{C} = -v \frac{\partial \tilde{C}}{\partial x} + D \frac{\partial^2 \tilde{C}}{\partial x^2}, \quad (3.6)$$

$$\tilde{C}(0, s) = \frac{M}{q}, \quad t \geq 0. \quad (3.7)$$

It can be easily shown that the solution of (3.6) and (3.7) is given by:

$$\tilde{C}(x, s) = \frac{M}{q} \exp\left(\frac{v - \sqrt{v^2 + 4Ds}}{2D} x\right). \quad (3.8)$$

The inverse Laplace transform of equation (3.8) gives the solution of the problem in the time domain:

$$C_F(x, t) = \frac{M}{q} \frac{x}{\sqrt{4\pi Dt^3}} \exp\left[-\frac{(x - vt)^2}{4Dt}\right]. \quad (3.9)$$

The corresponding BTC in $x = L$ is given by $q_c(L, t) = qC_F(L, t)$:

$$q_c(L, t) = M \frac{L}{\sqrt{4\pi Dt^3}} \exp\left[-\frac{(L - vt)^2}{4Dt}\right] = M f(t; D, v), \quad (3.10)$$

Therefore, the CBTC defined by (2.41) becomes:

$$\mathcal{M}(L, t) = \frac{ML}{\sqrt{4\pi D}} \int_0^t t'^{-3/2} \exp\left[-\frac{(L - vt')^2}{4Dt'}\right] dt'. \quad (3.11)$$

Notice that the solution given by (3.10), normalized by M , is the derivative with respect to time of the solution obtained by Ogata and Banks (1961) for the constant pulse boundary condition, i.e., for a continuous solute injection.

The analytical solution of the SDM, equation (2.12) with conditions (2.46) to (2.48), can also be obtained in terms of the resident concentration C , as shown, e.g., by Vanderborght et al. (2005), where the solution of the ADE, generalized to include adsorption and desorption, is obtained in semi-infinite soil profiles for the following initial and boundary conditions:

$$\begin{aligned} C(x, 0) &= g(x), \\ C_F(0, t) &= h(t), \\ \lim_{x \rightarrow +\infty} \frac{\partial C}{\partial x}(x, t) &= 0. \end{aligned}$$

From conditions (2.46) and (2.48), we have $g(x) = 0$ and $h(t) = M\delta(t)/q$. In this case, equation [17] of Vanderborght et al. (2005) becomes:

$$C(x, t) = \int_0^t \frac{M}{q} \delta(\tau) c_B(t - \tau; x) d\tau = \frac{M}{q} c_B(t; x), \quad (3.12)$$

where c_B is the transfer function, i.e., the solution of the problem for $g(x) = 0$ and $h(t) = \delta(t)$. If there is no sorption, the retardation factor R is equal to 1; under these conditions, the corresponding transfer function $c_{eq,B}$ given by equation [19] of Vanderborght et al. (2005) can be substituted in (3.12), so that the solution of the ADE for a pulse injection is obtained in terms of C :

$$C(x, t) = \frac{M}{q} \left\{ \frac{v}{\sqrt{\pi Dt}} \exp \left[-\frac{(x - vt)^2}{4Dt} \right] - \frac{v^2}{2D} \exp \left(\frac{vx}{D} \right) \operatorname{erfc} \left(\frac{x + vt}{\sqrt{4Dt}} \right) \right\}, \quad (3.13)$$

where erfc denotes the complementary error function.

It can be easily verified, by substituting the expression of C given by (3.13) in the definition of C_F (2.40), that the solution in terms of C_F given by (3.9) is obtained.

Notice that solution (3.13) permits to compute the concentration at the injection point $x = 0$:

$$C(0, t) = \frac{M}{q} \left[\frac{v}{\sqrt{\pi Dt}} \exp \left(-\frac{v^2 t}{4D} \right) - \frac{v^2}{2D} \operatorname{erfc} \left(\frac{vt}{\sqrt{4Dt}} \right) \right]. \quad (3.14)$$

Solution (3.13) for the resident concentration can be also obtained from the results of Lapidus and Amundson (1952).

3.2 Analytical solution for the UDPerM

We want to solve equations (2.35) and (2.36), with $\alpha = 0$, in the semi-infinite domain $x \in [0, +\infty)$, $t \in [0, +\infty)$, with conditions simulating a pulse injection, i.e., (2.54) to (2.56).

It can be noticed that the equations of the UDPerM are uncoupled, as well as the boundary conditions for the two domains. In particular, the equation and the boundary conditions for each of the two domains have the same form than the equation and boundary conditions of the SDM. Therefore, the solution in each of the two domains is given by the analytical solution of the SDM (3.9), with the parameters of the respective domain:

$$C_F^{(H)}(x, t) = \frac{M^{(H)}}{q^{(H)}} \frac{x}{\sqrt{4\pi D^{(H)} t^3}} \exp \left[-\frac{(x - v^{(H)} t)^2}{4D^{(H)} t} \right], \quad (3.15)$$

$$C_F^{(L)}(x, t) = \frac{M^{(L)}}{q^{(L)}} \frac{x}{\sqrt{4\pi D^{(L)} t^3}} \exp \left[-\frac{(x - v^{(L)} t)^2}{4D^{(L)} t} \right]. \quad (3.16)$$

Similarly, the solution of the UDPerM in terms of C is given for each of the two domains by the solution of the SDM (3.13), with the parameters of the respective domain.

In particular, the BTC at a certain distance L from the injection point is obtained from equation (2.30):

$$q_c(L, t) = \varepsilon^{(H)} M^{(H)} f\left(t; D^{(H)}, v^{(H)}\right) + \left(M - \varepsilon^{(H)} M^{(H)}\right) f\left(t; D^{(L)}, v^{(L)}\right), \quad (3.17)$$

where f was defined in equation (3.10).

Therefore, the CTBC defined by (2.41) becomes:

$$\begin{aligned} \mathcal{M}(L, t) = \int_0^t \left\{ \varepsilon^{(H)} M^{(H)} \frac{L}{\sqrt{4\pi D^{(H)} t'^3}} \exp\left[-\frac{(L - v^{(H)} t')^2}{4D^{(H)} t'}\right] + \right. \\ \left. + \varepsilon^{(L)} M^{(L)} \frac{L}{\sqrt{4\pi D^{(L)} t'^3}} \exp\left[-\frac{(L - v^{(L)} t')^2}{4D^{(L)} t'}\right] \right\} dt'. \end{aligned} \quad (3.18)$$

3.3 Temporal moments of the BTC

The moments of the BTC can be computed analytically, at least up to the third order, for both the SDM and the UDPerM. They can be obtained from definition (2.42), where $q_c = qC_F$, and C_F is given by (3.9) for the SDM and by (2.31) for the UDPerM, with $C_F^{(H)}$ and $C_F^{(L)}$ given by (3.15) and (3.16), respectively. The results up to the second order can be found also in Kreft and Zuber (1978).

In particular, as discussed in section 2.5, $M_0(L)$ represents the total mass of the solute that crosses the unit surface of the porous medium at a distance L from the injection point. As we are dealing with a non-reactive solute and, in the case of the SDM and UDPerM, the porous medium is assumed to contain no immobile component, the whole mass injected at $x = 0$ crosses the surface at a distance L , so that $M_0(L) = M$, $\forall L \geq 0$. This can be checked analytically from (2.42), with $r = 0$.

For the SDM, the normalized moments m_r , $r \leq 3$, are given by the following expressions:

$$m_1 = \frac{L}{v}, \quad (3.19)$$

$$m_2 = \left(\frac{L}{v}\right)^2 \left(1 + \frac{2}{Pe}\right), \quad (3.20)$$

$$m_3 = \left(\frac{L}{v}\right)^3 \left(1 + \frac{6}{Pe} + \frac{12}{Pe^2}\right), \quad (3.21)$$

where Pe is the Péclet dimensionless number defined by (2.21). For the UDPerM, m_r , $r \leq 3$, can be computed as:

$$m_r = \frac{1}{M} \left[\varepsilon^{(H)} M^{(H)} m_r^{(H)} + \left(M - \varepsilon^{(H)} M^{(H)}\right) m_r^{(L)} \right], \quad r = 1, 2, 3, \quad (3.22)$$

where $m_r^{(H)}$ and $m_r^{(L)}$ are given by the SDM expressions (3.19), (3.20) and (3.21) with the corresponding (H) or (L) parameters.

The central moments μ_2 and μ_3 can be obtained from the normalized moments by means of relations (2.44) and (2.45), which, for the SDM, reduce to:

$$\mu_2 = \left(\frac{L}{v}\right)^2 \frac{2}{Pe} = \frac{2LD}{v^3}, \quad (3.23)$$

$$\mu_3 = \frac{12LD^2}{v^5}, \quad (3.24)$$

so that the skewness is given by:

$$S = 3 \left(\frac{2D}{Lv}\right)^{1/2} = 3 \left(\frac{2}{Pe}\right)^{1/2}.$$

Numerical implementation of the SDM and DDMs

The analytical solutions for the SDM and for the UDPerM were obtained in chapter 3 in the case of a pulse injection. In order to apply these models for more general boundary conditions, e.g., in the case of a step injection, the superposition principle could be used to obtain the corresponding analytical solutions. As discussed in the introductory part of chapter 3, also the DPorM can be solved analytically, which is not the case for the CDPerM, to the author's knowledge, unless very restrictive hypothesis are applied (see also appendix A).

Therefore, a numerical scheme must be developed to solve the CDPerM. In this work, the numerical model was developed also for the SDM, DPorM and UDPerM, despite the availability of analytical solutions. This choice has a twofold motivation: on the first side, the numerical scheme for the solution of the CDPerM can be obtained by extending the numerical scheme for the solution of the UDPerM and of the SDM, which can be validated by comparison with the corresponding analytical solutions. On the other side, the numerical solution scheme can be useful for extending the solutions in future works to incorporate other processes involved in the solute transport.

In this chapter the numerical scheme adopted to implement the SDM and the DDMs is described. The equations are discretized with a finite difference Crank-Nicholson scheme, an explicit evaluation of the solute exchange term and an upwind technique for the convective terms. Moreover, a correction is applied to reduce the numerical dispersion determined by the truncation errors implied by the finite difference approximation of the equations.

Then, a validation of the codes is presented: in the case of the simulation of a pulse injection in a semi-infinite domain, the results of the numerical models are compared with those obtained by the analytical models developed in chapter 3 and with the results of the program HYDRUS-1D.

Notice that HYDRUS-1D implements the SDM, DPorM and DPerMs, as well as a parameter estimation technique, based on the Levenberg-Marquardt method, that includes several options to choose the kind of flow or transport data to use for the parameter estimation.

As will be explained in chapters 6 and 7, the transport models are calibrated with experimental data of \mathcal{M} in case studies A and B, of C_F in case study C and of C in case study D. The option to fit the \mathcal{M} data is not available in HYDRUS-1D and the option to fit the C_F data at the observation node is possible for all models but the DPerMs. Moreover, the source code of HYDRUS-1D is not freely available for the inverse models, so that it was not possible to modify the definition of the objective function as required by our examples. As a consequence, it was not possible to use HYDRUS-1D to calibrate the transport models with the data of the case studies considered in this work. It was not even possible to implement an inverse model based on the solution of the direct model

by HYDRUS-1D, since the source code is freely available only for the direct SDM and DPorM, but not for the DPerMs.

This remark shows that the implementation of the direct numerical models, presented in this chapter, and of their calibration, presented in chapter 5, is not an unnecessary work.

4.1 Numerical scheme for the SDM

4.1.1 Discretization of the spatial domain

Let $[0, L]$ be the spatial domain in which the transport equation is to be solved. In this work, it is assumed that $x = 0$ is the injection point and $x = L$ is the observation point, that is the position where the experimental data, volumetric concentration or solute flux, are measured. Since the boundary condition (2.47) is set at an infinite distance from the injection point, the domain of the numerical model has been extended to $[0, L_{\max}]$, with $L_{\max} \gg L$. An accurate solution of the transport equation is required only up to the observation point $x = L$; nevertheless, it is safer to keep a fine grid also for some distance beyond this position, in order to avoid rough finite difference approximations of the first and second order derivatives of the concentration in the vicinity of $x = L$. Then, it was chosen to use a fine grid up to twice the size of the physical domain, $2L$, and to widen the grid beyond that distance. In particular, the subdomain $[0, 2L]$ has been discretized with a regular grid of width Δx , whereas for $x \in [2L, L_{\max}]$ the grid spacing geometrically increases with common ratio $r = 1.4$. A graphical representation of the grid is shown in Figure 4.1.

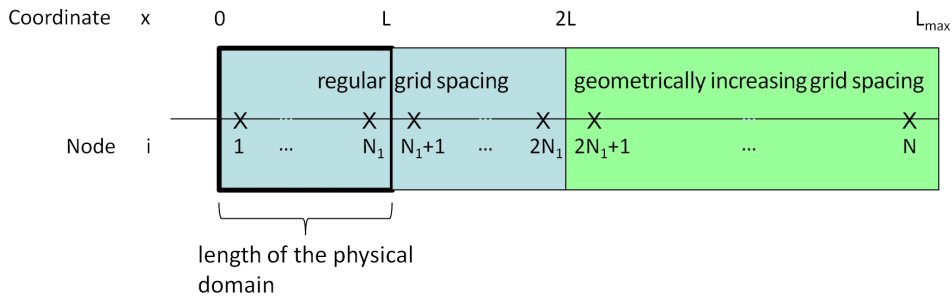


Figure 4.1: Schematic representation of the grid discretizing the domain.

A reference value Δx_0 is defined in order to minimize the effects of numerical dispersion (see section 4.1.5); the actual value of Δx is given by the best approximation of Δx_0 that permits to have an internode both at the injection point and at the observation point, i.e., $\Delta x = L/N_1$, where N_1 is the least integer greater than or equal to $L/\Delta x_0$.

The discrete spatial domain is then defined by the grid $x_i = x_{i-1} + \Delta x_{i-1}$, $i = 2, \dots, N$, with $x_1 = \Delta x/2$ and:

$$\Delta x_i = \begin{cases} \Delta x & i = 1, \dots, 2N_1 - 1 \\ r \Delta x_{i-1} & i = 2N_1, \dots, N - 1 \end{cases} ,$$

where N is the total number of nodes of the grid, with $x_N \leq L_{\max}$.

4.1.2 Discretization of the temporal domain

Let $[0, t_{\max}]$ be the temporal domain for which the transport equation is solved. The corresponding discrete temporal domain is given by the set $\{t_\ell, \ell = 0, \dots, N_t\}$, where $t_0 = 0$ and $t_{N_t} = t_{\max}$. The time discretization is not uniform: the time intervals $\{\Delta t_\ell = t_{\ell+1} - t_\ell, \ell = 0, \dots, N_t - 1\}$ are chosen to satisfy the following constraints:

- all the time intervals do not exceed a reference time interval Δt_{ref} which is set to minimize numerical instability and depends on the time scales of the particular case study: $\Delta t_\ell \leq \Delta t_{\text{ref}}, \ell = 0, \dots, N_t - 1$;
- one of the time levels must coincide with the end of the injection period. In other words, there exists an integer $\bar{\ell}$ such that $t_{\bar{\ell}} = \sum_{\ell=0}^{\bar{\ell}-1} \Delta t_\ell = T$. Notice that, for the simulation of a pulse injection, it has been assumed $T = 10^{-3}$ s;
- if $\{\tau_n, n = 1, \dots, N_{\text{data}}\}$ is the set of times corresponding to the experimental measurements, a set of integers $\{\ell_n, n = 1, \dots, N_{\text{data}}\}$ exists such that $t_{\ell_n} = \tau_n, n = 1, \dots, N_{\text{data}}$. In other words, the solution is computed for all times at which an experimental measurement is available.

The last constraint is not necessary for the general solution of the transport equation; its importance will become apparent for the calibration of the transport models (see chapters 5, 6 and 7), as the objective function will take into account the misfit between the experimental measurement at each time τ_n and the corresponding model outcome.

4.1.3 Discretization of the equation

The ADE (2.12) has been discretized with a Crank-Nicholson finite difference scheme and an upwind technique for the convective term. Therefore, the discrete counterpart of the ADE, for the generic node $i = 2, \dots, N - 1$ and time level $\ell = 0, \dots, N_t - 1$ is given by:

$$\begin{aligned} \frac{C_i^{\ell+1} - C_i^\ell}{\Delta t_\ell} = & \frac{1}{2} \left(-v \frac{C_i^\ell - C_{i-1}^\ell}{\Delta x_{i-1}} + D \frac{\frac{C_{i+1}^\ell - C_i^\ell}{\Delta x_i} - \frac{C_i^\ell - C_{i-1}^\ell}{\Delta x_{i-1}}}{\frac{\Delta x_i + \Delta x_{i-1}}{2}} \right) + \\ & + \frac{1}{2} \left(-v \frac{C_i^{\ell+1} - C_{i-1}^{\ell+1}}{\Delta x_{i-1}} + D \frac{\frac{C_{i+1}^{\ell+1} - C_i^{\ell+1}}{\Delta x_i} - \frac{C_i^{\ell+1} - C_{i-1}^{\ell+1}}{\Delta x_{i-1}}}{\frac{\Delta x_i + \Delta x_{i-1}}{2}} \right), \end{aligned} \quad (4.1)$$

where $C_i^\ell = C(x_i, t_\ell)$ denotes the concentration at node i and time level ℓ , that is at position $x = x_i$ and time $t = t_\ell$.

Boundary condition (2.47) can be easily discretized as:

$$C_N^\ell = 0, \quad \ell = 0, \dots, N_t.$$

Both boundary conditions (2.48) and (2.49) assign the solute flux at the inflow boundary $q_c(0, t)$. Recalling definition (2.11), the boundary conditions for a step injection (2.49)

and for a pulse injection (2.48) can be discretized as:

$$q_{c_0}^\ell = \frac{1}{\Delta t} \int_{t_\ell}^{t_{\ell+1}} q_c(0, t) dt = \begin{cases} \frac{M}{T} & \text{if } \ell = 0, \dots, \bar{\ell} - 1, \\ 0 & \text{if } \ell \geq \bar{\ell}. \end{cases} \quad (4.2)$$

The equation for node $i = 1$, which allows to compute the concentration C_1^ℓ , is now written in such a way to show explicitly the boundary condition at the injection point, given by (4.2):

$$\begin{aligned} \frac{C_1^{\ell+1} - C_1^\ell}{\Delta t} &= \varphi_0^\ell + \frac{1}{2} \left(-v \frac{C_1^\ell}{\Delta x} + D \frac{C_2^\ell - C_1^\ell}{\Delta x^2} \right) + \\ &+ \frac{1}{2} \left(-v \frac{C_1^{\ell+1}}{\Delta x} + D \frac{C_2^{\ell+1} - C_1^{\ell+1}}{\Delta x^2} \right), \end{aligned} \quad (4.3)$$

where the discrete function φ_0^ℓ is defined as

$$\varphi_0^\ell = \frac{q_{c_0}^\ell}{n\Delta x}$$

and, taking (4.2) into account, satisfies:

$$\varphi_0^\ell = \begin{cases} \frac{M}{n\Delta x T} & \text{if } \ell = 0, \dots, \bar{\ell} - 1, \\ 0 & \text{if } \ell \geq \bar{\ell}. \end{cases} \quad (4.4)$$

Notice that this scheme permits to have the correct amount of solute mass entering the domain; in fact, condition (4.2) implies:

$$\sum_{\ell=0}^{\bar{\ell}-1} q_{c_0}^\ell \Delta t_\ell = \int_0^T q_c(0, t) dt = M.$$

4.1.4 Solution of the discrete equation

The initial condition (2.46) can be easily discretized as:

$$C_i^0 = 0, \quad i = 1, \dots, N,$$

which sets the concentration at each node of the domain at the initial time $\ell = 0$. At each successive time step, the concentrations are computed by solving equations (4.1) and (4.3), which can be rewritten as the following tridiagonal system of $N - 1$ equations in the $N - 1$ unknowns $\mathbf{C}^{\ell+1} = \{C_i^{\ell+1}, i = 1, \dots, N - 1\}$, $\ell = 0, \dots, N_t - 1$:

$$(1 + b_1^\ell) C_1^{\ell+1} + c_1^\ell C_2^{\ell+1} = f_1^\ell, \quad (4.5)$$

$$a_i^\ell C_{i-1}^{\ell+1} + (1 + b_i^\ell) C_i^{\ell+1} + c_i^\ell C_{i+1}^{\ell+1} = f_i^\ell, \quad i = 2, \dots, N - 2 \quad (4.6)$$

$$a_{N-2}^\ell C_{N-2}^{\ell+1} + (1 + b_{N-1}^\ell) C_{N-1}^{\ell+1} = f_{N-1}^\ell, \quad (4.7)$$

or, in more compact form:

$$\mathbf{A}^\ell \mathbf{C}^{\ell+1} = \mathbf{f}^\ell, \quad (4.8)$$

where the elements A_{ij}^ℓ of the tridiagonal matrix \mathbf{A}^ℓ are given for $i, j = 1, \dots, N - 1$ by:

$$A_{ij}^\ell = \begin{cases} a_i^\ell & \text{if } j = i - 1, i > 1 \\ (1 + b_i^\ell) & \text{if } j = i, \\ c_i^\ell & \text{if } j = i + 1, i < N - 1 \\ 0 & \text{otherwise,} \end{cases}$$

with the following coefficients:

$$a_i^\ell = -\frac{\Delta t_\ell}{\Delta x_{i-1}} \left(\frac{v}{2} + \frac{D}{\Delta x_i + \Delta x_{i-1}} \right), \quad i = 2, \dots, N - 1,$$

$$b_i^\ell = \begin{cases} \frac{\Delta t_\ell}{2\Delta x} \left(v + \frac{D}{\Delta x} \right) & i = 1, \\ \frac{\Delta t_\ell}{\Delta x_{i-1}} \left(\frac{v}{2} + \frac{D}{\Delta x_i} \right) & i = 2, \dots, N - 1, \end{cases}$$

$$c_i^\ell = \begin{cases} -\frac{D\Delta t_\ell}{2\Delta x^2} & i = 1, \\ -\frac{D\Delta t_\ell}{\Delta x_i(\Delta x_{i-1} + \Delta x_i)} & i = 2, \dots, N - 2. \end{cases}$$

The vector \mathbf{f}^ℓ has the following components:

$$f_i^\ell = \begin{cases} (1 - b_1^\ell) C_1^\ell - c_1^\ell C_2^\ell + \Delta t_\ell \varphi_0 & i = 1, \\ -a_i^\ell C_{i-1}^\ell + (1 - b_i^\ell) C_i^\ell - c_i^\ell C_{i+1}^\ell & i = 2, \dots, N - 2, \\ f_{N-1}^\ell = -a_{N-1}^\ell C_{N-2}^\ell + (1 - b_{N-1}^\ell) C_{N-1}^\ell & i = N - 1. \end{cases}$$

The tridiagonal system (4.8) has been solved with the subroutine `tridag` developed by Press et al. (1989).

From the resulting concentrations $\mathbf{C}^\ell, \ell = 1, \dots, N_t$, it is possible to compute the flux concentrations at every internode $i + \frac{1}{2}$ using the discrete counterpart of definition (2.40), that is:

$$C_{F_{i+\frac{1}{2}}}^\ell = C_i^\ell - \frac{D}{v} \frac{C_{i+1}^\ell - C_i^\ell}{\Delta x_i}, \quad (4.9)$$

for $i = 1, \dots, N - 1$ and $\ell = 1, \dots, N_t$. From the flux-concentration $C_{F_{i+\frac{1}{2}}}^\ell$ it is also possible to compute the BTC as $q_{C_{i+\frac{1}{2}}}^\ell = q_{F_{i+\frac{1}{2}}}^\ell$, and the CBTC as the numerical approximation of the integral of $q_{C_{i+\frac{1}{2}}}^\ell$ over time, according to (2.41), which have been obtained with the trapezoid rule.

For the model calibration, the computation of the BTC and of the CBTC will be of particular interest at the observation point, $i = N_1$; this is the reason why the discretization of the domain was chosen to have an internode in the observation point.

4.1.5 Correction of truncation errors

It is well known that the finite difference approximation of the ADE introduces truncation errors. One of the first quantitative evaluations of the truncation errors was performed by Lantz (1971) for finite difference approximations of the 1D ADE, considering both implicit and explicit schemes and both centered and upwind approximations of the convective term. Further research in this field has progressively extended the analytical computation of the truncation errors and the corresponding development of corrected numerical schemes to the case of 2D transport equations with a first order reaction term, for uniform and variable discretization grids and for different finite difference schemes (Ataie-Ashtiani et al., 1995, 1996; Moldrup et al., 1996; Ataie-Ashtiani et al., 1999; Ataie-Ashtiani and Hosseini, 2005a,b).

As shown, e.g., by Ataie-Ashtiani et al. (1999), the finite difference approximation of the ADER, i.e., the ADE with a first order reaction term, introduces three forms of truncation errors: a second order truncation error, represented by numerical dispersion; a first order truncation error, represented by a numerical water velocity; a zeroth order truncation error, represented by a numerical reaction coefficient. In particular, for a conservative solute, i.e., in the absence of reaction terms in the ADE, the zeroth and first order errors vanish, so that the only effect of truncation errors is the introduction of numerical dispersion.

In this case the truncation error can then be removed, up to the second order in the grid spacing Δx , by solving the ADE with an effective dispersion coefficient, $D_e = D - D_{num}$, where D_{num} is a numerical dispersion coefficient.

The expression of D_{num} depends on the numerical scheme (explicit, Crank-Nicholson or implicit), on the numerical approximation of the convective term (centered or upwind) and on the spatial grid (uniform or variable). The different expressions of the ratio of the numerical to real dispersion coefficients D_{num}/D for a uniform grid are listed in Table 4.1 and are obtained from Ataie-Ashtiani et al. (1999) by setting to zero the first order reaction rate coefficient. The values of D_{num}/D are expressed as functions of the numerical Péclet number $Pe_{num} = v\Delta x/D$, which corresponds to (2.21), and of the Courant number $Cr = v\Delta t/\Delta x$.

	explicit	Crank-Nicholson	implicit
centered	$-\frac{Pe_{num} Cr}{2}$	0	$\frac{Pe_{num} Cr}{2}$
upwind	$\frac{Pe_{num}}{2} \left(1 - \frac{Cr}{2}\right)$	$\frac{Pe_{num}}{2}$	$\frac{Pe_{num}}{2} \left(1 + \frac{Cr}{2}\right)$

Table 4.1: Ratio of numerical to real dispersion coefficients, D_{num}/D , for different finite difference approximations of the ADE and a uniform grid.

The expressions listed in Table 4.1 hold for a uniform grid; for some numerical schemes the generalization to the variable grid is trivial, but, as shown, e.g., by Ataie-Ashtiani et al. (1995), in some finite difference schemes the variable space discretization can cause additional numerical errors with respect to the case of a uniform grid.

In order to properly correct the numerical scheme described in sections 4.1.1 to 4.1.4,

the truncation error for the numerical approximation of the ADE given by (4.1), i.e., for a Crank-Nicholson scheme and an upwind treatment of the convective term is now derived following Ataie-Ashtiani et al. (1999), for the simpler case of no reaction terms, but considering a variable grid.

The first step is to expand in Taylor series the concentrations appearing in the discrete form of the ADE, i.e., C_{i+1}^ℓ , C_{i-1}^ℓ , $C_i^{\ell+1}$, $C_{i+1}^{\ell+1}$ and $C_{i-1}^{\ell+1}$. The expansions of C about any grid point are obtained following two criteria: the third and higher order spatial derivatives are neglected (second order expansions) and the second and higher order temporal derivatives are expressed in terms of the spatial derivatives, using the ADE (2.12).

In particular, the expansions of C_{i+1}^ℓ and C_{i-1}^ℓ are readily obtained as:

$$C_{i+1}^\ell \approx C_i^\ell + \Delta x_i \frac{\partial C}{\partial x} + \frac{\Delta x_i^2}{2} \frac{\partial^2 C}{\partial x^2}, \quad (4.10)$$

$$C_{i-1}^\ell \approx C_i^\ell - \Delta x_{i-1} \frac{\partial C}{\partial x} + \frac{\Delta x_{i-1}^2}{2} \frac{\partial^2 C}{\partial x^2}. \quad (4.11)$$

The concentration at time $\ell + 1$ and at node i is approximated by the following Taylor series expansion around time ℓ :

$$C_i^{\ell+1} \approx C_i^\ell + \sum_{m=1}^{\infty} \left(\frac{\Delta t_\ell^m}{m!} \frac{\partial^m C}{\partial t^m} \right). \quad (4.12)$$

Differentiating the ADE (2.12), the time derivatives in equation (4.12) are expressed in terms of the spatial derivatives, where, again, the third and higher order spatial derivatives are neglected. Since the time derivatives of order $m \geq 3$ depend only on spatial derivatives of third and higher order, only the terms with $m = 1, 2$ are considered in the series (4.12). In particular, for $m = 2$:

$$\frac{\partial^2 C}{\partial t^2} \approx v^2 \frac{\partial^2 C}{\partial x^2}. \quad (4.13)$$

Substituting (4.13) in (4.12), it is obtained:

$$C_i^{\ell+1} \approx C_i^\ell + \Delta t_\ell \frac{\partial C}{\partial t} + \frac{\Delta t_\ell^2}{2} v^2 \frac{\partial^2 C}{\partial x^2}. \quad (4.14)$$

The Taylor expansion of $C_{i+1}^{\ell+1}$ is given by:

$$C_{i+1}^{\ell+1} \approx C_{i+1}^{\ell+1} + \Delta x_i \frac{\partial C^{\ell+1}}{\partial x} + \frac{\Delta x_i^2}{2} \frac{\partial^2 C^{\ell+1}}{\partial x^2}. \quad (4.15)$$

Substituting (4.14) in (4.15) and using again the differentiated ADE, it is obtained:

$$\begin{aligned} C_{i+1}^{\ell+1} \approx C_i^\ell &+ \Delta t_\ell \frac{\partial C}{\partial t} + \Delta x_i \frac{\partial C}{\partial x} + \\ &+ \left(\frac{\Delta t_\ell^2}{2} v^2 - \Delta x_i \Delta t_\ell v + \frac{\Delta x_i^2}{2} \right) \frac{\partial^2 C}{\partial x^2}. \end{aligned} \quad (4.16)$$

With the same method, the second order approximation of $C_{i-1}^{\ell+1}$ is obtained:

$$\begin{aligned}
 C_{i-1}^{\ell+1} \approx C_i^\ell &+ \Delta t_\ell \frac{\partial C}{\partial t} - \Delta x_{i-1} \frac{\partial C}{\partial x} + \\
 &+ \left(\frac{\Delta t_\ell^2}{2} v^2 + \Delta x_{i-1} \Delta t_\ell v + \frac{\Delta x_{i-1}^2}{2} \right) \frac{\partial^2 C}{\partial x^2}. \quad (4.17)
 \end{aligned}$$

The second step is to substitute the second order approximations of C_{i+1}^ℓ , C_{i-1}^ℓ , $C_i^{\ell+1}$, $C_{i+1}^{\ell+1}$ and $C_{i-1}^{\ell+1}$, i.e., expressions (4.10), (4.11), (4.14), (4.16) and (4.17) in the discrete ADE (4.6). The following equation is then obtained:

$$\frac{\partial C}{\partial t} = -v \frac{\partial C}{\partial x} + (D + D_{\text{num}}) \frac{\partial^2 C}{\partial x^2}, \quad (4.18)$$

where

$$D_{\text{num}} = \frac{v \Delta x_i}{2} = D \frac{Pe_{\text{num}_i}}{2}, \quad (4.19)$$

which trivially generalizes the corresponding expression for a uniform grid (Table 4.1).

As already mentioned, equation (4.18) clearly shows that the truncation error can be removed by replacing D with $D_e = D - D_{\text{num}}$ in the numerical equation (4.8). The correction has been applied here only in the fine grid region, i.e., for $i = 1, \dots, 2N_1$.

Moreover, since the effective dispersion D_e must be positive, then $D_{\text{num}} < D$, which implies $Pe_{\text{num}} < 2$. Therefore, the upper limit for the grid spacing is $\Delta x = 2D/v$, which is related to the grid spacing chosen for the regular grid discretizing the subdomain $[0, 2L]$ (see section 4.1.1). Specifically, $\Delta x_0 = \min(2D/v, \Delta L)$, where ΔL depends on the size of the domain of the particular case study and is needed to ensure that the grid is not too coarse for high Pe_{num} . In fact, it should be observed that the expressions of the corrections to the truncation errors hold for small Δx , as they are obtained from second order truncated Taylor series expansions in Δx .

In order to show the effects of numerical dispersion on the solution of the ADE and the effectiveness of the correction scheme, Figure 4.2 compares the time evolution of the concentration and the CBTC, computed for a pulse injection with the non-corrected and the corrected numerical model, with the analytical solution given in section 3.1 and with the solution obtained with the program HYDRUS-1D (see section 4.3.1). The parameters used in this simulation are reported in Table 4.2. Figure 4.2 shows that, in the case of the uncorrected numerical scheme, the presence of numerical dispersion causes a spreading of the concentration pulse and a corresponding decrease of the peak concentration with respect to the analytical solution, while the front of the CBTC is dampened; the introduction of the correction of the truncation errors in the numerical scheme clearly removes these effects, and the numerical solution matches the analytical solution with very good accuracy.

Finally, it is worth mentioning also the work of van Genuchten and Gray (1978), where a different method of analysis has been used to compute correction factors from the second to the fourth order, for several finite difference and finite elements schemes for solving the ADE. In particular, they developed both schemes for which only the truncation errors associated with the time derivative in the ADE are considered and schemes with space-time corrections, in which also the errors associated with the approximation of the space derivatives are considered. The application of the different corrected schemes to the simulation of a continuous injection of solute in a semi-infinite domain showed that the most accurate solutions were obtained when fourth order space-time corrections were applied to either the finite difference or the finite element scheme.

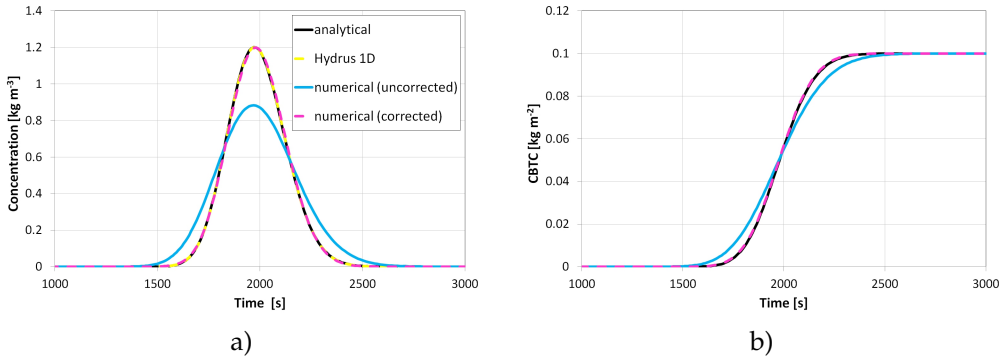


Figure 4.2: Comparison of the simulations of a pulse injection obtained with: analytical SDM (black line), HYDRUS-1D (yellow line), numerical SDM uncorrected and corrected for truncation errors (blue and pink line, respectively); a) time evolution of the concentration, b) cumulative breakthrough curve.

Parameter	Value	Unit
L	2.38	m
M	0.1	kg m ⁻²
v	$1.2 \cdot 10^{-3}$	m s ⁻¹
D	$7.0 \cdot 10^{-6}$	m ² s ⁻¹
n	0.2	

Table 4.2: Parameters used for the simulation of the pulse injection shown in Figure 4.2.

4.2 Numerical scheme for the DDMs

The equations of the DPorM, (2.17) and (2.18), with the corresponding boundary conditions, (2.50) to (2.53), and the equations of the DPerMs, (2.35) and (2.36), with the corresponding boundary conditions, (2.54) to (2.57), have been discretized with a numerical scheme similar to that developed for the SDM and described in section 4.1.

In particular, the model equations are approximated with a finite difference Crank-Nicholson scheme and the convective terms are computed with an upwind technique. The exchange term in the DPorM and the CDPerM is treated explicitly. This choice has a twofold motivation; in fact, the explicit evaluation of the exchange term permits to write the equations for the two domains as tridiagonal systems, as was already done for the SDM. An implicit or Crank-Nicholson treatment of the exchange term would have required the use of iterative methods to solve the resulting coupled set of discrete equations for the two domains. The second motivation is represented by the observation that the expressions of the truncation errors have the same form as in the SDM when the exchange term is treated explicitly. An attempt to extend the method explained in section 4.1.5 to the derivation of the truncation error in the case of a Crank-Nicholson treatment of the exchange term was not successful because of the coupling between the equations of the two domains, as shown in appendix B.

The discretization of the equations of the DPerMs (2.35) and (2.36) is then given, as

in (4.8), by:

$$\mathbf{A}^{(H)\ell} \mathbf{C}^{(H)\ell+1} = \mathbf{f}^{(H)\ell}, \quad (4.20)$$

$$\mathbf{A}^{(L)\ell} \mathbf{C}^{(L)\ell+1} = \mathbf{f}^{(L)\ell}, \quad (4.21)$$

where the coefficients of the matrices $\mathbf{A}^{(H)\ell}$ and $\mathbf{A}^{(L)\ell}$ are given by the same expressions of the coefficients of \mathbf{A}^ℓ with the parameters of the corresponding (H) or (L) domain. The vectors $\mathbf{f}^{(H)\ell}$ and $\mathbf{f}^{(L)\ell}$, instead, have a different expression, as the solute exchange term must be included:

$$f_i^{(H)\ell} = \begin{cases} (1 - b_1^{(H)\ell}) C_1^{(H)\ell} - c_1^{(H)\ell} C_2^{(H)\ell} + \Delta t_\ell \varphi_0^{(H)\ell} + \\ - \frac{\alpha \Delta t_\ell}{\varepsilon^{(H)} n^{(H)}} (C_1^{(H)\ell} - C_1^{(L)\ell}) & i = 1, \\ -a_i^{(H)\ell} C_{i-1}^{(H)\ell} + (1 - b_i^{(H)\ell}) C_i^{(H)\ell} - c_i^{(H)\ell} C_{i+1}^{(H)\ell} + \\ - \frac{\alpha \Delta t_\ell}{\varepsilon^{(H)} n^{(H)}} (C_i^{(H)\ell} - C_i^{(L)\ell}) & i = 2, \dots, N - 1, \end{cases}$$

where $\varphi_0^{(H)}$ is given by (4.4), with the parameters of the (H) domain. The components of $\mathbf{f}^{(L)\ell}$ are defined similarly, changing sign to the exchange term.

As mentioned above, the correction to the second order truncation errors has the same form derived for the SDM; specifically, the dispersion coefficient $D^{(H)}$ is replaced by the effective dispersion coefficient $D_e^{(H)} = D^{(H)} - D_{\text{num}}^{(H)}$, where $D_{\text{num}}^{(H)}$ is given by (4.19) with the parameters of the (H) domain. A similar replacement is done for $D^{(L)}$.

From the solution $\mathbf{C}^{(H)\ell}$ and $\mathbf{C}^{(L)\ell}$, the corresponding flux-concentrations $\mathbf{C}_F^{(H)\ell}$ and $\mathbf{C}_F^{(L)\ell}$ can be easily computed with expressions similar to (4.9) with the quantities of the corresponding domains. The solute fluxes are given by $q_{C_{i+\frac{1}{2}}}^{(H)\ell} = q^{(H)} C_{F_{i+\frac{1}{2}}}^{(H)\ell}$ and $q_{C_{i+\frac{1}{2}}}^{(L)\ell} = q^{(L)} C_{F_{i+\frac{1}{2}}}^{(L)\ell}$; finally, the BTC and CBTC are given by the discrete counterparts of (2.30) and (2.41) respectively.

The discretization of the equations of the DPorM (2.17) and (2.18) is simply obtained from (4.20) and (4.21) by setting $v^{(L)} = 0$ and $D^{(L)} = 0$, $\varepsilon^{(H)} n^{(H)} = n^{\text{mob}}$, $\varepsilon^{(L)} n^{(L)} = n^{\text{im}}$, $v^{(H)} = v$, $D^{(H)} = D$, $C^{(H)} = C^{\text{mob}}$, $C^{(L)} = C^{\text{im}}$, $M^{(H)} = M$ and $M^{(L)} = 0$.

4.3 Validation of the codes by comparison with the results of the analytical models and of HYDRUS-1D

The numerical scheme described in sections 4.1 and 4.2 for the solution of the single and dual domain models has been implemented in an original FORTRAN code, which was validated by comparing its results both with the analytical solutions presented in chapter 3 and with the numerical solutions obtained with the software HYDRUS-1D. The comparison has been performed for the transport simulation corresponding to the boundary conditions presented in section 2.5: an instantaneous injection of a conservative solute in a semi-infinite domain, initially free of solute, with a steady state saturated water flow and unitary hydraulic gradient.

Table 4.3 shows the input parameters of the different transport models that have been used for the code validation.

Model	Parameter	Value	Unit
SDM	D	$9.05 \cdot 10^{-4}$	$\text{m}^2 \text{s}^{-1}$
	v	$2.45 \cdot 10^{-3}$	m s^{-1}
	n	0.2	
	M	0.2766	kg m^{-2}
DPorM	D	$9.05 \cdot 10^{-4}$	$\text{m}^2 \text{s}^{-1}$
	v	$2.45 \cdot 10^{-3}$	m s^{-1}
	$n^{\text{mob}}, n^{\text{im}}$	0.2	
	α	10^{-7}	s^{-1}
		10^{-4}	s^{-1}
		10^{-2}	s^{-1}
	M	0.2766	kg m^{-2}
UDPerM and CDPorM	$D^{(H)}$	$8.49 \cdot 10^{-4}$	$\text{m}^2 \text{s}^{-1}$
	$D^{(L)}$	$5.83 \cdot 10^{-5}$	$\text{m}^2 \text{s}^{-1}$
	$v^{(H)}$	$3.15 \cdot 10^{-3}$	m s^{-1}
	$v^{(L)}$	$1.81 \cdot 10^{-3}$	m s^{-1}
	$\varepsilon^{(H)}$	0.475	
	$n^{(H)}, n^{(L)}$	0.2	
	$M^{(H)}$	0.3556	kg m^{-2}
	$M^{(L)}$	0.2043	kg m^{-2}
	M	0.2762	kg m^{-2}
	α	$1.05 \cdot 10^{-4}$	s^{-1}
		$1.05 \cdot 10^{-3}$	s^{-1}
$1.05 \cdot 10^{-2}$		s^{-1}	

Table 4.3: Input parameters of the transport models used for the code validation.

4.3.1 HYDRUS-1D

HYDRUS-1D (Šimůnek et al., 2009, 2005; Šimůnek and van Genuchten, 2008) is a public domain software package for simulating the one-dimensional movement of water, heat and multiple solutes in variably saturated porous media. HYDRUS-1D numerically solves, with a finite element technique, Richards' equation for saturated and unsaturated water flow and Fickian-based advective dispersive equations for heat and solute transport; moreover, it implements several approaches for simulating nonequilibrium water flow and solute transport, as the the dual-porosity model developed by van Genuchten and Wierenga (1976) and the dual-permeability model developed by Gerke and van Genuchten (1993) and Gerke and van Genuchten (1996), so that it is well suited for the validation of the codes that implement the single and dual domain models considered in this work.

Notice that, in the case of the DPerM, HYDRUS-1D and our model do not share the same strategy to determine the distribution of the solute injected in the porous medium between the two domains. In fact, HYDRUS-1D assumes that at the upstream boundary of the domain the local flux-averaged concentration in the fracture (fast domain in our DPerMs) equals the local flux-averaged concentration in the matrix (slow domain in our DPerMs), i.e., $C_F^{(H)}(0, t) = C_F^{(L)}(0, t) = C_F(0, t)$, whereas we assume that, in general, $C_F^{(H)}(0, t)$ can be different from $C_F^{(L)}(0, t)$, as implied by boundary conditions (2.56) or

(2.57). In other words, the mass of solute that enters the fractures per unit volume of solution in the fractures and the mass of solute that enters the matrix per unit volume of solution in the matrix are the same in HYDRUS-1D, whereas they can be different according to our model.

Therefore, in order to compare the results of our model with those of HYDRUS-1D, the values of $M^{(H)}$ and $M^{(L)}$ had to be chosen in such a way that $C_F^{(H)}(0, t) = C_F^{(L)}(0, t)$. Considering (2.56) or (2.57), this condition is equivalent to:

$$\frac{M^{(H)}}{q^{(H)}} = \frac{M^{(L)}}{q^{(L)}},$$

which, taking (2.58) into account, corresponds to:

$$M^{(H)} = M \frac{q^{(H)}}{q}, \quad M^{(L)} = M \frac{q^{(L)}}{q}. \quad (4.22)$$

The values reported in Table 4.3 satisfy this condition.

As a consequence, once the parameters M , $n^{(H)}$, $n^{(L)}$, $\varepsilon^{(H)}$, $\varepsilon^{(L)}$, $v^{(H)}$ and $v^{(L)}$ are fixed, $M^{(H)}$ and $M^{(L)}$ are known in HYDRUS-1D from (4.22); in our CDPerM, instead, one of the two parameters $M^{(H)}$ and $M^{(L)}$ remains unknown, but the other is determined from equation (2.58). Therefore, as will be shown in section 5.2.1, $M^{(H)}$ is one of the parameters to be estimated for the calibration of the CDPerM.

Moreover, HYDRUS-1D implements the expression of Gerke and van Genuchten (1996) for the mass transfer term, which is slightly different from the form proposed by Gerke and van Genuchten (1993) and reported in equation (2.39). Therefore, the simulations of HYDRUS-1D have been performed setting Γ_w to zero, while the solute mass transfer coefficient α_s , which is denoted as ω_{dp} in Šimůnek et al. (2009) and Mass.Tr. in the HYDRUS-1D interface, is set to $\alpha / (\varepsilon^{(L)} n^{(L)})$, as observed in section 2.4.2.

For convenience, the correspondence between the parameters of the SDM and DDMs and those of HYDRUS-1D is summarized in Table 4.4, which includes only the HYDRUS-1D parameters that are relevant to the simulations that are used for the model validation in this work; it is understood that all the parameters related to reactions, sources and sinks of solute, to the presence of multiple and multiphase solutes must be properly set to simulate the transport of a single, liquid phase, non-reactive solute in a medium with no sources or sinks.

Moreover, since the solute transport is simulated for a steady state saturated flow, the pressure head in the simulations of HYDRUS-1D is not computed from Richards' equations, but remains fixed to the initial value, which is set in such a way that $\nabla h = 1$.

4.3.2 Results

For the different transport models described in chapter 2, Figure 4.3 compares the concentration in $x = L$ as a function of time computed by our numerical model with those computed by HYDRUS-1D and, in the cases of the SDM and the UDPerM, also with the analytical solution reported in chapter 3. Figure 4.3 shows that the numerical results agree very well both with the analytical solutions and with the solution computed by HYDRUS-1D.

Moreover, interesting observations about the effect of solute exchange terms of different magnitude can be made by inspection of Figure 4.3.

For example, in the case of the DPorM, low and high values of the exchange term determine solutions that can be described well also by the SDM, as can be seen from

HYDRUS-1D		SDM and DDMs
Symbol in the user interface	Description	Correspondent quantity
<hr/> SDM		
Qs	saturated water content	n
Ks	saturated hydraulic conductivity	$nv/\nabla h$
Disp	longitudinal dispersivity	D/v
<hr/> DPorM		
Qs	saturated water content for the mobile region	n^{mob}
QsIm	saturated water content for the immobile region	n^{im}
Ks	saturated hydraulic conductivity	$nv/\nabla h$
Disp	longitudinal dispersivity	D/v
Alpha	mass transfer coefficient for solute exchange between mobile and immobile liquid regions	α
<hr/> DPerM		
Qs	saturated water content for the matrix	$n^{(L)}$
QsFr	saturated water content for the fracture	$n^{(H)}$
Ks	saturated hydraulic conductivity for the matrix	$n^{(L)}v^{(L)}/\nabla h$
KsFr	saturated hydraulic conductivity for the fracture	$n^{(H)}v^{(H)}/\nabla h$
Disp.M	longitudinal dispersivity for the matrix	$D^{(L)}/v^{(L)}$
Disp.F	longitudinal dispersivity for the fracture	$D^{(H)}/v^{(H)}$
w	ratio of the volume of the fracture domain and the total soil system	$\varepsilon^{(H)}$
Mass.Tr.	mass transfer coefficient for solute transfer between matrix and fracture	$\alpha/(\varepsilon^{(L)}n^{(L)})$
Bound.Cond.	concentration flux boundary condition	$C_F(0,0) = M/(nvT)$

Table 4.4: Correspondence between the parameters of HYDRUS-1D and the parameters of the SDM and DDMs.

graphs b) and d), whereas for intermediate values of the exchange the effect of dual-porosity becomes important (graph c)). This is in agreement with the discussion made in section 2.4.1.

For the CDPeM, low values of the exchange term correspond to the situation of two nearly independent domains as in the UDPeM, so that the solution in each of the two domains is well described by the SDM, as shown in graphs e) and f). The relevance of the CDPeM with respect to the UDPeM becomes apparent for intermediate values of the exchange term - graph g) - whereas for large values of the exchange term the two domains exchange solute so fast that they can be considered at equilibrium, so that the solution of the CDPeM can be described well also by the SDM - graph h).

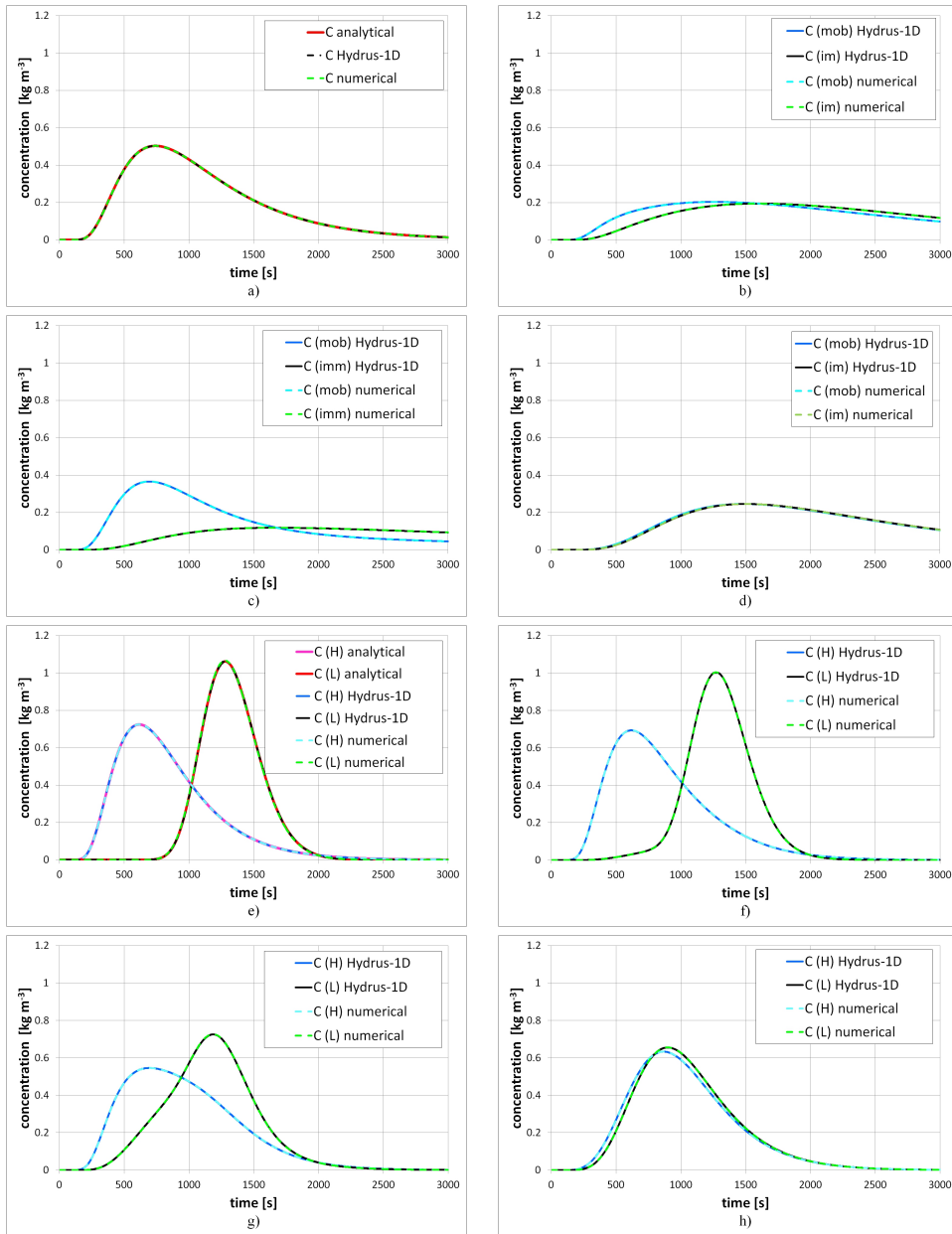


Figure 4.3: Comparison of the solute concentrations computed by our numerical model with those of HYDRUS-1D and with the analytical solution, for the geometry, initial and boundary conditions described in the text: SDM (a); DPoM (b, c, d, with $\alpha = 10^{-7} \text{ s}^{-1}, 10^{-4} \text{ s}^{-1}, 10^{-2} \text{ s}^{-1}$ respectively); UDPerM (e); CDPeM (f, g, h, with $\alpha = 1.05 \cdot 10^{-4} \text{ s}^{-1}, 1.05 \cdot 10^{-3} \text{ s}^{-1}, 1.05 \cdot 10^{-2} \text{ s}^{-1}$ respectively).

Calibration of the transport models

The transport models described in chapter 2 depend on a number of parameters that are characteristic of the particular site and are linked to the hydrogeologic features of the soil, to the types and proportions of the facies, to their organization and degree of connectivity. As observed by Köhne et al. (2009), the ongoing research is looking for “easily measurable proxy variables to represent the missing link between soil structure and model parameters”. Without such a link, the parameters of a transport model can be estimated through its calibration, that is, by fitting the experimental data, obtained from proper transport tests, with the predictions of the transport model.

In this chapter, the methods adopted to calibrate the different transport models are described. After a brief outline of the Levenberg-Marquardt method, which is the algorithm used for the model fitting, some remarks specific to the models calibration with the data of the case studies considered in this work are given; in particular, the parameters that must be estimated are listed for each model (SDM, DPorM, UDPerM and CD-PerM). Moreover, some issues on the uniqueness of the solution of the inverse problem are briefly discussed.

5.1 The Levenberg-Marquardt method

A thorough, although practical, description of the Levenberg-Marquardt method can be found in Press et al. (1989); here, only the main concepts are reviewed to fix the notation and to recall some features that will be useful later.

Given a set of data $\{y_i, i = 1, \dots, N_{\text{data}}\}$ and a model function $y(x; \mathbf{a})$, that depends on the parameters $\mathbf{a} = (a_1, \dots, a_M)$, the calibration or inverse problem consists in finding the best-fit (or optimal) parameters \mathbf{a}_{opt} , i.e., those parameters that give the best fit of the data with the model. In order to measure the agreement between the data and the model, a merit (or objective) function is often defined as:

$$\chi^2(\mathbf{a}) = \sum_{i=1}^{N_{\text{data}}} \left[\frac{y_i - y(x_i; \mathbf{a})}{\sigma_i} \right]^2, \quad (5.1)$$

where σ_i is the standard deviation associated with the measurement of y_i . Notice that, in practice, the measurement errors are never known and estimating σ_i is not an easy task. Therefore, a common approach is setting σ_i to a constant value ($\sigma=1$), as discussed by Press et al. (1989). This is also the approach adopted in this work.

The best-fit parameters \mathbf{a}_{opt} are obtained by minimization of the merit function χ^2 , which, in general, is a non linear function of the parameters \mathbf{a} . The Levenberg-Marquardt (LM) method is a standard algorithm to achieve this optimization.

The LM technique smoothly switches between the steepest descent method (far from the minimum) and the inverse-Hessian method when approaching the minimum.

In the vicinity of a current set of parameters \mathbf{a}_{cur} , χ^2 can be approximated by the following second order Taylor series:

$$\chi^2(\mathbf{a}) \approx \chi^2(\mathbf{a}_{\text{cur}}) + \nabla\chi^2(\mathbf{a}_{\text{cur}}) \cdot \delta\mathbf{a} + \frac{1}{2}\delta\mathbf{a}^T \cdot \mathbf{H}(\mathbf{a}_{\text{cur}}) \cdot \delta\mathbf{a}, \quad (5.2)$$

where $\delta\mathbf{a} = \mathbf{a} - \mathbf{a}_{\text{cur}}$, while $\nabla\chi^2$ and \mathbf{H} denote, respectively, the gradient and the Hessian matrix of χ^2 , whose components are given by:

$$\nabla\chi^2(\mathbf{a})|_j = \frac{\partial\chi^2}{\partial a_j}(\mathbf{a}) \text{ and } H_{jk}(\mathbf{a}) = \frac{\partial^2\chi^2}{\partial a_j \partial a_k}(\mathbf{a}), j, k = 1, \dots, M.$$

If $\mathbf{a} = \mathbf{a}_{\text{opt}}$, then the objective function χ^2 has a minimum there, $\nabla\chi^2(\mathbf{a}_{\text{opt}}) = 0$, which, considering (5.2), is equivalent to the following condition:

$$\mathbf{H}(\mathbf{a}_{\text{cur}}) \cdot (\mathbf{a}_{\text{opt}} - \mathbf{a}_{\text{cur}}) = -\nabla\chi^2(\mathbf{a}_{\text{cur}}), \quad (5.3)$$

and the best fit parameters can be computed through the inversion of the Hessian matrix:

$$\mathbf{a}_{\text{opt}} = \mathbf{a}_{\text{cur}} + \mathbf{H}(\mathbf{a}_{\text{cur}})^{-1} \cdot [-\nabla\chi^2(\mathbf{a}_{\text{cur}})]. \quad (5.4)$$

This expression represents the so-called inverse-Hessian method, which permits to compute the best fit parameters when the current set of parameters is not too far from the minimum, a condition which is necessary so that the approximation (5.2) holds.

Considering the definition of the objective function (5.1), the components of $\nabla\chi^2$ are given by:

$$\frac{\partial\chi^2}{\partial a_j} = -2 \sum_{i=1}^N \frac{[y_i - y(x_i; \mathbf{a})]}{\sigma_i^2} \cdot \frac{\partial y(x_i; \mathbf{a})}{\partial a_j} = -2\beta_j, \quad j = 1, \dots, M, \quad (5.5)$$

while the components of the Hessian matrix \mathbf{H} are approximated by:

$$\frac{\partial^2\chi^2}{\partial a_j \partial a_k} \approx 2 \sum_{i=1}^N \frac{1}{\sigma_i^2} \left[\frac{\partial y(x_i; \mathbf{a})}{\partial a_j} \cdot \frac{\partial y(x_i; \mathbf{a})}{\partial a_k} \right] = 2\gamma_{jk}, \quad j, k = 1, \dots, M, \quad (5.6)$$

as the second order derivatives of y are neglected, following the motivations of Press et al. (1989). They also observe the important fact that the approximation of the Hessian matrix \mathbf{H} has no effect at all on which final set of parameters is reached, but affects only the iterative route that is taken in getting there; in fact, the condition at the minimum is that $\nabla\chi^2(\mathbf{a}_{\text{opt}}) = 0$, independently of how \mathbf{H} is approximated.

For convenience of notation, the vector $\beta = -\nabla\chi^2/2$ and the matrix $\gamma = \mathbf{H}/2$ have been introduced in equations (5.5) and (5.6), so that equation (5.3) can be rewritten as:

$$\gamma \cdot \delta\mathbf{a} = \beta, \quad (5.7)$$

where $\delta\mathbf{a} = \mathbf{a}_{\text{next}} - \mathbf{a}_{\text{cur}}$ and \mathbf{a}_{next} indicates the next approximation of the parameters in the iterative procedure.

Far from the minimum, the Taylor expansion (5.2) is not a good approximation and, instead of the inverse-Hessian method, the steepest descent method can be used; this

method consists in iteratively approaching the minimum by a succession of steps in the parameter space down the gradient of the objective function:

$$\delta a_j = -\frac{1}{\lambda H_{jj}} \frac{\partial \chi^2}{\partial a_j}, \quad j = 1, \dots, M, \quad (5.8)$$

where λ is a positive dimensionless coefficient.

Equations (5.4) and (5.8) can be combined in the following way:

$$\boldsymbol{\gamma}' \cdot \boldsymbol{\delta a} = \beta, \quad (5.9)$$

where the matrix $\boldsymbol{\gamma}'$ is defined as:

$$\gamma'_{jk} = \begin{cases} \gamma_{jk} & \text{if } j \neq k, \\ \gamma_{jk}(1 + \lambda) & \text{if } j = k, \end{cases}$$

For large values of λ , the matrix $\boldsymbol{\gamma}'$ is forced to be diagonally dominant and (5.9) reduces to the steepest descent formula (5.8), whereas, for small values of λ , equation (5.9) reduces to the inverse-Hessian formula (5.4).

The LM algorithm can then be summarized as follows: starting from an estimate of the parameters \mathbf{a}_0 :

1. the objective function $\chi^2(\mathbf{a}_0)$ is computed;
2. λ is set to a small value, e.g., $\lambda = 0.001$;
3. n^{th} iterative step:
 - (a) equation (5.9) is solved for $\boldsymbol{\delta a}$, and the trial estimate is computed as $\mathbf{a}^{\text{tr}} = \mathbf{a}^{(n-1)} + \boldsymbol{\delta a}$;
 - (b) if $\chi^2(\mathbf{a}^{\text{tr}}) \geq \chi^2(\mathbf{a}^{(n-1)})$, then the value of λ is increased by a factor 10, the current estimate of the parameters is not changed, i.e., $\mathbf{a}^{(n)} = \mathbf{a}^{(n-1)}$ and $\chi^2(\mathbf{a}^{(n)}) = \chi^2(\mathbf{a}^{(n-1)})$, $n = n + 1$, and the algorithm goes back to point 3;
 - (c) if $\chi^2(\mathbf{a}^{\text{tr}}) < \chi^2(\mathbf{a}^{(n-1)})$, then the value of λ is decreased by a factor 10, the current estimate is updated, $\mathbf{a}^{(n)} = \mathbf{a}^{\text{tr}}$, $n = n + 1$, and the algorithm goes back to point 3.

5.1.1 The stopping criterium of the iterative LM process

Press et al. (1989) suggests to stop iterating on the first or second occasion that χ^2 decreases by a negligible amount, e.g., less than 0.01 absolutely or some fractional amount like 10^{-3} .

In this work, it was chosen to stop the iterative process when

$$\chi^2(\mathbf{a}^{(n-1)}) - \chi^2(\mathbf{a}^{(n)}) < \epsilon, \quad (5.10)$$

with $\epsilon = 10^{-6}$, for at least 20 successive iterative steps. This choice is motivated by the following facts:

- at each iterative step at which condition $0 < \chi^2(\mathbf{a}^{(n-1)}) - \chi^2(\mathbf{a}^{(n)}) < \epsilon$ holds, λ is divided by a factor 10 (see step 3(a) of the LM algorithm), so that, after 20 successive iterative steps in which the same condition holds, λ has decreased by 20 orders of magnitude; this means that the algorithm is very close to the minimum and that further iterative steps would not lead to significant variations in the estimated parameters;
- at each iterative step at which condition $\chi^2(\mathbf{a}^{(n-1)}) - \chi^2(\mathbf{a}^{(n)}) = 0$ holds, λ is multiplied by a factor 10 (see step 3(b) of the LM algorithm), so that, after 20 successive iterative steps in which the same condition holds, λ has increased by 20 orders of magnitude, a value so high that (5.9) reduces to (5.8), which in turn reduces to $\delta\mathbf{a} = 0$; in other words, the parameters are no more updated and it is not meaningful to continue the iterative process;
- finally, condition (5.10) can alternate between the two previous conditions, either $0 < \chi^2(\mathbf{a}^{(n-1)}) - \chi^2(\mathbf{a}^{(n)}) < \epsilon$ or $\chi^2(\mathbf{a}^{(n-1)}) - \chi^2(\mathbf{a}^{(n)}) = 0$ during the 20 iterative steps; as a consequence, λ is alternatively multiplied or divided by 10. This is what happens when the algorithm is moving in unsteep degenerate valleys of the parameter space; in this case, it is not meaningful to continue the iterative process, since the algorithm would remain confined in an almost flat region of the parameter space.

This stopping criterion does not guarantee that the best fit parameters given by the algorithm actually represent a good minimum for the objective function, as it happens if the algorithm remains confined in a flat region of the parameter space, or if some of the parameters yielded by the algorithm have unphysical values.

Moreover, the objective function can have a complex shape in the parameter space, with several local minima (see also section 5.2.2). Since the LM method is not a global optimization method, the best fit parameters found by the algorithm may represent a local minimum.

These observations highlight the importance of running the algorithm with several initializations, in order to sample a good part of the parameter space, and then to analyse the results for each initialization to assess if a reliable global minimum has been found.

5.1.2 Covariance, correlation and conditioning of the problem

The LM algorithm gives, together with the optimal parameters \mathbf{a}_{opt} , the corresponding covariance matrix, estimated as $\Gamma = \gamma^{-1}$, that is, half the inverse of the Hessian matrix $\mathbf{H}(\mathbf{a}_{\text{opt}})$.

The correlation matrix can be computed from the covariance matrix as:

$$\rho_{ij} = \Gamma_{ij}(\Gamma_{ii}\Gamma_{jj})^{-1/2}.$$

The computation of the covariance and correlation matrices for the optimal parameters requires the inversion of the Hessian matrix and, as a consequence, can be affected by its possible ill-conditioning. In order to analyze this problem, the condition number κ_2 of the Hessian matrix can be computed as the ratio of its maximum to minimum absolute eigenvalue. It is clear that the problem of the possible ill-conditioning of \mathbf{H} affects every step of the minimization process, since every step requires, for the solution of (5.9), the inversion of γ' , which is related to \mathbf{H} , relative to the current set of parameters. Nevertheless, in this thesis only the conditioning at the end of the minimization

process is investigated. In fact, as already mentioned, the approximation of \mathbf{H} during the minimization process can affect the path followed in the parameter space to arrive at the optimal values \mathbf{a}^{opt} , but not the values themselves, so that the possible ill-conditioning of \mathbf{H} has not shown any problem in the LM minimization.

5.2 Specific aspects of the calibration of the SDM and DDMs

5.2.1 Parameters to be estimated

Table 5.1 lists the parameters to be estimated for the calibration of the different transport models described in chapters 3 and 4 with the data of the case studies considered in this work.

As will be explained in chapters 6 and 7, the transport models are calibrated with experimental data of \mathcal{M} in case studies A and B, of C_F in case study C and of C in case study D. The corresponding objective functions are then defined in each case by setting y to the proper quantity (\mathcal{M} , C_F or C) in the general form of the objective function (5.1).

For each model, it is assumed that the injected mass per unit surface, M , and the porosity, n , are known parameters, as well as the local porosities of the two domains of the DPerMs which are assumed to be equal to the porosity of the medium: $n^{(H)} = n^{(L)} = n$. Notice that this assumption does not imply the equality between the volumes of solution (pore water) in the two domains. In fact, $V_p^{(H)} = \varepsilon^{(H)}n^{(H)}V$ and $V_p^{(L)} = \varepsilon^{(L)}n^{(L)}V$, and, in general, $\varepsilon^{(H)} \neq \varepsilon^{(L)}$.

For the numerical models, the parameters indicated in Table 5.1 are valid both for a pulse and for a step injection, and for experimental data of \mathcal{M} , q_c , C_F or C ; on the other hand, for the analytical SDM and UDPerM the parameters listed in the table are intended for the case of a pulse injection, as this is the only case for which the analytical solutions have been derived. Moreover, for the analytical UDPerM it is assumed that the experimental data to be fitted refer to the CBTC, \mathcal{M} , or to the solute flux, q_c , that is the model function y is represented by equation (3.18) or (3.17); it is important to notice that these functions depend on the product $\varepsilon^{(H)}M^{(H)}$, but not on the two parameters $\varepsilon^{(H)}$ and $M^{(H)}$ separately.

On the other hand, as shown in section (4.2), in order to numerically solve the equations of the DPerMs, both parameters $M^{(H)}$ and $\varepsilon^{(H)}$ must be specified, while $\varepsilon^{(L)}$ and $M^{(L)}$ are computed with the constraints (2.25) and (2.58).

As a consequence, when the experimental data refer to q_c or \mathcal{M} , the calibration of the analytical UDPerM requires the estimation, among the other parameters, of the product $\varepsilon^{(H)}M^{(H)}$, whereas for the calibration of the numerical UDPerM the two parameters $\varepsilon^{(H)}$ and $M^{(H)}$ must be estimated separately.

Finally, Table 5.1 shows that the number of parameters to be estimated ranges from two for the SDM to seven for the CDPerM.

5.2.2 Computational issues

Adaptive integration

When the model output to be used for the calibration of the analytical SDM and UDPerM is the CBTC, i.e., $y = \mathcal{M}$, the integrals which appear in (3.11) and (3.18), and in the derivatives of the CBTC with respect to the model parameters, which are required by the LM algorithm to compute the vector β , must be numerically calculated for a large

Model	Solution method	Parameters to be estimated	
SDM	analytical/ numerical	2	D, v
DPorM	numerical	4	$D, v, n^{\text{mob}}, \alpha$
UDPerM	analytical	5	$D^{(H)}, D^{(L)}, v^{(H)}, v^{(L)}, \varepsilon^{(H)}, M^{(H)}$
UDPerM	numerical	6	$D^{(H)}, D^{(L)}, v^{(H)}, v^{(L)}, \varepsilon^{(H)}, M^{(H)}$
CDPerM	numerical	7	$D^{(H)}, D^{(L)}, v^{(H)}, v^{(L)}, \varepsilon^{(H)}, M^{(H)}, \alpha$

Table 5.1: Parameters to be estimated for the calibration of the different transport models; it is understood that the analytical solution method refers to the pulse injection only, i.e., to the analytical models developed in chapter 3, while the numerical solution method refers both to the pulse and to the step injection, as described in chapter 4. The parameters listed for the analytical UDPerM are based on the assumption that the model function is the BTC or CBTC.

set of different values of the parameters \mathbf{a} . For some set of parameters, the BTC may have a narrow peak, and a very thin time discretization is required to correctly compute its integral. Such a fine discretization is clearly unnecessary far from the peak and it is unnecessary also for other sets of parameters, for which the BTC has a wide peak; moreover, a systematically fine discretization would significantly slow down the execution of the code. Therefore, an accurate calculation of these integrals has been obtained with an adaptive integration (McKeeman, 1962; Lyness, 1969; Forsythe et al., 1977), which allows to refine the time grid used for the computation of the integrals only when necessary, that is, when the integrand is rapidly varying.

Specifically, in the case of the analytical SDM, the peak time t_{peak} of the BTC corresponding to a set of parameters \mathbf{a} is obtained from (3.10):

$$t_{\text{peak}} = \frac{3D}{v^2} \left(\sqrt{1 + \left(\frac{Lv}{3D} \right)^2} - 1 \right). \quad (5.11)$$

Then, the adaptive integration can correctly take into account even a very narrow peak as follows. If $\{\tau_n, n = 0, \dots, N_{\text{data}}\}$, with $\tau_0 = 0$, is the set of times at which the CBTC of the SDM (3.11) is computed, and \bar{n} is the index such that $\tau_{\bar{n}} < t_{\text{peak}} < \tau_{\bar{n}+1}$, then the CBTC at the generic time $\tau_k > t_{\text{peak}}$ is computed as:

$$\mathcal{M}(\tau_k) = \sum_{n=0}^{\bar{n}-1} \mathcal{I}(\tau_n, \tau_{n+1}) + \mathcal{I}(\tau_{\bar{n}}, t_{\text{peak}}) + \mathcal{I}(t_{\text{peak}}, \tau_{\bar{n}+1}) + \sum_{n=\bar{n}+1}^{k-1} \mathcal{I}(\tau_n, \tau_{n+1}),$$

where $\mathcal{I}(a, b)$ denotes the approximation of the integral $\int_a^b q_c(t') dt'$ with the adaptive integration technique. For $\tau_k < t_{\text{peak}}$ the expression above reduces to:

$$\mathcal{M}(\tau_k) = \sum_{n=0}^{k-1} \mathcal{I}(\tau_n, \tau_{n+1}).$$

In the case of the analytical UDPerM, the integral in (3.18) is computed by adding the two integrals corresponding to the (H) and (L) domain, which are separately computed with the same technique described above for the SDM, where the proper peak times $t_{\text{peak}}^{(H)}$ and $t_{\text{peak}}^{(L)}$, given by expressions similar to (5.11), must be considered.

In the case of the numerical models, the time grid defined in section 4.1.2 is never too coarse, in order to prevent numerical instability; therefore, the computation of the integrals of the BTC and of its derivatives is simply obtained with the trapezoid rule.

Uniqueness issue for the solution of the inverse problem

As observed in section 5.1.1, the minimization of the objective function with the LM algorithm has been performed starting from several initializations in the parameter space. The best-fit parameters obtained for each initialization can represent the absolute (global) or a relative (local) minimum; in some cases, the objective function at the relative minima may have a small difference with respect to the absolute minimum, so that an accurate analysis is necessary to assess which minimum is physically more supported (as an example, see the discussion in section 6.1.6).

Moreover, for some initializations, the LM algorithm suffers from the well-known problem of gradient-type approaches, i.e., the search for the best-fit parameters can fall in regions of the parameter space where the objective function is almost constant so that a minimum cannot be found, as already discussed in section 5.1.1. In the following, the term “good initializations” will be used to indicate those initializations that let the LM algorithm work outside regions of the parameters space where either the graph of the objective function is flat or the parameters assume unphysical values.

As an example, for one of the numerical transport experiments of case study A (see section 6.1), Figure 5.1 shows the graph of the objective function, defined as the misfit between the experimental CBTC and the CBTC predicted by the SDM, in the parameter space (D, v) . The two graphs in Figure 5.1 refer to the same example, with the difference that plot a) has been obtained without the use of the adaptive integration. Plot b) shows that in large regions of the parameter space the graph of the objective function is nearly flat; if the initialization is chosen in these area, it is unlikely that the LM algorithm can reach the minimum.

Moreover, multiple minima may arise from numerical errors in the forward solution of the transport models, which can contribute to the roughness of the surface representing the objective function in the parameter space.

This is illustrated, e.g., by the previous example in Figure 5.1: if the adaptive integration is not used, the graph of the objective function changes significantly with respect to the case in which the integrals in the CBTC and in its derivatives are properly and accurately computed; in particular, Figure 5.1a shows two valleys, only one of which contains the minimum, so that the presence of the second valley may prevent the LM algorithm to find the minimum, as the iterative algorithm may be stuck in the wrong valley.

Notice that Figure 5.1b) shows the presence of a single minimum of the objective function. Nevertheless, for the more complex DDMs, for which the objective function is defined in a parameter space of higher dimension, the issue of the non-uniqueness of the solution of the inverse problem arises, as will be highlighted by the results of the calibration of the analytical UDPerM for case study A (see section 6.1.6).

Although some algorithms have been proposed to overcome the difficulties related to the presence of local minima, e.g., simulated annealing (see, e.g., Press et al. (1989) and Kirkpatrick et al. (1983)) or genetic algorithms (see, e.g., Goldberg (1989)), nevertheless their application to practical problems with complex objective functions is not yet fully satisfactory and a posterior analysis of the results of the minimization from the physical point of view, still appears to be a better approach.

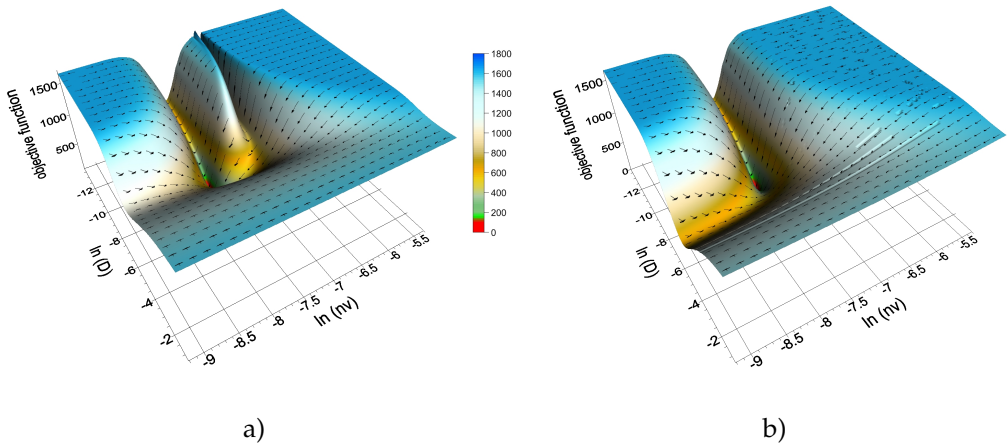


Figure 5.1: Graph of the objective function, measuring the misfit between the experimental and model CBTCs, in the parameter space (D, v) (logarithmic scale), for the SDM. a) without adaptive integration; b) with adaptive integration. The arrows indicate the gradient of the objective function.

Application of the transport models: interpretation of numerical tracer tests

This chapter and the following chapter 7 are devoted to the description of the four case studies of tracer tests analyzed in this work and to the presentation of the results of the interpretation of these tests with the different single and dual-domain models developed in the previous chapters. Specifically, this chapter deals with two case studies (A, section 6.1, and B, section 6.2) represented by numerical transport experiments conducted on blocks of sediments from “virtual” aquifers, which have been reconstructed with a stochastic simulation on the basis of field data. The two case studies are characterized by different depositional environments and by different spatial scales (meter scale for case study A and decameter scale for case study B).

The analyses performed for case studies A and B share the same main steps:

1. development of the geological and hydrostratigraphical model;
2. geostatistical simulation of the block of sediments, conditioned by the data resulting from step 1., in order to obtain the hydrofacies and hydraulic conductivity distribution in space;
3. development of the flow model;
4. performance of 3D numerical tracer tests with a particle tracking technique, in order to simulate an instantaneous injection of solute in the blocks of sediments;
5. interpretation of the results of the numerical tracer tests with the different 1D single and dual-domain transport models.

For case study A, steps 1. to 3. were the subjects of the Master thesis of Giulio Zappa (Zappa, 2002), whereas step 4. was performed by Laura Cattaneo in her Master thesis (Cattaneo, 2008). For case study B, steps 1. to 4. are part of the PhD thesis of Diana dell’Arciprete (dell’Arciprete, 2010). These results have been published on international journals (Zappa et al., 2006; Vassena et al., 2010; dell’Arciprete et al., 2012a,b), as explained in detail in the following sections. The original work of this thesis is related to step 5. for both case studies.

6.1 Case study A. Numerical tracer tests on meter scale blocks of sediments from an alluvial aquifer in the Ticino basin (Northern Italy)

The first case study has been presented and thoroughly described by Zappa et al. (2006); it consists of three prismatic blocks of sediments (model blocks, MBs), some

cubic meters in volume, dug at a quarry site into real sediments belonging to the Pleistocene sequences of the Ticino basin (Piedmont, Northern Italy) and, specifically, to the Albusciago Alloformation unit, which provides a good glacio-fluvial aquifer analogue. The details of the sedimentological description can be found in Zappa et al. (2006), together with the methods and results of the 3D geostatistical simulation and the flow modeling of the MBs, with the computation of the upscaled tensor of equivalent conductivity at the MB scale. For the Reader's convenience, the main concepts are recalled in section 6.1.1. The description of the numerical tracer tests performed on the MBs can be found in Vassena et al. (2010) and a corresponding summary is given in section 6.1.2. The experimental data are presented and discussed in section 6.1.3 and the objective functions used to calibrate the transport models are defined in section 6.1.4. Section 6.1.5 outlines the analysis performed to interpret the experimental data with the different transport models, whose results are presented in sections 6.1.6 to 6.1.10. Finally, some concluding remarks are given in section 6.1.11.

6.1.1 Geological and hydrostratigraphic features and geostatistical simulations of the blocks of sediments

The MBs are representative of common sedimentary facies: MB1 was dug into a sand dune above a gravel/sand cross-laminated bar unit, MB2 into a cross-stratified gravel/sand bar with patches of open framework clean gravel and MB3 into mostly disorganized gravel-sands; the three MBs are then representative of sand-gravel dunes (MB1), gravel bedforms (MB2) and poorly sorted, mass gravity deposits (MB3).

As described by Zappa (2002) and Zappa et al. (2006), a sedimentological description was obtained for each block, resulting in the facies classification of the sediments belonging to the lateral faces of the blocks.

Subsequently, porosity and permeability of the different facies were estimated comparing the results of laboratory analyses of samples of hydrofacies with empirical formulas and with literature data. In particular, porosity and permeability of sand-grade sediments were estimated by laboratory measurements of volumetric samples and by laboratory permeability tests on undisturbed and oriented samples; six samples of sands were collected, two for each direction, from MB1 (Zappa, 2002). The permeability of the fine gravel-grade sediments were estimated by comparing the results obtained with the Hazen's and Kozeny-Karman's empirical formulas and with literature data (Zappa et al., 2006); two samples were collected from MB1 for such permeability estimates. Finally, three infiltration tests, one for each MB, were performed in sites chosen in such a way to sample a small number of facies. Each test consisted of two or three repetitions of a two phase procedure: the first phase was conducted with a stationary head, the second phase with a time varying head (Zappa, 2002).

The facies maps of the lateral faces of the blocks were then analyzed from an hydrogeologic point of view in order to group the different lithological facies, according to their texture, structure and estimated conductivity value, in six operative facies¹, namely "pebbles and cobbles" (L, with null hydraulic conductivity), "fine sand" (fS, $K = 10^{-4}$ m/s), "coarse to medium sand" (cS, $K = 5 \cdot 10^{-4}$ m/s), "sandy gravel (poorly sorted)" (SG, $K = 6 \cdot 10^{-4}$ m/s), "fine sandy gravel (well sorted)" (fSG, $K = 2 \cdot 10^{-3}$ m/s) and "open framework gravel" (G, $K = 5 \cdot 10^{-2}$ m/s). The operative facies $L_{1/2}$ ($K = 2.8 \cdot 10^{-5}$ m/s) was used only for MB3 to consider the cobbles which occupy at least one half of two adjacent cells (see Figure 5 of Zappa et al. (2006)).

¹In the following, the terms facies or hydrofacies will be often used for these operative facies, for the sake of simplicity.

The hydrofacies maps of the lateral faces of each block were then discretized with 2 cm resolution and used to condition the 3D geostatistical simulation of the sediment volumes, obtained by Zappa et al. (2006) with a hierarchical modification of SISIM (Sequential Indicator Simulation). This method allows an efficient reproduction of the external geometry of individual sedimentary units and the simulation of their internal architecture. In particular, successive geostatistical simulations are realized for each facies and the simulation of the smallest elements of the sedimentary architecture are conditioned to the results of the simulation of the higher order bounding surfaces. The single geostatistical simulations are finally merged. Therefore, in order to simulate each block, many variograms have to be computed, one for each of the successive geostatistical simulations, which are performed with SISIM. These variograms, that can be found in the Master thesis of Zappa (2002), showed that MB1 is characterized by a horizontal anisotropic behaviour for the most abundant operative facies fS, cS and SG, for which the vertical variograms have short ranges (0.15 m to 0.3 m). MB2 is characterized by vertical ranges which are about 9 times shorter than horizontal ranges, showing a high degree of heterogeneity along the vertical direction, which results in an approximately layered conductivity field. The most abundant facies for MB3 are SG and fSG, for which the horizontal variograms have long ranges (2-3 m) and indicate anisotropy. For all three blocks the vertical and horizontal variograms for facies L are characterized by very short ranges and a high nugget effect, indicating that this operative facies, that represents pebbles and cobbles, is uncorrelated even at short distances and is randomly distributed in the volumes of sediments.

The geostatistical simulation permitted to obtain, for each block, the facies distribution and, consequently, the hydraulic conductivity field, with a resolution of 2 cm. Figure 6.1 shows the results of the geostatistical simulations and reports the size of the blocks.

All the three blocks are heterogeneous, but show different architectures and organization of the hydrofacies. Table 6.1 reports some parameters that highlight the different structures of the blocks, i.e., the variance of the logarithm of the hydraulic conductivity, $\text{var}[\ln K]$, which is commonly used to quantify the heterogeneity, and, for the most conductive hydrofacies G, the fraction of the total volume and the intrinsic connectivity, which is one of the new hydrofacies connectivity indicators, together with the total and normal connectivities, introduced by Vassena et al. (2010), where a comparison with other connectivity indicators already proposed in the literature can be found. For convenience, the definition of the intrinsic connectivity is here recalled.

Let Ω_p be a subset of the volume Ω composed by the hydrofacies p . Two points $\mathbf{x} \in \Omega$ and $\mathbf{y} \in \Omega$ are connected ($\mathbf{x} \leftrightarrow \mathbf{y}$) if there is a continuous path linking them and belonging to a single hydrofacies, i.e., belonging to Ω_p for some p . The intrinsic connectivity C_p^* of the hydrofacies p is defined as the probability that two distinct points belonging to Ω_p are connected, that is:

$$C_p^* = P[\mathbf{x} \leftrightarrow \mathbf{y} | \mathbf{x} \in \Omega_p, \mathbf{y} \in \Omega_p, \mathbf{x} \neq \mathbf{y}]. \quad (6.1)$$

In practice, if the domain Ω is discretized with \mathcal{N} points, if \mathcal{N}_p is the number of points belonging to Ω_p and C_p the number of non-trivial connections in Ω_p , i.e., avoiding trivial connections that correspond to a path linking a node with itself, then the intrinsic connectivity can be estimated as the ratio between C_p and the number of pairs of distinct points belonging to Ω_p :

$$C_p^* = C_p \cdot [\mathcal{N}_p(\mathcal{N}_p - 1) / 2]^{-1}. \quad (6.2)$$

In other words, the intrinsic connectivity is normalised (or conditioned) to an event related to the p facies only, so that it is an indicator of the connectivity of a facies within

itself.

Table 6.1 shows that $\text{var}[\ln K]$ for MB2 and MB3 is about two times that for MB1; MB2 is the block with the highest percentage of gravel; moreover, the intrinsic connectivity of gravel for MB1 and MB2 is about two orders of magnitude larger than that of MB3, which means that gravel is randomly distributed in MB3, while it is organized in connected volumes in MB1 and MB2.

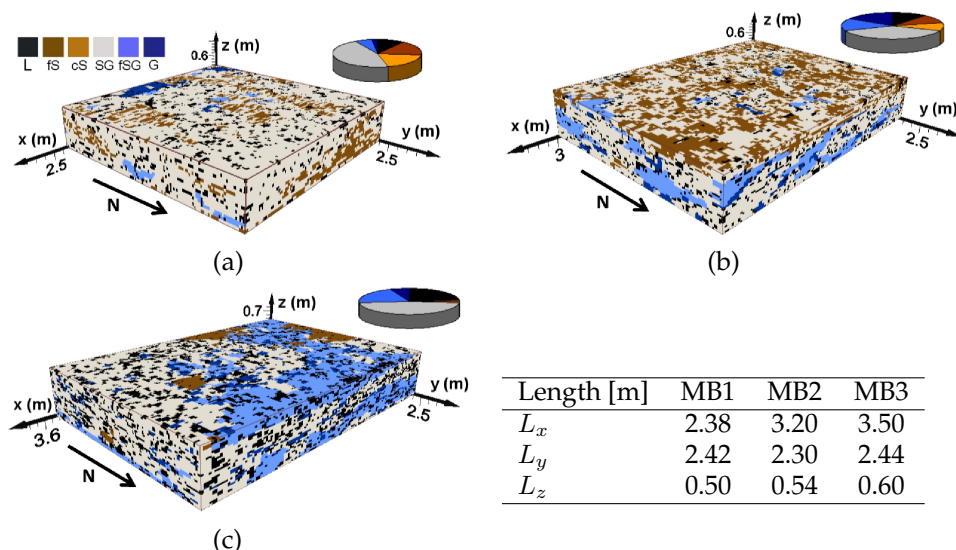


Figure 6.1: Results of the 3D geostatistical simulation of (a) MB1, (b) MB2, (c) MB3; the pie charts represent the facies proportions. Each color corresponds to one of the different operative facies described in the text: L, fS, cS, SG, fSG and G. The Table lists the length of the MBs along each direction. Modified from Zappa et al. (2006) and Vassena et al. (2010).

	MB1	MB2	MB3
$\text{var}[\ln K]$	1.52	3.61	3.21
Fraction of G	0.02	0.16	0.06
Intrinsic connectivity of G	0.3	0.4	0.004

Table 6.1: Variance of the logarithm of the hydraulic conductivity, $\text{var}[\ln K]$, fraction of the total volume occupied by the hydrofacies G (open framework gravel) and intrinsic connectivity of G.

6.1.2 Numerical experiments of non-reactive solute transport

Some numerical experiments of non-reactive solute transport were performed on these MBs, as described by Vassena et al. (2010). Each block was discretized in a square grid with a spacing of 2 cm, which is the same resolution of the conductivity field. The flow field was then computed with a conservative finite difference model for steady state saturated flow, where the internode conductivity was computed with harmonic averaging. Convective transport was modelled with a particle tracking technique based on the trilinear interpolation of the velocity and the integration of the motion equation of

each individual particle with a Runge Kutta fourth-order method (Anderson and Woessner, 1991). Reaction or local diffusion terms were neglected. Moreover, for the sake of simplicity, a constant porosity $n = 0.2$ was assumed. For each MB, six numerical experiments were conducted, by fixing the flow direction along the cartesian axes: notice that the horizontal axes run along the SN and WE directions. The following boundary conditions were assigned to simulate the flow field of each test: constant heads on the two faces perpendicular to the mean flow direction (unit hydraulic gradient) and no flow along faces parallel to the mean flow direction. The numerical experiments simulate an instantaneous injection of a certain mass of solute through the upstream face of each block, where about 3000 particles have been injected with a distribution proportional to Darcy's velocity in order to reproduce the experimental conditions of a laboratory test on the whole block. A graphical representation of the results of some of these numerical experiments is showed in Figure 6.2.

As described by Vassena et al. (2010), in the case of MB1, many particles travel in two fast sub-plumes corresponding to two PFPs along the WE direction, whereas most of the particles travel with the same velocity along the SN direction. In the case of MB2, fast PFPs are apparent in both flow directions, as a result of the high connectivity of gravel in this block. Finally, MB3 appears to be more isotropic, as a result of the random heterogeneity observed from the results of the geostatistical simulation; in fact, the particles travel in both directions with approximately the same velocity, without the development of faster sub-plumes.

Vassena et al. (2010) analysed these experiments through the computation of the dispersion tensor with a Lagrangian approach, i.e., from the second order moments of the particle distribution, and the comparison with the longitudinal dispersion coefficient obtained with an Eulerian approach, i.e., by fitting the BTCs with the solution of the ADE.

This case study was further analysed by Baratelli et al. (2011) and Baratelli et al. (2012), where both single and dual-domain models have been applied to interpret the results of the numerical experiments, as will be shown in the following sections.

6.1.3 Experimental data

The "experimental" data are the results of particle tracking numerical experiments; for each MB and for each flow direction along the cartesian axes, the virtual field data are then given by the arrival times τ_i , $i = 1, \dots, N_p$, of the N_p solute particles at the downstream face of the block. The arrival times of the fastest and the slowest particles are denoted respectively as $t_{\min} = \min\{\tau_i, i = 1, \dots, N_p\}$ and $t_{\max} = \max\{\tau_i, i = 1, \dots, N_p\}$, whereas $t_{P\%}$ denotes the time at which $P\%$ of the total particles injected has arrived at the end of the MB.

The particle tracking transport simulations used to generate data are 3D, but they are interpreted with 1D transport models along the flow direction. The spatial domain in which the transport models are solved to fit the experimental data is represented by $[0, L]$, where L is the length of each MB along the x or y direction, whose values are reported in Figure 6.1. The temporal domain is given by $[0, t_{\max}]$.

The "experimental" BTC at the downstream border of the block ($x = L$) and in the time interval $(t, t + \Delta t)$ can be computed as:

$$q_c^{\text{exp}}(t) = \frac{m_p N_p(t, t + \Delta t)}{A \Delta t},$$

where m_p is the mass of each individual solute particle and $N_p(t, t + \Delta t)$ is the number of particles that cross the downstream face of the block, of area A , in the time interval

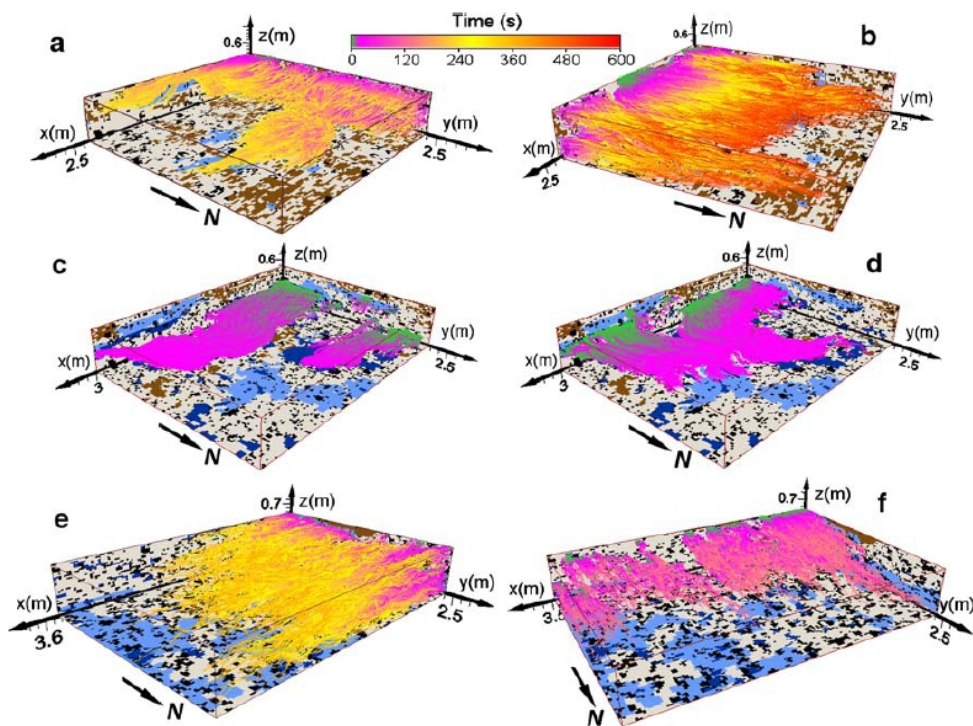


Figure 6.2: Evolution of the solute plumes for different flow orientations (WE flow direction in plots a, c, e; SN flow direction in plots b, d, f) and for the different MBs (MB1 in plots a and b, MB2 in plots c and d, MB3 in plots e and f). Dots represent the positions of the solute particles; the color scale refers to the time elapsed from the injection. From Vassena et al. (2010).

($t, t + \Delta t$): the experimental BTC can then be represented as an histogram, as shown in Figure 6.5 for three of the six tests.

The experimental histogram for MB1 EW (Figure 6.5a) is clearly bimodal, with two peaks that correspond to two groups of particles that travel fast in two PFPs with a moderate contrast of velocity, as shown also by Figure 6.1a.

The experimental histogram for MB2 WE (Figure 6.5b) shows an early peak, corresponding to the fast sub-plume traveling in the wide PFP that is visible in Figure 6.1c, and a long tail, corresponding to the slower particles of solute.

While the experimental BTCs of MB1 EW and MB2 WE show the typical effects of the presence of PFPs in the porous medium, the experimental histogram for MB3 WE (Figure 6.5c), instead, has the typical shape of a single homogeneous domain, as could be expected by inspection of Figure 6.1e.

The particles used for the particle tracking simulations are about 3000 (see Table 6.2); a much larger number of particles would have been needed to obtain a sufficient number of data to accurately estimate the instantaneous BTC. For this reason, it has been chosen to fit the CBTC, instead of the BTC, with the single and dual-domain transport models.

Differently from the BTC, the “experimental” CBTC can be computed at all the arrival times τ_i ; in particular, the CBTC is computed at times $t_k, k = 1, \dots, N_{\text{data}}$, where $N_{\text{data}} < N_p$, as some particles share the same arrival time. The CBTC is easily obtained

as $\mathcal{M}^{\text{exp}}(t_k) = N_p(t_k)m_p/A$, where $N_p(t_k)$ is the number of particles that have crossed the downstream face of the block by the time t_k , i.e., the number of particles for which $\tau_i \leq t_k$.

The values of the injected mass per unit surface M can be obtained from $M = N_p m_p/A$; for simplicity it is assumed that each particle carries a mass of solute numerically equal to the area A , i.e., $m_p/A = 1 \text{ kg/m}^2$, so that the total mass of solute injected per unit surface M coincides numerically with the number of injected particles N_p .

Moreover, recalling the notation introduced in section 2.5, the r -th order “experimental” absolute and central moments can be obtained, respectively, as:

$$M_r^{\text{exp}} = \frac{m_p}{A} \sum_{i=1}^{N_p} \tau_i^r, \quad (6.3)$$

$$\mu_r^{\text{exp}} = \frac{m_p}{AM_0^{\text{exp}}} \sum_{i=1}^{N_p} (\tau_i - m_1^{\text{exp}})^r, \quad (6.4)$$

where $m_1^{\text{exp}} = M_1^{\text{exp}}/M_0^{\text{exp}}$. Notice that, in agreement with the discussion made in sections 2.5 and 3.3, $M_0^{\text{exp}} = N_p m_p/A = M$, m_1^{exp} is the average arrival time of the particles at the outflux face, μ_2^{exp} is the variance of the distribution of the arrival times of the particles and $S^{\text{exp}} = \mu_3^{\text{exp}}/(\mu_2^{\text{exp}})^{1/2}$ is the skewness parameter representing the asymmetry of the distribution. The values of m_1^{exp} , $(\mu_2^{\text{exp}})^{1/2}$ and S^{exp} are reported in Table 6.2, together with the number of injected particles N_p . These results indicate that the first three temporal moments of the BTC cannot be used alone as signs for the presence of PFPs: in fact, the smallest values of m_1^{exp} are obtained for MB2, which is the MB where conductive hydrofacies are prevailing, as shown in section 6.1.1; nevertheless, m_1^{exp} can be small because of the PFPs (as is the case for MB2) but it can be small also if the porous domain is homogeneous and with high permeability. The highest values of μ_2^{exp} , which correspond to the widest distributions of the arrival times, are obtained for MB1 EW and MB3 WE, that is for porous domains with PFPs that determine double peaks in the BTC (as MB1 EW) but also for porous domains with random heterogeneity (as MB3 WE). Finally, in contrast to the remark of Stagnitti et al. (2000) recalled in section 2.5, the highest skewness S is obtained for both tests on MB3, which in 6.1.1 was shown to be disorganized and without PFPs.

Model block	Flow direction	N_p	m_1^{exp} [s]	$(\mu_2^{\text{exp}})^{1/2}$ [s]	S
MB1	NS	2839	1017	258.9	0.98
	EW	2766	914.9	401.7	0.35
MB2	NS	2610	186.3	246.9	4.63
	WE	2654	192.7	310.6	3.69
MB3	NS	3573	594.2	362.2	8.22
	WE	3604	810.2	416.3	6.42

Table 6.2: Number of injected particles and experimental moments for the different numerical tests of case study A.

6.1.4 Objective functions

As mentioned above, the different transport models are calibrated by fitting the experimental CBTC; the following objective function is then defined:

$$\chi_{\mathcal{M}}^2(\mathbf{a}) = \frac{1}{M^2 N_{\text{data}}} \sum_{i=1}^{N_{\text{data}}} [\mathcal{M}^{\text{exp}}(t_i) - \mathcal{M}(t_i; \mathbf{a})]^2, \quad (6.5)$$

where \mathbf{a} is the array of the parameters to be estimated, which are listed in Table 5.1. Definition (6.5) clarifies the remark, made in section 4.1.2, about the need to discretize the temporal domain in such a way that a time level exists for each experimental data, so that all the contributions to the sum in expression (6.5) can be evaluated.

The analytical models have also been calibrated by minimization of another objective function, which is based on the misfit between the model and experimental temporal moments of the BTC m_1 and μ_2 :

$$\chi_{\mu}^2(\mathbf{a}) = \chi_{m_1}(\mathbf{a})^2 + \chi_{\mu_2}(\mathbf{a})^2, \quad (6.6)$$

where

$$\chi_{m_1}(\mathbf{a}) = \frac{m_1(\mathbf{a}) - m_1^{\text{exp}}}{m_1^{\text{exp}}} \quad \text{and} \quad \chi_{\mu_2}(\mathbf{a}) = \frac{\mu_2(\mathbf{a}) - \mu_2^{\text{exp}}}{\mu_2^{\text{exp}}}$$

are the relative errors in the determination of the moments; recall that, as explained in section 2.5, m_1 is the first order normalized moment, i.e., the average arrival time of the solute, and μ_2 is the second order central moment, i.e., the variance of the distribution of the arrival times of the solute.

In the following, with the expression “calibration (or optimization) with respect to the CBTC” it is meant the calibration obtained through the minimization of the objective function $\chi_{\mathcal{M}}^2$, defined by (6.5). On the other hand, with “calibration (or optimization) with respect to the temporal moments of the BTC”, it is meant the calibration obtained through the minimization of the objective function χ_{μ}^2 , defined by (6.6), which takes into account the moments of the BTC of order $r \leq 2$.

6.1.5 Overview of the analysis

In section 6.1.6 the results of the calibration of the analytical SDM and UDPerM, with respect both to the CBTC and to the temporal moments of the BTC, are presented for each MB and for each flow direction (see Tables 6.3, 6.4 and 6.6).

For the calibration of the analytical SDM, 2500 initializations have been considered for each test, resulting from the cartesian product of 50 values of D and of 50 values of v taken in the intervals $[5 \cdot 10^{-5}, 5 \cdot 10^{-3}] \text{ m}^2/\text{s}$ and $[2.5 \cdot 10^{-3}, 2.5 \cdot 10^{-1}] \text{ m/s}$, respectively, with a logarithmic step; these values have been chosen based on the estimates of D and v given by Vassena et al. (2010).

For the calibration of the analytical UDPerM, 3125 initializations have been considered for each test, resulting from the cartesian product of 5 values for each of the five parameters of the analytical UDPerM (see Table 5.1) varying with a logarithmic step in the following intervals: $D^{(H)}, D^{(L)} \in [5 \cdot 10^{-5}, 5 \cdot 10^{-3}] \text{ m}^2/\text{s}$, $v^{(H)} \in [2.5 \cdot 10^{-3}, 2.5 \cdot 10^{-1}] \text{ m/s}$, $v^{(L)} \in [5 \cdot 10^{-5} \text{ m/s}, v^{(H)}]$, $\varepsilon^{(H)} M^{(H)} \in [1 \text{ kg/m}^2, M]$.

In section 6.1.7 the results of the calibration of the numerical models (SDM, DPorM, UDPerM and CDPerM) with respect to the CBTC are presented (see Tables 6.7 to 6.10). In particular, the calibration of the numerical SDM and UDPerM has been performed

to compare the results with those of the corresponding analytical models, as a further verification of the codes. The calibration of the DPerM and CPerM, instead, permits to investigate the role of the solute exchange term in the description of the transport experiments and to assess the importance of the coupling between the two domains of the DDMs. To these aims, only tens of initializations have been considered, for which the values of the parameters have been chosen based on the results of the minimization of the analytical models. One test for each MB has been analyzed; in particular, the tests for which the calibration of the analytical SDM gave the largest values of $\chi_{\mathcal{M}}$ have been chosen, that is: MB1 EW, MB2 WE and MB3 WE.

In order to quantify the improvement of the fit of the experimental data obtained with the DDMs with respect to that obtained with the SDM, a parameter Δ is defined as the relative difference of the objective function of the DDMs with respect to the objective function of the SDM:

$$\Delta = \frac{\chi_{\mathcal{M}}^{\text{SDM}} - \chi_{\mathcal{M}}^{\text{DDM}}}{\chi_{\mathcal{M}}^{\text{SDM}}}. \quad (6.7)$$

In other words, Δ represents the percentage of improvement of the fit of the experimental data obtained using a DDM instead of the SDM. The values of Δ are reported in Table 6.5.

Figures 6.3 to 6.6 represent the results of the calibration of the different transport models with respect to the CBTC, i.e., the outcomes of the optimization of $\chi_{\mathcal{M}}$. In particular, Figure 6.3 compares the optimal value of the objective function $\chi_{\mathcal{M}}$ for the different tests and transport models.

For the two tests in which the UDPerM gives the best improvement over the SDM, i.e., MB1 EW and MB2 WE, Figure 6.4 represents the experimental and analytical CBTCs for both the SDM and the UDPerM. The insets show the same curves for $t \leq t_{60\%}$, so that the first part of the CBTCs can be focused.

Figure 6.5 represents the BTCs, normalized with respect to M , at the downstream border of the domain for the following three tests: MB1 EW, MB2 WE and MB3 WE. In Figure 6.5, the histograms represent the experimental BTC, while the curves represent the best-fit obtained with the different transport models.

Finally, Figure 6.6 represents the two components of the analytical BTC of the UDPerM corresponding to the (H) and (L) domains, i.e., $\varepsilon^{(H)} q_c^{(H)}$ and $\varepsilon^{(L)} q_c^{(L)}$.

Notice that, as will be discussed later, the results of the numerical SDM and UDPerM coincide with those of the corresponding analytical models; therefore, in Figures 6.3 to 6.6 it is not necessary to specify whether the curves represent the outcomes of the analytical or of the numerical models.

In section 6.7 the relevance of the DDMs is analyzed in the framework of multi-objective optimization: two objective functions are defined, namely the misfit between the experimental and modelled CBTCs for early and late times, respectively. The geometry of the Pareto frontier is proposed as an indicator to assess the presence of PFPs in porous media.

6.1.6 Calibration of the analytical models

Analytical SDM: optimization with respect to the CBTC

The minimization of $\chi_{\mathcal{M}}^2$ with the good initializations has yielded a single minimum for each test; Table 6.3 reports the corresponding best-fit parameters.

Table 6.3 shows that MB2 is the block with the highest values of D and v for both directions. MB1 and MB2 present a very different dispersive behaviour along the two

considered flow directions, with the NS values that are five to six times the values for the other direction, while MB3 appears to be more isotropic. The velocities, instead, do not show significant variations with the flow direction. These results are in agreement with the qualitative interpretation of Figure 6.1.

From the analysis of Table 6.3 it can be argued that MB1 for the NS direction is well described by the SDM; considering the value of $\chi_{\mathcal{M}}$, the same conclusion can be drawn for MB3, even if the value of χ_{μ} is quite high. The high values of $\chi_{\mathcal{M}}$ for MB1 EW and MB2 WE, instead, indicate that in those cases the SDM poorly fits the experimental data, so that an improvement is expected from the DDM approach.

Table 6.3 also includes the values of χ_{μ} , χ_{m_1} and χ_{μ_2} which are computed for the values of D and v that yield the minimum of $\chi_{\mathcal{M}}$: they are quite high, except for MB1 NS, and this is mainly due to χ_{μ_2} , whereas $|\chi_{m_1}| \leq 11\%$.

Model block	Flow direction	D [10^{-4} m ² /s]	v [10^{-3} m/s]	$\chi_{\mathcal{M}}$ %	χ_{m_1} %	χ_{μ_2} %	χ_{μ} %
MB1	NS	1.74	2.39	0.49	-0.43	-8.04	8.05
	EW	9.05	2.45	3.11	6.17	81.5	81.7
MB2	NS	157	13.8	1.11	-10.6	-55.0	56.0
	WE	890	14.7	4.93	6.64	75.7	76.0
MB3	NS	9.74	4.21	0.46	-2.44	-51.5	51.5
	WE	10.7	4.44	0.44	-2.64	-50.4	50.5

Table 6.3: Case study A: results of the optimization of $\chi_{\mathcal{M}}^2$ for the analytical SDM.

Analytical UDPerM: optimization with respect to the CBTC

For the UDPerM the problem of the non-uniqueness of the solution of the inverse problem arises for the minimization of both $\chi_{\mathcal{M}}$ and χ_{μ} .

For all the tests, the LM algorithm finds the absolute minimum for most of the good initializations. However, the algorithm also finds local minima, that cannot be ignored *a priori*, because the difference of the corresponding values of $\chi_{\mathcal{M}}$ with respect to the absolute minimum is small.

In order to clarify this observation, the most significant minima for each test are listed in Table 6.4. The criteria applied to select these minima are the fact that the values of $\chi_{\mathcal{M}}$ and χ_{μ} are the smallest available and no parameter attains unphysical values. The third column of Table 6.4 contains the codes with which the different minima are labelled, whereas the eighth column lists the ratio $\varepsilon^{(H)} M^{(H)}/M$, which represents the fraction of the total mass entering the high- K domain, and which gives a better physical insight than the parameter $\varepsilon^{(H)} M^{(H)}$ alone. Finally, the last column reports the fraction $\varepsilon^{(H)}$ of the total domain occupied by the high- K domain, which can be computed from relations (2.25) and (2.26) as:

$$\varepsilon^{(H)} = \frac{q - q^{(L)}}{q^{(H)} - q^{(L)}},$$

where the values of q are the estimates of the SDM (Table 6.3).

In some cases, the best-fit parameters of the UDPerM describe a medium which is equivalent to a single domain medium. For example, the absolute minimum A for the test MB1 NS corresponds to a prevalent low- K domain, whereas the local minimum B corresponds to a prevalent high- K domain, but these solutions do not significantly

Model block	Flow dir.	Min. code	$D^{(H)}$ [10^{-4} m ² /s]	$D^{(L)}$ [10^{-4} m ² /s]	$v^{(H)}$ [10^{-3} m/s]	$v^{(L)}$ [10^{-3} m/s]	$\varepsilon^{(H)}M^{(H)}/M$ %	χ_M %	χ_{m_1} %	χ_{μ_2} %	χ_μ %	$\varepsilon^{(H)}$ %
MB1	NS	A	$3.54 \cdot 10^{-2}$	1.84	2.44	2.39	2.64	0.30	-0.35	-4.87	4.88	5.98
		B	1.67	$2.45 \cdot 10^{-1}$	2.41	1.43	98.5	0.43	-0.08	-3.05	3.05	98.3
		C	$1.50 \cdot 10^{-7}$	1.74	3.00	2.39	0	0.49	-0.43	-8.04	8.05	0.01
	EW	A	8.49	$5.83 \cdot 10^{-1}$	3.15	1.81	70.7	0.56	0.35	4.74	4.75	47.5
MB2	NS	A	16.7	173	22.5	12.9	7.02	0.85	-7.04	-42.6	43.1	9.70
		B	147	78.0	17.7	5.27	81.4	0.92	0.39	14.8	14.8	68.7
		C	147	8.17	15.3	2.14	96.1	0.92	0.35	7.67	7.68	89.0
		D	$6.48 \cdot 10^{-1}$	145	69.0	13.7	2.43	1.04	-11.5	-57.4	58.5	0.26
	WE	A	96.0	295	100	9.34	39.0	1.36	8.38	59.3	59.9	5.89
MB3	NS	A	$6.99 \cdot 10^{-2}$	9.49	6.84	4.17	1.88	0.32	-2.32	-51.6	51.7	1.35
		B	9.51	$6.49 \cdot 10^{-2}$	4.26	2.43	98.7	0.43	-2.57	-52.9	53.0	97.4
		C	9.62	$4.75 \cdot 10^{-1}$	4.23	0.74	99.5	0.44	-0.43	-20.1	20.1	99.4
		D	9.74	$3.29 \cdot 10^{-9}$	4.21	4.17	100	0.46	-2.44	-51.4	51.5	100
	WE	A	9.45	9.65	4.94	3.79	59.8	0.25	-1.87	-45.8	45.8	56.3
		B	9.49	6.49	4.80	3.20	81.8	0.25	-1.87	-45.8	45.8	77.1
		C	10.5	$8.69 \cdot 10^{-8}$	4.45	2.40	100	0.47	-2.82	-51.6	51.7	99.5

Table 6.4: Case study A: results of the optimization of χ_M^2 for the analytical UDPerM.

differ from each other, because they correspond to similar physical situations. In fact the values of D and v of the dominant domain – (L) domain for A and (H) domain for B – are very close to each other. Moreover the relative error in the determination of m_1 and μ_2 is slightly less for B than for the absolute minimum A. Finally, minimum C represents a single (L) domain, whose parameters D and v , as well as the misfit functions, coincide with those of the SDM (Table 6.3).

Similar remarks apply to the MB2 NS test, for which the absolute minimum A and the local minima B and C represent similar physical situations in the sense that the parameters D and v of the dominant domains are close to each other; however, notice that the value of χ_μ is the smallest for C. Minimum D corresponds to a nearly single (L) domain, whose parameters D and v are quite similar to the solution of the SDM of Table 6.3 and to the parameters of the dominant (L) domain for minimum A and (H) domain for minima B and C.

For MB1 EW and MB2 WE, only one minimum is listed in Table 6.4 and it characterises a proper dual-domain medium which cannot be accurately described by the SDM. In particular, for MB1 EW the values of χ_M for other local minima found by the algorithm, and not listed in Table 6.4, are more than five times higher and correspond to the SDM solution. The absolute minimum of χ_M for the UDPerM is such that the fraction of the high- K domain is 47.5%, so that this is indeed a dual-domain case, with $v^{(H)} \simeq 1.7v^{(L)}$. As expected, the UDPerM greatly improves the fit of the experimental data: in fact χ_M and χ_μ decrease by a factor of 5.6 and 17 respectively from the corresponding SDM values, with $\Delta = 82\%$ (Table 6.5). This improvement is evidenced also by Figure 6.3, which compares the values of the objective function χ_M for the SDM and for the absolute minima of the UDPerM.

Concerning MB2 WE, the local minima, which are not listed in Table 6.4, correspond to the SDM solution of Table 6.3 with a χ_M value 3.6 times greater than that corresponding to the absolute minimum. The latter represents a dual domain composed of approximately 6% of high- K domain with a Darcy velocity 10 times greater than the flow velocity in the low- K domain ($v^{(H)} \simeq 10v^{(L)}$). As expected the UDPerM permits to improve the solution of the SDM, as χ_M decreases from 4.93% to 1.36% and $\Delta = 72\%$; however, the value of χ_μ still remains high, although it decreases from 76% to 59.9%.

Figures 6.4 and 6.6 highlight some differences between MB1 EW and MB2 WE. In fact Figure 6.4a shows that both the SDM and the UDPerM provide a good fit of the experimental data for $t < 750$ s, whereas for greater times the better performance of the UDPerM becomes apparent. This is consistent with the interpretation of Figure 6.6a, which shows that at $t \approx 750$ s the first particles travelling in the (L) domain reach the end of the MB, so that for early times the medium behaves like a single (H) domain. In the case of MB2 WE, instead, Figure 6.4b shows that the improvement of the fit obtained with the UDPerM is important at early times ($t < 100$ s), while for greater times both models fit the experimental data well. This is consistent with Figure 6.6b, where it is apparent that the particles of the (H) domain are so fast that they arrive at the end of the MB for $t \leq 100$ s (see also the value of $v^{(H)}$ in Table 6.4); then, for late times, the medium behaves as a single (L) domain.

Figure 6.5 shows that the UDPerM is able to reproduce both the double peak in the BTC of MB1 EW and the early peak and the tail in the BTC of MB2 WE.

Concerning the third MB, all the results for MB3 NS reported in Table 6.4 correspond to a nearly single domain, with the parameters D and v of the dominant domain that are close to those obtained for the SDM (Table 6.3). However it can be noticed that χ_μ for the local minimum C is less than a half of the value for the other minima: among the

local minima, C is characterised by the smallest value of $v^{(L)}$ and by the greatest value of $D^{(L)}$, i.e., for this minimum we have the greatest differences between the parameters of the dominant and non-dominant domains.

For the MB3 WE test, the fraction of the high- K domain for the absolute minimum A is 56.3% and for the local minimum B is 77.1%. At a first glance these percentages could support the hypothesis that MB3 WE should be interpreted with a UDPerM rather than with a SDM. However, the (H) and (L) parameters show similar values of D and v and therefore the minima A and B describe a physical situation similar to that of the local minimum C and of the SDM (see also Table 6.3). This conclusion is supported by Figure 6.6c, which shows, in the case of minimum A, that the BTCs of the (H) and (L) domain have similar peak times and variances; moreover, the BTCs of the SDM and the UDPerM (Figure 6.5c) nearly coincide and approximate well the experimental histogram, which is clearly unimodal and typical of a single-domain medium.

In all the tests, both $\chi_{\mathcal{M}}$ and χ_{μ} obtained with the UDPerM are smaller than those obtained with the SDM (see also Figure 6.3). This improvement is particularly important for MB1 EW and MB2 WE, i.e., for those examples where the presence of PFPs is more evident, as shown by Figure 6.1, as well as by Zappa et al. (2006) and Vassena et al. (2010).

Model block	Flow direction	DPorM	UDPerM	CDPerM
MB1	NS		38%	
	EW	24%	82%	82%
MB2	NS		23%	
	WE	63%	72%	74%
MB3	NS		31%	
	WE	43%	43%	43%

Table 6.5: Case study A: values of Δ , the relative improvement of the fit of the CBTC obtained with the DDMs with respect to that of the SDM. Missing values refers to tests for which the fit obtained from the SDM was very good and therefore the DPorM and CDPerM were not applied.

Optimization of the analytical SDM and UDPerM with respect to the temporal moments of the BTC

The results of the minimization of χ_{μ}^2 for the SDM are reported in Table 6.6.

The minimization of χ_{μ}^2 for the SDM requires the solution of the system of equations (3.19) and (3.23) in the two unknowns D and v , where the left-hand sides are given by the experimental values of m_1 and μ_2 reported in Table 6.2. Then, the LM algorithm was applied to check the fitting procedure only: the results of the minimization of χ_{μ}^2 coincide for all the tests with those obtained from the solution of (3.19) and (3.23). In this case the LM algorithm does not suffer the problem of falling in a region of the parameter space where χ_{μ}^2 is almost constant. Table 6.6 includes the values of $\chi_{\mathcal{M}}$ computed for the values of D and v that yield the minimum of χ_{μ} : they are quite high except for MB1 NS and they are greater than the optimal values of $\chi_{\mathcal{M}}$ by a factor varying between 1.5 and 14. The values of χ_{μ} , χ_{m_1} and χ_{μ_2} are not reported in Table 6.6, as they are very close to zero.

The results of the minimization of $\chi_{\mu'}^2$ reported in Table 6.6, show that, in agreement

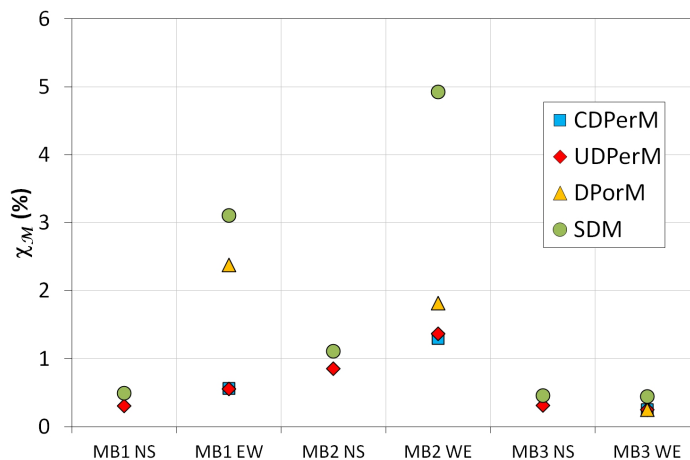


Figure 6.3: Optimal values of $\chi_{\mathcal{M}}$ for the different tests of case study A: SDM (green circles), DPorM (yellow triangles), UDPerM (red diamonds), CDPerM (blue squares).

with the results of the optimization of $\chi_{\mathcal{M}}^2$, MB1 and MB2 are anisotropic with respect to the longitudinal dispersion coefficient, even if the difference between the values of D for the two flow directions is less than that observed in Table 6.3.

The comparison of the results obtained for the two types of objective functions shows that the values of v are very similar, whereas the values of D show larger differences, even if they share the same order of magnitude.

The results of the optimization of χ_{μ}^2 for the analytical UDPerM are not reported here, because the equations for m_1 and μ_2 depend on five unknowns, thus the problem is clearly underdetermined and therefore it is not possible to find a unique minimum of χ_{μ}^2 .

For the same reason, the optimization with respect to the moments of the BTC will not be carried on for the numerical DDMs.

Model block	Flow direction	D [10^{-4} m ² /s]	v [10^{-3} m/s]	$\chi_{\mathcal{M}}$ %
MB1	NS	1.87	2.38	0.84
	EW	5.97	2.60	5.42
MB2	NS	249	12.3	5.06
	WE	614	15.7	7.50
MB3	NS	18.6	4.11	6.36
	WE	20.0	4.32	5.76

Table 6.6: Case study A: results of the optimization of χ_{μ}^2 for the analytical SDM.

6.1.7 Calibration of the numerical models

Tables 6.7 to 6.10 report the best-fit parameters, together with the corresponding value of the objective function $\chi_{\mathcal{M}}$, given by the different numerical transport models for each

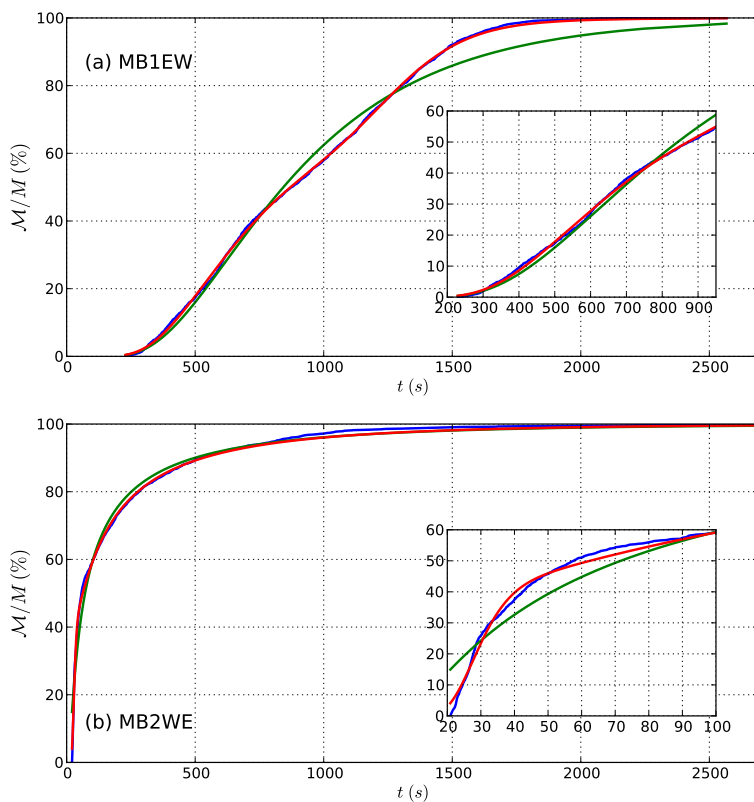


Figure 6.4: Case study A: CBTCs, normalized with respect to M , for MB1 EW (a) and MB2 WE (b). Blue line is the experimental CBTC; green and red lines are the model CBTCs for the SDM and the UDPerM respectively. The insets show the same curves for $t \leq t_{60\%}$.

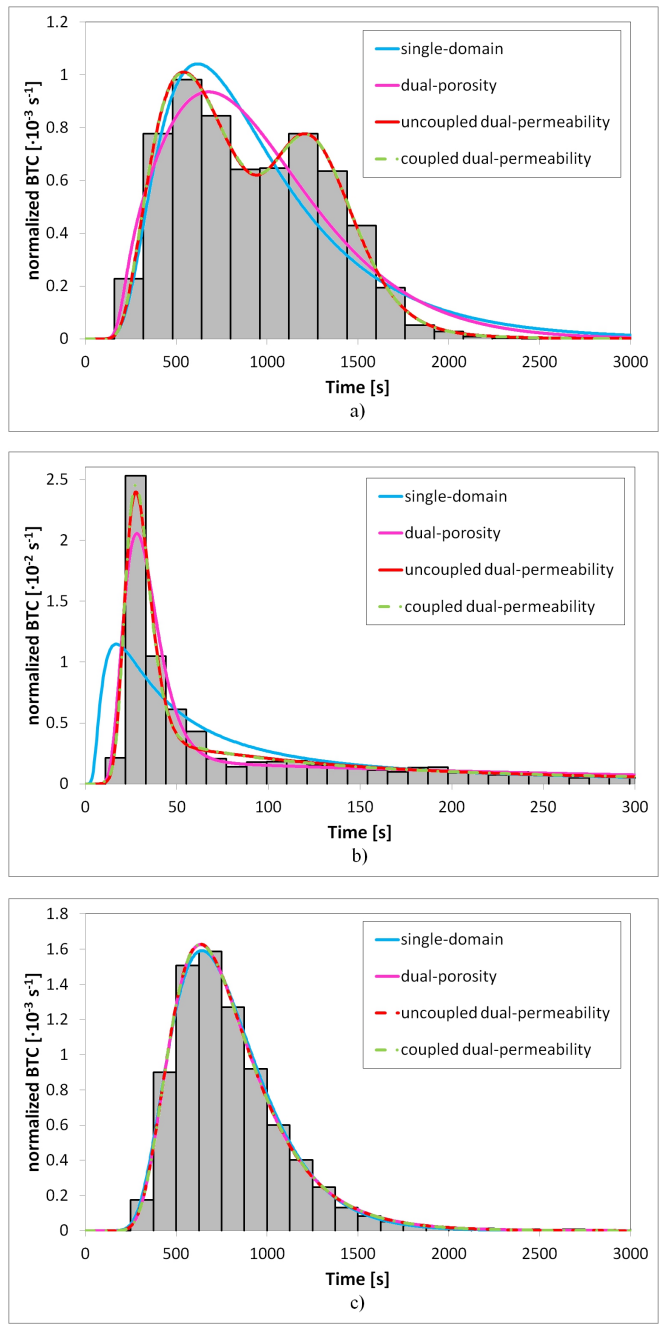


Figure 6.5: Case study A: BTCs, normalized with respect to M , for MB1 EW (a), MB2 WE (b) and MB3 WE (c). The histogram represents the experimental BTC, while the curves represent the best-fit of the transport models: SDM (blue line), DPorM (purple line), UDPerM (red line), CDPerM (green line).

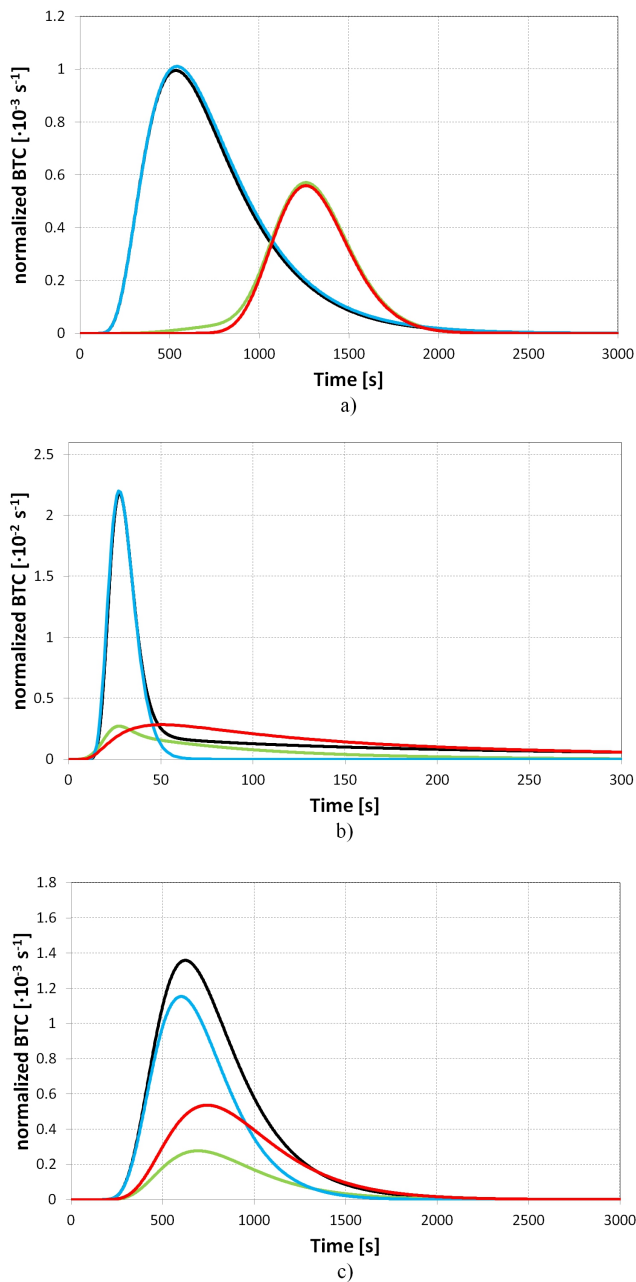


Figure 6.6: Case study A: components relative to the two domains of the BTC of the UDPerM (H - blue line, L - red line) and of the CDPerM (H - black line, L - green line), i.e., $\varepsilon^{(H)} q_c^{(H)}$ and $\varepsilon^{(L)} q_c^{(L)}$, for MB1 EW (a), MB2 WE (b) and MB3 WE (c).

test considered. As explained in section 6.1.5, only one flow direction for each MB has been analyzed, choosing those tests for which the calibration of the analytical SDM gave the largest optimal values of $\chi_{\mathcal{M}}$, that is: MB1 EW, MB2 WE and MB3 WE.

In Tables 6.9 and 6.10 the parameter $\varepsilon^{(H)}n^{(H)}$ represents the volume of pore water in the fast domain per unit volume of the porous medium, and it corresponds to n^{mob} for the DPorM.

Notice that the values of the parameters identified by the numerical implementation of the SDM and the UDPerM coincide with those identified by the analytical implementation and reported in Tables 6.3 and 6.4. In particular, it is important to observe that the parameters $\varepsilon^{(H)}$ and $M^{(H)}$ are not uniquely identified by the numerical inverse UDPerM (Table 6.9), in the sense that different initializations lead to different couples of values for these parameters; nevertheless, all these couples are characterized by the fact that their product is constant and equal to the parameter $\varepsilon^{(H)}M^{(H)}$ identified by the analytical inverse UDPerM.

Table 6.5 and Figure 6.3 show that the DPorM improves the fit of the SDM, but it does not perform as well as the UDPerM, since $\Delta = 24\%$ for MB1 and $\Delta = 63\%$ for MB2. Figure 6.5 shows that the DPorM describes quite well the early peak and the tail of the experimental BTC of MB2 WE, but it is not able to reproduce the double peak of MB1 EW.

Regarding MB3, it can be seen that all the transport models give almost the same results (see also Figure 6.5c) and even the standard SDM provides a good fit of the experimental data, with an average squared difference between the model and the experimental CBTC which is only the 0.4% of the total mass injected per unit surface (Table 6.7). It can be noticed from Table 6.5 that for this block the DDMs permit, anyway, a 43% decrease of the objective function.

It is important to observe that, for all the blocks, the CDPerM (Table 6.10) gives almost the same minimum of the objective function $\chi_{\mathcal{M}}$ as the UDPerM (Table 6.9); this is confirmed by Figure 6.3 and by the values of Δ in Table 6.5. Consequently, as can be seen in Figure 6.5, the corresponding BTCs coincide. In other words, the introduction of the exchange term in the DPerM does not lead to a significant improvement of the fit. It is interesting to understand how this is related to the optimal parameters for the two dual-permeability approaches; by comparing Tables 6.9 and 6.10, it can be seen that for MB1 the optimal parameters of the UDPerM and of the CDPerM are almost equal, and the exchange coefficient is small, so that the two DPerMs actually describe the same physical situation. This is confirmed by Figure 6.6a, where the BTCs of the two domains differ only very slightly between the coupled and the uncoupled model.

The CDPerM has an optimal $v^{(L)}$ which is almost negligible for MB2, so that the CDPerM actually reduces to the DPorM. Moreover, for both MB2 and MB3, the mass of solute that enters the fast domain is larger for the CDPerM than for the UDPerM; these differences are compensated by the exchange term whose coefficient α is larger for MB2 and MB3 than for MB1.

The role of the solute exchange term in the description of these transport experiments can be further analyzed by comparing the typical solute exchange time with the typical times of advective transport, as shown in the next section.

6.1.8 Characteristic transport times

Table 6.11 reports the ratio of the characteristic exchange time (τ_e) to the characteristic time of advective transport (t_T) and the dimensionless numbers Pe and $\mathcal{A}E$ defined for

Test	D [10^{-4} m ² /s]	v [10^{-3} m/s]	$\chi_{\mathcal{M}}$ %
MB1 EW	9.05	2.45	3.1
MB2 WE	890	14.7	4.9
MB3 WE	10.7	4.44	0.4

Table 6.7: Case study A: results of the calibration of the numerical SDM.

Test	D [10^{-4} m ² /s]	v [10^{-3} m/s]	n^{mob} [10^{-2}]	α [10^{-4} s ⁻¹]	$\chi_{\mathcal{M}}$ %
MB1 EW	5.39	7.04	7.15	9.12	2.38
MB2 WE	1.52	84.5	4.20	8.90	1.82
MB3 WE	9.46	4.70	18.7	0.61	0.25

Table 6.8: Case study A: results of the calibration of the DPorM.

the DPorM in section 2.4.1, together with the analogous quantities defined for the CDPerM in section 2.4.2.

Notice that, for the DPorM, considering definitions (2.22), (2.23) and (2.24), the ratio between the typical times, τ_e/t_T , is related to the dimensionless number $\mathcal{A}E$ by:

$$\mathcal{A}E = \frac{n^{\text{mob}} \tau_e}{\ln 2 t_T}. \quad (6.8)$$

Since $n = 0.2$ and $0 < n^{\text{mob}} \leq n$, (6.8) implies that $\mathcal{A}E$ can vary from 0 to $\frac{n}{\ln 2} \frac{\tau_e}{t_T} \approx 0.3 \frac{\tau_e}{t_T}$ as a linear function of n^{mob} .

For the CDPerM, the corresponding definitions in section 2.4.2 yield:

$$\mathcal{A}E^{(H)} = \frac{\varepsilon^{(H)} n^{(H)} v^{(H)}}{v \ln 2} \frac{\tau_e}{t_T} = \frac{n^{(H)}}{\ln 2} \frac{\varepsilon^{(H)} v^{(H)}}{\varepsilon^{(H)} v^{(H)} + \varepsilon^{(L)} v^{(L)}} \frac{\tau_e}{t_T}, \quad (6.9)$$

where the hypothesis $n^{(H)} = n$ as been applied; a similar expression holds for $\mathcal{A}E^{(L)}$.

MB1

Table 6.11 shows that, in the case of MB1, the exchange term for the DPorM is greater than both the convective and the dispersive terms ($\mathcal{A}E < 1 < Pe$), and the characteristic times τ_e and t_T have the same order of magnitude, which implies an important effect of dual-porosity, i.e., strong asymmetry of the BTC (see section 2.4.1).

For the CDPerM, instead, the convective term is greater than the exchange and the dispersive terms for both the fast and the slow domains ($1 < Pe^{(H)} < \mathcal{A}E^{(H)}$ and $1 < \mathcal{A}E^{(L)} < Pe^{(L)}$), and $\tau_e/t_T \gg 1$, that is, the solute exchange is slow and does not significantly influence the solute concentration, in agreement with Figure 6.6a. Since the hydrodispersive parameters of the two domains are very different (see Table 6.10), the fact that the exchange is not important implies that the transport properties of MB1 are well described by an equivalent superposition of two independent and mobile domains, as observed in section 6.1.6. The exchange term is important in the equivalent description of the DPorM to compensate for the fact that one of the two domains is immobile; on the other hand, the two domains of the CDPerM take into account both groups of fast

Test	$D^{(H)}$ [10 ⁻⁴ m ² /s]	$D^{(L)}$ [10 ⁻⁴ m ² /s]	$v^{(H)}$ [10 ⁻³ m/s]	$v^{(L)}$ [10 ⁻³ m/s]	$\varepsilon^{(H)}$ %	$M^{(H)}$ [10 ³ kg/m ²]	$\varepsilon^{(H)}M^{(H)}/M$ %	$\varepsilon^{(H)}n^{(H)}$ [10 ⁻²]	χ_M %
MB1 EW	8.48	$5.82 \cdot 10^{-1}$	3.15	1.81	14.5	13.4	70.7	2.91	0.56
MB2 WE	96.1	294	100	9.33	10.7	9.72	39.1	2.13	1.36
MB3 WE	9.44	9.64	4.94	3.78	17.9	12.0	59.6	3.59	0.25

Table 6.9: Case study A: results of the calibration of the numerical UDPertM.

Test	$D^{(H)}$ [10 ⁻⁴ m ² /s]	$D^{(L)}$ [10 ⁻⁴ m ² /s]	$v^{(H)}$ [10 ⁻³ m/s]	$v^{(L)}$ [10 ⁻³ m/s]	$\varepsilon^{(H)}$ %	$M^{(H)}$ [10 ³ kg/m ²]	α [10 ⁻⁴ 1/s]	$\varepsilon^{(H)}M^{(H)}/M$ %	$\varepsilon^{(H)}n^{(H)}$ [·10 ⁻²]	χ_M %
MB1 EW	8.41	$5.66 \cdot 10^{-1}$	3.18	1.80	29.1	6.77	$4.65 \cdot 10^{-2}$	71.2	5.82	0.56
MB2 WE	86.2	379	98.4	$6.00 \cdot 10^{-8}$	19.6	7.50	6.27	55.3	3.92	1.30
MB3 WE	9.25	11.6	4.75	3.17	72.2	4.99	1.30	100.0	14.4	0.25

Table 6.10: Case study A: results of the calibration of the CDPerM.

and slow solute particles, so that, for both domains, the exchange term diminishes its importance with respect to the convective term.

MB2

The results of the DPorM for MB2 show that $\tau_e/t_T \gg 1$; according to the discussion in section 2.4.1, this means that the solute exchange is slow and the DPorM is nearly equivalent to the SDM. Nevertheless, $\mathcal{A} \approx 1 < Pe$, that is, the exchange term gives approximately the same contribution to the temporal variation of the concentration as the convective term. However, since $\tau_e/t_T \gg 1$, a less important contribution of the exchange term, that is a larger value of \mathcal{A} , would have been expected. The apparent contradiction can be explained taking into account relation (6.8) and the small value of n_{mob} (see Table 6.8).

For the CDPorM, the value of τ_e/t_T shows that the exchange is faster than for the DPorM and that the convective term is larger than the exchange term only for the fast domain, but not for the slow domain. Table 6.10 shows that the hydrodispersive parameters of the two domains are very different. From this analysis it can be concluded that for MB2 the CDPorM is characterized by a slightly more important role of the solute exchange term with respect to MB1.

MB3

Both the results of the DPorM and of the CDPorM indicate that MB3 can be effectively described by a SDM. In fact, in the case of the DPorM, $\tau_e/t_T \gg 1$ and $1 < \mathcal{A} < Pe$.

In the case of the CDPorM, the convective term is larger than the exchange term only for the fast domain, but not for the slow domain, as for MB2. Moreover, $\tau_e/t_T \approx 1$, that is, the solute exchange occurs with approximately the same velocity of the convective transport; nevertheless, Table 6.10 shows that the hydrodispersive parameters of the two domains are very similar, so that the CDPorM is equivalent to the SDM.

Remarks

The analysis presented in this section showed some interesting aspects, which are summarized in the following points.

- DPorM: the parameters τ_e/t_T and \mathcal{A} do not carry the same information, as \mathcal{A} also depends on n^{mob} , as shown by (6.8). The analysis of both parameters is then necessary to assess the effects and the importance of the solute exchange term in each case. The most representative example for this feature is MB2.
- CDPorM: the relation between τ_e/t_T and $\mathcal{A}^{(H)}$ (and, similarly, between τ_e/t_T and $\mathcal{A}^{(L)}$), given by (6.9), is more complex than for the DPorM, but also in this case, the different parameters do not give equivalent information, even if they often lead to similar conclusions. Moreover, for the interpretation of τ_e/t_T , $\mathcal{A}^{(H)}$ and $\mathcal{A}^{(L)}$, it is very important to consider the values of the parameters of the two domains ($v^{(H)}$, $v^{(L)}$, $D^{(H)}$, $D^{(L)}$), as already observed in section 2.4.2 (the most representative examples are MB1 and MB3). In fact, a very slow exchange between two domains with different hydrodispersive features implies a description equivalent to the UDPorM and not to the SDM; on the other hand, an important exchange between two domains that share the same hydrodispersive parameters implies a description equivalent to the SDM.

		MB1 EW	MB2 WE	MB3 WE
DPorM	τ_e/t_T	2.2	22	15
	$\mathcal{A}E$	0.23	1.3	4.1
	Pe	31	17	17
CDPerM	τ_e/t_T	140	7.1	6.6
	$\mathcal{A}E^{(H)}$	17	2.0	1.5
	$\mathcal{A}E^{(L)}$	23	$5.1 \cdot 10^{-9}$	0.39
	$Pe^{(H)}$	9.0	34	18
	$Pe^{(L)}$	76	$4.8 \cdot 10^{-9}$	9.6

Table 6.11: Case study A: ratio of the characteristic exchange time (τ_e) to the characteristic time of advective transport (t_T) and dimensionless numbers Pe and $\mathcal{A}E$ for the DPorM and the CDPerM.

6.1.9 Results on the conditioning of the Hessian matrix of the objective function and on the correlation matrix

As explained in section 5.1.2, the condition number κ_2 of the Hessian matrix $\mathbf{H}(\mathbf{a}_{\text{opt}})$ of the objective function $\chi_{\mathcal{M}}$ at the end of the minimization process can be computed to analyze the conditioning of the computation of the inverse of the Hessian matrix and therefore of the corresponding computation of the covariance and correlation matrices.

Table 6.12 reports such condition numbers for the different transport models and blocks of sediments. It can be seen that κ_2 increases with the complexity of the model, but it is greater for the UDPerM than for the CDPerM. The greatest condition numbers are obtained for the UDPerM and for MB1 and MB3; as a consequence, in these cases the inversion of the Hessian matrix yields some non-acceptable negative diagonal elements in the covariance matrix, which do not allow the computation of the correlation between the corresponding parameters. In the other cases, the analysis of the correlation matrix ρ has shown that, for all the blocks, $\varepsilon^{(H)}$ and $M^{(H)}$ have a correlation close to 1, both for the UDPerM and the CDPerM, which is consistent with the previous remark on the uniqueness of the product $\varepsilon^{(H)}M^{(H)}$ and on the non-uniqueness of the two separate parameters. Moreover, in the case of the CDPerM the correlation among all the parameters is always greater than 0.7, which is not the case for the UDPerM.

	MB1 EW	MB2 WE	MB3 WE
SDM	4.7	2.5	5.1
DPorM	$8.4 \cdot 10^6$	$2.7 \cdot 10^4$	$9.6 \cdot 10^6$
UDPerM (analytical)	$1.1 \cdot 10^{15}$	$7.9 \cdot 10^{10}$	$2.9 \cdot 10^{20}$
UDPerM (numerical)	$1.4 \cdot 10^{29}$	$2.6 \cdot 10^{25}$	$4.3 \cdot 10^{28}$
CDperM	$4.7 \cdot 10^{23}$	$1.5 \cdot 10^{19}$	$4.1 \cdot 10^{23}$

Table 6.12: Case study A: condition numbers of the Hessian matrix of the objective function $\chi_{\mathcal{M}}$.

6.1.10 Single and dual domain media in a multi-objective framework

The results presented in sections 6.1.6 and 6.1.7 have been obtained by minimization of the objective function $\chi_{\mathcal{M}}^2$ defined in (6.5), which is based on the fit of the whole

experimental CBTC, i.e., for times t_k ranging from the arrival time of the fastest particle, t_{\min} , to that of the slowest particle, t_{\max} .

Obviously, the SDM can describe a medium with only a single flow velocity. Therefore if a porous medium has a dual behaviour, i.e. if it is characterized by the presence of PFPs, the SDM can fit well the portion of the BTC corresponding to the fast particles, to the slow particles or a compromise between them. It is then clear that the calibration problem for dual domain media could be considered in a multi-objective framework.

The multi-objective optimization of hydrologic models is characterised by the definition of two (or more) objective functions that describe different aspects of the system behaviour and are often aggregated, through a weighted sum, into a single global objective function. A multi-objective calibration problem usually does not have a single global solution, but a Pareto set (or frontier) of optimal solutions (Gupta et al., 1998; Yapo et al., 1998; Boyle et al., 2000, 2001; Madsen, 2003; Vrugt et al., 2003; Blasone et al., 2007), whose elements are such that by moving from one element to the others, one of the objective functions decreases, whereas the other objective functions increase.

The discussion in section 6.1.6 about the CBTCs shown in Figure 6.4 suggests to consider the following two objective functions:

$$\chi_{P\%}^2(\mathbf{a}) = \frac{1}{M^2 N_{P\%}} \sum_{i=1}^{N_{P\%}} [\mathcal{M}^{\text{exp}}(t_i) - \mathcal{M}(t_i; \mathbf{a})]^2,$$

$$\chi_{(100-P)\%}^2(\mathbf{a}) = \frac{1}{M^2 (N_{\text{data}} - N_{P\%})} \sum_{i=N_{P\%}+1}^{N_{\text{data}}} [\mathcal{M}^{\text{exp}}(t_i) - \mathcal{M}(t_i; \mathbf{a})]^2,$$

where $N_{P\%}$ is the cardinality of the set $\{t_k \leq t_{P\%}, k = 1, \dots, N_{\text{data}}\}$, so that $\chi_{P\%}^2$ represents the misfit between the CBTCs for $t \leq t_{P\%}$, i.e., the first $P\%$ of the injected particles is taken into account in the computation of the mean squared error. On the other hand $\chi_{(100-P)\%}^2$ considers the remaining $(100 - P)\%$ of the injected particles. The minimization of $\chi_{P\%}^2$ and $\chi_{(100-P)\%}^2$ permits to best fit different portions of the experimental CBTC, corresponding respectively to the early times, $t \in [t_{\min}, t_{P\%}]$, and to the late times, $t \in [t_{P\%}, t_{\max}]$.

Figure 6.7 plots the values assumed by $\chi_{P\%}$ and $\chi_{(100-P)\%}$ when the parameters $\mathbf{a} = (D, v)^T$ vary in an interval around the best-fit values computed by the analytical SDM (Table 6.3), for three different percentages of the particles ($P=6, 50$ and 90), for MB1 NS and MB2 WE. These graphs give a rough representation of the structure of the Pareto frontier, the exact determination of which would require specific techniques described, e.g., by Vrugt et al. (2003). Anyway this is beyond the scopes of the present analysis. The aim here is to assess whether the Pareto set could be an indicator of the ‘‘duality’’ of a porous medium. In particular the red dots correspond to the points that belong to the Pareto frontier, as estimated on the basis of the data drawn in the same figure.

The graphs for the MB1 NS and MB2 WE tests show some important differences that can be linked to the different nature of the two examples, single-domain and dual-domain medium, respectively.

In the case of MB1 NS, for $P=6$, Figure 6.7a shows that the Pareto set reduces to a very small region, possibly a single point, as the two objective functions decrease simultaneously. The same result is observed for $P=50$ and $P=90$ (Figures 6.7b and 6.7c), i.e., it seems to be independent of the percentage of the particles considered. This is in agreement with the outcomes of section 6.1.6, which have shown that MB1 NS is a single-domain medium. In fact in the case of a single-domain medium the SDM solution

describes well the whole experimental CBTC and not only the first or the last part of the curve.

In the case of MB2 WE, that has been shown to be dual (sections 6.1.6 and 6.1.7), Figure 6.7d exhibits a Pareto front characterized by the fact that decreasing $\chi_{6\%}$ causes the increase of $\chi_{(100-6)\%}$ and vice versa. This is exactly what is expected in the case of a dual-domain medium. In fact, as previously mentioned, a SDM solution cannot describe the whole experimental CBTC of a dual-domain medium: fitting well the first part of the curve, for $t \in [t_{\min}, t_{6\%}]$, results in a bad fit of the last part, for $t \in [t_{6\%}, t_{\max}]$.

Figures 6.7e and 6.7f show that for high values of P the graphs are quite similar to those of a single-domain medium (compare Figures 6.7c and 6.7f). This can be explained by the fact that, for $P=6$, $\chi_{6\%}$ includes only the fastest 6% of the particles injected, i.e., it includes only the particles traveling in the (H) domain. For high values of P , instead, $\chi_{P\%}$ considers the particles traveling in both (H) and (L) domains, so that the duality of the medium cannot be resolved. For instance, for $P=90$, $\chi_{90\%}$ attempts to best fit a SDM solution to the experimental data for $t \in [t_{\min}, t_{90\%}]$, i.e., for almost the whole set of experimental data, which is not possible for a SDM solution, as already discussed.

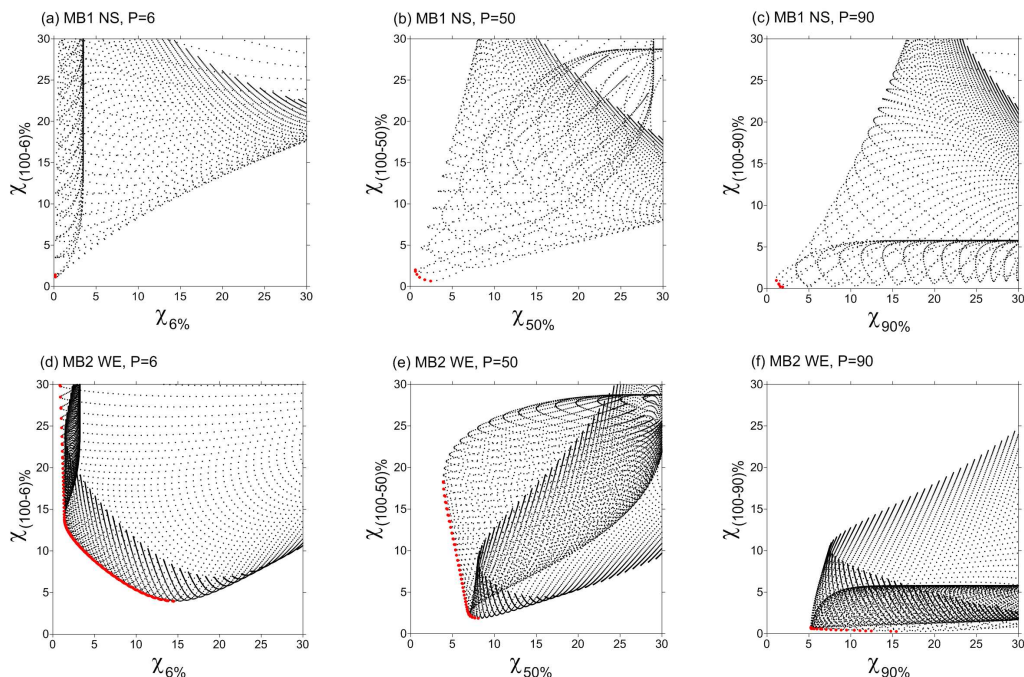


Figure 6.7: Qualitative estimate of the Pareto set for MB1 NS and MB2 WE and for $P=6, 50, 90$. Each graph plots the percentage values of the objective functions $\chi_{P\%}$ and $\chi_{(100-P)\%}$ computed for different values of the parameters of the SDM and the red dots correspond to the points belonging to the Pareto frontier.

6.1.11 Concluding remarks on case study A

Comparison of the results of the different transport models

For all tests, the UDPerM improves the fit of the experimental data with respect to the classical SDM. Such improvement is small for MB1 NS, MB2 NS and both tests on MB3,

whereas it is significant for MB2 EW and MB1 WE.

The results of the hydrostratigraphic analysis and of the geostatistical simulation (see section 6.1.1), as well as the interpretation of the evolution of the solute plumes shown in Figure 6.2 and of the experimental BTCs shown in Figure 6.5, highlight that MB1 and MB2 are characterized by PFPs in the WE direction, a feature that is missing in MB3.

Therefore, it can be concluded that those tests for which the presence of PFPs is more evident (MB1 EW and MB2 WE) are described with a far greater effectiveness by the UDPerM than by the SDM; on the other hand, those tests with less marked presence of PFPs (MB1 NS, MB2 NS and MB3) are efficiently described by the standard SDM.

Moreover, taking Table 6.1 into account, the fraction of the highly permeable materials, as gravel, and the degree of heterogeneity, which can be quantified by $\text{var}[\ln K]$, are not the most important parameters controlling the existence of PFPs. In fact, MB3 has about three times more gravel than MB1 and it is more heterogeneous than MB1, as shown by the values of $\text{var}[\ln K]$. The key factor in controlling the existence of PFPs is the spatial arrangement of the highly permeable materials, i.e., if they are connected or not; in fact, Table 6.1 shows that gravel connectivity for MB1 and MB2 is two orders of magnitude larger than for MB3. As a further support of this observation, the interpretation of the numerical tracer tests showed that MB3 behaves like a homogeneous domain, while the BTC of MB1 EW and of MB2 WE are highly asymmetrical and characterized either by double peaks (MB1 EW) or by an early peak and a long tail (MB2 WE), which are clear effects of PFPs.

For all tests, the fit of the CDPerM basically coincides with the fit of the UDPerM; in other words, the introduction of the solute exchange term between the fast and the slow domains does not lead to a significant further improvement of the description of the experimental data.

The DPerMs are able to describe the typical effects of the presence of PFPs on the solute transport, that is, the double peak in the BTC of MB1 EW and the early peak and the tail in the BTC of MB2 WE.

On the other hand, the DPorM improves the fit of the SDM, but it does not perform as well as the UDPerM; in particular, the DPorM can describe quite well the early peak and the tail in the BTC of MB2 WE, but it obviously cannot reproduce double peaks in the BTCs.

Therefore, among the three DDMs considered in this work, the UDPerM is the model that most efficiently describes the transport properties of those blocks characterized by structured heterogeneity and presence of PFPs.

Uniqueness of the estimated parameters

The calibration of the SDM results in a unique set of best-fit parameters. On the other hand, the issue of non-uniqueness arises for the calibration of the DDMs, which makes important to analyze the sets of parameters corresponding to the different minima (global and local), in order to assess which solution is physically more acceptable.

For example, such analysis, performed on the results of the calibration of the analytical UDPerM (section 6.1.6), shows that the local minima obtained from the calibration of the UDPerM often correspond to the physical situation described by the SDM. In other words, for local minima, one domain is usually dominant and the calibrated values of D and v for this domain are close to those obtained by the calibration of the SDM. For the tests that present a clear “dual” behaviour, the local minima are characterised by a misfit much greater than that of the absolute minimum.

Optimization with respect to the temporal moments of the BTC

The optimization of χ_{μ}^2 for the SDM gives results which are similar to those obtained with the optimization of $\chi_{\mathcal{M}}^2$, especially regarding the estimates of the velocity. Nevertheless, this kind of optimization is not suitable for the calibration of the DDMs, for which the problem is underdetermined.

6.2 Case study B. Numerical tracer tests on a decameter scale block from a point bar channel aquifer analogue in the Lambro basin (Northern Italy)

The second case study consists of a prismatic block of sediments, around 100 m³ in volume, dug in a quarry site into real sediments of an alluvial aquifer analogue.

The study site is located in the southern Lambro Valley (Northern Italy, south of Milan), where the Lambro River, a left tributary of the Po River, is a meandering stream encased in a post-glacial terraced valley, within the Pleistocene sediments of the Lario sandur. A volume of approximately 30,000 m³ (47 m×75 m×8.6 m) was dug into an aquifer analogue exposed in a quarry at this site, specifically, into sands and gravels of a point-bar/channel association of Holocene age. This case study has been extensively described and analysed from the hydrostratigraphic point of view by dell'Arciprete (2010) and dell'Arciprete et al. (2012a), where the details on the geostatistical simulations can also be found; the main concepts are recalled in section 6.2.1. The numerical tracer tests and the connectivity analysis are presented in dell'Arciprete et al. (2012b) and summarized in sections 6.2.2 and 6.2.3. The experimental data resulting from the numerical tracer tests are presented and discussed in section 6.2.4, whereas the results of their interpretation with the single and dual-domain transport models are given in sections 6.2.5 and 6.2.6. Finally, some concluding remarks are given in section 6.2.7.

6.2.1 Geological and hydrostratigraphic features and ensembles of geostatistical simulations of the block of sediments

The geological and hydrostratigraphic model of the site was elaborated starting from the stratigraphical, sedimentological and geophysical analysis of the quarry volume (Bersezio et al., 2004, 2007; dell'Arciprete et al., 2012a).

The paper by dell'Arciprete et al. (2012a) presented and discussed the results of the 3D geostatistical simulations, which were performed both on the entire volume of sediments and on a subregion represented by a prismatic block of dimensions 11.4 m×11.4 m×2.85 m, named "test volume". The test volume, which was discretized with a regular grid with spacing 0.2 m×0.2 m×0.05 m, is small enough to permit the simulation of the facies distribution with good resolution for a large number of stochastic realizations and the corresponding simulation of solute transport experiments. Moreover, from the hydrostratigraphic point of view, this test volume can be considered as representative of the behaviour of the whole studied domain. For these reasons, the test volume is the second case study considered in the present work.

Four hydrofacies were assumed in the geostatistical simulation, based on the analysis of conductivity values obtained by laboratory tests on samples and the comparison with literature data: least permeable ($K = 5 \cdot 10^{-5} \text{ ms}^{-1}$, very fine sand and minor silt-clay - F), poorly permeable ($K = 5 \cdot 10^{-4} \text{ ms}^{-1}$, sand from point-bar and channel fill bedforms - S), permeable ($K = 5 \cdot 10^{-3} \text{ ms}^{-1}$, sandy gravel and gravelly sand from scroll bars - SG) and most permeable ($K = 5 \cdot 10^{-2} \text{ ms}^{-1}$, open framework gravels - G). An

ensemble of 50 equiprobable realizations was obtained with two different methods of geostatistical simulation: Sequential Indicator Simulation (SISIM, see, e.g., Deutsch and Journel (1992)) and MPS (Multiple Point Simulation, see, e.g., Strebelle (2002)). Two representative examples of the results of the geostatistical simulation are shown in Figure 6.8. The experimental and model variograms used for the SISIM simulations can be found in the electronic supplementary material of dell’Arciprete et al. (2012a) and are reported in Figure 6.9 for the Reader’s convenience. The experimental variograms have been described with different models for the different hydrofacies and for the different directions. Specifically, for facies F the model variogram is a linear combination of a gaussian and a spherical variogram with a very large horizontal range (140 m) and a vertical range (3 m) of the same order of magnitude as the vertical size of the block. For facies S, a linear combination of an exponential and a gaussian variogram has been used, with ranges smaller than the block scale (3 m horizontally and 0.5 m vertically). For facies SG an exponential variogram is assumed, with ranges similar to those of facies S. Finally, for facies G a linear combination of an exponential and a spherical variogram was used with small values of the range: 1 m and 5 m along the two horizontal directions and 0.3 m along the vertical direction.

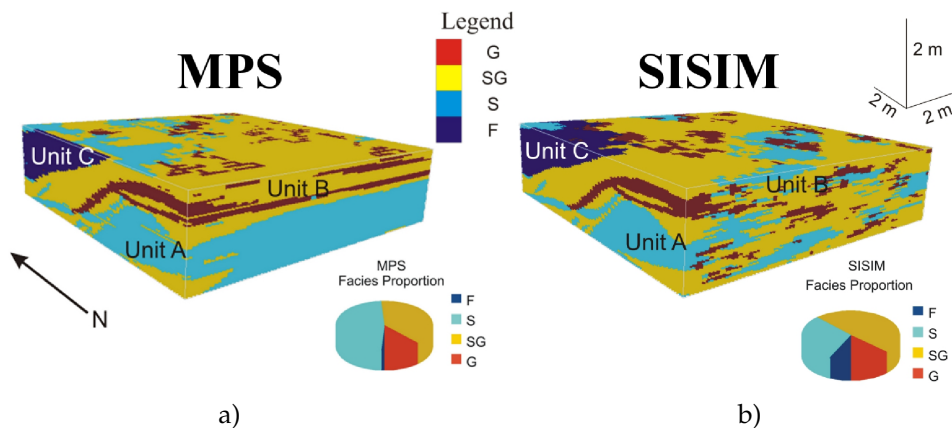


Figure 6.8: Results of one of the 50 equiprobable geostatistical simulations obtained with a) MPS and b) SISIM; the pie charts represent the facies proportions. From dell’Arciprete et al. (2012b).

As discussed by dell’Arciprete et al. (2012a) and dell’Arciprete et al. (2012b), the volumes simulated by the two geostatistical simulation methods have different features. In fact, the volumes simulated by MPS are more structured and are often characterized by the presence of connected bands of permeable sediments (G, SG, S) that can represent the PFPs; on the other hand, the MPS simulations cannot take into account the geometry and distribution of the F hydrofacies bodies. For example, Figure 6.8a clearly shows connected channels of gravel, which is the most conductive facies considered, while the F proportion is almost negligible. The volumes simulated by SISIM are more disorganized; on the other hand, all the hydrofacies, including F, have a good and realistic spatial continuity (see Figure 6.8b). The spatial average and variance of $\ln K$ have been computed for each realization and the ensemble expected values are listed in Table 6.13, which shows that the difference among the two ensembles is related to the spatial variability more than to the averaged K . The different architecture of the volumes simulated by MPS and SISIM significantly influences their transport properties and, to a less extent,

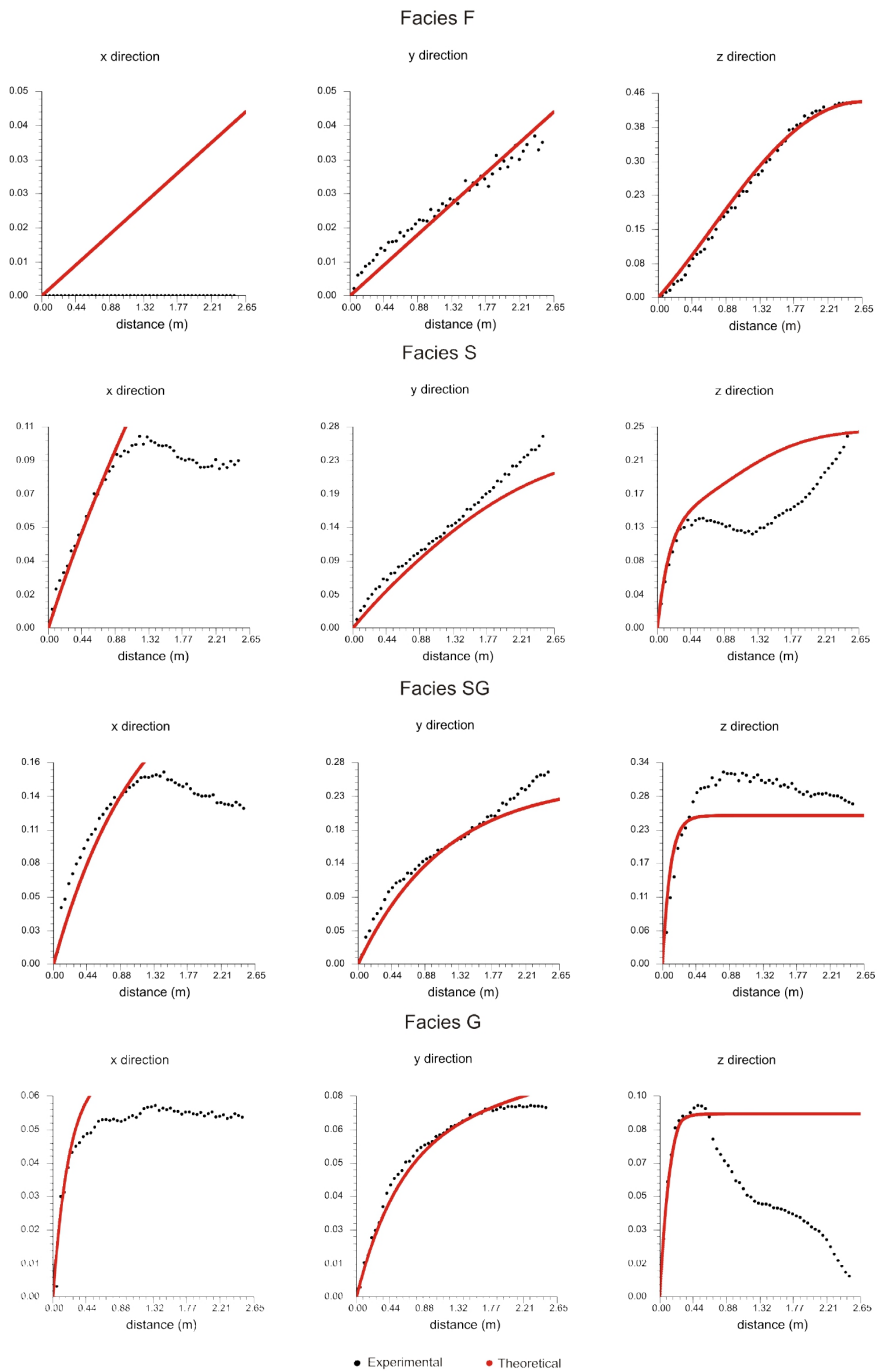


Figure 6.9: Experimental (black dots) and model (red lines) variograms for the four hydrofacies and for the three directions. From the electronic supplementary material of dell’Arciprete et al. (2012a).

their flow properties, as will be shown in the following sections 6.2.2 to 6.2.2.

Notice that, in the following, the two ensembles of simulations performed with SISIM and MPS will be denoted as ensembles \mathcal{A} and \mathcal{B} , respectively. The comparison of the two simulation techniques has already been discussed by dell’Arciprete et al. (2012a). In this study, the two methods are used to generate two different ensembles of realizations, which represent possible realizations that can be found in the field, with the objective of analyzing the effects of the different features of the two ensembles on the corresponding flow and transport properties.

Ensemble	Average	Variance
\mathcal{A}	-6.0	8.8
\mathcal{B}	-6.2	11.6

Table 6.13: Ensemble expected values of the spatial average and variance of hydraulic conductivity (in ms^{-1}) for both ensembles (\mathcal{A} : SISIM; \mathcal{B} : MPS); from dell’Arciprete et al. (2012b).

6.2.2 Numerical experiments of non-reactive solute transport on the ensembles of equiprobable realizations of the block

The test volume was further analysed by dell’Arciprete et al. (2012b), where the flow and transport modeling and the connectivity analysis are conducted with the same methods summarized in section 6.1 for the three MBs: flow modeling, particle tracking numerical tracer tests simulating an instantaneous injection, transport modeling with single and dual-domain models. In this case only one flow direction is considered: the solute is injected instantaneously through the NS face of the block, and the flow field is determined by a unit hydraulic gradient along the EW direction. The porosity of the sediments is assumed constant, $n = 0.4$, following the results of laboratory tests on samples that have not shown clear variations among the different facies; a uniform value of porosity was then used so that the numerical transport experiments reveal the effects of differences in hydraulic conductivity only. Six representative examples of the results of the numerical transport experiments ($\mathcal{A}06$, $\mathcal{A}44$, $\mathcal{A}47$, $\mathcal{B}00$, $\mathcal{B}41$ and $\mathcal{B}15$) are shown in Figure 6.10, where each point represents the position of a solute particle during its motion.

These realizations are chosen as representative of extreme situations of facies connectivity among the 50 available simulations. In fact SG facies is less connected than S facies for simulations $\mathcal{A}44$ and $\mathcal{B}41$, whereas the opposite inequality is verified for simulations $\mathcal{A}47$ and $\mathcal{B}15$; the connectivities of all facies are close to the ensemble averages for simulations $\mathcal{A}06$ and $\mathcal{B}00$.

As a general remark, the plumes movement is faster in the volumes of ensemble \mathcal{B} than in the volumes of ensemble \mathcal{A} . Moreover, volumes of ensemble \mathcal{B} show a striking contrast between the upper part, where particles move fast, and the lower part where they travel slowly: in particular, in $\mathcal{B}41$ the upper layer of the block acts as a PFP, whereas in $\mathcal{B}15$ a preferential channel is apparent (see Figure 6.10). As shown by dell’Arciprete et al. (2012b), the connectivity of the G hydrofacies bodies is the dominant feature in the realizations of ensemble \mathcal{B} .

Realizations of ensemble \mathcal{A} appear less structured and the presence of PFPs is not as evident as for ensemble \mathcal{B} , apart from a few cases which show a different behaviour: for instance in simulation $\mathcal{A}47$, which is characterized by highly connected SG hydrofacies bodies, the particles are faster than in simulations $\mathcal{A}06$ and $\mathcal{A}44$.

Differently from case study A, when a single realization was analysed, in this case 50 equiprobable realizations of the same block were performed with each simulation

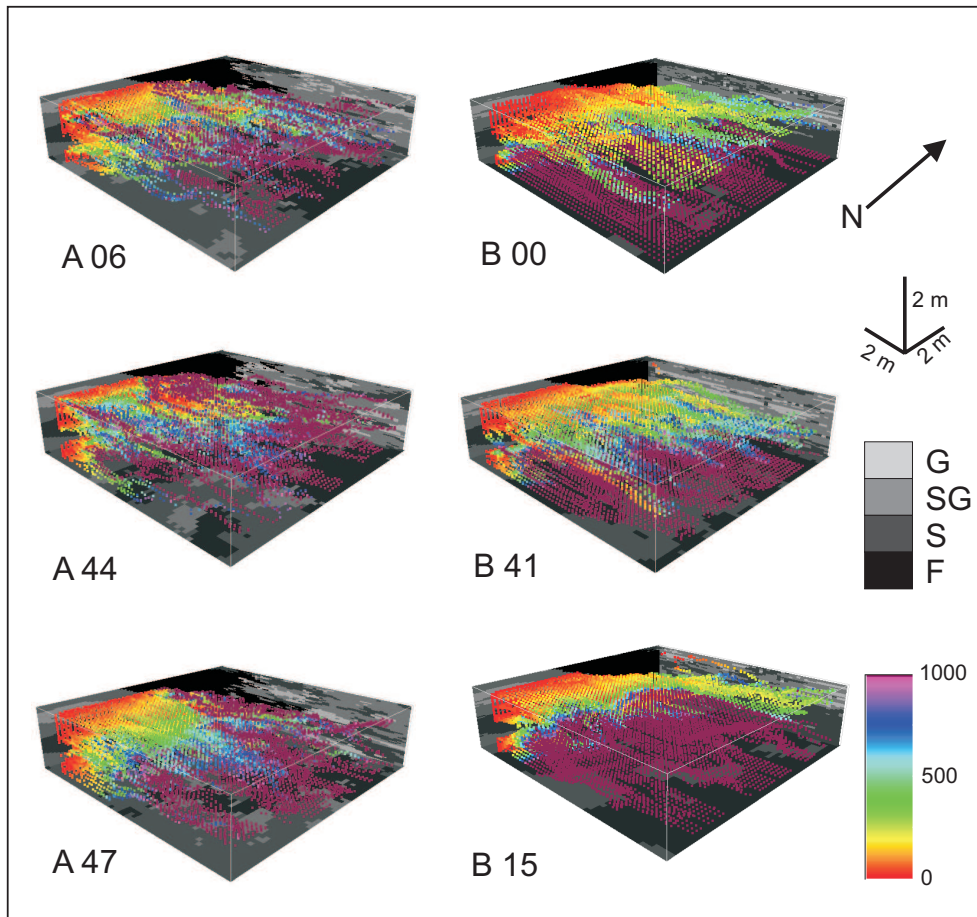


Figure 6.10: Plots of the trajectories of the solute particles for six realizations obtained with SISIM (A) and with MPS (B); the color scale refers to the time, in seconds, elapsed from the injection time; the gray scale shows the simulated hydrofacies. From dell’Arciprete et al. (2012b).

method, so that it is possible to perform a statistical analysis of the results. For example, as will be shown in sections 6.2.5 and 6.2.6, the frequency distributions of the flow and transport parameters, as well as of the connectivity indicators, can be obtained and a principal component analysis can be applied to assess which quantities are statistically the most relevant for the relationship between connectivity indicators and flow and transport properties (dell’Arciprete et al., 2012b).

6.2.3 Connectivity analysis: flow and transport indicators, hydrofacies connectivity indicators, percolating clusters

In dell’Arciprete et al. (2012b) a connectivity analysis has been performed for the 50 realizations of both ensembles. The analysis is based on the computation of some connectivity indicators (four of the nine flow, transport and statistical connectivity indicators suggested in Knudby and Carrera (2005) and two of the three hydrofacies connectivity indicators proposed by Vassena et al. (2010)) and on the statistical analysis of percolating clusters.

The distribution of the connectivity indicators showed that the realizations of ensemble \mathcal{A} are less structured than the realizations of ensemble \mathcal{B} and that PFPs are present in most of the realizations of ensemble \mathcal{B} while they are almost absent in those of ensemble \mathcal{A} . It is interesting to notice that the transport indicator $CT2$, which is the skewness of the time distributions, attains small values for ensemble \mathcal{B} and large values for ensemble \mathcal{A} ; in other words, the skewness is smaller for the blocks of sediments characterized by PFPs, in agreement with what observed in section 6.1.3 for case study A.

The frequency distribution of the intrinsic connectivity confirms that ensemble \mathcal{B} consists of blocks with a more organized structure, and consequently well-defined PFPs, whereas ensemble \mathcal{A} consists of blocks which are less structured. In fact, the intrinsic connectivity of the G facies is significantly higher for ensemble \mathcal{B} than for ensemble \mathcal{A} , showing the presence of well-connected high-permeability bodies which could represent the PFPs in the considered region of the aquifer analogue.

In percolation theory, a percolating cluster is a connected domain which has infinite extension (Stauffer and Aharony, 1994): in this case, a percolating cluster is a connected component that extends from one side to the other of the simulated domain along at least one direction (Lee et al., 2007). In dell’Arciprete et al. (2012b) it is shown that the behaviour of the most permeable facies G has different patterns for the two ensembles. In fact, the realizations of ensemble \mathcal{A} show more variability than those of ensemble \mathcal{B} , as most of them have one percolating cluster, but two percolating clusters are found for six realizations and no percolating cluster is found for six other realizations. On the other hand, all the realizations of ensemble \mathcal{B} have one percolating cluster, but there is one realization for which two percolating clusters are found. Checking the geometrical features of these clusters, it is interesting to notice that they percolate along the x - y plane for ensemble \mathcal{B} , whereas they mostly percolate along the x direction (25 clusters), the x - y plane (14 clusters) and the whole space (nine clusters) for ensemble \mathcal{A} . Furthermore, for the realizations of ensemble \mathcal{B} , more than 77% of the volume occupied by facies G belongs to the percolating cluster, with an average value close to 90%; on the other hand, for the realizations of ensemble \mathcal{A} , the portion of the volume occupied by facies G belonging to the percolating cluster never exceeds 70% and has an average value of about 40%. In other words, the facies G is represented by a large number of small-size connected and non-connected components for ensemble \mathcal{A} , while for ensemble \mathcal{B} most of the facies G belongs to the percolating cluster.

Then the results of the computation of the different connectivity indicators and the

analysis of the percolating clusters are in agreement with the observations drawn from the results of the geostatistical simulation: the ensemble \mathcal{B} shows a more definite connectivity pattern of most-permeable hydrofacies with respect to the ensemble \mathcal{A} , for which the connectivity pattern is less precisely defined and more varying among the 50 realizations.

6.2.4 Experimental data

As described in section 6.2.1, 50 equiprobable realizations of the same block of sediments have been achieved with SISIM (ensemble \mathcal{A}) and 50 with MPS (ensemble \mathcal{B}).

The numerical experiments of non-reactive solute transport have been conducted, for each realization, with the same methods used for case study A, so that the considerations on the experimental data and the objective functions made in sections 6.1.3 and 6.1.4 hold also in this case. In particular, the experimental data are represented by the arrival times of the solute particles at the downstream face of the block, which allow the computation of the “experimental” BTCs and CBTCs.

The experimental BTCs for some realizations are represented by the histograms in Figures 6.13 and 6.14. The BTCs resulting from the transport experiments performed on the realizations of ensemble \mathcal{A} are very similar to each other; consequently, any instance of BTC is representative of the whole ensemble \mathcal{A} . An example is plotted in Figure 6.13 for realization $\mathcal{A}44$, which shows that the experimental BTC has the shape typical of a single homogeneous porous medium.

A greater variability is observed among the results of the transport experiments performed on the realizations of ensemble \mathcal{B} , as shown by Figure 6.14. For example, both $\mathcal{B}15$ and $\mathcal{B}41$ (Figures 6.14b and 6.14c, respectively) are characterized by high peaks for early times, followed by very low and wide peaks for later times: such results are the consequence of the presence of PFPs, which have already been highlighted in these two realizations by Figure 6.10. On the other hand, the realization $\mathcal{B}00$, for which, as discussed in section 6.2.2, the connectivity of all facies are close to the ensemble averages, behaves as a single domain medium (Figure 6.14a).

These results are in agreement with those of the geostatistical simulation and of the connectivity analysis recalled in sections 6.2.1 and 6.2.3, as well as with the qualitative interpretation of Figure 6.10, which showed that the volumes simulated by SISIM are more disorganized, i.e., they lack PFPs, whereas most of the volumes simulated by MPS are characterized by structured heterogeneity and by PFPs.

For each realization, about 4000 solute particles are used for the particle tracking simulations; therefore, for the same reasons of case study A, it is chosen to fit the experimental CBTCs with the transport models, so that the objective function to be minimized is given again by $\chi_{\mathcal{M}}$, defined by (6.5).

Moreover, it has been chosen to fit the experimental CBTCs with the analytical SDM and UDPerM only; the first reason of this choice is that the results of case study A showed that the introduction of the exchange term between the two domains of the DDMS, which is the characteristic feature of the DPorM and CDPerM, does not lead to a significant improvement of the fit with respect to the UDPerM. The second reason is that a statistical analysis on the 100 realizations of the block is more easily obtained with the analytical models, whose calibration is computationally much faster than the calibration of the numerical models.

6.2.5 Calibration of the analytical models

The distributions of the v and D values obtained from the optimization of $\chi_{\mathcal{M}}$ with the SDM (Figure 6.11) show clear differences for the two ensembles. In fact, the distributions of the transport parameters D and v for ensemble \mathcal{A} are quite narrow, which means that the parameters of the SDM are well identified for the realizations of this ensemble. On the contrary, ensemble \mathcal{B} is characterized by much wider distributions of D and v , which means that the single-domain approach is not suitable to describe the transport properties of most volumes of this ensemble.

It is interesting to compare Figure 6.11 with Figure 6.12, which shows the distribution of the values of K_{xx} , that is, of the xx component of the equivalent hydraulic conductivity tensor \mathbf{K}_{eq} , computed for the two ensembles by the 3D groundwater flow model `mgup3D` (Zappa et al., 2006), as explained by dell’Arciprete et al. (2012b).

It is apparent, from Figures 6.11 and 6.12, that the differences between the two ensembles are poorly reflected in \mathbf{K}_{eq} , but they significantly influence the transport properties D and v . In other words, hydrodispersive parameters and travel times are influenced by the geological features shown by the two ensembles and by the corresponding heterogeneity of the K field much more than \mathbf{K}_{eq} .

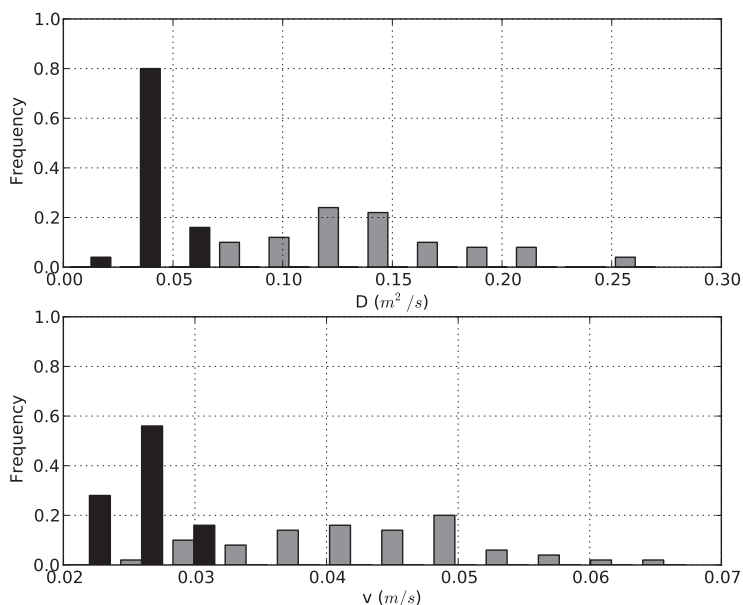


Figure 6.11: Distribution of the values of D (top) and v (bottom) obtained with the optimization for the SDM of the realizations of ensembles \mathcal{A} (black bars) and \mathcal{B} (gray bars).

Figure 6.13 shows the best fit obtained with the analytical SDM and UDPerM for $\mathcal{A44}$; this realization has been chosen as representative of ensemble \mathcal{A} since, as already mentioned in section 6.2.4, the results obtained for all the realizations of this ensemble are very similar. In this figure, the “experimental” BTC (gray histogram) is compared with the BTCs fitted for the SDM (green line) and for the UDPerM (black line), which is the sum of the two BTCs for the high (blue line) and the low (red line) conductivity domains. It can be seen that the two transport models give similar results; in particular, the contribution of the (L) domain to the BTC of the UDPerM is very small, so that the

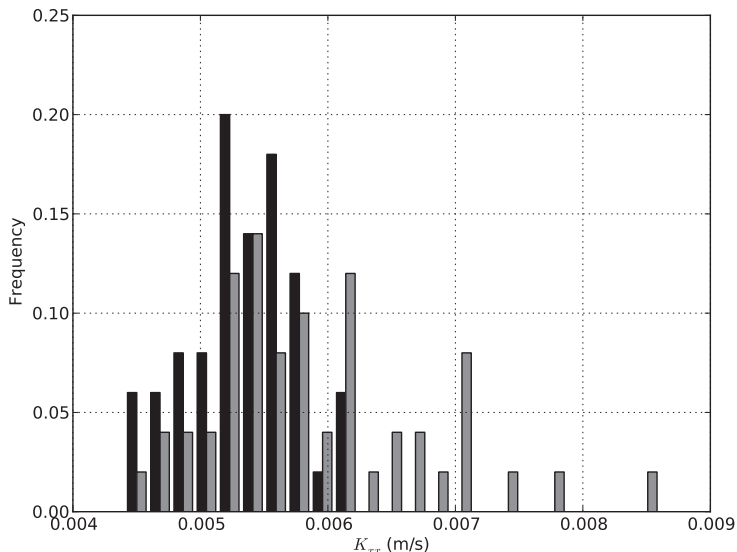


Figure 6.12: Distribution of K_{xx} for the simulations of ensembles \mathcal{A} (black bars) and \mathcal{B} (gray bars).

description of the block given by the UDPerM is equivalent to the description of a SDM.

In Figure 6.14, the BTCs given by the SDM and UDPerM for three realizations of ensemble \mathcal{B} ($\mathcal{B}00$, $\mathcal{B}15$ and $\mathcal{B}41$) are shown with the same plot format as Figure 6.13: the different behaviour of the volumes of ensemble \mathcal{B} is apparent.

The realization $\mathcal{B}00$, for which the connectivities of all facies are close to the ensemble averages, behaves as a single domain medium. In fact, the BTC of the UDPerM is similar to the BTC of the SDM and only slightly improves the fit of the experimental data.

In the case of $\mathcal{B}15$ and $\mathcal{B}41$, instead, the UDPerM significantly improves the fit of the BTCs by taking into account both the faster part of the plume and the slower one; specifically, Figure 6.14 shows that the (H) and (L) components of the BTC of the UDPerM are able to describe the high and narrow peak for early times and the wide and low peak for late times, respectively.

A more thorough assessment of the results obtained with the UDPerM is given by Figures 6.15 and 6.16, which show the frequency distribution of the values of the longitudinal dispersion coefficients and of the velocities in the two domains, obtained for both ensembles. It is apparent that the spread of the values for the ensemble \mathcal{B} (gray bars) is wider than that for \mathcal{A} , for all the quantities. Moreover, it is also apparent that the values of $v^{(H)}$ are higher for \mathcal{B} than for \mathcal{A} and that the differences between the distributions of $v^{(H)}$ and $v^{(L)}$ are more important for \mathcal{B} than for \mathcal{A} . In other words, these frequency distribution plots suggest the great relevance of the UDPerM for ensemble \mathcal{B} .

The latter remark is confirmed by the visualization of the improvements in the results due to the UDPerM for both ensembles which is given in Figure 6.17, where the relative difference between the SDM and UDPerM merit functions $\chi_{\mathcal{M}}$, i.e., parameter Δ defined by (6.7), is shown. For ensemble \mathcal{B} a high percentage of tests corresponds to the greatest values of the misfit between SDM and UDPerM. On the other hand the improvement given by the UDPerM for ensemble \mathcal{A} is less important. This is the consequence of the

fact that the two ensembles represent different geometries, which are well fitted in the case of ensemble \mathcal{A} with a SDM, whereas the UDPerM is optimal to fit the BTCs and gives significant improvements to the results of ensemble \mathcal{B} .

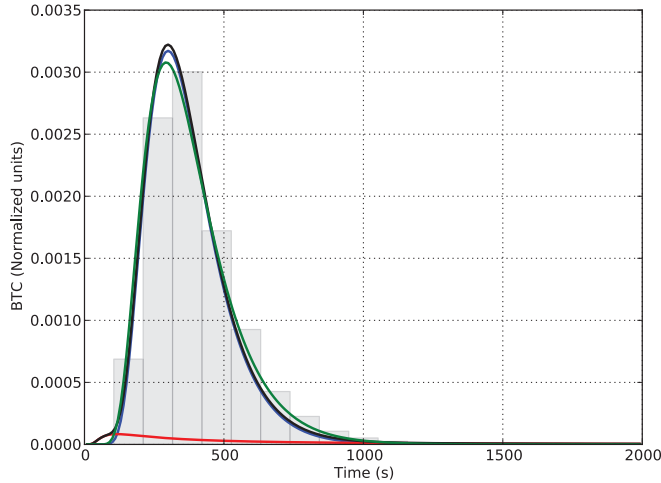


Figure 6.13: BTC for a typical realization of ensemble \mathcal{A} (A44). The correspondent particles paths are shown in Fig. 6.10. The gray bars show the experimental BTC, the green line the BTC fitted for the SDM, the black line the BTC fitted for the UDPerM, which is the sum of the two BTCs for the high (blue line) and the low (red line) conductivity domains.

6.2.6 Principal component analysis of the equivalent flow and transport parameters and of the connectivity indicators

The use of two ensembles of equiprobable realizations of the same block of sediments permits to analyze the correlation between the connectivity indicators and the equivalent flow and transport parameters by means of multivariate statistical analysis and, specifically, with the principal component (PC) analysis, as discussed in detail by dell’Arciprete et al. (2012b).

30 parameters have been considered in the PCA, among them: K_{xx} , v , D , $v^{(H)}$, $v^{(L)}$, $D^{(H)}$, $D^{(L)}$, $\varepsilon^{(H)}M^{(H)}$, the average arrival time of the solute particles \bar{t} , $t_{5\%}$, $t_{50\%}$, the flow and transport connectivity indicators ($CT1$, $CT2$, $CF1$, $CF2$), the total and intrinsic connectivity indicators for the four facies.

For the first PC of ensemble \mathcal{A} , the coefficients with the highest absolute values correspond to v , K_{xx} , $t_{50\%}$ and $v^{(H)}$. The second PC is controlled by $CT1$, $CF2$, D and the connectivity indicators for the G facies. The connectivity indicators of the S facies are among the parameters with the highest contribution to the third order PC, together with \bar{t} . Therefore, it appears that the main PC represents the flow characteristics of the medium, whereas the transport properties, which appear in the second PC, are mainly related to the “fast” portion of the medium. The effects of the sparse low-permeability facies appear only on PCs with orders greater than three.

For the first PC of ensemble \mathcal{B} , K_{xx} has the coefficient with the highest absolute value, followed by the total connectivity of the G facies, $t_{50\%}$ and \bar{t} . The second and third

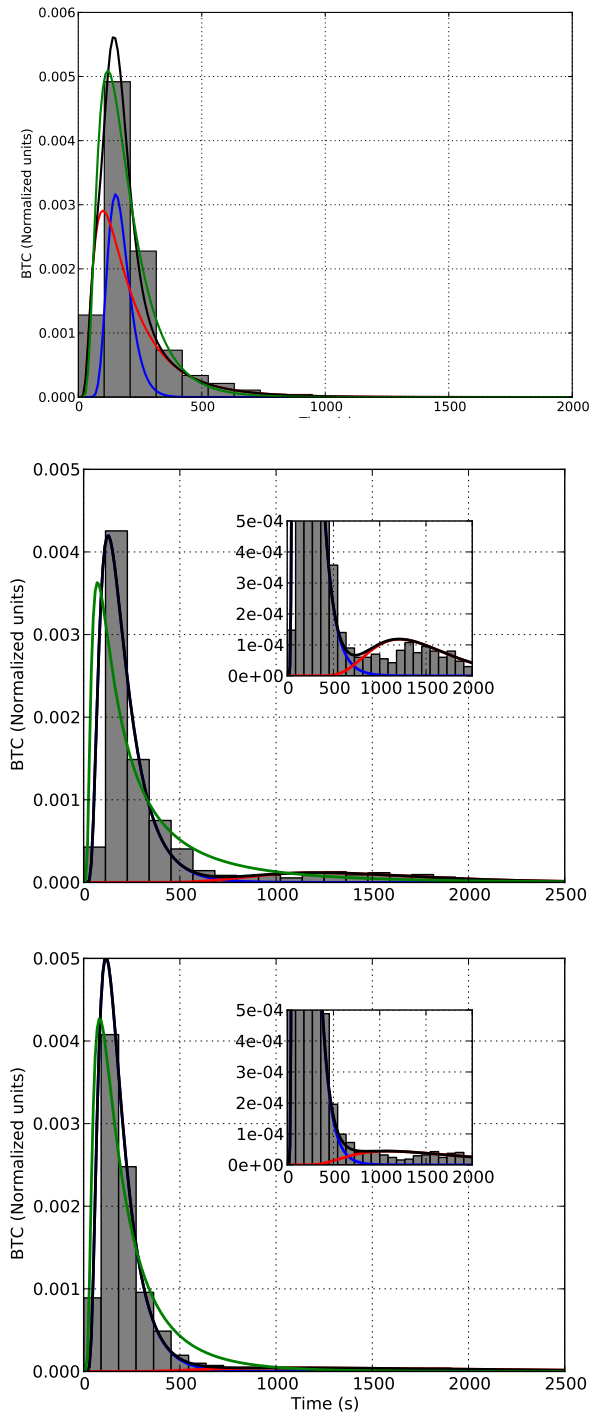


Figure 6.14: BTC for the realizations B_{00} (top), B_{15} (middle) and B_{41} (bottom). The particles path are shown in Fig. 6.10. The gray bars show the experimental BTC, the green line the BTC fitted for the SDM, the black line the BTC fitted for the UDPerM, which is the sum of the two BTCs for the high (blue line) and the low (red line) conductivity domains.

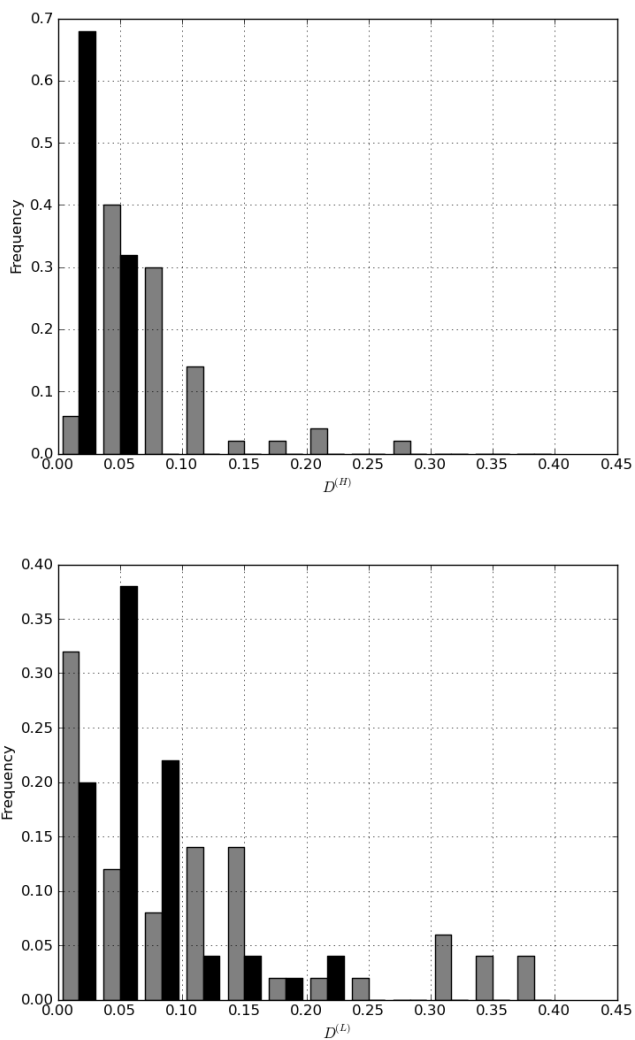


Figure 6.15: Distribution of the values of $D^{(H)}$ (top) and $D^{(L)}$ (bottom) obtained with the optimization for the UDPerM of the realizations of ensembles \mathcal{A} (black bars) and \mathcal{B} (gray bars).

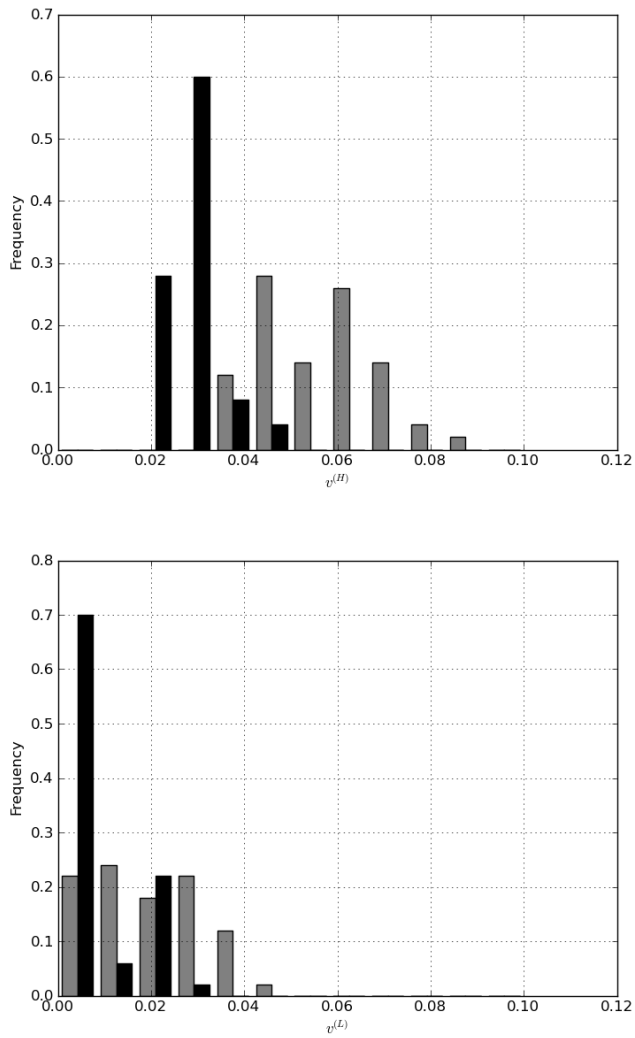


Figure 6.16: Distribution of the values of $v^{(H)}$ (top) and $v^{(L)}$ (bottom) obtained with the optimization for the UDPerM of the realizations of ensembles \mathcal{A} (black bars) and \mathcal{B} (gray bars).

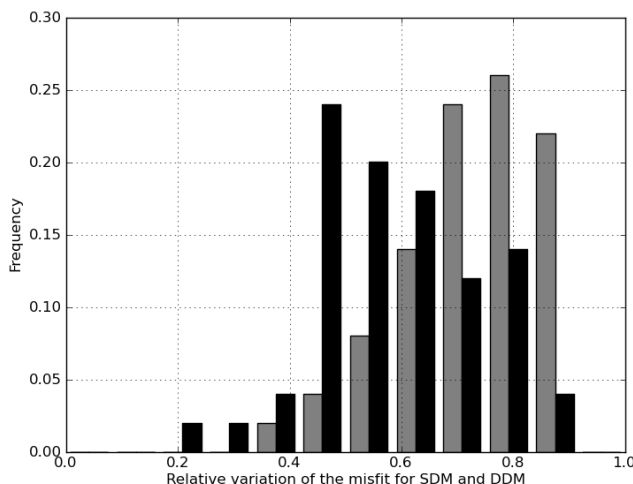


Figure 6.17: Frequency distribution of the relative variation between the SDM and UDPerM merit functions of the realizations of ensembles \mathcal{A} (black bars) and \mathcal{B} (grey bars).

PCs for this ensemble are controlled, respectively, by $CF2$, by the total and intrinsic connectivity of the SG facies and by $D^{(H)}$, D , $t_{5\%}$, v . These results are quite consistent with those obtained for ensemble \mathcal{A} , in the sense that flow parameters play a significant role, whereas the transport parameters are related with the connectivity indicators of the most permeable facies and only to a minor extent to the connectivity indicator of sparse less permeable facies.

6.2.7 Concluding remarks on case study B

The application of the SDM and UDPerM to interpret the numerical transport experiments performed on the two ensembles of simulations has shown that the different heterogeneity patterns of the different realizations significantly influence the transport properties, whereas the flow properties are less affected.

The SDM fits quite well the data of the tests on most of the realizations of ensemble \mathcal{A} , which are obtained with SISIM, whereas, for most of the realizations of ensemble \mathcal{B} , which are obtained with MPS, the UDPerM can fit the data significantly better than the SDM.

This conclusion has been drawn from the comparison between the frequency distributions of the best-fit parameters of the SDM and UDPerM for the two ensembles and, for some tests, between the experimental and the model BTCs, as well as from the analysis of the relative reduction of the objective function obtained with the UDPerM with respect to that obtained with the SDM.

It is interesting to note that the improvement of the fit with the UDPerM is accompanied by a widening of the distribution of the optimal values for ensemble \mathcal{B} , as shown by Figures 6.15 and 6.16. In other words, the improvement given by the UDPerM is achieved at the expense of the variability of the calibrated physical parameters ($v^{(H)}$, $v^{(L)}$, $D^{(H)}$, $D^{(L)}$).

As recalled in section 6.2.3, the connectivity analysis on the two ensembles has shown

that most of the realizations of MPS are characterized by structured heterogeneity and presence of PFPs, whereas most of the realizations of SISIM are less structured, with the different hydrofacies randomly distributed in the domain.

Therefore, the analysis conducted for case study B confirms the role that the sediments connectivity plays to determine the solutes fate in groundwater. Specifically, the relevance of the UDPerM with respect to the SDM is in agreement with the connectivity analysis: the UDPerM efficiently describes the transport properties of those porous media characterized by a large connectivity of the most permeable facies, that is, characterized by PFPs.

In other words, a qualitative correlation between transport properties and connectivity indicators has been observed. A quantitative analysis of the relationship between facies connectivities and flow and transport parameters has been attempted through the PCA of thirty variables for the two ensembles.

For both ensembles, the connectivities of the most permeable facies G show a good importance, as they appear among the most relevant quantities on the low-order PCs, whereas less permeable facies have a more significant contribution to the high-order PCs. With regard to the transport parameters of the SDM and UDPerM used to interpret the numerical tracer tests, $v^{(L)}$ and $D^{(L)}$ are not significantly correlated with the other parameters considered in the PCA. This can be stated as follows: the use of the UDPerM may effectively improve the fit of the BTCs, but the physical parameters for the slow, low K domain are of minor importance for the description of the transport features.

Application of the transport models: interpretation of laboratory and field tracer tests

In this chapter the different single and dual-domain transport models are applied to interpret two real tracer tests, conducted either in laboratory, on a 20-centimeter-long sand column (case study C, section 7.1), or in the field, at the Cape Cod site (case study D, section 7.2). The latter is a 3D tracer test at hectometer scale, for which the features of the solute plume suggest that the 1D transport modeling may be meaningful.

7.1 Case study C. Real tracer test on a decimeter scale sand column

7.1.1 Experimental set up and data

The third case study considered in this work consists of a laboratory test conducted by Ivan Toloni (Toloni, 2011) at LHyGeS (Laboratoire d'Hydrologie et de G ochimie de Strasbourg, Universit  de Strasbourg) on a plexiglass column (see Figure 7.1) of length $L = 28$ cm and diameter $2r = 2.6$ cm, filled with sand coming from the quarry of Kaltenhouse (67 - Bas-Rhin). The sand is composed of quartz (silicate, 96.69%), orthoclase (feldspar, 2.89%) and variscite (phosphate, 0.42%), with an average grain diameter of about 500 μm . A constant porosity, $n = 0.35$, is assumed. A solution of E124, an anionic alimentary red dye which does not react with bases like the sand, has been injected through the top surface of the column with a flow rate $Q = 1$ mL/min for a duration $T = 10$ min. The concentration of the injected solution is $C_0 = 0.1$ g/L.

A fraction collector was used to sample the solution dropping out from the bottom of the column as a function of time, and a spectrophotometer was employed to measure the tracer concentration of the samples. Therefore, the experimental data are represented by the measurements of the flux-averaged concentration $C_F(t_k)$ at the bottom of the column at the times t_k , $k = 1, \dots, N_{\text{data}}$. The experiment lasted for about 160 min; the tracer started to arrive to the bottom of the column around 55 min after injection, and the collection of water samples occurred at intervals ranging from 3 min (initially) to 9 min (at the end of the experiment), resulting in $N_{\text{data}} = 30$ non-zero concentration measurements.

The resulting BTC (see Figure 7.2) is characterized by a significant tailing, which is unexpected, as the sand column is homogeneous. Toloni (2011) suggests that this behaviour may be due to a possible adsorption of the red dye on the grains of sand, which may occur for low flow rates, or to experimental problems, like a possible dispersion effect introduced from the diffuser in the injection operation. This experiment has been interpreted with both SDM and DDMs, as discussed in Baratelli et al. (2012) and in section 7.1.2.

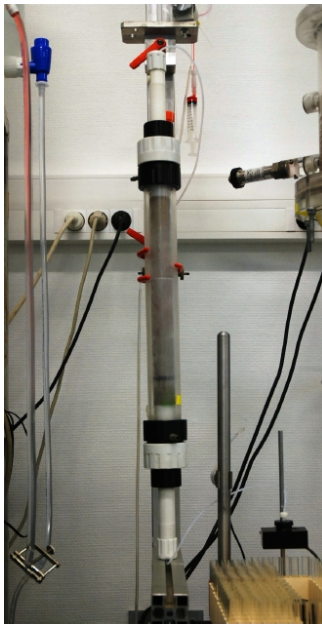


Figure 7.1: Experimental set up for case study C (photograph taken by Ivan Toloni at LHyGeS).

7.1.2 Results of the calibration of the SDM and DDMs

In this case study it is possible to directly fit the experimental measurements without having to compute the CBTCs, differently from case studies A and B; therefore, the following objective function, based on the misfit between the experimental and the model C_F , has been optimized to calibrate the transport models:

$$\chi_{C_F}^2(\mathbf{a}) = \frac{1}{C_0^2 N_{\text{data}}} \sum_{i=1}^{N_{\text{data}}} [C_F^{\text{exp}}(t_i) - C_F(t_i; \mathbf{a})]^2. \quad (7.1)$$

All the numerical transport models (SDM, DPorM, UDPerM, CDPerM) have been applied to interpret this experiment. Tables 7.1 to 7.4 report the best-fit parameters, together with the corresponding value of the objective function χ_{C_F} , obtained with the different transport models. Figure 7.2 shows the experimental measurements of the flux-averaged concentrations C_F at the bottom of the column as a function of time and the best-fit obtained with the different transport models. Finally, Table 6.5 reports the values of Δ , Table 6.11 the characteristic times and the dimensionless numbers Pe and $\mathcal{A}E$ and Table 6.12 the condition numbers κ_2 of the Hessian matrix computed for the optimal parameters.

As a general observation, the DDMs significantly improve the fit of the experimental data obtained with the SDM, with a relative reduction Δ of the objective function that ranges from 52% to 58% (Table 7.5). Figure 7.2 shows that this improvement is mainly related to the better description of the peak and of the tail of the BTC. On the other hand, there are only minor differences between the descriptions of the three different DDMs that have been considered here, i.e., DPorM, UDPerM, CDPerM.

In particular, if we compare the parameters identified by the DPorM (Table 7.2) and

by the CDPerM (Table 7.4), we can notice that $D \approx D^{(H)}$, $v \approx v^{(H)}$, $n^{\text{mob}} \approx \varepsilon^{(H)} n^{(H)}$ and the exchange coefficients are very similar for the DPorM and the CDPerM. Moreover, Table 7.4 shows that $\varepsilon^{(H)} M^{(H)} / M \approx 100\%$. In other words, the DPorM and the CDPerM describe two physical situations which are very similar: in fact, all the injected mass of solute initially enters the mobile or the fast domain. In the case of the DPorM the mobile domain exchanges solute with an immobile domain, while in the case of the CDPerM the fast domain, which has the same transport properties (v and D) as the mobile domain of the DPorM, exchanges solute with another mobile domain; this difference allows the objective function of the CDPerM to slightly decrease with respect to the DPorM, with a corresponding 2% reduction of Δ . Instead, in the case of the UDPerM, the fast domain has approximately the same velocity and dispersion as for the CDPerM, but the mass of solute that enters the fast domain of the UDPerM is about 65% of the total injected mass, and the remaining mass enters the slow domain to compensate for the absence of the exchange between the two domains. As a result, the UDPerM performs slightly worse than the DPorM and the CDPerM, which means that the exchange term between the two domains of the DDMs plays a non negligible role in the interpretation of this tracer experiment. This is confirmed also by the characteristic times reported in Table 7.6, where it is shown that τ_e has approximately the same order of magnitude as t_T , both for the DPorM and for the CDPerM, and by the dimensionless numbers \mathcal{A} , $\mathcal{A}^{(H)}$ and $\mathcal{A}^{(L)}$, which are close to 1.

As already observed for case study A (section 6.1.9), the condition number κ_2 increases with the complexity of the model. The condition number for the DPorMs are several orders of magnitude lower than those computed for the MBs of case study A; consequently, in this case there was no problem in the inversion of the Hessian matrix for the computation of the correlation matrices.

7.1.3 Concluding remarks on case study C

Despite the fact that the column contains homogeneous sand, a significant tailing has been observed in the BTC measured at the bottom of the column. All the DDMs describe quite accurately this behaviour, which is not the case for the SDM, with only minor differences between the predictions of the three types of DDMs.

Since the porous domain is homogeneous, the observed anomalous dispersion cannot be related to the heterogeneity of the hydraulic conductivity field. As mentioned in section 7.1.1, this effect could be due to a possible adsorption of the red dye on the grains of sand or to experimental problems. Another possibility is the presence of a density effect, i.e., of a vertical sinking of the solution containing the tracer, which has a higher density than the “pure” water (without the tracer). Such effects are very evident, e.g., in the case of salt-water intrusion in native groundwater, where the relative density difference can be as large as 0.035 (Istok and Humphrey, 1995). Nevertheless, relevant plume sinking can be observed also for much smaller density contrasts. In particular, Istok and Humphrey (1995) showed that buoyancy-induced vertical flow of a bromide tracer plume can occur for injected concentrations as small as 50 mg/L. This result was obtained by investigating two-well forced gradient tracer tests in a physical meter-scale aquifer model containing a homogeneous and isotropic sand pack. Istok and Humphrey (1995) also observed that the occurrence of such density-induced sinking results in an increase of the apparent longitudinal and transverse solute dispersion; moreover, the peak concentration decreases and the concentration remains above background levels for longer periods of time, i.e., a tailing is observed in the BTCs. In case study C the concentration of the injected solution is $C_0=100$ mg/L, which is above the limit identi-

fied by Istok and Humphrey (1995). Therefore, the possibility of a density effect must be considered for the interpretation of the tailing observed in the BTC.

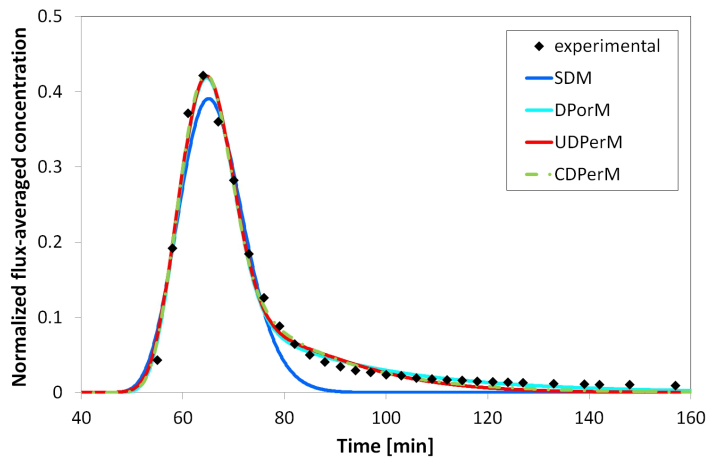


Figure 7.2: Case study C: flux-averaged concentrations C_F , normalized by the concentration of the injected solution C_0 , at the bottom of the column. The black diamonds represent the experimental data, while the curves represent the best fit obtained with the different transport models: SDM (blue line), DPorM (light blue line), UDPerM (red line), CDPeRM (green line).

D	v	χ_{CF}
$[\text{m}^2/\text{s}]$	$[\text{m}/\text{s}]$	$\%$
$6.99 \cdot 10^{-7}$	$1.51 \cdot 10^{-4}$	2.5

Table 7.1: Case study C: results of the calibration of the SDM.

D	v	n_i^{mob}	α	χ_{CF}
$[\text{m}^2/\text{s}]$	$[\text{m}/\text{s}]$		$[\text{s}^{-1}]$	$\%$
$4.43 \cdot 10^{-7}$	$1.57 \cdot 10^{-4}$	$2.70 \cdot 10^{-1}$	$7.05 \cdot 10^{-5}$	1.12

Table 7.2: Case study C: results of the calibration of the DPorM.

$D^{(H)}$	$D^{(L)}$	$v^{(H)}$	$v^{(L)}$	$\varepsilon^{(H)}$	$M^{(H)}$	$\varepsilon^{(H)} M^{(H)} / M$	$\varepsilon^{(H)} n^{(H)}$	χ_{CF}
$[\text{m}^2/\text{s}]$	$[\text{m}^2/\text{s}]$	$[\text{m}/\text{s}]$	$[\text{m}/\text{s}]$	$\%$	$[\text{kg}/\text{m}^2]$	$\%$		$\%$
$4.51 \cdot 10^{-7}$	$1.73 \cdot 10^{-6}$	$1.58 \cdot 10^{-4}$	$9.90 \cdot 10^{-5}$	41.5	$8.18 \cdot 10^{-8}$	64.93	$1.47 \cdot 10^{-1}$	1.22

Table 7.3: Case study C: results of the calibration of the UDPerM.

$D^{(H)}$	$D^{(L)}$	$v^{(H)}$	$v^{(L)}$	$\varepsilon^{(H)}$	$M^{(H)}$	α	$\varepsilon^{(H)} M^{(H)} / M$	$\varepsilon^{(H)} n^{(H)}$	χ_{CF}
$[\text{m}^2/\text{s}]$	$[\text{m}^2/\text{s}]$	$[\text{m}/\text{s}]$	$[\text{m}/\text{s}]$	$\%$	$[\text{kg}/\text{m}^2]$	$[\text{1}/\text{s}]$	$\%$		$\%$
$3.87 \cdot 10^{-7}$	$2.08 \cdot 10^{-6}$	$1.59 \cdot 10^{-4}$	$5.57 \cdot 10^{-5}$	64.3	$8.13 \cdot 10^{-8}$	$8.28 \cdot 10^{-5}$	100.0	$2.28 \cdot 10^{-1}$	1.07

Table 7.4: Case study C: results of the calibration of the CDPerM.

DPorM	56%
UDPerM	52%
CDPerM	58%

Table 7.5: Case study C: values of Δ , the relative difference of the objective function of the DDMs with respect to the objective function of the SDM.

DPorM	τ_e/t_T	5.5
	\mathcal{A}	2.2
	Pe	99
CDPerM	τ_e/t_T	3.7
	$\mathcal{A}^{(H)}$	1.6
	$\mathcal{A}^{(L)}$	0.30
	$Pe^{(H)}$	110
	$Pe^{(L)}$	7.5

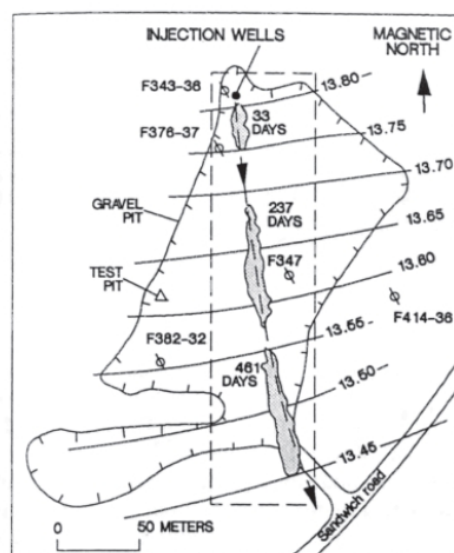
Table 7.6: Case study C: ratio of the characteristic exchange time (τ_e) to the characteristic time of advective transport (t_T) and dimensionless numbers Pe and \mathcal{A} for the DPorM and the CDPerM.

SDM	$4.5 \cdot 10^2$
DPorM	$7.7 \cdot 10^{10}$
UDPerM	$6.2 \cdot 10^{13}$
CDperM	$5.5 \cdot 10^{14}$

Table 7.7: Case study C: condition numbers of the Hessian matrix of the objective function χ_{CF} .

7.2 Case study D. Large-scale natural gradient tracer test at hectometer scale performed in a sand and gravel aquifer at the Cape Cod site

The study site is located at Cape Cod, Massachusetts, where a large-scale tracer test was conducted in an unconfined stratified sand and gravel aquifer (see Figure 7.3). The hydrogeologic and hydrological characteristics of the field site and the details of the realization of the tracer test are described by LeBlanc et al. (1991), where the main features of the movement of the tracer cloud are also discussed. For the sake of clarity, only the main concepts are reported in the following sections 7.2.1 to 7.2.3. The experimental data are presented in section 7.2.4; in particular, proper averages of the experimental concentrations are computed at some fixed distances from the injection wells, so that it is possible to apply the 1D transport models developed in the previous chapters. The results of the calibration of the transport models, obtained through the optimization of the objective functions defined in section 7.2.5, are presented and discussed in section 7.2.6. Finally, some concluding remarks are given in section 7.2.7.



EXPLANATION






-  AREA OF TRACER CLOUD IN WHICH BROMIDE CONCENTRATIONS EXCEEDED 1 MILLIGRAM PER LITER
-  AREA OF MULTILEVEL SAMPLER ARRAY — Shows area in figure 10.
-  —13.45— WATER-TABLE CONTOUR, AUGUST 2, 1985 — Shows altitude of water table. Contour interval 0.05 meters. Datum is sea level.
-  —▶— PREDICTED PATH OF TRACER CLOUD
-  OBSERVATION WELLS

Figure 7.3: Tracer test at Cape Cod (LeBlanc et al., 1991). In the shaded areas the bromide concentrations exceeded 1 milligram per liter; the solid lines are the contours of the height of the water table; the arrows indicate the predicted path of the tracer cloud.

7.2.1 Hydrologic characteristics of the site

The observations of the water table height during the period of the tracer test showed that the aquifer was characterized by a nearly horizontal groundwater flow, with horizontal hydraulic gradients varying with time from 0.0014 to 0.0020, and very small vertical gradients, which were less than 0.00012, corresponding to a head difference of 0.3 cm over a distance of 25 m. The estimate of the average groundwater velocity is 0.4 m/d, which is obtained by applying the Darcy's law with the estimates of the hydraulic gradient, of the hydraulic conductivity ($K=110$ m/d) and of the effective porosity ($n_e = 0.39$) coming from field measurements at the site.

7.2.2 The tracer test

Three tracers were used in this test: a non-reactive tracer, bromide, and two reactive tracers, lithium and molybdate. On July 1985, a 7.6 m³ volume of a solution with the three tracers was injected into three wells for a 17 hour period, with a total rate of water injection of 7.6 L/min. The spatio-temporal evolution of the tracer clouds was then monitored for three years - until June 1988 - through an array of 656 multilevel samplers (MLSs) covering a width from 12 to 22 m, a length of 282 m and spanning a vertical distance from 3.6 m to 10.7 m long. The MLSs were installed at successive stages during the test: in particular, given the position of the tracer cloud and the simultaneous direction of groundwater flow, the evolution of the cloud could be estimated and the location of the next set of MLSs chosen in order to intercept the solute movement. The first sampling was performed 13 days after injection, and then 18 successive campaigns of sampling followed during the three years of the test. For each campaign, water samples were collected from the subset of MLSs that, according to the previous round data, were expected to cover the area occupied by the tracer cloud. The solute concentration of each water sample was then measured with different methods as, in the case of bromide, ion-selective electrode, ion chromatography and an autofluorescence technique. The bromide cloud was monitored only until December 1986, when the bromide itself left the monitored region; instead, the lithium and molybdate clouds could still be observed after three years from the injection, since these reactive tracers are adsorbed on the grains of the sediments, and, therefore, their movement in the aquifer is slower than that of the bromide.

7.2.3 Main features of the tracer cloud

The bromide moved basically along the direction of groundwater flow and was characterized by a significant longitudinal spreading, whereas the spreading along the direction transverse to water flow and, especially, along the vertical direction was much smaller. For example, 461 days after injection, the bromide cloud had spread more than 80 m longitudinally, but was only 14 m wide and 4-6 m thick (see also Figure 7.4b). Moreover, the bromide cloud moved downward about 4 m because of a combination of the effects of precipitation and of a density-induced sinking, which is more important in the early stages of the test when the higher concentrations of solutes determine a higher density contrast between the injected solution and the native groundwater. This downward movement can be seen, e.g., in Figure 7.5. The bromide concentration of the injected solution is $C_0 = 640$ mg/L, which is well above the lower limit established by Istok and Humphrey (1995) for the presence of density-induced sinking of the plume (see also section 7.1.3); therefore, density-induced sinking is likely to be one of the processes that determine anomalous dispersion at the Cape Cod site. The estimate of the average

velocity of the bromide cloud during the test was 0.42 m/d, which coincides with the estimate of the average groundwater velocity obtained with Darcy's law. Moreover, the pattern of the bromide concentration in the plume was complex and characterized by asymmetry; such a result is a consequence of the aquifer heterogeneity. For example, the presence of very permeable layers near the water table, which could act as channels for preferential water flow and tracer transport, was observed at the site.

Despite these complexities, LeBlanc et al. (1991) concluded that the movement of the tracer cloud can be predicted with sufficient accuracy from the measurements of the time evolution of the water table elevation and of the corresponding gradient and observed that the movement of the cloud follows the temporal changes of the direction of the hydraulic gradient. Therefore, they stressed the importance of the accurate definition of the water table in the study of contaminant transport in similar unconfined aquifers.

7.2.4 Experimental data

The bromide concentrations have been measured during 16 campaigns at about monthly intervals, from 13 days to 511 days after injection; the campaign times are denoted with t_ℓ , $\ell = 1, \dots, 16$, and their values are listed in Figure 7.4a. As described in section 7.2.2, water samples were collected during each campaign from a subset of the MLSs intercepting the bromide cloud; therefore, for each campaign, that is, at a certain time t_ℓ after injection, the experimental data are given by a set of bromide resident concentrations $C(x, y, z)$ at the position (x, y) of the MLSs and at the depth z of their sampling ports.

The location of the MLSs and of the three injection wells is represented in Figure 7.4a. Moreover, in order to show the horizontal movement of the bromide cloud, Figure 7.4b plots in the horizontal plane xy the maximum bromide concentration along z , at 33, 237 and 461 days after injection.

As already observed in section 7.2.3, the bromide cloud spreads mainly along the average direction of groundwater flow (compare with Figure 7.3), while the spreading along the transverse and vertical directions is much smaller. Therefore, it may be meaningful to interpret these 3D concentration data with the 1D transport models developed in this work.

To this aim, five vertical cross-sections of the 3D domain have been fixed by choosing five subsets of MLSs aligned approximately perpendicularly to the direction of the average groundwater flow, as shown in Figure 7.4a. The average concentration over each section has then been computed for each time, as explained in detail in the following.

Since in each campaign solute concentrations have been monitored only at a subset of the MLSs, it is then necessary to introduce the following definition.

For any section n , $\mathcal{L}_n \subset \{1, \dots, 16\}$ includes the codes of the measurement campaigns during which data have been collected for that section. In other words, concentration data are collected at time t_ℓ for section n , if $\ell \in \mathcal{L}_n$. The cardinality of \mathcal{L}_n is denoted with $N_{\text{data},n}$.

The sampled area A_n^ℓ of section n at time t_ℓ , $\ell \in \mathcal{L}_n$, is defined as the area that covers all the sampling points of the MLSs considered at section n and time t_ℓ , that is:

$$A_n^\ell = \sqrt{(x_{2,n}^\ell - x_{1,n}^\ell)^2 + (y_{2,n}^\ell - y_{1,n}^\ell)^2} \cdot \Delta z_{\text{max},n}^\ell,$$

where $(x_{1,n}^\ell, y_{1,n}^\ell)$ and $(x_{2,n}^\ell, y_{2,n}^\ell)$ are the coordinates of the two extreme MLSs, i.e., the most eastern and western MLSs, and $\Delta z_{\text{max},n}^\ell$ is the maximum vertical distance spanned by the sampling ports of the MLSs, at section n and time t_ℓ .

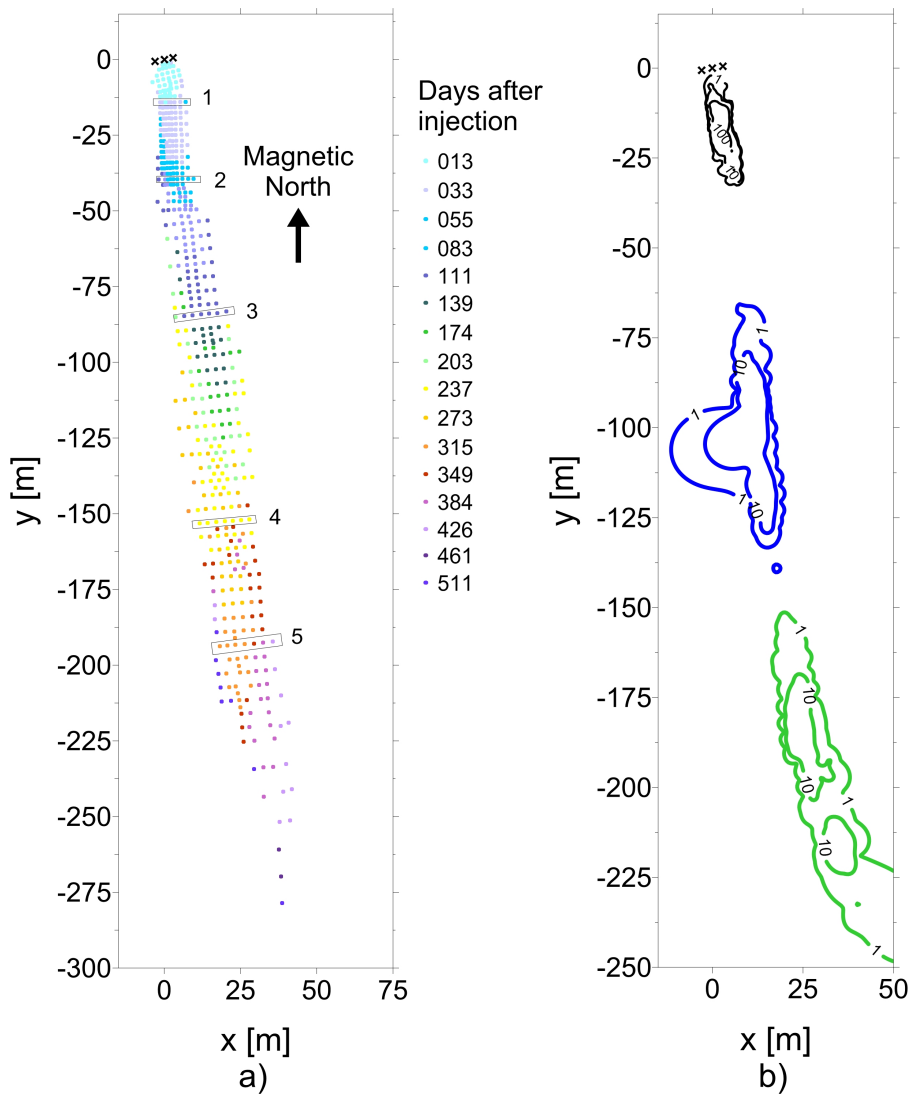


Figure 7.4: a) location of injection wells (crosses) and MLSs (dots); the five sections for which the average concentrations have been computed for the 1D transport modeling are also shown. b) contours of the maximum bromide concentration (in milligrams per liters) at 33 days (black line), 237 days (blue line) and 461 days (green line) after injection. Origin of magnetic north-oriented coordinate system is the central injection well. Redrawn from LeBlanc et al. (1991).

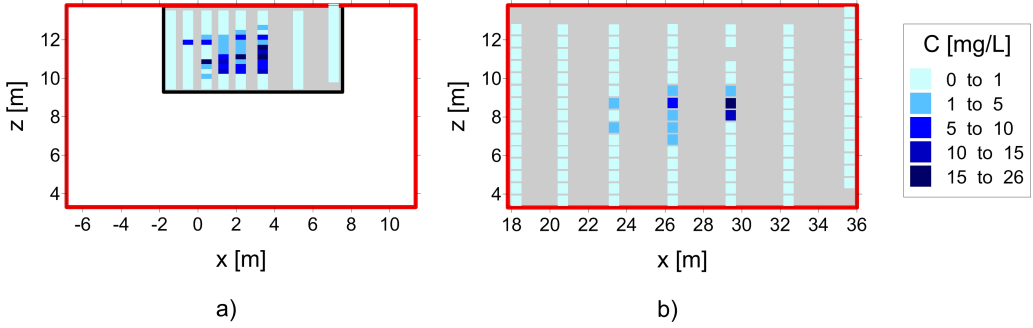


Figure 7.5: Measured concentrations at section $n=1$ and time $t_3 = 55$ d (plot a) and at section $n = 5$ and time $t_{16} = 511$ d (plot b). The sampled surfaces, over which the average concentrations \bar{C}_n^ℓ are computed, are highlighted with a gray background. The red border marks off the surfaces over which the equivalent 1D concentrations C_n^ℓ are computed.

Moreover, let A_{\max} be the maximum of the sampled areas A_n^ℓ , for $\ell \in \mathcal{L}_n$ and $n = 1, \dots, 5$.

Let \bar{C}_n^ℓ be the concentration averaged over all the sampling points belonging to section n at time t_ℓ , $\ell \in \mathcal{L}_n$.

As described above, at each section and time, water samples are collected for concentration measurement only from the subset of MLSs that is estimated to intercept the tracer cloud, assuming that the concentration is zero in the other MLSs; consequently, the average concentrations \bar{C}_n^ℓ for the different sections and times are computed over different areas. In particular, because of dispersion, geometrical spreading and, possibly, of the density effect (see section 7.1.3), as the distance from the injection wells increases, the tracer cloud widens and then the area sampled by the MLSs increases.

As an example, in Figure 7.5 the concentrations measured at the first section $n=1$ and time $t_3=55$ d (plot a) are compared with those measured at the last section $n=5$ and time $t_{16}=511$ d (plot b). In this figure, the sampled areas, over which the average concentrations \bar{C}_n^ℓ are computed, are highlighted with a gray background. It was obtained $A_1^3=30.2$ m², $\bar{C}_1^3 = 2.13$ mg/L, $A_5^{16} = A_{\max} = 155.0$ m² and $\bar{C}_5^{16} = 0.60$ mg/L.

Since this tracer test is interpreted with 1D transport models, the concentrations must be averaged over surfaces of the same area, which in our case is chosen as the maximum sampled area A_{\max} . To this aim, the equivalent 1D concentrations at section n and time t_ℓ are defined as:

$$C_n^\ell = \bar{C}_n^\ell \frac{A_n^\ell}{A_{\max}}, \quad n = 1, \dots, 5, \ell \in \mathcal{L}_n. \quad (7.2)$$

This definition derives from the assumption that the concentration is zero outside the sampled surface.

Coming back to the example sketched in Figure 7.5, equation (7.2) yields $C_1^3 = 0.41$ mg/L and $C_5^{16} = \bar{C}_5^{16} = 0.60$ mg/L and the surfaces over which these equivalent 1D concentrations are computed are marked off with a red border.

The experimental data defined by (7.2) are represented, e.g., in Figure 7.6a as diamonds connected by thin lines, where each colour corresponds to a different section. It can be seen that the concentration peaks become smaller and wider as the distance from the injection wells increases, as a consequence of both dispersion in the heteroge-

neous aquifer and of geometrical spreading. A contribution to this reduction of the peak concentration might also be given by the plume sinking (see section 7.1.3).

Some other important observations for the transport modeling can be introduced.

LeBlanc et al. (1991) highlighted that the variations of the water table elevation and of the magnitude and direction of the hydraulic gradient were very small in the first 17 months of the tracer test; consequently, groundwater flow can be considered as steady with a good approximation during the monitoring period of the bromide cloud.

The duration of the injection is $T=17$ hours, which is a very short time with respect to the time scales with which the tracer moved in the aquifer; therefore, in this work, the Cape Cod tracer test has been modelled as an instantaneous injection, that is, boundary conditions (2.48), (2.52) and (2.56) have been applied.

The mass of solute injected per unit surface is given by $M = m_{\text{Br}^-}/A_{\text{max}}$, where $m_{\text{Br}^-}=4.9$ kg is the total bromide mass that was injected. The bromide concentration of the injected solution was 640 mg/L, which is very large compared to the natural bromide concentration at the site, which was estimated around 0.1 mg/L.

7.2.5 Objective functions

In order to fit the experimental data C_n^ℓ with the transport models developed in the previous chapters, the following objective function is defined:

$$\chi_C^2(\mathbf{a}) = \frac{1}{N_{\text{data}}^{\text{tot}}} \sum_{n=1}^5 \sum_{\ell \in \mathcal{L}_n} [C_n^\ell - C(x_n, t_\ell; \mathbf{a})]^2, \quad (7.3)$$

where $N_{\text{data}}^{\text{tot}} = \sum_{n=1}^5 N_{\text{data},n}$ is the total number of experimental data for all sections and times.

The minimization of this objective function gives the same weight to the misfit between experimental and model concentrations for all the five sections of the domain.

Other objective functions χ_n can be defined by taking into account the misfit for the single section n , that is:

$$\chi_n^2(\mathbf{a}) = \frac{1}{N_{\text{data},n}} \sum_{\ell \in \mathcal{L}_n} [C_n^\ell - C(x_n, t_\ell; \mathbf{a})]^2, \quad (7.4)$$

for $n = 1, \dots, 5$.

7.2.6 Results of the calibration

Figures 7.6, 7.7 and 7.8 represent the results of the calibration of the SDM, DPorM and UDPerM, respectively. These figures share the same format: plot a) shows the results of the optimization of the objective function χ_C^2 , defined by (7.3), that is, the concentrations data of all the five sections are fitted simultaneously; plots b) to f) show the results of the optimization of the objective functions χ_n^2 , $n = 1, \dots, 5$, defined by (7.4), i.e., the data of the individual sections are fitted with the transport models. Moreover, the results obtained through the optimization of χ_C^2 are compared in Figure 7.9 for the SDM, DPorM and UDPerM and in Figure 7.10 for the UDPerM and CDPerM. Finally, Figure 7.11 shows the values of χ_C and χ_n computed with the optimal parameters for χ_C^2 .

As shown in Figures 7.10 and 7.11, the results of the two DPerMs are almost coincident; therefore, the following discussion on the results of the UDPerM hold for the CDPerM as well.

Concerning the outcomes of the optimization with respect to the single sections, a common result of the calibration of the SDM, DPorM and UDPerM is that the fit of the data of the first and second section leads to a very bad description of the data corresponding to the further three sections, for which the prediction of the peak time is clearly underestimated (see plots b and c of Figures 7.6, 7.7 and 7.8). On the other hand, the fit of the data of the third, fourth or fifth section describes the data of the remaining sections quite well, even if with some exceptions; for example, in some cases the peak time for the second section is slightly overestimated (see plots 7.6d, 7.7d, e and f, 7.8d and f) and the height of the peaks of the first two sections is underestimated (see plots 7.6e and f and 7.8f) or overestimated as in plot 7.8e.

It should be noticed that the first two sections are characterized by few data ($N_{\text{data},1} = 3$ and $N_{\text{data},2} = 6$), so that the model calibration from these two single sections is not reliable.

It is interesting to observe the results of the calibration of the UDPerM with respect to χ_4^2 (plot 7.8e): the model fits the data of the fourth section very well; nevertheless, due to the low sampling rate, the model concentration has a behaviour that is not realistic on the basis of the experimental data. The two peaks of the model concentration clearly correspond to the fast and slow domains of the UDPerM.

Concerning the results of the optimization with respect to all five sections, the improvement of the fit relative to the SDM, defined by (6.7), is $\Delta = 17\%$ for the DPorM and $\Delta = 14\%$ for the UDPerM and the CDPerM; in other words, all the three DDMs fit the data better than the SDM (see also Figure 7.11), with minor differences between each of them. Nevertheless, plots 7.7a and 7.8a show that the description of the experimental data given by the DPorM and UDPerM is not accurate for all sections.

The best-fit parameters obtained for each model show that the estimate of the velocity v is very similar to the estimate given by LeBlanc et al. (1991), that is, as recalled in section 7.2.1, $v = 0.42$ m/d; in fact $v = 0.49$ m/d for the SDM, $v = 0.45$ m/d for the DPorM, $v = 0.47$ m/d for the UDPerM and $v = 0.46$ m/d for the CDPerM.

Both the inspection of Figure 7.9 and the values of Δ , which are smaller than those obtained in the previous case studies, point out that it is not possible to obtain a good fit of the data of all five sections neither with a SDM nor with the DDMs. This result may be due to the 1D modeling of an actually 3D tracer test, and to the computation of the average concentrations \mathcal{C} with (7.2).

7.2.7 Concluding remarks on case study D

The calibration of the transport models against the concentration data of a single section, i.e., the calibration obtained through the optimization of $\chi_{\bar{n}}$, does not always give reliable results; in fact, the best-fit parameters for section \bar{n} often give a bad fit for the other sections $n \neq \bar{n}$. This is particularly evident for $\bar{n} = 1$ and $\bar{n} = 2$.

One of the possible explanations of this result is the low sampling rate, that characterizes all sections and, especially, $n=1$ and $n=2$.

Moreover, it should be considered that the five sections are located at distances from the injection wells ranging from about 15 m to about 200 m; therefore, the calibration of the transport models against the data of one single section implies the transport modeling of a domain whose size ranges in the same interval. The effective parameters of the

transport models are, in general, scale dependent (see, e.g., Giudici (2010)) so that the best-fit parameters are likely to be different for the different sections.

Since it was observed that, for $\bar{n} \geq 3$, the fit for the other sections $n \neq \bar{n}$ is, in general, satisfactory, then the low sampling rate seems to play a relevant role in the explanation of these results; nevertheless, the scale dependence of the effective parameters also represents an issue that should be taken into account for the interpretation of the results.

The calibration against the concentration data of all five sections, i.e., the calibration obtained through the optimization of χ_C , seems to be a better approach than the former one, considering that the objective is the determination of effective parameters that allow the description of the transport properties for the whole studied region.

The results of this calibration showed that all the three DDMs fit the data slightly better than the SDM, with only minor differences between the DPorM, UDPerM and CDPerM. Specifically, the best fit obtained with the two DPerMs is almost the same, a result that holds for the first type of optimization as well. Nevertheless, it is important to stress that even the DDMs are not able to describe the data of all sections with very good accuracy.

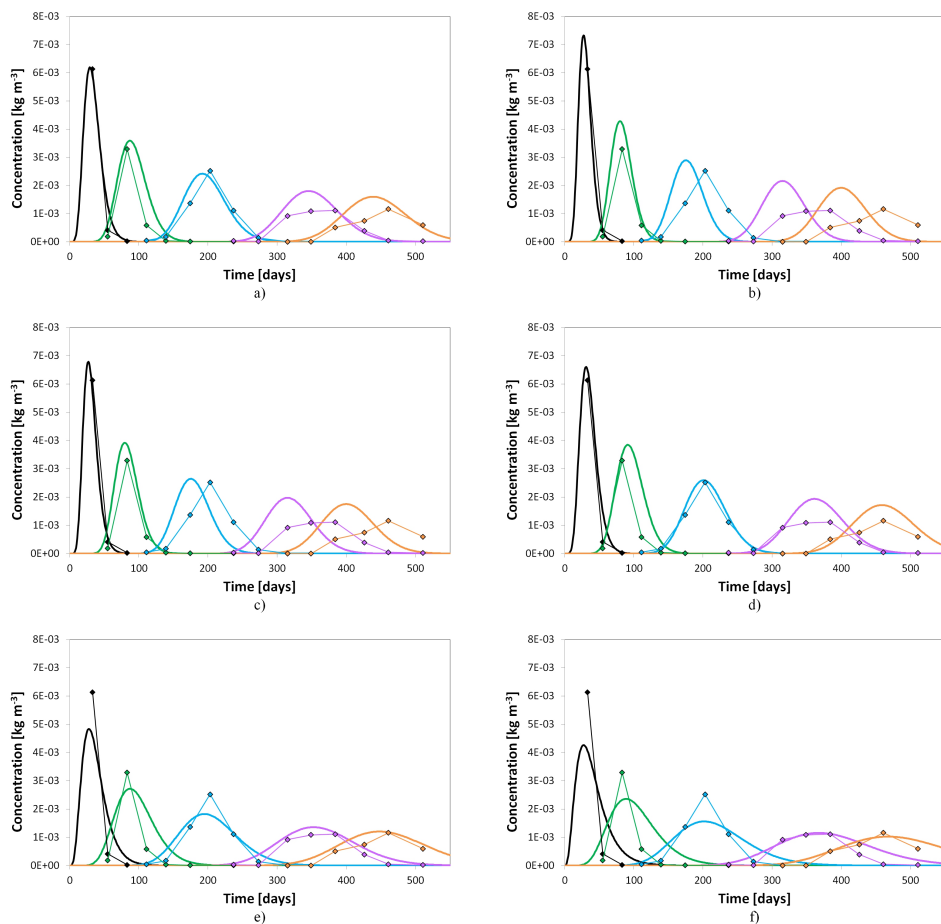


Figure 7.6: Case study D: experimental (diamonds and thin lines) and model (thick lines) concentrations given by the calibration of the SDM with χ_C (a) and χ_n , $n = 1, \dots, 5$ (b to f). Different colours are used to represent the data for the different sections: black for section 1, green for section 2, blue for section 3, purple for section 4, orange for section 5.

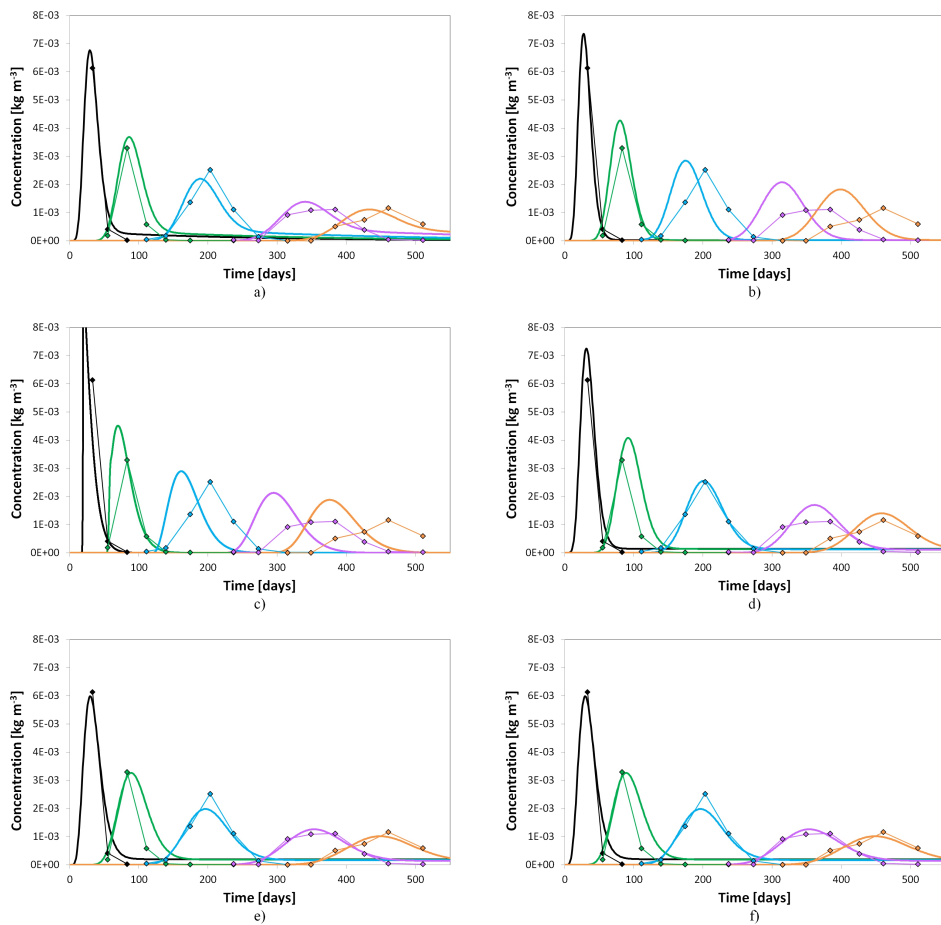


Figure 7.7: Case study D: experimental (diamonds and thin lines) and model (thick lines) concentrations given by the calibration of the DPorM with χ_c (a) and χ_n , $n = 1, \dots, 5$ (b to f). Different colours are used to represent the data for the different sections (see Figure 7.6).

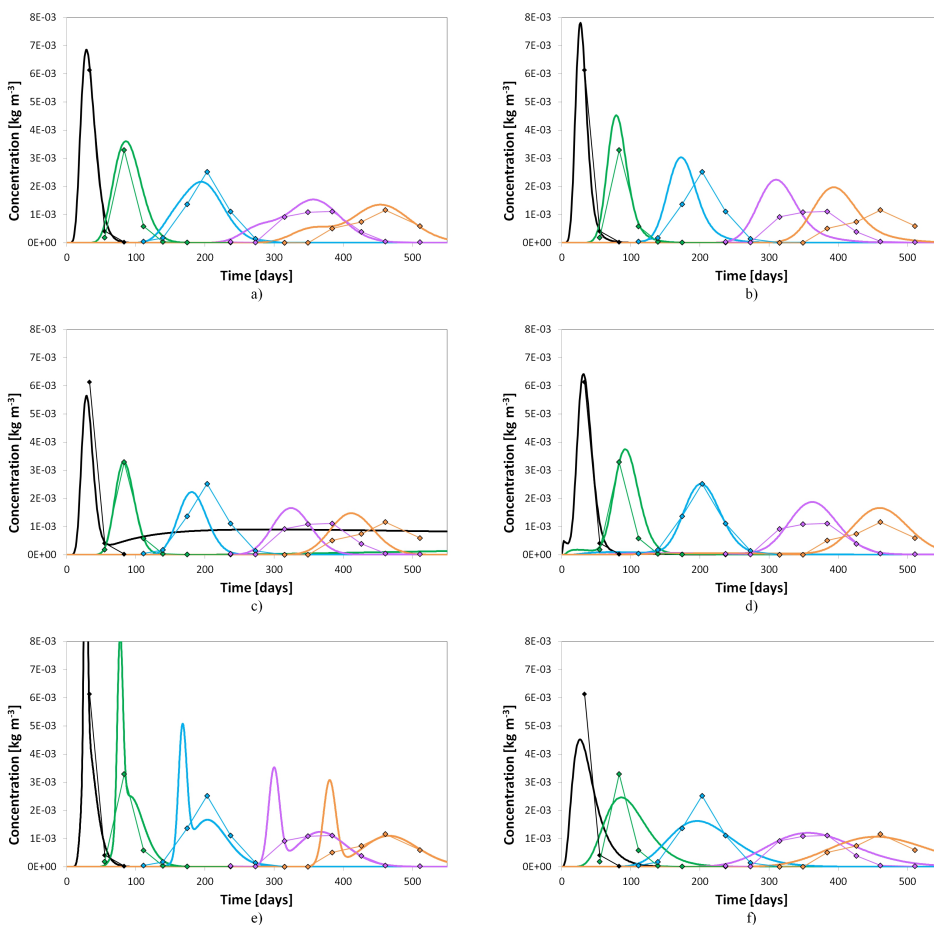


Figure 7.8: Case study D: experimental (diamonds and thin lines) and model (thick lines) concentrations given by the calibration of the UDPerM with χ_C (a) and χ_n , $n = 1, \dots, 5$ (b to f). Different colours are used to represent the data for the different sections (see Figure 7.6).

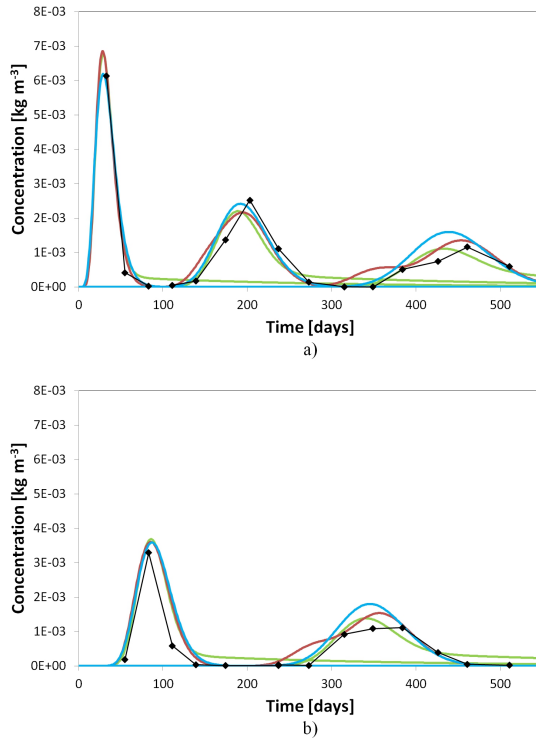


Figure 7.9: Case study D: experimental (black diamonds and thin lines) and model (thick lines) concentrations given by the calibration of the SDM (blue line), DPorM (green line) and UDPerM (red line) with respect to χ_C : a) sections 1, 3 and 5; b) sections 2 and 4.

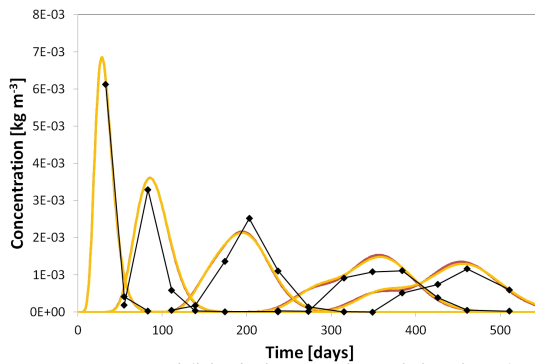


Figure 7.10: Case study D: experimental (black diamonds and thin lines) and model concentrations given by the calibration of the UDPerM (red line) and CDPorM (yellow line) with respect to χ_C . The results for the two models are almost identical.

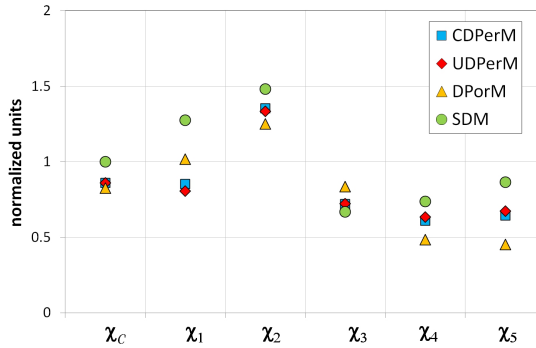


Figure 7.11: Objective functions χ_C and χ_n , $n = 1, \dots, 5$, obtained with the minimization of χ_C^2 for each model. The values are normalized with the optimal χ_C for the SDM.

7.3 Comments on the advantages of using either the solute concentration or the temporal moments of the BTC for the inversion of the transport models

As discussed in sections 6.1.4 and 6.2.4, in case studies A and B, it was chosen to use the CBTC data for the inversion of the transport models; this choice was justified by the fact that those cases consist of numerical particle tracking experiments, which do not allow a precise estimate of the concentrations or of the BTC, unless a much greater number of particles is used in the simulations. In some tests of case study A, the inversion has been also performed using the temporal moments of the BTC of order $r \leq 2$, and it was observed that, for the SDM, the results were very similar to those obtained using the CBTC, whereas for the UDPerM the inverse problem is underdetermined.

On the other hand, in case studies C and D, it was chosen to use the flux or resident concentrations for the inversion, as these are the real hard data obtained from the laboratory and field experiments.

The computation of the time integrals, that are present in the definitions of the CBTC (2.41) and of the temporal moments of the BTC (2.42), permits to dampen the errors which affect the experimental measurements of the concentration; this fact would clearly support the use of the CBTC or the temporal moments of the BTC for the inversion. Moreover, the first two temporal moments of the BTC are related to the average arrival times of the solute and to the variance of the distribution of the arrival times, i.e., to basic features of the solute plume that is important that the models are able to describe.

Nevertheless, a proper computation of the experimental CBTC or of the temporal moments of the experimental BTC from the measurements of concentrations requires a sufficiently high sampling rate, which would be possible for a laboratory test, like case study C, but is more difficult to carry out for a large scale field test like case study D.

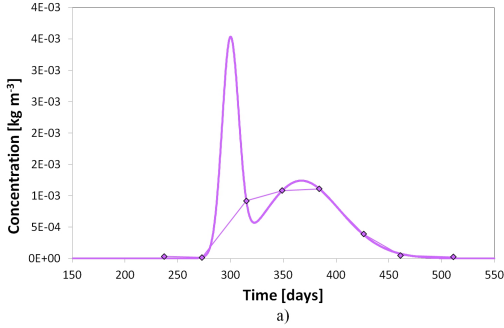
In order to illustrate a possible merit of the use of the temporal moments of the BTC for the inversion of the transport models, the results of the calibration of the UDPerM with respect to χ_4 , represented in Figure 7.8e), are considered. As observed in section 7.2.6, the best-fit concentration curve for section $n=4$ is characterized by a very small misfit with respect to the experimental data, but its shape is not realistic. It is likely that, in this case, the use of the the temporal moments for the inversion would have not given this unrealistic result.

This hypothesis is supported by Figure 7.12, which reports the values of the temporal moments, up to the second order, of the concentration curve for section $n=4$ in the following cases: plot a) corresponds to Figure 7.8e), i.e., it refers to the best-fit of the UDPerM obtained through the optimization of χ_4 ; plot b) corresponds to Figure 7.8a), i.e., it refers to the best-fit of the UDPerM obtained through the optimization of χ_C ; plot c) corresponds to Figure 7.7e), i.e., it refers to the best-fit of the DPorM obtained through the optimization of χ_4 . The estimate of the experimental moments is reported in the bottom of Figure 7.12.

It is apparent that the different curves are characterized by different temporal moments; specifically, it can be noticed that the best approximation of the experimental moments M_0^{exp} and m_1^{exp} is obtained with the curve in plot c), that is, with the DPorM, whereas the best approximation of μ_2^{exp} is obtained with the curves in plots a) and b), that is, with the UDPerM. Since the curve in plot c) is more realistic than the curves in plots a) and b), it would have been expected that all the three experimental moments would have been better approximated with the curve in plot c). Nevertheless, it should be noticed that the curve in plot c), as well as most of the curves predicted by the DPorM (see figure 7.7), is characterized by a significant tail. As a consequence, the values of the moments reported in plot c) are, actually, the temporal moments of the truncated concentration curve.

This example shows that the use of the temporal moments in the inversion of the transport models could favor curves which are more realistic (plot c), despite their higher misfit with respect to the concentration data. Nevertheless, especially in the case of the DPorM, an accurate estimate of the model parameters with the method of moments requires proper techniques to match the temporal moments of the truncated concentration curve, as done, e.g., by Luo et al. (2006) for the SDM.

Furthermore, given the large number of parameters of the DDMs, the inversion of such models with the method of moments requires also the use of temporal moments of order higher than 2, otherwise the inverse problem would be underdetermined, as shown in section 6.1.6 for case study A. Nevertheless, as discussed by Jacobsen et al. (1992), the use of the higher order temporal moments can result in an unreliable parameter estimation; in fact, the proper computation of the higher order temporal moments can be significantly affected by small experimental errors in the tail of the BTC. Jacobsen et al. (1992) also observe that the concentration data obtained through conservative transport experiments in lysimeters are poorly described both by the standard SDM and by a two-region model, equivalent to the DPorM, when the parameters of the models are estimated with the method of moments, whereas the non-linear least-squares inversion using the concentration data has a greater flexibility and yields a better description of the experimental data; this conclusion supports the use of the concentration data, instead of the temporal moments of the BTC, in case studies C and D.

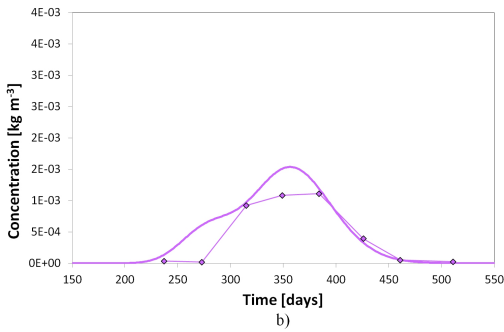


$$M_0 = 1.8 \cdot 10^{-1} \text{ kg d m}^{-3}$$

$$m_1 = 3.5 \cdot 10^2 \text{ d}$$

$$\mu_2 = 2.1 \cdot 10^3 \text{ d}^2$$

$$\chi_4 = 1.8 \cdot 10^{-5} \text{ kg m}^{-3}$$

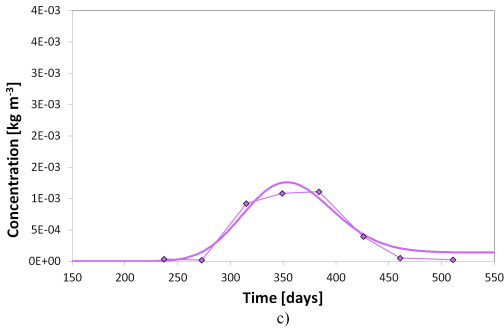


$$M_0 = 1.8 \cdot 10^{-1} \text{ kg d m}^{-3}$$

$$m_1 = 3.5 \cdot 10^2 \text{ d}$$

$$\mu_2 = 2.3 \cdot 10^3 \text{ d}^2$$

$$\chi_4 = 2.6 \cdot 10^{-4} \text{ kg m}^{-3}$$



$$M_0 = 1.5 \cdot 10^{-1} \text{ kg d m}^{-3}$$

$$m_1 = 3.7 \cdot 10^2 \text{ d}$$

$$\mu_2 = 3.4 \cdot 10^3 \text{ d}^2$$

$$\chi_4 = 1.2 \cdot 10^{-4} \text{ kg m}^{-3}$$

Experimental moments:

$$M_0^{\text{exp}} = 1.3 \cdot 10^{-1} \text{ kg d m}^{-3}$$

$$m_1^{\text{exp}} = 3.6 \cdot 10^2 \text{ d}$$

$$\mu_2^{\text{exp}} = 1.9 \cdot 10^3 \text{ d}^2$$

Figure 7.12: Comparison of the concentration curves and of their temporal moments for section $n=4$. Plot a): best-fit of the UDPerM obtained through the minimization of χ_4 . Plot b): best-fit of the UDPerM obtained through the minimization of χ_c . Plot c): best-fit of the DPorM obtained through the minimization of χ_4 .

In this work, 1D single and dual-domain transport models (SDM, DPorM, UDPerM, CDPerM) have been implemented and calibrated with the data of four different case studies, which include both numerical and real (laboratory and field) transport experiments performed at different spatial scales in alluvial sediments with different heterogeneity patterns.

In order to study the different situations, initial and boundary conditions have been applied to the models to describe both a pulse and a step solute injection. In particular, the SDM and UDPerM have been solved analytically in the case of a pulse injection, whereas a numerical scheme has been developed to solve these models and the coupled DPorM and CDPerM for both a pulse and a step injection. The numerical models have been validated by comparing their results with those given by HYDRUS-1D and, for the uncoupled models, with the analytical solution.

Some general concluding remarks can be drawn from the results of the application of the transport models to the different case studies.

Comparison of the performance of the different transport models

The DDMs permit to significantly improve, with respect to the SDM, the fit of the experimental data resulting from transport experiments in structured heterogeneous porous media characterized by the presence of PFPs (e.g., MB1 and MB2 for case study A and ensemble \mathcal{B} for case study B). On the other hand, when the PFPs are less marked, as for media which are homogeneous or characterized by a fully random or unstructured heterogeneity pattern, the SDM was shown to efficiently describe the experimental data (e.g., MB3 for case study A and ensemble \mathcal{A} for case study B).

Regarding the comparison between the performances of the three DDMs considered in this work, i.e., DPorM, UDPerM and CDPerM, the UDPerM is the model that most efficiently describes the transport properties of the sediments characterized by the presence of PFPs.

In fact, both DPerMs can describe the typical effects of PFPs on the solute transport, such as the presence of double peaks or of an early peak and a long tail in the BTCs, which are determined by velocity contrasts between the solute particles that travel in the high-permeability PFPs and in the low-permeability sediments. Nevertheless, the comparison of the results of the two DPerMs showed that, in all the tests, the CDPerM does not lead to a significant further improvement of the fit obtained with the UDPerM, so that the introduction of the exchange term between the two domains of the UDPerM is not important for the description of the transport properties of the portions of alluvial aquifers considered in this work. This may be explained considering that if the solute exchange is slow, then the description of the CDPerM is equivalent to that of the UDPerM;

on the other hand, if the solute exchange is fast, the concentrations in the two domains are at equilibrium, so that the description of the CDPerM is equivalent to that of a SDM. Since the results of the two DPerMs are equivalent, the UDPerM is preferable for two reasons: it has fewer parameters to be estimated in the model calibration and, at least for the pulse injection, it can be solved analytically; consequently, the calibration of the UDPerM is computationally much faster and robust.

Concerning the comparison between the DPerMs and the DPorM, it was shown that in case study A the DPerMs describe the experimental data significantly better than the DPorM, whereas in case studies C and D the DPerMs do not improve significantly the fit of the DPorM. These remarks can be justified in a relatively simple way. Case study A consists of three heterogeneous blocks of sediments, which are composed of hydrofacies characterized by different values of K and with different arrangements among the MBs. For MB1 and MB2, the highly conductive facies are connected to form PFPs, which give rise to asymmetric BTCs, with double peaks (see Figure 6.5a) or early peak and tailing (see Figure 6.5b). The DPerMs permit to take properly into account both the particles of solute that travel along the PFPs, i.e., in the fast domain, and the slower particles that travel in the less permeable sediments, i.e., in the slow domain. The DPorM, instead, is not a good model for these kinds of heterogeneous domains, as it assumes that the second domain is immobile. On the other hand, case study C consists of a homogeneous sand column, for which the asymmetry and tailing of the BTC cannot be related to the presence of PFPs, but it is probably due to the adsorption of the red dye on the sand, that may be possible at low flow rates, as suggested by Toloni (2011). In this case, the DPorM is a good model, as the adsorbed solute particles correspond to the particles in the immobile domain. Another possible explanation of the observed tailing is represented by the density-induced sinking that, according to the results of Istok and Humphrey (1995), may occur for the injected concentration used in this experiment.

In case study D, when the model calibration is performed for all the five sections simultaneously, the DPorM and the DPerMs share a similar value of the optimal objective function, which is a common result with case study C. Therefore, this result may be explained by the hypothesis that, as in case study C, the Cape Cod site is not characterized by the presence of PFPs. Nevertheless, it was shown that the SDM does not describe accurately the experimental data and that the DDMs perform slightly better than the SDM, even if the improvement is not so striking as in the other case studies. This result can have different explanations: it may be just due to the higher number of parameters of the DDMs that allows to improve the fit of the experimental data with respect to the SDM, or to effects caused by the 1D modeling of the 3D tracer test; it may also have more physical justifications, as the presence of some low-permeability sediments that store the tracer and form an immobile domain or the presence of a density-induced sinking of the tracer plume, which is well-established for this site by the analyses of, e.g., LeBlanc et al. (1991); Garabedian et al. (1991); Zhang et al. (1998). A connectivity analysis could help to choose the correct interpretation but is not available for the Cape Cod site. However, the few following remarks could provide some arguments for these hypotheses.

The estimated value of $\text{var}[\ln K]$ is 0.26 (LeBlanc et al., 1991), which is very small with respect to the values of this parameter for the blocks of case study A and B (see Tables 6.1 and 6.13) or for other sites, as the MADE site, for which $\text{var}[\ln K]=4.5$ (Rehfeldt et al., 1992). This observation supports the hypothesis that the Cape Cod site is more homogeneous than the other examples considered in this work; nevertheless, as stated in section 6.1.11, the main factor that controls the presence of PFPs is not $\text{var}[\ln K]$, but the connectivity of the high-permeability facies.

Konikow (2011) observes that “the applications of numerical solute-transport models

indicate that conventional numerical models based on the Fickian ADE can adequately simulate transport of non reactive and reactive solute species in this aquifer", referring to the modeling works by Garabedian et al. (1991), Zhang et al. (1998) and Parkhurst et al. (2003).

As the medium can be considered quite homogeneous and the SDMs applied in previous works were satisfactory, the improvement of the fit of experimental data given by the DDMs in this work is hardly related to the presence of very low- K or even immobile domains.

Moreover, the results for MB3 of case study A have not shown relevant improvements of the DDMs with respect to the SDM, despite the high number of parameters of the DDMs, which, therefore, should not be the main factor to reduce the misfit between model outcomes and observations.

As a consequence, the ability of the DDMs to simulate the deviations from the assumed average 1D flow and to take partially into account the effects of the density-induced sinking seem to be the most plausible reasons for the slightly improved descriptions of case study D provided by the DDMs with respect to the SDM.

The conclusions in this paragraph have been drawn from the results of different approaches: comparison between the best-fit parameters of the transport models, between the graphs of the BTCs or CBTCs, as well as between the characteristics times for advection and exchange and between two dimensionless numbers that permit to quantitatively assess the relative importance of the three transport mechanisms that are considered at "large" scale: advection, dispersion and coupling between slow/fast or mobile/immobile domains.

Relation between the effective parameters of the transport models and the heterogeneity pattern

For both case studies A and B, an accurate geological and hydrostratigraphical model, a geostatistical simulation and a connectivity analysis permitted to obtain a detailed characterization of the heterogeneity pattern of the blocks of sediments. In both cases, a qualitative correlation between the connectivity indicators and the transport properties has been observed; the relevance of this relation has been primarily shown by the results of the statistical analysis on the two ensembles of equiprobable realizations in case study B.

A quantitative analysis of the relation between connectivity indicators and effective flow and transport parameters of the SDM and UDPerM has been attempted with a PCA, which was performed on the ensembles of equiprobable geostatistical realizations of case study B. This analysis has shown that the connectivities of the most permeable facies G appear among the most relevant quantities of the low-order PCs, as well as the hydrodispersive parameters of the fast domain of the UDPerM, whereas the parameters of the slow domain are of minor importance for the description of the transport features.

Therefore, this study provides further evidence about the statement proposed by several Authors (e.g., Fogg (1986); Poeter and Townsend (1994); Scheibe and Yabusaki (1998); LaBolle and Fogg (2001); Zinn and Harvey (2003); Zappa et al. (2006); Konikow (2011)) that the interconnectedness of high-conductivity sediments is more important than the actual conductivity values to control the solute fate and to determine non-Fickian transport behaviour.

Moreover, it is shown that a preliminary analysis of the volume of sediments, based on sedimentological, geostatistical and connectivity analysis, is important to decide

whether a dual domain approach, which requires more computational effort than a classical SDM, is necessary.

Remarks on the calibration with the LM algorithm

In this work, the models calibration is based on the LM algorithm, which is a standard non-linear least-squares approach. The model calibration for the UDPerM showed the well known difficulties of the inverse problems when non-linear least squares are applied. In particular, a gradient-based algorithm might fail to find a minimum, if it explores a region of the parameter space for which the objective function is quite constant, or might fall into a local minimum, so that the issue of the non-uniqueness of the solution of the inverse problem arises and an analysis of the best-fit parameters corresponding to the different minima is necessary. The results of the application of the analytical UDPerM to case study A showed that the local minima obtained from the calibration of the UDPerM often correspond to the physical situation described by the SDM.

The performed tests confirmed the importance of the initial set of parameters in order to reach the global minimum of the objective function, which shows a complex dependence on several variables, and to find a physically plausible solution of the problem. On the other hand, the LM method proved to be quite robust with respect to the Hessian matrix of the objective function, which could often be ill-conditioned; the inverse of the Hessian matrix enters in the LM algorithm and is used also to estimate the correlation matrix of the parameters around the optimal values. No particular problems had to be faced during the search for the solution, but the ill-conditioning of the Hessian matrix prevented to draw conclusions about the uncertainty on the fitted parameters for some cases.

Pareto set as a possible indicator of PFPs

The analysis of the results of model calibration for the SDM in case study A within the framework of multi-objective optimization provides interesting information. In particular if the misfit between experimental and modelled CBTCs is split in the contribution of early and late times, then it is possible to draw an approximation of the Pareto frontier. For those cases which can be satisfactorily represented with a SDM, the Pareto frontier reduces to a single point. On the other hand, for those tests which present clear effects of PFPs and which require the UDPerM to improve the fit of the experimental data, the Pareto frontier is a wider set. These results suggest that the Pareto set could effectively be an indicator of the presence of PFPs in heterogeneous porous media.

Scale dependence of the best modelling approach

In this work the relevance of the DDMs is assessed for case studies involving very different scales of observation and data: from the 20-centimeter-long column of case C, to the meter- and decameter-sized blocks of cases A and B, to the 200-meter-long region studied in the Cape Cod field tracer test of case D. It would then be interesting to assess whether the relevance of the single and dual-domain models depends on the scale of observation.

Several theoretical and experimental studies on field tracer tests have highlighted some fundamental differences between the solute transport in large scale aquifers and in laboratory columns. In particular, as shown and discussed, e.g., by Dagan (1982, 1984); Gelhar and Axness (1983); Garabedian et al. (1991); Gelhar et al. (1992), the evolution of a plume in an aquifer cannot be explained using a constant dispersivity value, as

assumed by the Fickian theory; in fact, it was observed that the values of the dispersivity obtained at field sites are much larger than the values obtained in laboratory and that, even at a given scale of observation, the longitudinal dispersivity ranges over two or three orders of magnitude. Moreover, it was observed that the longitudinal dispersivity linearly increases with the displacement distance and gradually approaches a constant asymptotic value if the hydraulic conductivity field is stationary (i.e., statistically homogeneous) and has a finite correlation scale. Such results show that, at a sufficiently large scale of observation, a classical Fickian approach, with a constant macrodispersion coefficient, could be used to effectively describe the solute transport, whereas at smaller scales different non-Fickian models should be used to correctly describe and predict the solute movement.

In a similar way, the DDMs are relevant for the description of solute transport in structured heterogeneous porous formations when observed at small scales; as the scale of observation increases, it might be expected that the small-scale “dual” behaviour is averaged over larger volumes, so that the DDMs become less relevant and the solute transport can be effectively described by a SDM.

Nevertheless, this is not a general conclusion, as the large-scale behaviour is strongly affected by the sediments connectivity, which determines non-local effects in the solute transport, which cannot be described by a classical SDM. In particular, if the high-permeability sediments are poorly connected, then it is likely that the large-scale representation of the aquifer is that of a homogenous domain, since the small-scale effects of heterogeneity are averaged over large volumes. On the contrary, if the aquifer is characterized by a large connectivity of high-permeability sediments, i.e., by PFPs, then the DDMs should be more relevant than a SDM even at large-scale, because such models can properly describe the sub-plumes traveling with different velocities in the PFPs and in the low-permeability sediments.

These observations are supported by the results obtained by Zinn and Harvey (2003), who highlighted that very different flow and transport behaviours can occur in conductivity fields characterized by the same lognormal univariate K distribution and the same isotropic spatial covariance function, but with different connectivity patterns. Therefore, information on the connectedness of geologic media may be necessary to choose the form of the transport model to be applied in each specific situation.

In this work, it was observed that DDMs are relevant in case studies A, B (for ensemble \mathcal{B}) and C, that is, at scale lengths from 10 cm to 10 m, whereas for the Cape Cod tracer test the DDMs bring less significant improvement to the description of the SDM. Such results are in agreement with the above discussion; in fact, as previously mentioned, the Cape Cod site is not characterized by strong hydraulic conductivity contrasts and the presence of PFPs seems not to be an important feature of this site. It is then expected that the SDM properly describes the large-scale behaviour of the solute plume and that the DDMs do not show a major relevance, which is exactly what has been observed in the results of section 7.2.

Final remarks

The comparison of the different dual-domain approaches considered in this work indicates that, in order to correctly describe the transport of solutes in alluvial sediments characterized by the presence of PFPs, the UDPerM should be used. In other words, it is necessary that both domains are mobile; on the other hand, the two domains can be considered independent.

As mentioned in the Introduction, most applications of DDMs to saturated porous

media refer to the DPorM. In this work, it was shown that the DPerM approach is more relevant than the DPorM for the description of the transport properties of heterogeneous alluvial aquifers with PFPs, for which the velocity contrasts caused by the heterogeneity of the porous medium is not so strong as, e.g., for fractured rocks.

This conclusion is well supported by the results of the analysis of the numerical transport experiments (case studies A and B), which were performed at relatively small spatial scales (meter to decameter), so that a detailed hydrofacies characterization and connectivity analysis were possible.

The Cape Cod tracer test represents a first step towards the generalization of this conclusion for alluvial aquifers at the scales of interest for practical applications (e.g., for the modeling of a possible contamination event or for the design of a contaminated aquifer remediation).

Considerations on the analytical solution of the CDPerM

The CDPerM with the initial and boundary conditions describing a pulse injection in a semi-infinite domain has been solved numerically in chapter 4. In fact, it was not possible to obtain an analytical solution of the coupled equations (2.35) and (2.36), for $x \in [0, +\infty)$ and $t \in [0, +\infty)$, with boundary conditions (2.54) to (2.55). Analytical solutions of initial-boundary value problems for linearly coupled systems of partial differential equations (PDEs) similar to those of the CDPerM can be found in the literature only in some special cases or with different boundary conditions.

For example, Skopp et al. (1981) proposed a perturbation method to solve the model equations for small interaction coefficient, i.e., for small α . In particular, their solution is not valid when the dimensionless interaction coefficient $\alpha L/(nv)$ is larger than 1.5.

The results of Walker (1987), together with those of Hill and Aifantis (1980), Hill (1981), Veling (2002) and Vanderborght et al. (2005), show that the analytical solution of equations (2.35) and (2.36) could be obtained with the method used in these works only in one of the two following situations:

- a) the condition $D^{(H)}/v^{(H)} = D^{(L)}/v^{(L)}$ holds;
- b) the spatial domain is infinite, $-\infty < x < +\infty$.

Condition a) does not hold in general for a dual-permeability medium. Moreover, as stated at the beginning of this chapter, in our case the domain is semi-infinite, so that neither condition b) holds.

In particular, Hill (1981) proposes the solution of the following system of coupled equations:

$$\frac{\partial u}{\partial t} = D_1 L(u) - au + bv, \quad (\text{A.1})$$

$$\frac{\partial v}{\partial t} = D_2 L(v) + cu - dv, \quad (\text{A.2})$$

where L is a linear spatial operator not involving time. The solution is given, both for zero and non-zero Dirichlet boundary data, in terms of integrals of two functions that solve the corresponding uncoupled problem, $\partial h/\partial t = L(h)$, with proper initial and boundary conditions. Equations (2.35) and (2.36) can be cast in the same form as equations (A.1) and (A.2), only if condition a) holds; in that case the operator L would be defined as:

$$L = -\frac{v}{D} \frac{\partial}{\partial x} + \frac{\partial^2}{\partial x^2}.$$

One of the applications presented in Hill (1981) is the model of an arms race, whose equations are analogous to (2.35) and (2.36) and are solved in a semi-infinite spatial domain with Dirichlet boundary conditions and a restrictive assumption equivalent to a) that allows to rewrite such equations in the form (A.1) and (A.2).

Walker (1987) proposes a method to solve analytically the following coupled set of PDEs:

$$\frac{\partial u}{\partial t} = -\sigma \frac{\partial u}{\partial x} + (1 + \beta)\mathbf{L}u - au + bv + \eta_1(\mathbf{x}, t) \quad \mathbf{x} \in \mathcal{V}, \quad (\text{A.3})$$

$$\frac{\partial v}{\partial t} = -\sigma \frac{\partial v}{\partial x} + \beta\mathbf{L}v + cu - dv + \eta_2(\mathbf{x}, t) \quad \mathbf{x} \in \mathcal{V}, \quad (\text{A.4})$$

with the initial conditions $u(\mathbf{x}, 0) = f_1(\mathbf{x})$ and $v(\mathbf{x}, 0) = f_2(\mathbf{x})$, where \mathbf{L} is a linear time-independent operator, a, b, c, d, β and σ are constants, f_1, f_2, η_1 and η_2 are given functions and \mathcal{V} is the spatial domain. If \mathcal{V} is finite, then the boundary conditions are represented by: $K_{ij}u = \xi_{ij}$ and $M_{ij}v = \chi_{ij}$, for $\mathbf{x} \in \mathcal{S}_j$, where K_{ij} and M_{ij} are linear time-independent operators, ξ_{ij}, χ_{ij} are given functions and \mathcal{S}_j are subsurfaces of the boundary of \mathcal{V} .

Walker (1987) showed that if $\sigma \neq 0$, then analytical solutions can generally be obtained only if \mathcal{V} is infinite in extent in the x coordinate; if $\sigma = 0$, instead, solutions can be obtained for a finite \mathcal{V} , with the boundary conditions stated above. In particular, the solution of these equations consists in a convolution of the Green's function corresponding to the operator \mathbf{L} and a function independent of \mathbf{L} .

Walker (1987) also applied his results to the modeling of the two-dimensional movement of solutes in a double-porous medium. Specifically, equations (A.3) and (A.4) reduce to the CDPerM equations (2.35) and (2.36) with the following substitutions:

$$\beta = \frac{D^{(L)}}{D^{(H)} - D^{(L)}},$$

$$\sigma = \frac{D^{(H)}v^{(L)} - D^{(L)}v^{(H)}}{D^{(H)} - D^{(L)}},$$

$$\mathbf{L} = \left(D^{(H)} - D^{(L)}\right) \frac{\partial^2}{\partial x^2} - \left(v^{(H)} - v^{(L)}\right) \frac{\partial}{\partial x},$$

and by setting $\eta_1 = \eta_2 = 0$, $a = b = \alpha / (\varepsilon^{(H)}n^{(H)})$, $c = d = \alpha / (\varepsilon^{(L)}n^{(L)})$.

Notice that, with these substitutions, condition $\sigma = 0$ corresponds to condition a), in which case the analytical solution could be derived in a finite (or semi-infinite) domain. The solution of the dual-permeability problem with $\sigma \neq 0$ is obtained by Walker (1987) for an infinite spatial domain, that is in situation b). Despite the fact that this solution is not applicable to our case, the Walker interestingly shows that, for short times, the two domains act independently from each other, while, for long times, the heterogeneous medium acts as a homogeneous medium with parameters (velocity and dispersion coefficient) that average the parameters of the two domains.

Velting (2002), by generalizing the method proposed by Walker (1987) to a system of three coupled equations, presented the analytical solution for the following triple-porosity problem, which consists in one PDE and two ordinary differential equations:

$$\frac{\partial c_1}{\partial t} = \mathbf{L}c_1 + \sum_{j=1}^3 a_{1j}c_j, \quad c_1(x, 0) = 0, \quad c_1(0, t) = c_b,$$

$$\frac{\partial c_i}{\partial t} = \sum_{j=1}^3 a_{ij} c_j, \quad c_i(x, 0) = 0, \quad i = 2, 3,$$

where \mathbf{L} is a linear second-order time-independent operator in x and a_{ij} are real constants. The solution is obtained, for $x \in [0, +\infty)$ and $t \in (0, +\infty)$, as the sum of several integrals that involve the following functions: w , which is the solution of the corresponding uncoupled problem, i.e., $\partial w / \partial t = \mathbf{L}w$ with $w(x, 0) = 0$ and $w(0, t) = c_b$; the Bessel functions I_0 and I_1 ; the Goldstein J -function.

Veling (2002) also observes that a solution to the initial value problem given by a system of three coupled PDEs of the same form as (A.1) and (A.2) can be obtained generalizing the technique developed by Walker (1987); this can be done in an infinite domain, in agreement with the results of Walker (1987) for two coupled PDEs.

Finally, Vanderborght et al. (2005) started from the results of Walker (1987) and reported the solution of the CDPeRM equations in an infinite soil profile with an initial concentration distribution of the form $\delta(x)$.

On the determination of the truncation errors for a Crank-Nicholson upwind approximation of the CDPerM

In this appendix the method developed by Ataie-Ashtiani et al. (1999) and outlined in section 4.1.5 is applied to determine the truncation errors for the finite difference approximation of the equations of the CDPerM with a Crank-Nicholson scheme, an upwind treatment of the convective term and a variable spatial grid.

For ease of notation, let $C^{(H)}$ and $C^{(L)}$ be denoted as C and B , respectively, $v^{(H)}$ and $v^{(L)}$ as v_1 and v_2 , $D^{(H)}$ and $D^{(L)}$ as D_1 and D_2 , $\varepsilon^{(H)}$ and $\varepsilon^{(L)}$ as ε_1 and ε_2 , $n^{(H)}$ and $n^{(L)}$ as n_2 and n_2 . With this notation, the equations of the CDPerM (2.35) and (2.36) become:

$$\frac{\partial C}{\partial t} = -v_1 \frac{\partial C}{\partial x} + D_1 \frac{\partial^2 C}{\partial x^2} - \frac{\alpha}{\varepsilon_1 n_1} (C - B), \quad (\text{B.1})$$

$$\frac{\partial B}{\partial t} = -v_2 \frac{\partial B}{\partial x} + D_2 \frac{\partial^2 B}{\partial x^2} + \frac{\alpha}{\varepsilon_2 n_2} (C - B). \quad (\text{B.2})$$

The Crank-Nicholson upwind finite difference approximation of equations (B.1) and (B.2), for the generic node i and at the time level ℓ , is given by:

$$\begin{aligned} \frac{C_i^{\ell+1} - C_i^\ell}{\Delta t_\ell} = & D_1 \left[\frac{1}{2} \frac{\frac{C_{i+1}^{\ell+1} - C_i^{\ell+1}}{\Delta x_i} - \frac{C_i^{\ell+1} - C_{i-1}^{\ell+1}}{\Delta x_{i-1}}}{\frac{1}{2}(\Delta x_{i-1} + \Delta x_i)} + \frac{1}{2} \frac{\frac{C_{i+1}^\ell - C_i^\ell}{\Delta x_i} - \frac{C_i^\ell - C_{i-1}^\ell}{\Delta x_{i-1}}}{\frac{1}{2}(\Delta x_{i-1} + \Delta x_i)} \right] + \\ & - v_1 \left[\frac{1}{2} \frac{C_i^{\ell+1} - C_{i-1}^{\ell+1}}{\Delta x_{i-1}} + \frac{1}{2} \frac{C_i^\ell - C_{i-1}^\ell}{\Delta x_{i-1}} \right] + \\ & - \frac{\alpha}{\varepsilon_1 n_1} \left[\frac{1}{2} (C_i^{\ell+1} - B_i^{\ell+1}) + \frac{1}{2} (C_i^\ell - B_i^\ell) \right], \quad (\text{B.3}) \end{aligned}$$

$$\begin{aligned}
\frac{B_i^{\ell+1} - B_i^\ell}{\Delta t_\ell} = & D_2 \left[\frac{1}{2} \frac{\frac{B_{i+1}^{\ell+1} - B_i^{\ell+1}}{\Delta x_i} - \frac{B_i^{\ell+1} - B_{i-1}^{\ell+1}}{\Delta x_{i-1}}}{\frac{1}{2}(\Delta x_{i-1} + \Delta x_i)} + \frac{1}{2} \frac{\frac{B_{i+1}^\ell - B_i^\ell}{\Delta x_i} - \frac{B_i^\ell - B_{i-1}^\ell}{\Delta x_{i-1}}}{\frac{1}{2}(\Delta x_{i-1} + \Delta x_i)} \right] + \\
& - v_2 \left[\frac{1}{2} \frac{B_i^{\ell+1} - B_{i-1}^{\ell+1}}{\Delta x_{i-1}} + \frac{1}{2} \frac{B_i^\ell - B_{i-1}^\ell}{\Delta x_{i-1}} \right] + \\
& + \frac{\alpha}{\varepsilon_2 n_2} \left[\frac{1}{2} (C_i^{\ell+1} - B_i^{\ell+1}) + \frac{1}{2} (C_i^\ell - B_i^\ell) \right]. \tag{B.4}
\end{aligned}$$

Approximating the different quantities in equations (B.3) and (B.4) with second order Taylor expansions, as explained in section 4.1.5, it is obtained:

$$\begin{aligned}
\left(1 + \frac{\alpha \Delta t_\ell}{2\varepsilon_1 n_1}\right) \frac{\partial C}{\partial t} = & -v_1 \frac{\partial C}{\partial x} + \left(D_1 + \frac{v_1 \Delta x_{i-1}}{2} - \frac{\alpha \Delta t_\ell^2}{4\varepsilon_1 n_1} v_1^2\right) \frac{\partial^2 C}{\partial x^2} + \\
& - \frac{\alpha}{\varepsilon_1 n_1} (C - B) + \frac{\alpha \Delta t_\ell}{2\varepsilon_1 n_1} \frac{\partial B}{\partial t} + \frac{\alpha \Delta t_\ell^2}{4\varepsilon_1 n_1} v_2^2 \frac{\partial^2 B}{\partial x^2},
\end{aligned}$$

$$\begin{aligned}
\left(1 - \frac{\alpha \Delta t_\ell}{2\varepsilon_2 n_2}\right) \frac{\partial B}{\partial t} = & -v_2 \frac{\partial B}{\partial x} + \left(D_2 + \frac{v_2 \Delta x_{i-1}}{2} + \frac{\alpha \Delta t_\ell^2}{4\varepsilon_2 n_2} v_2^2\right) \frac{\partial^2 B}{\partial x^2} + \\
& + \frac{\alpha}{\varepsilon_2 n_2} (C - B) - \frac{\alpha \Delta t_\ell}{2\varepsilon_2 n_2} \frac{\partial C}{\partial t} - \frac{\alpha \Delta t_\ell^2}{4\varepsilon_2 n_2} v_1^2 \frac{\partial^2 C}{\partial x^2},
\end{aligned}$$

which can be rewritten as:

$$\begin{aligned}
\frac{\partial C}{\partial t} = & - (v_1 + v_1^{\text{num}}) \frac{\partial C}{\partial x} + (D_1 + D_1^{\text{num}}) \frac{\partial^2 C}{\partial x^2} - \frac{\alpha}{\varepsilon_1 n_1} (C - B) + \\
& + \frac{\alpha \Delta t_\ell}{2\varepsilon_1 n_1} \frac{\partial B}{\partial t} + \frac{\alpha \Delta t_\ell^2}{4\varepsilon_1 n_1} v_2^2 \frac{\partial^2 B}{\partial x^2}, \tag{B.5}
\end{aligned}$$

$$\begin{aligned}
\frac{\partial B}{\partial t} = & - (v_2 + v_2^{\text{num}}) \frac{\partial B}{\partial x} + (D_2 + D_2^{\text{num}}) \frac{\partial^2 B}{\partial x^2} + \frac{\alpha}{\varepsilon_2 n_2} (C - B) + \\
& - \frac{\alpha \Delta t_\ell}{2\varepsilon_2 n_2} \frac{\partial C}{\partial t} - \frac{\alpha \Delta t_\ell^2}{4\varepsilon_2 n_2} v_1^2 \frac{\partial^2 C}{\partial x^2}, \tag{B.6}
\end{aligned}$$

where a numerical velocity and a numerical dispersion coefficient have been intro-

duced for each of the two domains:

$$\begin{aligned}
 v_1^{\text{num}} &= -\frac{\alpha\Delta t_\ell v_1}{2\varepsilon_1 n_1 + \alpha\Delta t_\ell}, \\
 D_1^{\text{num}} &= \frac{-2\alpha\Delta t_\ell D_1 + 2\varepsilon_1 n_1 \Delta x_{i-1} v_1 - \alpha\Delta t_\ell^2 v_1^2}{2(2\varepsilon_1 n_1 + \alpha\Delta t_\ell)}, \\
 v_2^{\text{num}} &= \frac{\alpha\Delta t_\ell v_2}{2\varepsilon_2 n_2 - \alpha\Delta t_\ell}, \\
 D_2^{\text{num}} &= \frac{2\alpha\Delta t_\ell D_2 + 2\varepsilon_2 n_2 \Delta x_{i-1} v_2 + \alpha\Delta t_\ell^2 v_2^2}{2(2\varepsilon_2 n_2 - \alpha\Delta t_\ell)}.
 \end{aligned}$$

As shown in section 4.1.5, the objective of this method is to group all the terms in such a way as to define numerical coefficients (a numerical velocity, a numerical dispersion coefficient and a numerical solute exchange coefficient), so that the corrected scheme is easily obtained by replacing the “true” coefficients with effective coefficients.

It is apparent that the equation for C , (B.5), contains two terms depending on $\frac{\partial B}{\partial t}$ and $\frac{\partial^2 B}{\partial x^2}$, respectively, while the equation for B , (B.6), contains two analogous terms depending on C . These terms cannot be included neither in the convective term nor in the dispersive term nor in the exchange term.

As a consequence, a correction scheme for the numerical approximation of the equations of the CDPerM, given by (B.1) and (B.2), cannot be easily obtained with this method.

This negative result is determined by the Crank-Nicholson treatment of the solute exchange term. For this reason, as explained in section 4.2, in this work it has been chosen to treat explicitly the solute exchange term in both the DPorM and the CDPerM.

References

- Anderson M.P. and Woessner W.W. (1991). *Applied groundwater modeling-simulation of flow and advective transport*. Academic Press, San Diego.
- Ataie-Ashtiani B. and Hosseini S.A. (2005a). Numerical errors of explicit finite difference approximation for two-dimensional solute transport equation with linear sorption. *Environ. Modell. Softw.*, 20:817–826.
- Ataie-Ashtiani B. and Hosseini S.A. (2005b). Error analysis of finite difference methods for two-dimensional advection-dispersion-reaction equation. *Adv. Water Resour.*, 28: 793–806.
- Ataie-Ashtiani B., Lockington D.A., and Volker R.E. (1995). Comment on removing numerically induced dispersion from finite difference models for solute and water transport in unsaturated soils. *Soil Sci.*, 160:442–443.
- Ataie-Ashtiani B., Lockington D.A., and Volker R.E. (1996). Numerical correction for finite difference solution of the advection-dispersion equation with reaction. *J. Contam. Hydrol.*, 23:149–156.
- Ataie-Ashtiani B., Lockington D.A., and Volker R.E. (1999). Truncation errors in finite difference models for solute transport equation with first-order reaction. *J. Contam. Hydrol.*, 35:409–428.
- Baratelli F., Giudici M., and Vassena C. (2011). Single and dual domain models to evaluate the effects of preferential flow paths in alluvial porous sediments. *Transport Porous Med.*, 87:465–484, doi:10.1007/s11242-010-9695-4.
- Baratelli F., Giudici M., and Parravicini G. (2012). Interpretation of transport experiments in alluvial sediments with single and dual-domain models. In preparation for *Transport Porous Med.*
- Bardsley W.E. (2003). Temporal moments of a tracer pulse in a perfectly parallel flow system. *Adv. Water Resour.*, 26:599–607.
- Barenblatt J.I., Zheltov I.P., and Kochina I.N. (1960). Basic concepts in the theory of seepage of homogeneous liquids in fissured rocks. *J. Appl. Math. Mech.*, 24:1286–1303.
- Bear J. (1979). *Hydraulics of groundwater*. Dover publications, Inc. Mineola, New York.
- Bear J. and Cheng A.H.-D. (2010). *Modeling groundwater flow and contaminant transport*. Springer.
- Bellin A., Salandin P., and Rinaldo A. (1992). Simulation of dispersion in heterogeneous porous formations: statistics, first-order theories, convergence of computations. *Water Resour. Res.*, 28(9):2211–2227.
- Berkowitz B. and Scher H. (1998). Theory of anomalous chemical transport in random fracture network. *Phys. Rev. E*, 57(5):5858–5869.

- Berkowitz B., Cortis A., Dentz M., and Scher H. (2006). Modeling non-fickian transport in geological formations as a continuous time random walk. *Rev. Geophys.*, 44(2):RG2003, doi:10.1029/2005RG000178.
- Bersezio R., Pavia F., Baio M., Bini A., Felletti F., and Rodondi C. (2004). Aquifer architecture of the Quaternary alluvial succession of the Southern Lambro Basin (Lombardy, Italy). *Il Quaternario*, 17(2/1):361–378.
- Bersezio R., Giudici M., and Mele M. (2007). Combining sedimentological and geophysical data for high resolution 3-D mapping of fluvial architectural elements in the Quaternary Po plain (Italy). *Sedimentary Geology*, 202:230–248.
- Bibby R. (1981). Mass transport of solutes in dual-porosity media. *Water Resour. Res.*, 17(4):1075–1081.
- Blasone R.S., Madsen H., and Rosbjerg D. (2007). Parameter estimation in distributed hydrological modelling: comparison of global and local optimisation techniques. *Nord. Hydrol.*, 38(4-5):451–476.
- Boyle D.P., Gupta H.V., and Sorooshian S. (2000). Toward improved calibration of hydrologic models: combining the strengths of manual and automatic methods. *Water Resour. Res.*, 36(12):3663–3674.
- Boyle D.P., Gupta H.V., Sorooshian S., Koren V., Zhang Z., and Smith M. (2001). Toward improved streamflow forecasts: value of semidistributed modeling. *Water Resour. Res.*, 37(11):2749–2759.
- Cattaneo L. (2008). Effetti dell'eterogeneità a scala fine sui processi di trasporto in mezzi porosi. Master's thesis, Università degli Studi di Milano.
- Charbenau R.J. (2006). *Groundwater hydraulics and pollutant transport*. Waveland Press.
- Cho J.S., Kim S.M., and Iordache I. (2011). Analysis of passive remediation of contaminated groundwater with dimensionless numbers. In: *2011 International Conference on Environment and BioScience*. IPCBEE vol.21 (2011), IACSIT Press, Singapore.
- Cirpka O.A. and Kitadinis P.K. (2000). Characterization of mixing and dilution in heterogeneous aquifers by means of local temporal moments. *Water Resour. Res.*, 36(5): 1221–1236.
- Coats K.H. and Smith B.D. (1964). Dead-end pore volume and dispersion in porous media. *Soc. Pet. Eng. J.*, 3(3):245–255.
- Dagan G. (1982). Stochastic modeling of groundwater flow by unconditional and conditional probabilities. 2. The solute transport. *Water Resour. Res.*, 18(4):835–848.
- Dagan G. (1983). Stochastic modelling of solute transport by groundwater flow: state of the art. In: *Relation of Groundwater Quantity and Quality (Proceedings of the Hamburg Symposium, August 1983)*. IAHS Publ. no. 146.
- Dagan G. (1984). Solute transport in heterogeneous porous formations. *J. Fluid Mech.*, 145:151–177.
- Dagan G. (1988). Time-dependent macrodispersion for solute transport in anisotropic heterogeneous aquifers. *Water Resour. Res.*, 24(9):1491–1500.
- Dagan G. (1989). *Flow and transport in porous formations*. Springer, New York.
- Dagan G. (1990). Transport in heterogeneous porous formations: spatial moments, ergodicity, and effective dispersion. *Water Resour. Res.*, 26(6):1281–1290.
- Dagan G. and Bresler E. (1979). Solute dispersion in unsaturated heterogeneous soil at field scale: I. Theory. *Soil Sci. Soc. Am. J.*, 43:461–467.
- Dagan G. and Neuman S.P. (1997). *Subsurface flow and transport: a stochastic approach*. Cambridge, UK: Cambridge University Press.
- de Marsily G. (1986). *Quantitative Hydrogeology. Groundwater Hydrology for Engineers*.

- Academic Press.
- dell'Arciprete D. (2010). *Connectivity, flow and transport models in a point bar-channel aquifer analogue*. PhD thesis, Università degli Studi di Milano.
- dell'Arciprete D., Bersezio R., Felletti F., Giudici M., Comunian A., and Renard P. (2012a). Comparison of three geostatistical methods for hydrofacies simulation: a test on alluvial sediments. *Hydrogeol J.*, 20:299–311, doi:10.1007/s10040-011-0808-0.
- dell'Arciprete D., Vassena C., Baratelli F., Giudici M., Bersezio R., and Felletti F. (2012b). Connectivity and Single/Dual domain transport models: tests on a point bar-channel analogue. In preparation for *Hydrogeol J.*
- Dentz M. and Berkowitz B. (2003). Transport behavior of a passive solute in continuous time random walks and multirate mass transfer. *Water Resour. Res.*, 39(5):1111, doi:10.1029/2001WR001163.
- Deutsch C.V. and Journel A.G. (1992). *Geostatistical software library and user's guide*. Oxford University Press, New York.
- Domenico P.A. and Schwartz F.W. (1998). *Physical and chemical hydrogeology*. John Wiley & Sons, 2nd edition.
- Feehley C.E. and Zheng C. (2000). A dual-domain mass transfer approach for modeling solute transport in heterogeneous aquifers: Application to the Macrodispersion Experiment (MADE) site. *Water Resour. Res.*, 36(9):2501–2515.
- Fetter C.W. (1999). *Contaminant hydrogeology*. Prentice-Hall, Upper Saddle River, New Jersey, 2nd edition.
- Fetter C.W. (2001). *Applied hydrogeology*. Prentice Hall, Upper Saddle River, New Jersey, 4 edition.
- Feyen J., Jacques D., Timmerman A., and Vanderborght J. (1998). Modelling water flow and solute transport in heterogeneous soils: a review of recent approaches. *J. Agr. Eng. Res.*, 70:231–256.
- Fitts C.R. (2002). *Groundwater science*. Academic Press.
- Flach G.P., Crisman S.A., and III F.J. Molz (2004). Comparison of single-domain and dual-domain subsurface transport models. *Ground Water*, 42(6):815–828.
- Fogg G.E. (1986). Groundwater flow and sand body interconnectedness in a thick multiple-aquifer system. *Water Resour. Res.*, 22:679–694.
- Forsythe G.E., Malcom M.A., and Moler C.B. (1977). *Computer methods for mathematical computations*. Englewood Cliffs, NJ: Prentice Hall.
- Garabedian S.P., LeBlanc D.R., Gelhar L.W., and Celia M.A. (1991). Large-scale natural-gradient tracer test in sand and gravel, Cape Cod, Massachusetts: 2. Analysis of spatial moments for a nonreactive tracer. *Water Resour. Res.*, 27(5):911–924.
- Gelhar L.W. and Axness C.L. (1983). Three-dimensional stochastic analysis of macrodispersion in aquifers. *Water Resour. Res.*, 19(1):161–180.
- Gelhar L.W., Welty C., and Rehfeldt K.R. (1992). A critical review of data on field-scale dispersion in aquifers. *Water Resour. Res.*, 28(7):1995–1974.
- Gerke H.H. (2006). Preferential flow descriptions for structured soils. *J. Plant Nutr. Soil Sci.*, 169:382–400.
- Gerke H.H. and van Genuchten M.T. (1993). A dual-porosity model for simulating the preferential movement of water and solutes in structured porous media. *Water Resour. Res.*, 29:305–319.
- Gerke H.H. and van Genuchten M.T. (1996). Macroscopic representation of structural geometry for simulating water and solute movement in dual-porosity media. *Adv. Water Resour.*, 19(6):343–351.

- Ginn T.R. (2001). Stochastic-convective transport with nonlinear reactions and mixing: finite streamtube ensemble formulation for multicomponent reaction systems with intra-streamtube dispersion. *J. Contam. Hydrol.*, 47:1–28.
- Ginn T.R., Haeri H., Massoudieh A., and Foglia L. (2009). Notes on groundwater age in forward and inverse modeling. *Transport Porous Med.*, 79:117–134.
- Giudici M. (2010). Modeling water flow and solute transport in alluvial sediments: scaling and hydrostratigraphy from the hydrological point of view. *Mem. Descr. Carta Geol. d'It.*, XC:113–120.
- Giudici M., Bersezio R., Felletti F., Baratelli F., Cattaneo L., Cavalli E., dell'Arciprete D., Mele M., Pessina L., and Vassena C. (2011). A multidisciplinary study of sediments' connectivity and transport parameters for aquifer analogues. In: *Models - Repositories of Knowledge (Proceedings ModelCARE2011 held at Leipzig, Germany, in September 2011) (IAHS Publ.)*.
- Goldberg D.E. (1989). *Genetic algorithms in search, optimization and machine learning*. Addison-Wesley Longman Publishing Co., Inc. Boston, MA, USA.
- Guadagnini A. and Neuman S.P. (1999). Nonlocal and localized analysis of conditional mean steady state flow in bounded, randomly nonuniform domains: 1. Theory and computational approach. *Water Resour. Res.*, 35(10):2999–3018.
- Gupta H.V., Sorooshian S., and Yapo P.O. (1998). Toward improved calibration of hydrologic models: multiple and noncommensurable measures of information. *Water Resour. Res.*, 34(4):751–763.
- Haggerty R. and Gorelick S.M. (1995). Multiple-rate mass transfer for modeling diffusion and surface reactions in media with pore-scale heterogeneity. *Water Resour. Res.*, 31(10):2383–2400.
- Haggerty R. and Gorelick S.M. (1998). Modeling mass transfer processes in soil columns with pore-scale heterogeneity. *Soil Sci. Soc. Am. J.*, 62:62–74.
- Haggerty R., McKenna S.A., and Meigs L.C. (2000). On the late-time behavior of tracer test breakthrough curves. *Water Resour. Res.*, 36(12):3467–3479.
- Harvey C. and Gorelick S.M. (2000). Rate-limited mass transfer or macrodispersion: Which dominates plume evolution at the Macrodispersion Experiment (MADE) site? *Water Resour. Res.*, 36(3):637–650.
- Hill J.M. (1981). On the solution of reaction-diffusion equations. *IMA J. Appl. Math.*, 27:177–194.
- Hill J.M. and Aifantis E.C. (1980). On the theory of diffusion in media with double diffusivity II. Boundary-value problems. *Q. J. Mech. Appl. Math.*, 33:23–41.
- Istok J.D. and Humphrey M.D. (1995). Laboratory investigation of buoyancy-induced flow (plume sinking) during two-well tracer tests. *Ground Water*, 33(4):597–604.
- Jacobsen O.H., Leij F.J., and van Genuchten M.T. (1992). Parameter determination for chloride and tritium transport in undisturbed lysimeters during steady flow. *Nordic Hydrol.*, 23:89–104.
- Jarvis N.J., Jansson P.E., Dik P.E., and Messing I. (1991). Modeling water and solute transport in macroporous soils. I. Model description and sensitivity analysis. *J. Soil. Sci.*, 42:59–70.
- Julian H.E., Boggs J.M., Zheng C., and Feehley C.E. (2001). Numerical simulation of a natural gradient tracer experiment for the Natural Attenuation Study: flow and physical transport. *Ground Water*, 39(4):534–545.
- Kirkpatrick S., Gelatt C.D., and Vecchi M.P. (1983). Optimization by simulated annealing. *Science*, 220(4598):671–680.

- Knudby C. and Carrera J. (2005). On the relationship between indicators of geostatistical, flow and transport connectivity. *Adv. Water Resour.*, 28(4):405–421, doi:10.1016/j.advwatres.2004.09.001.
- Köhne J.M., Köhne S., and Šimůnek J. (2009). A review of model applications for structured soils: a) Water flow and tracer transport. *J. Contam. Hydrol.*, 104:4–35.
- Konikow L.F. (2011). The secret to successful solute-transport modeling. *Ground Water*, 49(2):144–159.
- Kreft A. and Zuber A. (1978). On the physical meaning of the dispersion equation and its solutions for different initial and boundary conditions. *Chem. Eng. Sci.*, 33:1471–1480.
- Kuntz D. and Grathwohl P. (2009). Comparison of steady-state and transient flow conditions on reactive transport of contaminants in the vadose soil zone. *J. Hydrol.*, 369: 225–233.
- LaBolle E.M. and Fogg G.E. (2001). Role of molecular diffusion in contaminant migration and recovery in alluvial aquifer system. *Transport Porous Med.*, 42:155–179.
- Lantz R.B. (1971). Quantitative evaluation of numerical diffusion (truncation error). *Soc. Petrol. Eng. J.*, 11:315–320.
- Lapidus L. and Amundson N.L. (1952). Mathematics of adsorption in beds. VI. The effect of longitudinal diffusion in ion exchange and chromatographic columns. *J. Phys. Chem.*, 56:984–988.
- Lassey K.R. (1988). Unidimensional solute transport incorporating equilibrium and rate-limited isotherms with first-order loss: 1. Model conceptualizations and analytic solutions. *Water Resour. Res.*, 24(3):343–350.
- LeBlanc D.R., Garabedian S.P., Hess K.M., Gelhar L.W., Quadri R.D., Stollenwerk K.G., and Wood W.W. (1991). Large-scale natural gradient tracer test in sand and gravel, Cape Cod, Massachusetts I. Experimental design and observed tracer movement. *Water Resour. Res.*, 27(5):895–910.
- Lee S.Y., Carle S.V., and Fogg G.E. (2007). Geologic heterogeneity and a comparison of two geostatistical models: Sequential Gaussian and transition probability-based geostatistical simulation. *Adv. Water Resour.*, 30:1914–1932.
- Lim K.T. and Aziz K. (1995). Matrix-fracture transfer shape factors for dual-porosity simulators. *J. Pet. Sci. Eng.*, 13:169–178.
- Liu G., Zheng C., and Gorelick S.M. (2004). Limits of applicability of the advection-dispersion model in aquifers containing high-conductivity channels. *Water Resour. Res.*, 40(8):W08308, doi:10.1029/2003WR002735.
- Liu G., Zheng C., and Gorelick S.M. (2007). Evaluation of the applicability of the dual-domain mass transfer model in porous media containing connected high-conductivity channels. *Water Resour. Res.*, 43(12):W12407, doi:10.1029/2007WR005965.
- Liu G., Zheng C., Tick C.R., Butler Jr. J.J., and Gorelick S.M. (2010). Relative importance of dispersion and rate-limited mass transfer in highly heterogeneous porous media: analysis of a new tracer test at the Macrodispersion Experiment (MADE) site. *Water Resour. Res.*, 46(3):W03524, doi:10.1029/2009WR008430.
- Luo J., Cirpka O.A., and Kitadinis P.K. (2006). Temporal-moment matching for truncated breakthrough curves for step or step-pulse injection. *Adv. Water Resour.*, 29:1306–1313.
- Luo J., Cirpka O.A., Dentz M., and Carrera J. (2008). Temporal moments for transport with mass transfer described by an arbitrary memory function in heterogeneous media. *Water Resour. Res.*, 44(1):W01502, doi:10.1029/2007WR006262.
- Lyness J.N. (1969). Notes on the adaptive Simpson quadrature routine. *J. ACM*, 16(3): 483–495.

- Ma L. and Selim H.M. (1995). Transport of a nonreactive solute in soils: a two-flow domain approach. *Soil Sci.*, 159(4):224–234.
- Mackay D.M., Freyberg D.L., and Roberts P.V. (1986). A natural gradient experiment on solute transport in a sand aquifer: 1. Approach and overview of plume movement. *Water Resour. Res.*, 22(13):2017–2029.
- Madsen H. (2003). Parameter estimation in distributed hydrological catchment modelling using automatic calibration with multiple objectives. *Adv. Water Resour.*, 26: 205–216.
- McKeeman W.M. (1962). Algorithm 145: Adaptive numerical integration by Simpson's rule. *Commun. ACM*, 5(12):604.
- Moldrup P., Kruse C.W., Yamaguchi T., and Rolston D.E. (1996). Modelling diffusion and reaction in soils: I. A diffusion and reaction corrected finite difference calculation scheme. *Soil Sci.*, 161:347–354.
- Morales-Casique E., Neuman S.P., and Guadagnini A. (2006). Non-local and localized analyses of non-reactive solute transport in bounded randomly heterogeneous porous media: Theoretical framework. *Adv. Water Resour.*, 29(5):1238–1255.
- Naff R.L. (1992). Arrival times and temporal moments of breakthrough curves for an imperfectly stratified aquifer. *Water Resour. Res.*, 28(1):53–68.
- Neuman S.P. (2004). Stochastic groundwater models in practice. *Stoch. Environ. Res. and Risk Ass.*, 18:268–270.
- Neuman S.P. and Tartakovsky D. (2009). Perspective on theories of non-fickian transport in heterogeneous media. *Adv. Water Resour.*, 32:670–680.
- Ogata A. and Banks R.B. (1961). A solution of the differential equation of longitudinal dispersion in porous media. *U.S. Geological Survey Professional Paper 411-A*.
- Ostensen R.W. (1998). Tracer tests and contaminant transport rates in dual-porosity formations with application to the WIPP. *J. Hydrol.*, 204:197–216.
- Parker J.C. and van Genuchten M.T. (1984). Flux-averaged and volume-averaged concentrations in continuum approaches to solute transport. *Water Resour. Res.*, 20(7): 866–872.
- Parkhurst D.L., Stollenwerk K.G., and Colman J.A. (2003). Reactive-transport simulation of phosphorus in the sewage plume at the Massachusetts Military Reservation, Cape Cod, Massachusetts. Technical report, U.S. Geological Survey Water-Resources Investigation Report.
- Poeter E. and Townsend P. (1994). Assessment of critical flow path for improved remediation management. *Ground Water*, 32:439–447.
- Press W.H., Flannery B.P., Teukolsky S.A., and Vetterling W.T. (1989). *Numerical Recipes: the Art of Scientific Computing (Fortran version)*. Cambridge University Press, Cambridge.
- Puente C.E., Robayo O., and Sivakumar B. (2001). A fractal-multifractal approach to groundwater contamination. 2. Predicting conservative tracers at the Borden site. *Stoch. Env. Res. Risk A.*, 15:372–383.
- Rao P.S.C., Jessup R.E., Rolston D.E., Davidson J.M., and Kilcreas D.P. (1980a). Experimental and mathematical description of nonadsorbed solute transfer by diffusion in spherical aggregates. *Soil Sci. Soc. Am. J.*, 44:684–688.
- Rao P.S.C., Rolston D.E., Jessup R.E., and Davidson J.M. (1980b). Solute transport in aggregated porous media: theoretical and experimental evaluation. *Soil Sci. Soc. Am. J.*, 44:1139–1146.
- Rausch R., Schäfer W., Therrien R., and Wagner C. (2005). *Solute transport modelling. An*

- introduction to models and solution strategies*. Gebr. Borntraeger Verlagsbuchhandlung, Berlin - Stuttgart.
- Rehfeldt K.R., Boggs J.M., and Gelhar L.W. (1992). Field study of dispersion in a heterogeneous aquifer, 3, Geostatistical analysis of hydraulic conductivity. *Water Resour. Res.*, 28(12):3309–3324.
- Ronayne M.J., Gorelick S.M., and Zheng C. (2010). Geological modeling of submeter scale heterogeneity and its influence on tracer transport in a fluvial aquifer. *Water Resour. Res.*, 46(10):W10519, doi:10.1029/2010WR009348.
- San Jose Martinez F., Pachepsky Y., and Rawls W. (2007). Fractional advective-dispersive equation as a model of solute transport in porous media. In: Sabatier J., Agrawal O.P., and Tenreiro Machado J.A., editors, *Advances in Fractional Calculus*, pages 199–212. Springer Netherlands.
- Scheibe T. and Yabusaki S. (1998). Scaling of flow and transport behaviour in heterogeneous groundwater systems. *Adv. Water Resour.*, 22:223–238.
- Schwartz R.C., Juo A.S.R., and McInnes K.J. (2000). Estimating parameters for a dual-porosity model to describe non-equilibrium, reactive transport in a fine-textured soil. *J. Hydrol.*, 229:149–167.
- Seeboonruang U. and Ginn T.R. (2006). Upscaling heterogeneity in aquifer reactivity via exposure-time concept: Forward model. *J. Contam. Hydrol.*, 84:127–154.
- Skopp J., Gardner W.R., and Tyler E.J. (1981). Solute movement in structured soils: two-region model with small interaction. *Soil Sci. Soc. Am. J.*, 45:837–842.
- Stagnitti F., Allinson G., Morita M., Nishikawa M., Il H., and Hirata T. (2000). Temporal moments analysis of preferential solute transport in soils. *Environ. Model. Assess.*, 5: 229–236.
- Stauffer D. and Aharony A. (1994). *Introduction to percolation theory*. Taylor & Francis, London.
- Strebelle S. (2002). Conditional simulation of complex geological structures using multiple-point statistics. *Math. Geol.*, 34(1):1–21.
- Sudicky E.A. (1986). A natural gradient experiment on solute transport in a sand aquifer: spatial variability of hydraulic conductivity and its role in the dispersion process. *Water Resour. Res.*, 22(13):2069–2082.
- Thorbjarnarson K.W. and Mackay D.M. (1997). A field test of tracer transport and organic contaminant elution in a stratified aquifer at the Rocky Mountain Arsenal (Denver, Colorado, U.S.A.). *J. Contam. Hydrol.*, 24:287–312.
- Toloni I. (2011). Methodological and experimental study of the transport of nanoparticles in an unsaturated porous medium. Master's thesis, Università degli Studi di Milano.
- Toride N., Leij F.J., and van Genuchten M.T. (1993). A comprehensive set of analytical solutions for nonequilibrium solute transport with first-order decay and zero-order production. *Water Resour. Res.*, 29(7):2167–2182.
- van Genuchten M.T. and Gray W.G. (1978). Analysis of some dispersion corrected numerical schemes for solution of the transport equation. *Int. J. Numer. Meth. Eng.*, 12: 387–404.
- van Genuchten M.T. and Parker J.C. (1984). Boundary conditions for displacement experiments through short laboratory soil columns. *Soil Sci. Soc. Am. J.*, 48:703–708.
- van Genuchten M.T. and Wierenga P.J. (1976). Mass transfer studies in sorbing porous media I. Analytical solutions. *Soil Sci. Soc. Am. J.*, 40(4):473–481.
- Vanderborght J., Kasteel R., Herbst M., Javaux M., Thiéry D., Vanclooster M., Mouvet C., and Vereecken H. (2005). A set of analytical benchmarks to test numerical models of

- flow and transport in soils. *Vadose Zone J.*, 4:206–221.
- Varni M. and Carrera J. (1998). Simulation of groundwater age distributions. *Water Resour. Res.*, 34(12):3271–3281.
- Vassena C., Cattaneo L., and Giudici M. (2010). Assessment of the role of facies heterogeneity at the fine scale by numerical transport experiments and connectivity indicators. *Hydrogeol J.*, 18:651–668, doi:10.1007/s10040-009-0523-2.
- Veling E.J.M. (2002). Analytical solutions for triple-porosity problems. In: Hassanizadeh S.M., Schotting R.J., Gray W.G., and Pinder G.F., editors, *Computational methods in water resources, Proceedings of the XIVth Conference on Computational Methods in Water Resources (CMWR XIV), June 23-28, 2002, Delft, The Netherlands*, pages 623–630, volume I. Elsevier Science B.V., Amsterdam, The Netherlands.
- Vrugt J.A., Gupta H.V., Bastidas L.A., Bouten W., and Sorooshian S. (2003). Effective and efficient algorithm for multiobjective optimization of hydrologic models. *Water Resour. Res.*, 39(8):1214, doi:10.1029/2002WR001746.
- Šimůnek J. and van Genuchten M.T. (2008). Modeling nonequilibrium flow and transport processes using HYDRUS. *Vadose Zone J.*, 7(2):782–797.
- Šimůnek J., Jarvis N.J., van Genuchten M.T., and Gärdenäs A. (2005). Error analysis of finite difference methods for two-dimensional advection-dispersion-reaction equation. *Adv. Water Resour.*, 28:793–806.
- Šimůnek J., Šejna M., Saito H., Sakai M., and van Genuchten M.T. (2009). *The HYDRUS-1D software package for simulating the one-dimensional movement of water, heat and multiple solutes in variably-saturated media. Version 4.08*. Department of environmental sciences, University of California, Riverside.
- Walker G.R. (1987). Solution to a class of coupled linear partial differential equations. *IMA J. Appl. Math.*, 38:35–48.
- Warren J.E. and Root P.J. (1963). The behavior of naturally fractured reservoirs. *Soc. Pet. Eng. J.*, 4:73–84.
- Yapo P.O., Gupta H.V., and Sorooshian S. (1998). Multi-objective global optimization for hydrologic models. *J. Hydrol.*, 204:83–97.
- Ye M., Neuman S.P., Guadagnini A., and Tartakovsky D.M. (2004). Nonlocal and localized analysis of conditional mean transient flow in bounded, randomly heterogeneous porous media. *Water Resour. Res.*, 40(5):W05104, doi:10.1029/2003WR002099.
- Zappa G. (2002). La permeabilità dei sedimenti fluvioglaciali: simulazione geostatistica tridimensionale e modellazione del flusso idrico alla scala delle facies. Master's thesis, Università degli Studi di Milano.
- Zappa G., Bersezio R., Felletti F., and Giudici M. (2006). Modeling heterogeneity of gravel-sand, braided stream, alluvial aquifers at the facies scale. *J. Hydrol.*, 325:134–153.
- Zhang H., Schwartz F.W., Wood W.W., Garabedian S.P., and LeBlanc D.R. (1998). Simulation of variable-density flow and transport of reactive and nonreactive solutes during a tracer test at Cape Cod, Massachusetts. *Water Resour. Res.*, 34(1):67–82.
- Zhang Y. and Benson D.A. (2008). Lagrangian simulation of multidimensional anomalous transport at the MADE site. *Geophys. Res. Lett.*, 35(7):L07403, doi:10.1029/2008GL033222.
- Zhang Y., Benson D.A., and Baeumer B. (2007a). Predicting the tails of breakthrough curves in regional-scale alluvial systems. *Ground Water*, 45(4):473–484.
- Zhang Y., Benson D.A., Meerschaert M.M., and LaBolle E.M. (2007b). Space-fractional advection-dispersion equations with variable parameters: Diverse formulas, numeri-

- cal solutions, and applications to the Macrodispersion Experiment site data. *Water Resour. Res.*, 43(5):W05439, doi:10.1029/2006WR004912.
- Zheng C. and Gorelick S.M. (2003). Analysis of solute transport in flow fields influenced by preferential flowpaths at the decimeter scale. *Ground Water*, 41(2):142–155.
- Zheng C., Bianchi M., and Gorelick S.M. (2011). Lessons learned from 25 years of research at the MADE site. *Ground Water*, 49(5):649–662.
- Zimmerman R.W., Chen G., Hadgu T., and Bodvarsson G.S. (1993). A numerical dual-porosity model with semianalytical treatment of fracture/matrix flow. *Water Resour. Res.*, 29(7):2127–2137.
- Zinn B. and Harvey C.F. (2003). When good statistical models of aquifer heterogeneity go bad: A comparison of flow, dispersion, and mass transfer in connected and multivariate Gaussian hydraulic conductivity fields. *Water Resour. Res.*, 39(3):1955–1974.

List of Publications

As of January 2013

Refereed publications

- Giudici, M., **Baratelli, F.**, Castellani, G., and C. Vassena. 2012. Modeling the Antarctic ice sheet and ice shelves: assessing the effects of uncertainty on the model parameters by sensitivity analysis. In *Ice Sheets: Dynamics, Formation and Environmental Concerns* (J. Müller and L. Koch, Eds.), 121-142. Nova Science Publishers, Inc., Hauppauge, N.Y.
- **Baratelli, F.**, Giudici, M., and C. Vassena. 2012. A sensitivity analysis for an evolution model of the Antarctic ice sheet, *Reliability Engineering & System Safety*, **107**, 64-70.
- **Baratelli, F.**, Giudici, M. & C. Vassena. 2011. Dynamics of ice sheets: a critical review of the shallow-ice approximation. *Bollettino Geofisico*, anno XXXIV(1-4), 5-18.
- **Baratelli, F.**, Giudici, M., and C. Vassena. 2011. Single and dual-domain models to evaluate the effects of preferential flow paths in alluvial sediments. *Transport in Porous Media*, **87**(2), 465-484.

Publications in preparation

- **Baratelli, F.**, Giudici, M., and G. Parravicini, Interpretation of transport experiments in alluvial sediments with single and dual-domain models. In preparation for *Transport in Porous Media*.
- dell'Arciprete, D., **Baratelli, F.**, Bersezio, R., Felletti, F., Giudici, M., and C. Vassena. Single and dual domain transport models in a point bar-channel analogue. In preparation for *Hydrogeology Journal*.

Publications in conference proceedings and extended abstracts

- **Baratelli, F.**, Cattaneo, L., Vassena, C., Giudici, M., and G. Parravicini, Interpretation of numerical transport experiments in alluvial sediments with single-domain, dual-porosity and dual-permeability models, Geophysical Research Abstracts, Vol. 14, EGU2012-9222, 2012.

- **Baratelli, F.**, Castellani, G., Vassena, C., and M. Giudici, A sensitivity analysis for a thermomechanical model of the Antarctic ice sheet and ice shelves, *Geophysical Research Abstracts*, Vol. 14, EGU2012-9151, 2012.
- Giudici, M., Bersezio, R., **Baratelli, F.**, Cattaneo, L., dell'Arciprete, D., Felletti, F., and C. Vassena, Sediments' connectivity and transport properties: examples from alluvial aquifer analogues, *Epitome* (ISSN 1972-1552), 4, 21, doi:10.1474/Epitome.04.0059.Geoitalia2011, 2011.
- Castellani, G., Vassena, C., **Baratelli, F.**, and M. Giudici, Modeling the Antarctic ice sheet and ice shelves in the last 200,000 years, *Epitome* (ISSN 1972-1552), 4, 237, doi:10.1474/Epitome.04.0877.Geoitalia2011, 2011.
- Giudici, M., Bersezio, R., Felletti, F., **Baratelli, F.**, Cattaneo, L., Cavalli, E., dell'Arciprete, D., Mele, M., Pessina, L., and C. Vassena, A multidisciplinary study of sediments' connectivity and transport parameters for aquifer analogues, in *Models - Repositories of Knowledge (Proceedings ModelCARE2011 held at Leipzig, Germany, in September 2011)* (IAHS Publ.)
- Pessina, L., **Baratelli, F.**, Bersezio, R., Cattaneo, L., Cavalli, E., Felletti, F., Giudici, M., Mele, M., and C. Vassena, Fine scale 3D integrated study of fluvio-glacial sediments, *Geophysical Research Abstracts* (ISSN 1029-7006), 13, EGU2011-5843, 2011.
- **Baratelli, F.**, Bersezio, R., Giudici, M., Cattaneo, C., Vassena, C., dell'Arciprete, D., and F. Felletti, Sediments' connectivity and transport properties, *Geophysical Research Abstracts* (ISSN 1029-7006), 13, EGU2011-5981, 2011.
- Balconi, C., **Baratelli, F.**, Giudici, M., and C. Vassena, Modeling the Evolution of the Antarctic Ice Sheet in the 200 ky, *Procedia Social and Behavioral Sciences* (ISSN: 1877-0428), 2, 7603-7604, doi:10.1016/j.sbspro.2010.05.138, 2010.
- **Baratelli, F.**, Cattaneo, L., Giudici, M., and C. Vassena, Solute transport in geological porous media: estimation of dispersion coefficients, *Procedia Social and Behavioral Sciences* (ISSN: 1877-0428), 2, 7605-7606, doi:10.1016/j.sbspro.2010.05.139, 2010.
- dell'Arciprete, D., **Baratelli, F.**, Bersezio, R., Felletti, F., Giudici, M., and C. Vassena, Relating facies connectivity to flow and transport properties for a point bar-channel aquifer analogue, XVIII International Conference on Water Resources CMWR 2010 (J. Carrera, ed.) CIMNE, Barcelona, <http://congress.cimne.com/cmwr2010/Proceedings/docs/p140.pdf>, 2010.
- dell'Arciprete, D., **Baratelli, F.**, Bersezio, R., Felletti, F., Giudici, M., and C. Vassena, The characterization of a point bar-channel aquifer analogue: from geostatistical simulation to solute transport through hydrofacies connectivity, *Geophysical Research Abstracts* (ISSN 1029-7006), 12, EGU2010-4046, 2010.
- **Baratelli, F.**, Giudici, M., and C. Vassena, Interpretation of numerical transport tests with single and dual porous medium approaches, *Geophysical Research Abstracts* (ISSN 1029-7006), 12, EGU2010-4060, 2010.
- **Baratelli, F.**, Giudici, M., and C. Vassena, Dinamica delle calotte glaciali: una revisione critica della SIA (shallow-ice approximation), *Environment, including global change – Contributi e autori*, 8, 2009.

- Balconi, C., **Baratelli, F.**, Giudici, M., and C. Vassena, Verso la modellazione del reticolo idrografico subglaciale antartico: modellazione dinamica della calotta, *Environment, including global change – Contributi e autori*, 24, 2009.

Acknowledgments

I am deeply grateful to Professor Mauro Giudici for having guided my way in scientific education and research during these seven years, ranging from hydrology to glaciology; thanks for his continuous support and enthusiasm, for his constructive optimism when facing occasional bad results, for giving me the opportunity to keep alive the fascinating field of ice-sheet modeling, initiated with my Master thesis, while developing a challenging PhD project on solute transport in groundwater.

I warmly acknowledge Professor Guido Parravicini for his clarifications of continuum physics and for his valuable assistance with the search for analytical solutions.

My sincere gratitude to the two referees, Professors Ghislain de Marsily and Tim Ginn, for having accepted to review my work, for their positive comments, insightful observations and useful suggestions that definitely improved this manuscript.

Thanks to all those who provided the data of the different case studies: Denis LeBlanc of U.S. Geological Survey for the Cape Cod field tracer test, Ivan Toloni, François Lehmann, Philippe Ackerer of LHyGeS (Laboratoire d'Hydrologie et de Géochimie de Strasbourg, Université de Strasbourg) for the laboratory tracer test on the sand column, Diana dell'Arciprete and Laura Cattaneo of Dipartimento di Scienze della Terra (Milano) for the numerical tracer tests on the block of sediments.

I would like to thank my office mates and dear friends, Chiara and Laura, for sharing with me the joyful, funny and difficult moments encountered during these years, as well as for making more pleasant the conferences, by means of cultural and culinary digressions. Thanks also to Diana, for her company during the travels to my first two conferences.

Many friends are to thank outside the research group, especially my old friend Daniela for all the useful and pleasant chats during our evening walks in Cene, and Anna and Simona, for the great experiences we lived together, particularly the treks in the Alps and the Dolomites.

My family has always been a continuous source of affection and support: my warmest thanks to my parents Marina and Adriano, to my sister Valentina, to the little Federico, despite/because of his never-ending calls distracting me from work, and to the affectionate Sissi.

At last, I am simply truly grateful to my dearest Pascal, my inspiring strength and precious happiness, for being with me, for the enchanting unmarked path he is tracing with me, for the outstanding landscapes we have shared both in the mountains and in our souls.

*On the gentle snowy slope of Altino,
January 2013*